Bayesian Inference in Statistical Analysis of Paleoclimate Records

by

Seonmin Ahn

B.S., Korea Advanced Institute of Science and Technology; Daejeon, Korea, 2007

M.S., Korea Advanced Institute of Science and Technology; Daejeon, Korea, 2009

Sc.M., Brown University; Providence, RI, 2011

A dissertation submitted in partial fulfillment of the

requirements for the degree of Doctor of Philosophy

in The Division of Applied Mathematics at Brown University

PROVIDENCE, RHODE ISLAND

May 2016

This dissertation by Seonmin Ahn is accepted in its present form
by The Division of Applied Mathematics as satisfying the
dissertation requirement for the degree of Doctor of Philosophy.

Date________________ ____

Charles E. Lawrence, Ph.D., Advisor

Recommended to the Graduate Council

Date________________ ____

Timothy Herbert, Ph.D., Reader

Date________________ ____

Lorraine Lisiecki, Ph.D., Reader

Approved by the Graduate Council

Date________________ ____

Peter Weber, Dean of the Graduate School

Vitae

Seonmin Ahn was born on January 2, 1985, in Daegu, Korea. She received her Bachelor's of Science in Applied Mathematics and Civil & Environmental Engineering from the Korea Advanced Institute of Science and Technology (KAIST) in 2007 and her Master's of Science in Mathematical Sciences under the supervision of Professor Chang-Ock Lee from KAIST in 2009. In 2010, she began studying in the Division of Applied Mathematics at Brown University on a five-year scholarship from SAMSUNG and received her second Master's of Science degree in 2011. In addition to several teaching assistantships, she taught Statistical Inference (summer 2015) as the primary instructor. As a Ph.D. candidate in the Division of Applied Mathematics at Brown University, she has been advised and mentored by Professor Charles E. Lawrence and defended her Ph.D. thesis on April 22, 2016.

Acknowledgements

There are many people who have made this journey possible and I would like to take this opportunity to extend my deep gratitude to them.

First and foremost, I would like to sincerely thank my advisor, Professor Charles Lawrence for his support and encouragement over the years. I would also like to thank Professor Timothy Herbert and Professor Lorraine Lisiecki for being on my committee and for giving me invaluable feedback on my thesis. It has been a privilege to work with these professors as well as Professor Baylor Fox-Kemper and Dr. Deborah Khider. I am grateful to my former advisor, Professor Chang-Ock Lee, for the support he offered me for so many years. I would also particularly like to thank my friends and colleagues who walked this journey with me.

Most importantly, I want to thank my family. I deeply appreciate their limitless support and belief in me. Lastly, I would love to thank my husband, Hansem, along with my lovely daughter, Anne, for always being there for me.[1]

---

[1] Korean Translation: 박사과정이라는 긴 여정을 마무리할 수 있도록 도움을 주신 분들에게 감사의 인사를 드립니다.

무엇보다 박사과정동안 저를 지도해주신 Charles Lawrence 교수님께 큰 감사를 드립니다. 또한 저의 논문 심사를 해 주신 Timothy Herbert 교수님, Lorraine Lisiecki 교수님께도 감사의 말씀을 전합니다. 박사과정동안 함께 연구할 기회를 주신 세 교수님, 그리고 Baylor Fox-Kemper 교수님, Deborah Khider 박사님, 진심으로 감사드립니다. 석사과정동안 저를 지도해주시고, 박사과정을 시작할 수 있도록 도움을 주신 이창옥 교수님께도 감사의 말씀을 전합니다. 함께 박사과정 생활을 했던 친구들에게도 함께 해주어 고맙다는 인사를 전합니다.

마지막으로, 언제나 저를 믿고 지지해준 가족들, 그리고 언제나 저를 웃음짓게 해주는 한샘이와 사랑스런 딸에게 고마운 마음을 전합니다.

Abstract of “ Bayesian Inference in Statistical Analysis of Paleoclimate Records ”
by Seonmin Ahn, Ph.D., Brown University, May 2016

Studies in paleoclimatology should be accompanied by uncertainty analyses, as uncertainty is found within the very first measurements of the proxies imprinted in geological records. From there, due to the nature of measurements and the complexity of the methods, uncertainty continues to increase throughout the process of analysis. Complete descriptions of paleoclimate records are achieved only through using algorithms that consider uncertainties that are inherent to both paleoclimate records and methods of analysis.

In this thesis, we introduce three statistical tools based on Bayesian inference to analyze paleoclimate records and present results using the three tools. First, we construct a probabilistic stack from globally distributed benthic $\delta^{18}O$ records using a profile hidden Markov model. Next, we investigate the relative timings of glacial terminations between the eastern and western tropical Pacific by combining three statistical tools: Bayesian calibration, HMM-Match algorithm, and Bayesian change point algorithm. Lastly, we analyze multidimensional paleoclimate proxies measured from the core at the central Peru margin to obtain their cross-correlation and underlying state changes using the Kalman filter and the autoregressive hidden Markov model. we expect the statistical tools that we introduce in this thesis to play a critical role in rigorously analyzing paleoclimate data.

Contents

List of Tables

List of Figures

CHAPTER ONE

Introduction

Paleoclimatology encompasses a diverse range of studies, which include core excavation, proxy measurement, modeling of climate change, pattern recognition, and so on. Several factors make paleoclimate research more challenging, such as complexity of modeling due to a large number of variables that affect climate changes and limitations in records of high quality. Furthermore, we obtain data imprinted in the earth, including sediment cores, ice sheets, and tree rings. For instance, while there is no way to measure the historic extent of glaciers, the ratio of oxygen in ocean sediments provides a proxy for this climate parameter. This results from the fact that the heavier isotope ^{18}O precipitates preferentially each time vapor condenses as water vapor travels poleward, thus leaving a higher percentage of ^{18}O in the ocean when there is more ice on the earth's land surface. Throughout the process of obtaining data as well as the analysis of this data, we often rely on deterministic methods rather than probabilistic ones in paleoclimate analysis. However, an analysis considering uncertainty is necessary, especially when dealing with low-resolution records, because uncertainty of information is a reflection of the trustworthiness of apparent differences. In this thesis, we present statistical tools based on Bayesian inference to better analyze paleoclimate records. Chapters 2 and 3 concern how to better quantify uncertainty in the timing of paleoclimate events while Chapter 4 concerns a better statistical understanding of auto- and cross-correlation of proxy time series.

The hidden Markov model (HMM) is a well-known and widespread statistical tool for time series analysis. The basic theory of the HMM was established by Baum and his colleagues in the late 1960s [107, 10, 9]. The HMM was then further developed as a tool for speech recognition [89, 154], and analysis of biological sequences [26, 6]. Moreover, the HMM has been also widely used in several disciplines, such as economics for stock market forecasting [65], climatology for precipitation analysis [80, 217], and image analysis for face identification [132, 170].

The HMM is composed of observed variables and hidden variables. Measured data corresponds to observed variables and latent states under these measurements correspond to the hidden variables. Through the analysis of measurements, the HMM enables us to explain both observed variables and hidden states, which follow the Markov property. The Markov property states that given the present state, the future state does not depend on the past states. For instance, if the changes of sedimentation rate follow the Markov property, this implies that the future rate, which is conditional on both past and present rates, directly depends only on the present rate, not on the past rates. Intuitively this means that everything we need to know about history to predict the future rate is captured in the current rate. The parameters of HMM describe the transitions among latent states and patterns of observed variables depending on hidden variables. In HMM terminology, they are considered as transition probability and emission probability, respectively. These unknown parameters are determined based on observed values, using the Baum-Welch expectation-maximization algorithm. This algorithm iteratively finds estimates which maximize the likelihood of the observed data.

In Chapter 2, we collect globally distributed benthic $\delta^{18}O$ records and combine them to construct one representative time series, called the Prob-stack, using a profile HMM. The benthic $\delta^{18}O$ proxy represents the global nature of ice volume signal and deep water temperature. Thus, the stack provides better information than a single record can provide. Benthic stacks have been extensively employed as measures of global climate change and stratigraphic alignment targets found in age model developments or lead/lag relationship analysis. While there have been a large number of studies constructing a new benthic stack (e.g., [84, 151, 153, 206, 161, 8, 177, 95, 82, 112]), algorithms for constructing a stack have been much less studied. Among these stacks, the LR04 stack [112] is notable because it was the first benthic $\delta^{18}O$

stack composed of more than three records and extends beyond 850ka by using an automated algorithm based on dynamic programming. However, the algorithm determines alignments of benthic $\delta^{18}O$ records deterministically without considering the uncertainty of alignments. To address this limitation, we develop a probabilistic stack which incorporates the variability among multiple records used to construct it and the uncertainty in alignments of records to the stack, which have not been included in previous studies.

In Chapter 3, we analyze the relative timing of glacial terminations between the eastern tropical Pacific and the western tropical Pacific using sea surface temperature (SST) records. Comparing timing in paleoclimate records is often limited to a visual comparison by plotting two time series together or a comparison of single estimates from each record. However, more detailed quantitative analysis is required so that it reflects uncertainties originating from the proxies and the algorithm for the timings. Thus, we design the combination of three statistical tools, which are Bayesian calibration [99, 98], HMM-match algorithm [110], and Bayesian change point algorithm [167, 166], to obtain the probability distribution of termination timing. The distribution from each record is then compared with the distribution from the reference record to estimate the probability distribution of the lead/lag length, that represents whether the termination in the record of interest occurred earlier than that in the reference record. We compare the termination timings between the eastern tropical Pacific and western tropical Pacific based on this combination method, and analyze the uncertainties to find where they originated.

In Chapter 4, we analyze multidimensional paleoclimate proxies, SST, C_{37}, $\delta^{15}N$, and $\%N$, from the central Peru margin to find their correlations and changes in their variability over the Holocene epoch (present - 11ka). These four proxies are high-resolution, but they have different patterns of measurements, i.e., their spacings are irregular, and not the same as each other. Unless we measure proxies with an aim for multidimensional analysis from the beginning, it is difficult to collect evenly spaced proxies that share the same pattern of measurements in paleoclimate studies. In this study, we treat the multidimensional records as evenly spaced data with missing parts and estimate the expected values of the missing parts by the Kalman filter. The Kalman filter estimates the expected values taking into account the proxy model and all observed data, so it gives a better estimate than a simple interpolation. Both the HMM and the autoregressive HMM (AR-HMM) are employed with the assumption that these proxies undergo changes of hidden states depending on the variability of the proxies. The HMM assumes that observed values are independent of each other given their states, but the AR-HMM also considers the direct dependencies among observations. We expect these models to find the correlations among the four proxies and their underlying state changes.

The studies in these three chapters are in collaboration with my advisor and colleagues, and each chapter includes materials from the draft of the preliminary paper associated with these studies. See footnote for detailed collaboration information in each chapter.

Chapter Two

A probabilistic Pliocene-Pleistocene stack of benthic $\delta^{18}O$ using a profile hidden Markov model

2.1 Background & Summary

A benthic $\delta^{18}O$ stack is a representative time series that describes the global nature of ice volume and deep water temperature signals by combining benthic $\delta^{18}O$ records from different locations. Due to the usefulness of stacks as measures of global climate change and stratigraphic alignment targets, a progression of stacks (e.g., [84, 151, 153, 206, 161, 8, 177, 95, 82, 112]) has been created over the past 30 years as more data have become available. The LR04 stack [112] is one of the most widely used for age model developments and lead/lag relationship analysis [28, 88, 152, 29] because it describes the mean of 57 globally distributed records and continuously spans the Pliocene and Pleistocene (0-5.3 Myr). The LR04 stack was constructed through pairwise alignment of records using segments of high resolution records and dynamic programming optimization [111]. This automated algorithm finds the global optimal alignment that minimizes the measures of sequence similarity by comparing stratigraphic features and taking into account undesirable changes in accumulation rate. After aligning the records, the average of all $\delta^{18}O$ measurements within each time interval was used to represent each stack point. Because the algorithm finds alignments deterministically and returns only the best solution, the LR04 stack does not reflect uncertainties in the alignments. Furthermore, using such a deterministic stack as a stratigraphic reference provides no information about statistical significance. To address this limitation, we present here a probabilistic stack, called the Prob-stack, which describes changes in the global mean value of $\delta^{18}O$, including its variability across benthic $\delta^{18}O$ records and uncertainties in alignments.

The Prob-stack is constructed from 180 individual benthic $\delta^{18}O$ records. For each time interval, we estimate the probability distribution of $\delta^{18}O$ values, i.e. the mean and variance terms of a normal distribution. For purposes of display and comparison with LR04, we describe a time series of the estimated $\delta^{18}O$ mean for each point in the Prob-stack (the "Prob-mean"), along with the LR04 stack in Figure 2.1. The Prob-mean is only a partial representation of the Prob-stack because it does not include the essential uncertainty component of the full Prob-stack. The Prob-mean agrees well with the LR04 stack in most time intervals, except for a few small phase shifts between the two stacks. In particular, a 5-kyr phase shift around 75 ka likely stems from either stretching or lower compression ratio near the tops of most sediment cores. The Prob-mean and LR04 stack show differences in their extremes which are labeled by Marine Isotope Stage (MIS) numbers [155]. For instance, the G8 (2762ka) glacial max is better resolved in the Prob-mean, but the Prob-stack has a large $\delta^{18}O$ uncertainty at G8. Prob-mean eliminates the double peak at K1 (3080ka) and has minimal (practically nonexistent) change in $\delta^{18}O$ between KM4 (3170ka) through M1 (3235ka). MG2 (3355ka) is somewhat older (>10-kyr) than in the LR04 stack, and intervals between MG8 (3500ka) and MG10 (3545ka) have a noticeably different appearance. Additionally, variance near the end of Prob-mean (around ST4 (4980ka) and T1 (4990ka)) is smaller than in LR04. Overall, the Prob-mean is slightly smoother than the LR04 stack, a reflection of the probabilistic nature of the HMM algorithm. Because HMM incorporates alignment uncertainty, it allocates input points to the sets of stack points corresponding to all possible times for which the input may have been deposited rather than to only the single best time point. The resulting spread tends to smooth the time series corresponding to the mean value at each time step. In addition, the availability of more records may contribute to smoothing.

The Pliocene-Pleistocene Prob-stack presented in this study describes the distribution of global trend in benthic $\delta^{18}O$ and its variance across the individual benthic $\delta^{18}O$ records for each time interval. The Prob-mean alone should not be used for stratigraphic alignment because such an approach fails to account for the uncertainty of the stack and is equivalent to reverting to a deterministic stack. Also, the size of 95% confidence band compared to the size of the mean value should be considered when interpreting the Prob-stack. As the Prob-stack contains time-varying variance information, the stratigraphic alignment of a record to the Prob-stack can produce age estimates and confidence limits of these age estimates reflecting the variability of the stack. The Prob-stack serves as a more complete description of global benthic $\delta^{18}O$ variability than the LR04 stack and provides additional functionality as a stratigraphic tool for Pliocene-Pleistocene studies.

In the following sections, we describe the profile hidden Markov model and the Baum-Welch expectation-maximization method, which are used to construct the Prob-stack. We validate the Prob-stack through comparisons with the LR04 stack and sensitivity analyses. Then, we introduce two applications of the Prob-stack: assessment of the uncertainty in ages and lead/lag relationships. [1]

2.2 Method

2.2.1 Data collection

The Prob-stack contains all 57 of the records [39, 179, 165, 160, 157, 191, 192, 112, 158, 36, 178, 76, 30, 23, 11, 124, 180, 125, 12, 15, 53, 142, 123, 52, 121, 159, 66, 68, 150, 73, 74, 2, 58, 63, 190, 86, 13, 172, 57, 208, 181, 130, 126, 83, 139, 135, 182, 78]

---

[1] The work in this chapter is in collaboration with my advisor Dr. Charles E. Lawrence of Brown University, Dr. Lorraine Lisiecki of the University of California, Santa Barbara, and Dr. Deborah Khider of the University of California, Santa Barbara. This chapter includes materials from the draft of the preliminary paper associated with this work.

in the LR04 stack plus an additional 123 benthic $\delta^{18}O$ records [185, 87, 42, 93, 97, 94, 33, 44, 133, 22, 35, 186, 13, 116, 174, 175, 71, 127, 173, 55, 210, 171, 172, 90, 198, 115, 137, 119, 81, 77, 47, 56, 199, 75, 37, 120, 203, 194, 216, 138, 215, 196, 197, 195, 148, 147, 50, 211, 128, 117, 214, 187, 168, 21, 181, 20, 156, 149, 146, 189, 204, 3, 38, 67, 114, 7, 45, 24, 31, 136, 200, 18, 193, 102, 134, 209, 106, 48, 53, 113, 145, 141, 207, 101, 169, 130, 72, 17, 51, 131, 1, 70, 5, 126, 140, 122, 85, 83, 164]. The sites of these records are well distributed in latitude, longitude, and depth (Figure 2.2), and the records have large variations in terms of resolution and time span (Figure 2.3). Each of the collected records covers at least 150-kyr and has an average resolution better than 4-kyr. To reduce computing time and memory use, a few records were sliced into multiple files when a record contained an irregular resolution. Detailed information about the records is given in the metadata table (Appendix A).

Most of the benthic $\delta^{18}O$ measurements comprising the records considered for this study were made on specimens of either Uvigerina peregrina or Cibicidoides wuellerstorfi, with the appropriate species offset corrections as either defined in the original publication or using the offset from [179].

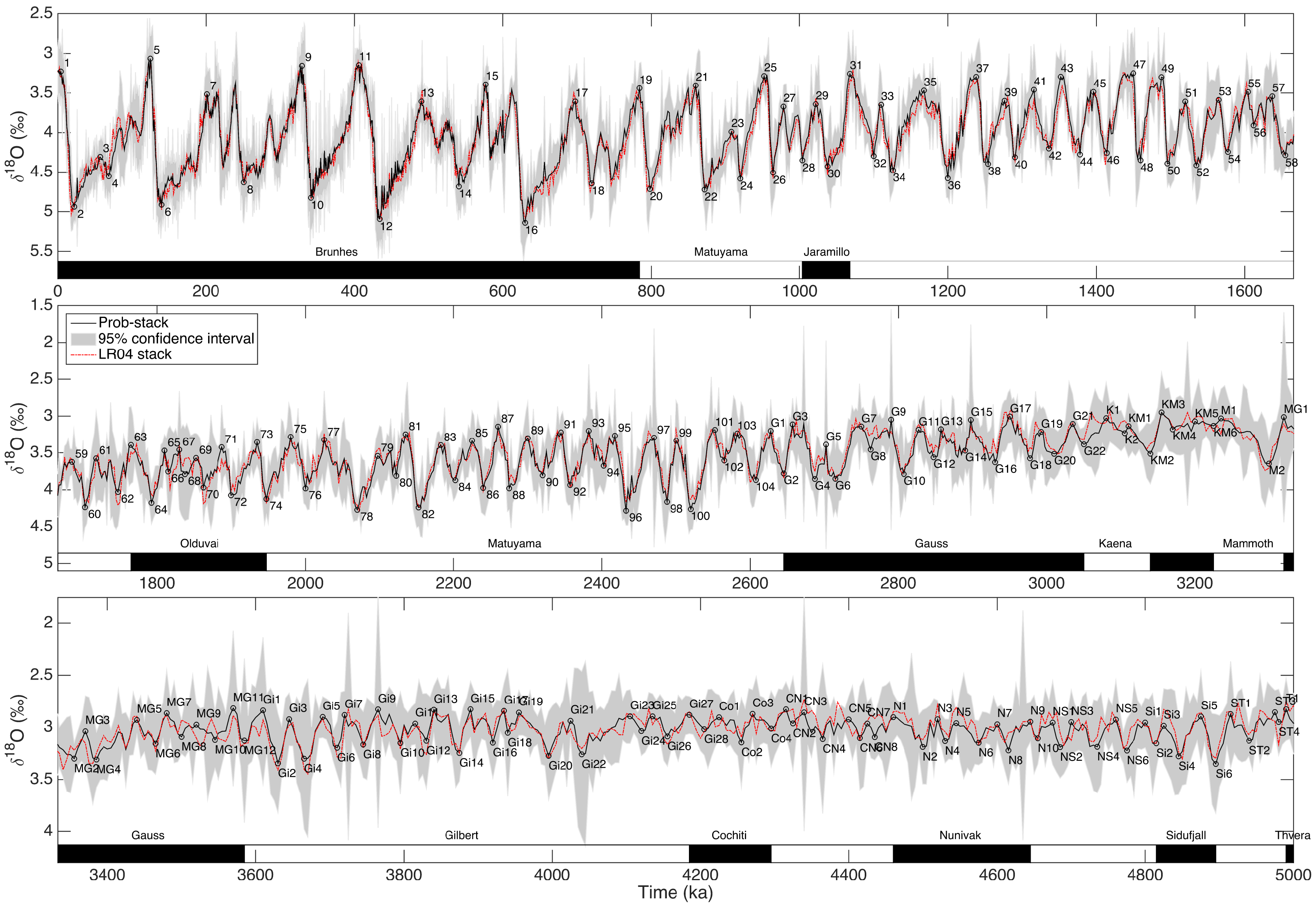

Figure 2.1: The Prob-stack constructed using 180 globally distributed benthic $\delta^{18}O$ records. The stack is plotted with MIS labels and magnetic polarity reversal stages. Note that the scale of the vertical axis changes across panels.

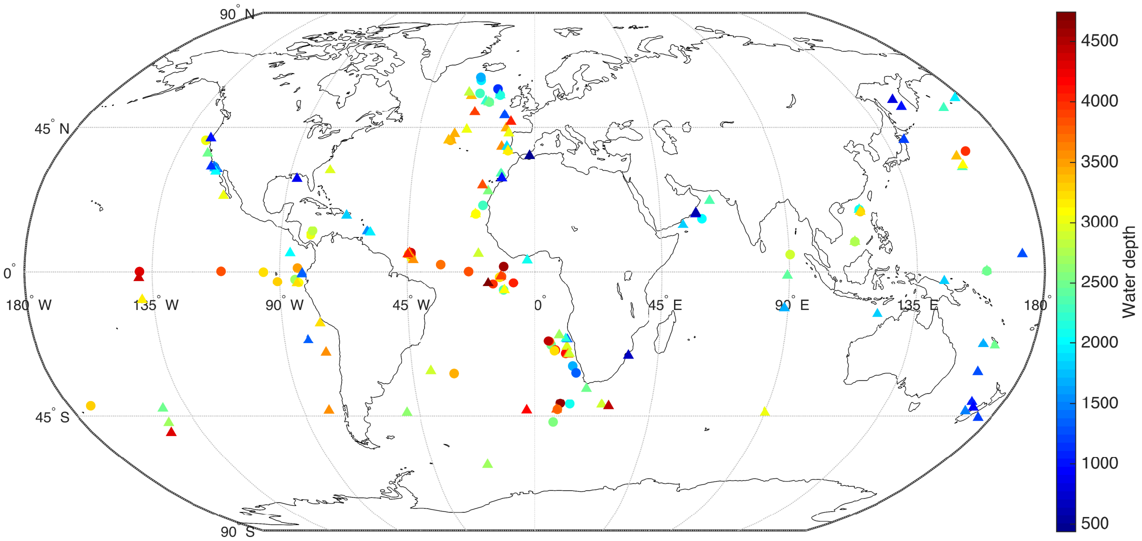

Figure 2.2: Location of the cores used in this study. The colors represent water depths of the sites. Circle: cores used to construct the LR04 stack. Triangle: cores which are newly added to construct the Prob-stack.

2.2.2 Profile hidden Markov model (HMM)

The construction of a probabilistic benthic $\delta^{18}O$ stack is done in two steps: determining the probabilistic alignments of individual records to the stack and updating the parameters of the stack based on these alignments. Through iteration of these two steps, we can construct a new stack while probabilistically aligning records to the stack.

To this end, we need a probabilistic model which describes a stack, records, and alignments of these records to the stack. This model is based on the HMM-Match algorithm [110] which is a probabilistic method to align a single record to a specified target. The profile HMM extends HMM-Match in two ways: it builds a new stack rather than aligning the records to an existing one, and permits the variances of points in the stack to be time-varying. A brief description of the probabilistic model is provided here. The full description of the model can be found in [110]. Based on the probabilistic model, we explain how to construct a stack which maximizes the

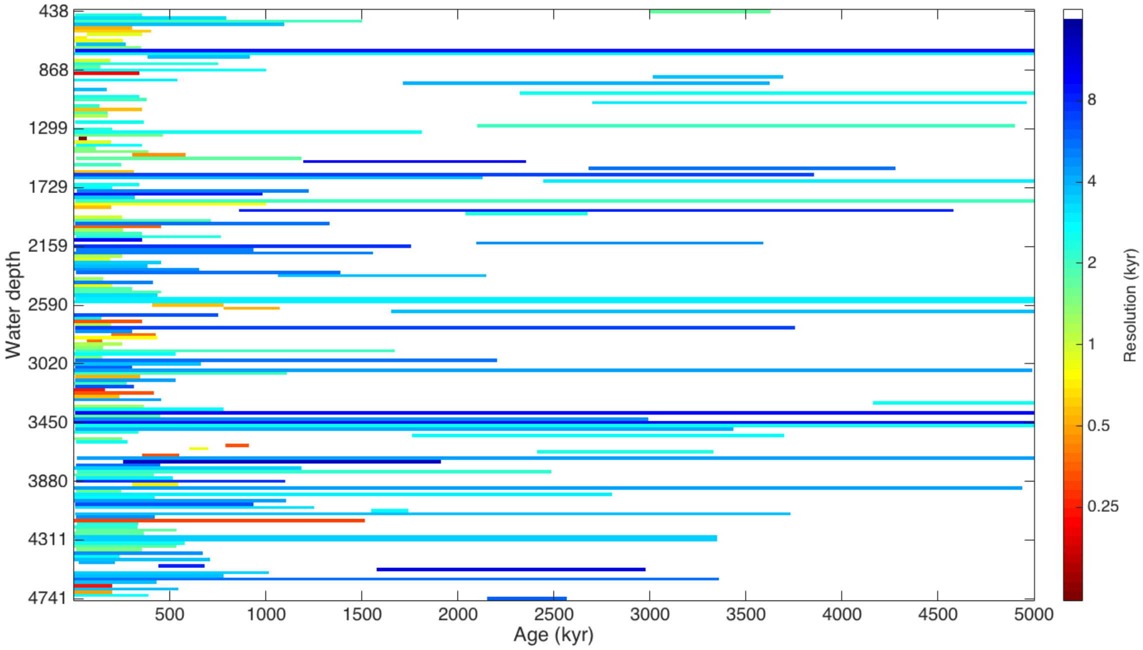

Figure 2.3: Coverage of the cores. The colors represent the average resolutions of records.

likelihood of records through the Baum-Welch expectation-maximization algorithm [154, 46], which is also briefly described below.

2.2.2.1 Probabilistic models of the Prob-stack and benthic $\delta^{18}O$ records

The probabilistic stack includes the signal of global ice volume and deep water temperature, and the variability of this signal. Let $\{s_t\}$ be a sequence of random variables, which represents the probabilistic stack, and assume that $\{s_t\}$ follow the normal distribution with mean μ_t and variance σ_t^2.

$$s_t \sim \mathcal{N}(\mu_t, \sigma_t^2) \tag{2.1}$$

Then, μ_t and σ_t^2 represent the signal and the variance of the signal respectively, allowing both to vary with age, t. Note that the variance term represents the variability of $\delta^{18}O$ signals across multiple records and not the error of the mean value. Thus, the variance term can explain the possible range of an unobserved record.

Since each record also represents the signal of global ice volume and deep water temperature, it follows the same distribution with the probabilistic stack. Thus, we consider each record to be a randomly drawn sample from the common stack model. In HMM terminology, it is considered as an "emission" of the model. Systematic differences between the probabilistic stack and individual records arise from three sources: alignment uncertainty, spatial variability between records, and inter-laboratory offsets [144]. These factors can be modelled with a normal distribution considering a mean shift from the stack. Let $d_{i,j}$ be the j^{th} data point of record i. Then, $d_{i,j}$ follows a normal distribution with mean$\tau_i + \mu_t$ and variance σ_t^2, where τ_i is the mean shift of record i, when the age estimate of the j^{th} data point is t. This is written as follows:

$$d_{i,j}|A_{i,j} = t \sim \mathcal{N}(\tau_i + \mu_t, \sigma_t^2) \tag{2.2}$$

where $A_{i,j}$ refers to the synchronous age assignment of the j^{th} data point of the record i. The alignment procedure synchronizes ages from multiple records, i.e., it finds data points assigned to the same age. Because it does not return the estimation of an absolute age, we call it a synchronous age estimate. We define an alignment of record as a vector of synchronous age estimate: $A_i = (A_{i,1}, A_{i,2}, \cdots, A_{i,m_i})$, where m_i is the number of data points in record i. If exact age assignments for all data points $d_{i,j}$ were possible, then we could immediately construct the stack using these assignments. However, age assignments always include uncertainty. The goal of this study is to construct a stack which reflects such uncertainty. To this end, we employ a modified version of the HMM-Match algorithm [110] to generate samples of age assignments.

2.2.2.2 Probabilistic model of age assignments

Here we describe the probabilistic model of age assignments in the HMM-Match algorithm [110]. This method finds samples of the pointwise age estimate $A_{i,j}$ for each data point $d_{i,j}$. Whereas the stack spans most of the Pliocene-Pleistocene, most records cover only some portions of the the total length. Thus, it is required to roughly select an initial target, which is a segment of the stack corresponding to each record.

There are three possible states for the alignment between a target and $d_{i,j}$: matching, insertion, or deletion. When a target and a record span the same interval, all data points of a record are considered as emitted data from a target and all alignment states are matching. On the other hand, if their spans are different, the alignment states can be either insertions or deletions at the top or bottom of the records. When a record covers a longer interval than a target, we treat the additional part of the record as inserted data. Alternatively, if a record spans a shorter interval than a target, we assume that the corresponding data in the record is deleted.

In addition to the three alignment states, we consider one more state, matching-end. The matching-end state indicates that the matched portion is over, and the rest of the states are either insertions or deletions. Figure 2.4 illustrates the flows of state changes. Begin and End indicate that alignment begins and ends, respectively. Without the matching-end state, a matching state has four possible choices for the next state: matching, insertion, deletion, or end. The probability of staying in matching states is almost always nearly one because we have a long series of one-to-one alignments of a record to the stack. Thus, transitions from matching to insertion or deletion rarely occurs. Adding the matching-end state prevents such situations, so it enables the algorithm to enter an insertion state or deletion state at the end more

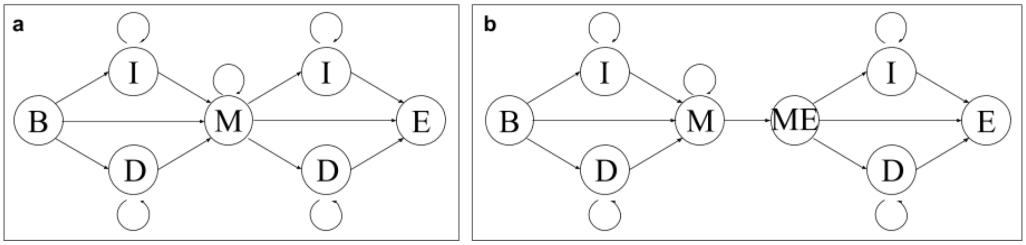

Figure 2.4: Flows of state changes in (a) the original HMM-Match algorithm and (b) the modified version for this study. The letters are as follows: B stands for begin, E stands for end, I stands for insertion, D stands for deletion, M stands for matching, and ME stands for matching-end. Possible state transitions are illustrated with arrows. A rotating arrow represents alignments that can remain in the current state.

frequently, which gives more flexibility in alignments.

Because sedimentation rates vary both spatially and temporarily, finding matched portions of a record does not give us a synchronous age estimate. Therefore, it is necessary to allow for differences in sedimentation rates between various records and over time within specific records to determine age estimates. Based on the ratio of two lengths, the length between $d_{i,j}$ and $d_{i,j+1}$ and the length between $A_{i,j}$ and $A_{i,j+1}$, the matching state is categorized into 17 states from a 4:1 (expansion) to a 1:4 (contraction).

This model assumes that a sedimentation rate between points $j+1$ and $j+2$ of a record, given all previous sedimentation rates, depends only on one immediate previous sedimentation rate between points j and $j+1$, which yields the Markov property of this HMM algorithm. That is, the conditional probability of the rate from $d_{i,j+1}$ and $d_{i,j+2}$ depends directly only on the rate from $d_{i,j}$ and $d_{i,j+1}$ and not on any previous rates given the current rate. This property is written with corresponding age estimates as follows:

$$P(A_{i,j+1}|A_{i,j}, A_{i,j-1}, \cdots, A_{i,2}, A_{i,1}) = P(A_{i,j+1}|A_{i,j}, A_{i,j-1}) \tag{2.3}$$

Thus, while all rates are dependent on one another, the rate at any given point in a record is only indirectly dependent on the historic rates only through the most recent rate. This model is called the hidden Markov model (HMM) [46, 154] because the unknown states follow the Markov property and these can be inferred through observations, which are the benthic records. In HMM terminology, equations (2.1) and (2.2) refer to the emission model, and equation (2.3) represents the transition model. Because we construct a stack by aligning multiple records simultaneously rather than aligning one single record to a target, the model is called the profile HMM. The advantage of the profile HMM over the deterministic approach employed in the construction of LR04 is that it returns confidence intervals for the stack. Also, probabilistic algorithms do not require us to model outliers separately in probabilistic algorithms; the algorithm assigns a small probability to outliers of $\delta^{18}O$ values and extreme expansions or contractions instead.

2.2.3 Baum-Welch Expectation-Maximization algorithm

The probabilistic model includes multiple unknown parameters: $\{\mu_t, \sigma_t^2\}$ which describe the mean $\delta^{18}O$ and attached variance for each time step t, $\{\tau_i\}$ which is the set of parameters representing a mean shift of each record, and $\{\phi_i\}$ which accounts for the set of parameters concerning the alignment of the record i. More precisely, $\{\phi_i\}$ includes state transition probabilities and initial state probabilities.

Let Θ refer to the set of all theses unknown parameters. The unknown parameters are learned by the iterative Baum-Welch algorithm [46, 154]. This algorithm finds parameters which maximize the likelihood of records. Because we assume that each record is emitted from the stack independently, the total likelihood of records becomes

$$P(\mathcal{R}|\Theta) = P(\text{record}_1, \text{record}_2, \cdots, \text{record}_N|\Theta) = \prod_{i=1}^{n} P(\text{record}_i|\Theta), \tag{2.4}$$

where $\mathcal{R}$ refers the set of all records, $(\text{record}_1, \text{record}_2, \cdots, \text{record}_N)$. The algorithm starts by setting initial values of unknown parameters, say Θ_1, to be their best guesses. Then, it iterates two steps: the expectation-step (E-step) and maximization-step (M-step). In the k^{th} E-step, we find the likelihood with the current set of parameters Θ_k. Then, in the k^{th} M-step, we find the new set of parameters Θ_{k+1} which maximizes the likelihood of the records.

It can be shown that maximizing the likelihood, $P(\mathcal{R}|\Theta)$, is equivalent to maximizing the expected value of $\log P(\mathcal{R}, \mathcal{A}|\Theta)$ over the distribution of $\mathcal{R}$ given Θ_k [46], where $\mathcal{A}$ represents the set of age estimates $(A_1, A_2, \cdots, A_N)$:

$$Q(\Theta|\Theta_k) = \sum_{\mathcal{A}} P(\mathcal{A}|\mathcal{R}, \Theta) \log P(\mathcal{R}, \mathcal{A}|\Theta) \tag{2.5}$$

Using the Bayes rule, the log likelihood of record i can be written as

$$\log P(\mathcal{R}|\Theta) = \log P(\mathcal{R}, \mathcal{A}|\Theta) - \log P(\mathcal{A}|\mathcal{R}, \Theta)$$

Multiplying by $P(\mathcal{A}|\mathcal{R}, \Theta_k)$ and marginalizing out $\mathcal{A}$ yields

$$\begin{aligned} \sum_{\mathcal{A}} P(\mathcal{A}|\mathcal{R}, \Theta_k) \log P(\mathcal{R}|\Theta) &= \sum_{\mathcal{A}} P(\mathcal{A}|\mathcal{R}, \Theta_k) \left(\log P(\mathcal{R}, \mathcal{A}|\Theta) - \log P(\mathcal{A}|\mathcal{R}, \Theta)\right) \\ \log P(\mathcal{R}|\Theta) &= Q(\Theta|\Theta_k) - \sum_{\mathcal{A}} P(\mathcal{A}|\mathcal{R}, \Theta_k) \log P(\mathcal{A}|\mathcal{R}, \Theta) \end{aligned}$$

In the k^{th} M-step, we want to find Θ_k such that

$$\log P(\mathcal{R}|\Theta_{k+1}) - \log P(\mathcal{R}|\Theta_k) > 0$$

That is,

$$Q(\Theta_{k+1}|\Theta_k) - Q(\Theta_k|\Theta_k) + \sum_{\mathcal{A}} P(\mathcal{A}|\mathcal{R},\Theta_k) \log \frac{P(\mathcal{A}|\mathcal{R},\Theta_k)}{P(\mathcal{A}|\mathcal{R},\Theta_{k+1})} > 0$$

As the last term of the left hand side is the relative entropy, it is always non-negative. Thus,

$$\Theta_{k+1} = \text{argmax}_{\Theta} Q(\Theta|\Theta_k). \tag{2.6}$$

The E-step and M-step evaluate $Q(\Theta|\Theta_k)$ and maximize $Q(\Theta|\Theta_k)$, respectively.

2.2.3.1 Expectation-step: forward algorithm and backward sampling algorithm

The E-step is composed of two procedures: the forward algorithm and the stochastic backward sampling algorithm. Remark that there are two methods for accounting for down stream dependencies: backward summation and backward sampling. Here, as in the HMM-Match, we use backward sampling.

The forward algorithm finds the likelihood of a record considering all possible alignments starting from the top of each record:

$$P(\text{record}_i|\Theta) = \sum_{A_i} P(\text{record}_i, A_i|\Theta)$$

The total likelihood of all records can then be computed from equation (2.4). We marginalize out all possible alignments with the help of the forward variable.

The forward variable of the record i, $\alpha_i(j,k,l)$, is a joint probability of record values up to the j^{th} point and the age assignments of the j^{th} and $(j-1)^{\text{th}}$ points, that is,

$$\alpha_i(j,k,l) = P(d_{i,1}, d_{i,2}, \cdots, d_{i,j}, A_{i,j} = k, A_{i,j-1} = l|\Theta).$$

The forward variable can be decomposed into the products of the emission the transition probabilities as follows:

$$\begin{aligned}
\alpha_i(j,k,l) &= P(d_{i,1}, d_{i,2}, \cdots, d_{i,j}, A_{i,j} = k, A_{i,j-1} = l|\Theta) \\
&= \sum_{a_1,a_2,\cdots,a_{j-2}} P(d_{i,1}, d_{i,2}, \cdots, d_{i,j}, A_{i,1} = a_1, A_{i,2} = a_2, \\
&\qquad\qquad \cdots, A_{i,j-2} = a_{j-2}, A_{i,j-1} = l, A_{i,j} = k|\Theta) \\
&= \sum_{a_1,a_2,\cdots,a_{j-2}} P(A_{i,1} = a_1) \cdot P(A_{i,2} = a_2|A_{i,1} = a_1) \\
&\qquad\qquad \cdot \prod_{n=3}^{j} P(A_{i,n} = a_n|A_{i,n-1} = a_{n-1}, A_{i,n-2} = a_{n-2}) \\
&\qquad\qquad \cdot \prod_{n=1}^{j} f(d_{i,n}|A_{i,n} = a_n, \Theta)
\end{aligned} \tag{2.7}$$

where $a_j = k$ and $a_{j-1} = l$. There are two kinds of state transitions: transitions from the Begin state to the End state, as described in Figure 2.4, and transitions due to changes in sedimentation rates while staying in the matching state. To describe these two state transitions, we introduce two functions: ϕ and ρ. Let ϕ_{AB} be a transition probability from state A to state B where A and B can be either B (begin), E (end), M (matching), I (insertion), D (deletion), or ME (matching end). Let $\rho(r_{j-1}, r_j)$ be a transition probability from rate r_{j-1} to rate r_j where

$$r_j = \frac{A_{i,j} - A_{i,j-1}}{d_{i,j} - d_{i,j-1}}. \tag{2.8}$$

Note that ϕ should be estimated for each record, but ρ is fixed as in the HMM-Match algorithm [110].

The first three terms of equation (2.7) can be rewritten using ϕ and ϕ. The first term $P(A_{i,1} = a_1)$, which is the probability of the age assignment of the first data point, becomes

$$P(A_{i,1} = a_1) = (\phi_{BM})^{1-\chi^t} \left[(\phi_{BD})^{l_D^t - 1}(\phi_{DD})^{l_D^t}(\phi_{DM})^{l_D^t - 1}\right] \left[(\phi_{BI})^{l_I^t - 1}(\phi_{II})^{l_I^t}(\phi_{IM})^{l_I^t - 1}\right],$$

where

$$\chi^t = \begin{cases} 0 & \text{if } l_D^t = l_I^t = 0 \\ 1 & \text{otherwise,} \end{cases}$$

and l_D^t and l_I^t represent the length of deletion states and insertion states at the top of the core i, respectively. The second term $P(A_{i,2} = a_2 | A_{i,1} = a_1)$ represents the probability of the age assignment of the second data point given the first age assignment.

$$P(A_{i,2} = a_2 | A_{i,1} = a_1) = P\left(r_1 = \frac{a_2 - a_1}{d_{i,2} - d_{i,1}}\right) \cdot \phi_{MM}.$$

An initial sedimentation rate r_1 is determined using the first two age assignments, and these two age assignments imply that an alignment stays in the matching state. The third term $P(A_{i,n} = a_n | A_{i,n-1} = a_{n-1}, A_{i,n-2} = a_{n-2})$ represents the changes in sedimentation rates from r_{n-1} to r_n.

$$P(A_{i,n} = a_n | A_{i,n-1} = a_{n-1}, A_{i,n-2} = a_{n-2}) = \begin{cases} \rho(r_{n-1}, r_n) \cdot \phi_{MM} & \text{if } n < L_i \text{ or } a_n < T \\ \rho(r_{n-1}, r_n) \cdot \phi^b & \text{if } a_n = L_i, \end{cases}$$

where L_i is the length of record i and T is the length of target. Before reaching these two limits, an alignment stays in the matching state, so the third term includes ϕ_{MM}.

Once an alignment reaches these limits, we need to take into account insertion states and deletion states for the bottom of the core i as we did for the top of the core i, using the state transition term ϕ^b defined as follows:

$$\phi^b = \phi_{MM}\phi_{MMe}(\phi_{MeE})^{1-\chi^b}\left[(\phi_{MeD})^{l_D^b-1}(\phi_{DD})^{l_D^b}(\phi_{DE})^{l_D^b-1}\right]\left[(\phi_{MeI})^{l_I^b-1}(\phi_{II})^{l_I^b}(\phi_{IE})^{l_I^b-1}\right],$$

where

$$\chi^b = \begin{cases} 0 & \text{if } l_D^b = l_I^b = 0 \\ 1 & \text{otherwise,} \end{cases}$$

and l_D^b and l_I^b represent the length of deletion states and insertion states at the bottom of the core, respectively.

The last term of equation (2.7) is the emission probability. Each data point of the benthic $\delta^{18}O$ records is assumed to follow the normal distribution as described in equation (2.2), so the emission probability of $d_{i,j}$ given its age assignment $A_{i,j} = k$ and Θ becomes

$$f(d_{i,j}|A_{i,j} = k, \Theta) = \frac{1}{\sqrt{2\pi\sigma_k^2}} \exp\left(-\frac{(d_{i,j} - (\tau_i + \mu_k))^2}{2\sigma_k^2}\right). \tag{2.9}$$

Instead of marginalizing out age assignments, the forward variables can be evaluated recursively.

$$\begin{aligned}
\alpha_i(j,k,l) &= P(d_{i,1}, d_{i,2}, \cdots, d_{i,j}, A_{i,j} = k, A_{i,j-1} = l|\Theta) \\
&= \sum_m P(d_{i,1}, d_{i,2}, \cdots, d_{i,j}, A_{i,j} = k, A_{i,j-1} = l, A_{i,j-2} = m|\Theta) \\
&= \sum_m f(d_{i,j}|A_{i,j} = k, \Theta) \cdot P(A_{i,j} = k|A_{i,j-1} = l, A_{i,j-2} = m) \\
&\qquad\qquad \cdot P(d_{i,1}, d_{i,2}, \cdots, d_{i,j-1}, A_{i,j-1} = l, A_{i,j-2} = m|\Theta) \\
&= f(d_{i,j}|A_{i,j} = k, \Theta) \sum_m P(A_{i,j} = k|A_{i,j-1} = l, A_{i,j-2} = m)\alpha_i(j-1, l, m)
\end{aligned}$$

Once we evaluate all forward variables, we can find the likelihood of record i, and then the total likelihood of all records.

$$\begin{aligned}
&P(\mathrm{record}_1, \mathrm{record}_2, \cdots, \mathrm{record}_n|\Theta) \\
&= \prod_{i=1}^{n} P(\mathrm{record}_i|\Theta) \\
&= \prod_{i=1}^{n} \sum_{A_i} P(\mathrm{record}_i, A_i|\Theta) \\
&= \prod_{i=1}^{n} \sum_{A_i} \sum_{k,l} P(d_{i,1}, d_{i,2}, \cdots, d_{i,L_i}, A_{i,L_i} = k, A_{i,L_i-1} = l|\Theta) \\
&= \prod_{i=1}^{n} \sum_{A_i} \sum_{k,l} \alpha_i(L_i, k, l)
\end{aligned}$$

Backward sampling algorithm

The stochastic backward sampling algorithm draws samples of alignments A_i^* following

$$P(A_i^*|\mathrm{record}_i, \Theta_k) = \frac{P(\mathrm{record}_i|A_i^*, \Theta_k)P(A_i^*|\Theta_k)}{\sum_{A_i} P(\mathrm{record}_i|A_i, \Theta_k)P(A_i|\Theta_k)} \tag{2.10}$$

where every term in the right hand side, including the summation in the denominator, is evaluated from the forward algorithm. We use 1000 stochastic back trace samples for each record. The samples are independent of each other and representative of the space of all alignments.

For each sample, we start sampling from the last two age estimates, A_{i,L_i} and A_{i,L_i-1}. The probability of the last two age estimates, given record i, can be obtained using the forward variables:

$$\begin{aligned} & P(A_{i,L_i} = k, A_{i,L_i-1} = l | d_{i,1}, d_{i,2}, \cdots, d_{i,L_i}) \\ & = \frac{P(A_{i,L_i} = k, A_{i,L_i-1} = l, d_{i,1}, d_{i,2}, \cdots, d_{i,L_i})}{\sum_{k,l} P(A_{i,L_i} = k, A_{i,L_i-1} = l, d_{i,1}, d_{i,2}, \cdots, d_{i,L_i})} \\ & = \frac{\alpha(L_i, k, l)}{\sum_{k,l} \alpha(L_i, k, l)} \end{aligned} \tag{2.11}$$

Once we sample the last two age estimates, we can continue sampling backwards, again using the forward variables as follows:

$$\begin{aligned} & P(A_{i,j-2} = m | d_{i,1}, d_{i,2}, \cdots, d_{i,j}, A_{i,j} = k, A_{i,j-1} = l) \\ & = \frac{f(d_{i,j} | A_{i,j} = k) P(A_{i,j} = k | A_{i,j-1} = l, A_{i,j-2} = m) P(d_{i,1}, d_{i,2}, \cdots, d_{i,j-1}, A_{i,j-1} = l, A_{i,j-2} = m)}{P(d_{i,1}, d_{i,2}, \cdots, d_{i,j}, A_{i,j} = k, A_{i,j-1} = l)} \\ & = \frac{f(d_{i,j} | A_{i,j} = k) P(A_{i,j} = k | A_{i,j-1} = l, A_{i,j-2} = m) \alpha(j-1, l, m)}{\alpha(j, k, l)} \end{aligned} \tag{2.12}$$

These forward and backward algorithms for each record correspond to the E-step of the HMM-Match method.

2.2.3.2 Maximization-step

The M-step updates the maximum likelihood estimates of unknown parameters Θ, i.e. τ_i, ϕ_i, the means μ_t and the variances σ_t^2 of the stack points using the sample alignments generated from equations (2.10, 2.11, 2.12). Let $\tilde{\mathcal{A}}$ be the set of samples for all records:

$$\tilde{\mathcal{A}} = (\tilde{A}_1, \tilde{A}_2, \cdots, \tilde{A}_N),$$

where $\tilde{A}_i$ be the set of samples for record i. Note that we have 1000 samples for each record. The goal of the M-step is to maximize the total likelihood using all samples $\tilde{\mathcal{A}}$. As derived above, to maximize the total likelihood (2.4) is equivalent to maximize

$Q(\Theta|\Theta_k)$ (2.5). Because we have samples $\tilde{\mathcal{A}}$ following the posterior probability of alignments (2.10), we estimate $Q(\Theta|\Theta_k)$ using the samples.

$$Q(\Theta|\Theta_k) \approx \tilde{Q}(\Theta|\Theta_k) = \sum_{\tilde{\mathcal{A}}} \log P(\mathcal{R}, \tilde{\mathcal{A}}|\Theta_k) = \log \prod_{i=1}^{N} P(R_i, \tilde{A}_i|\Theta_k)$$

As derived in (2.7), the term $P(R_i, \tilde{A}_i|\Theta_k)$ contains the transition probability terms and the emission probability terms:

$$\begin{aligned} P(R_i, \tilde{A}_i|\Theta_k) &= P(d_{i,1}, d_{i,2}, \cdots, d_{i,L_i}, A_{i,1} = a_1, A_{i,2} = a_2, \\ &\qquad \cdots, A_{i,L_i-2} = a_{L_i-2}, A_{i,L_i-1} = a_{L_i-1}, A_{i,L_i} = a_{L_i}|\Theta_k) \\ &= P(A_{i,1} = a_1) \cdot P(A_{i,2} = a_2|A_{i,1} = a_1) \\ &\qquad \cdot \prod_{n=3}^{L_i} P(A_{i,n} = a_n|A_{i,n-1} = a_{n-1}, A_{i,n-2} = a_{n-2}) \\ &\qquad \cdot \prod_{n=1}^{L_i} f(d_{i,n}|A_{i,n} = a_n, \Theta_k) \end{aligned}$$

For each record i, we update parameters τ_i and ϕ_i.

$$(\tau_i, \phi_i) = \operatorname{argmax} \log P(R_i, \tilde{A}_i|\Theta_k)$$

The mean shift τ_i is contained in the emission probability term. Thus,

$$\begin{aligned} \tau_i &= \operatorname{argmax} \log P(R_i, \tilde{A}_i|\Theta_k) \\ &= \operatorname{argmax} \log \prod_{n=1}^{L_i} f(d_{i,n}|A_{i,n} = a_n, \Theta_k) \\ &= \operatorname{argmax} \sum_{n=1}^{L_i} \log \left(\frac{1}{\sqrt{2\pi\sigma_t^2}} \exp\left(-\frac{(d_{i,j} - \mu_t) - \tau_i))^2}{2\sigma_t^2} \right) \right) \\ &= \frac{\sum_1^{L_i} (d_{i,j} - \mu_t)}{L_i} \end{aligned} \tag{2.13}$$

To update τ_i in the k^{th} iteration, we use μ_t which is obtained in the $(k-1)^{\text{th}}$ iteration. There is no closed form for ϕ_i, so we find it numerically using the MATLAB function $fmincon$.

Consider that we are updating the t^{th} point of the stack, s_t. It is the emission probability term that includes the parameters of the stack, μ_t and σ_t^2. Thus, it is enough to consider the emission probability to find these two estimators:

$$\begin{aligned}
(\mu_t, \sigma_t^2) &= \operatorname{argmax} \log \prod_{i=1}^{N} \prod_{n=1}^{L_i} f(d_{i,j} | A_{i,j} = a_j, \Theta_k) \\
&= \operatorname{argmax} \log \prod_{i=1}^{N} \prod_{\substack{j \text{ s.t.} \\ A_{i,j}=t}} f(d_{i,j} | A_{i,j} = t, \Theta_k) \\
&= \operatorname{argmax} \sum_{i=1}^{N} \sum_{\substack{j \text{ s.t.} \\ A_{i,j}=t}} \log \left(\frac{1}{\sqrt{2\pi\sigma_t^2}} \exp\left(-\frac{(d_{i,j} - \tau_i) - \mu_t))^2}{2\sigma_t^2} \right) \right)
\end{aligned}$$

After collecting all sampled $\delta^{18}O$ values that are aligned to the stack point s_t, we find the maximum likelihood estimators for μ_t and σ_t^2 which are the mean and the variance of the aligned samples. Note that we should take into account the mean shift when computing the mean of the aligned samples. Here we are using the mean shift estimated using (2.13) in the kth iteration.

$$\begin{aligned}
\mu_t &= \frac{\sum_{i=1}^{N} \sum_{\substack{j \text{ s.t.} \\ A_{i,j}=t}} (d_{i,j} - \tau_i)}{(\text{Number of samples aligned to } s_t)} \\
\sigma_t^2 &= \frac{\sum_{i=1}^{N} \sum_{\substack{j \text{ s.t.} \\ A_{i,j}=t}} (d_{i,j} - \tau_i - \mu_t)^2}{(\text{Number of samples aligned to } s_t)}
\end{aligned}$$

These two estimators determine the distribution of the stack point s_t.

The algorithm of constructing a probabilistic stack can be summarized as follows:

1. Set initial values for unknown parameters.
2. Run the E-step for each record.
    - (a) Forward algorithm computes the likelihood of a record considering all possible alignments.
    - (b) Backward sampling draws possible alignments with the stack based on the probability computed from the forward algorithm.
3. Compute the total likelihood of all records.
4. Run the M-step for each record and update the stack for each time step.
5. Run the E-step for each record as step 2.
6. Compute the total likelihood of all records. Stop if the total likelihood does not improve by more than 0.1%, otherwise go to step 4.

We set initial values of the stack to be the LR04 stack. This implies that the Prob-stack share the same time domain as the LR04 stack (Table 2.1), and that we take the LR04 age model as initial condition. Note that, however, we do not employ the LR04 stack values in updating the probabilistic stack. Only the data points in the individual records are employed according to their age assignment samples. This allows the final solution to converge to a result different from the initial target, as demonstrated below. Also, the profile HMM does not require any other age information except choosing a target for each record. A target can be selected with rough age estimates because the algorithm detects matched portions by allowing insertion and deletion states at the top and the bottom of a record. More discussion on initial values is given in the Technical Validation.

Table 2.1: Interval sizes of the stack.

Time [Ma]	Interval Size [kyr]
0 - 0.6	1.0
0.6 - 1.5	2.0
1.5 - 3.0	2.5
3.0 - 5.0	5.0

A probabilistic stack reflects the uncertainty by using the samples of age assignments. Analysis of the HMM-Match algorithm demonstrates that the variance of age assignments decreases approximately linearly with the resolution of the records [110]. Thus, the contribution of data from low-resolution records spreads to a relatively large number of stack points, while the data from high-resolution records tend to be aligned over a smaller number of stack points. In this manner, the algorithm naturally gives more weight to high resolution records within each stack bin.

2.2.4 Code availability

Open sources software and its manual are available at https://github.com/seonminahn/HMM-Stack for researchers to construct their own stack using benthic $\delta^{18}O$ records. However, we note that such a construction of the stack will require extensive use of high performance computing resources. Constructing the Prob-stack took about one month with 200 computing nodes as it takes over 100 hours for a high-resolution record to complete one iteration.

2.3 Technical validation

2.3.1 Comparison between the LR04 stack and the Prob-LR04-stack mean

To evaluate how the results of the profile HMM alignment compare with those from the deterministic pairwise alignment used in LR04, we created the Prob-LR04-stack, which uses the same 57 records that are contained in the LR04 stack. Because the LR04 and Prob-LR04 stacks contain exactly the same data, any differences between these two stacks must derive from the techniques used to create them. The means of Prob-LR04-stack and LR04 are very similar (Figure 2.5); the main differences are small age offsets (similar to those observed in the full Prob-stack), and that the Prob-LR04 mean is slightly smoother than LR04 due to the probabilistic nature of the alignment, which spreads the effects of uncertain age assignments across multiple time points.

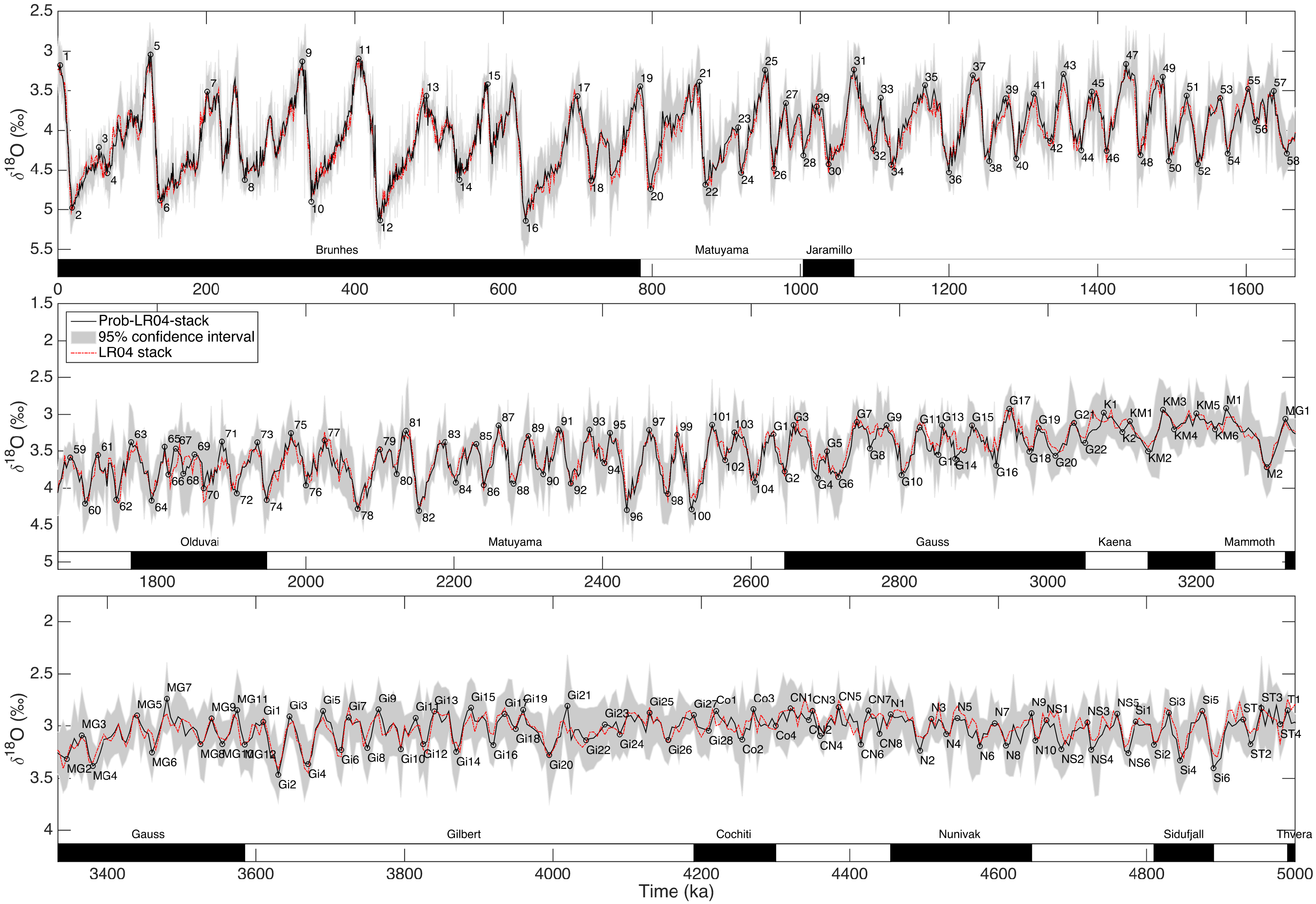

Figure 2.5: The Prob-LR04-stack constructed using the same 57 records that are contained in the LR04 stack. The stack is plotted with MIS labels and magnetic polarity reversal stages. Note that the scale of the vertical axis changes across panels.

Table 2.2: Relative difference in variances between the Prob-stack and the Prob-LR04-stack. A positive value implies that the Prob-stack represents higher variability.

Time [Ma]	Relative difference in variances between two Prob-stacks [%]
0 - 0.5	25.59
0.5 - 1.0	5.23
1.0 - 1.5	-4.81
1.5 - 2.0	-0.74
2.0 - 2.5	5.31
2.5 - 3.0	11.56
3.0 - 3.5	17.49
3.5 - 4.0	30.30
4.0 - 4.5	25.96
4.5 - 5.0	24.44

2.3.2 Comparison between the Prob-stack and the Prob-LR04-stack

It is also of interest to examine the differences that result from the additional 123 records contained in the full Prob-stack compared to the 57 in the Prob-LR04-stack (Figure 2.6). The average difference in the mean signal is less than 0.06‰, but the Prob-stack is smoother than the Prob-LR04-stack because it includes a larger number of benthic $\delta^{18}O$ records. Figure 2.7 shows the number of records used to construct each point of the two stacks. The confidence limit of the Prob-stack is 12% larger than the Prob-LR04-stack overall, but it varies from -5% to 30%, depending on intervals (Table 2.2). The difference emerges from the diversity of an additional set of records added to the Prob-stack. This indicates that the variability within the 57 cores used in the Prob-LR04-stack was less than that captured in the larger data set. Note that the confidence band does not decrease by using a larger number of records because the variance term explains the variability of records rather than the error of the mean value.

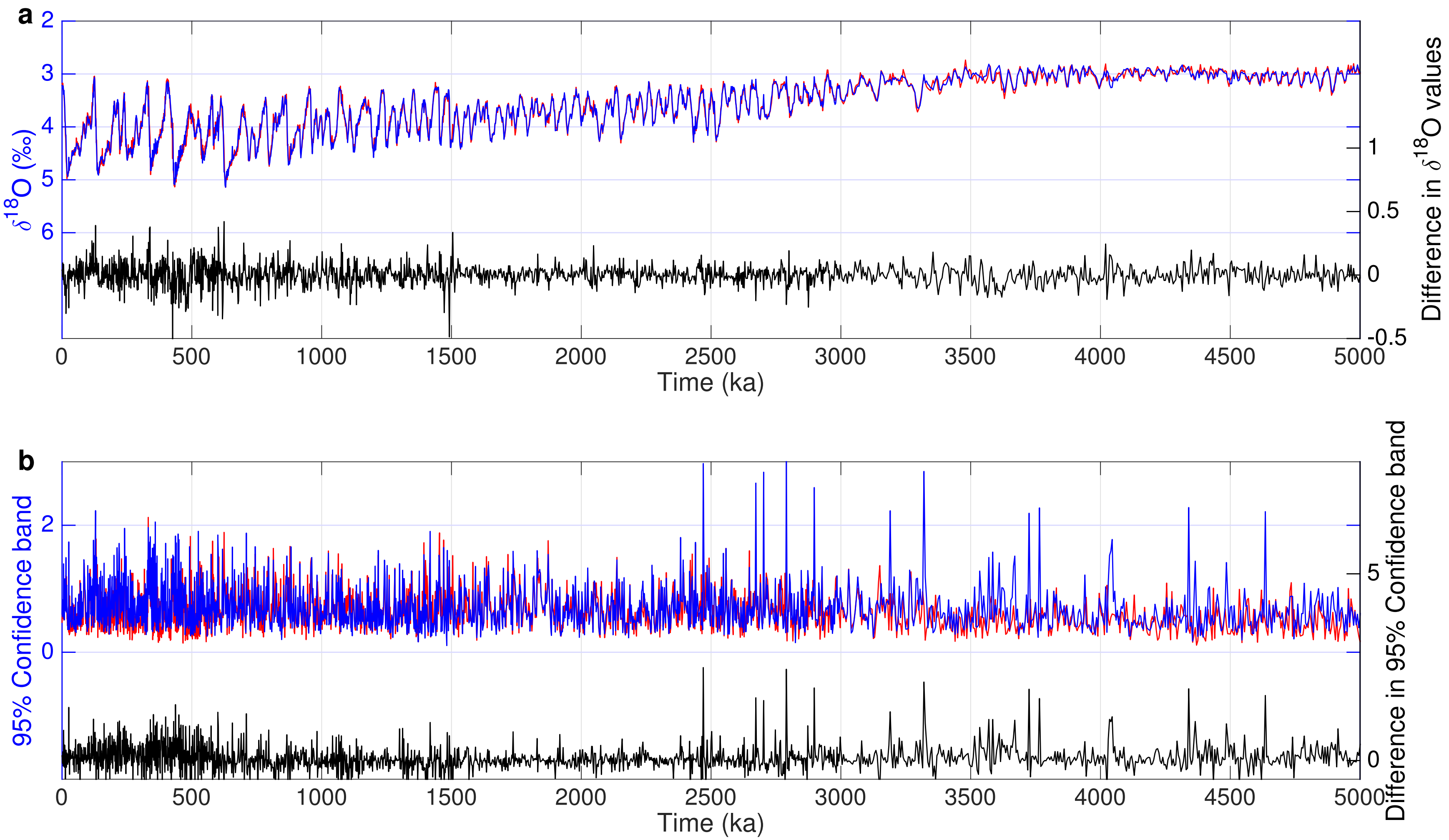

Figure 2.6: Comparison between the Prob-stack and the Prob-LR04-stack. The red lines and the blue lines represent the results of the Prob-LR04-stack and the Prob-stack, respectively. The black line represents the difference between the two stacks. The upper panel (a) and the lower panel (b) show the mean and the 95% confidence interval of the stacks, respectively.

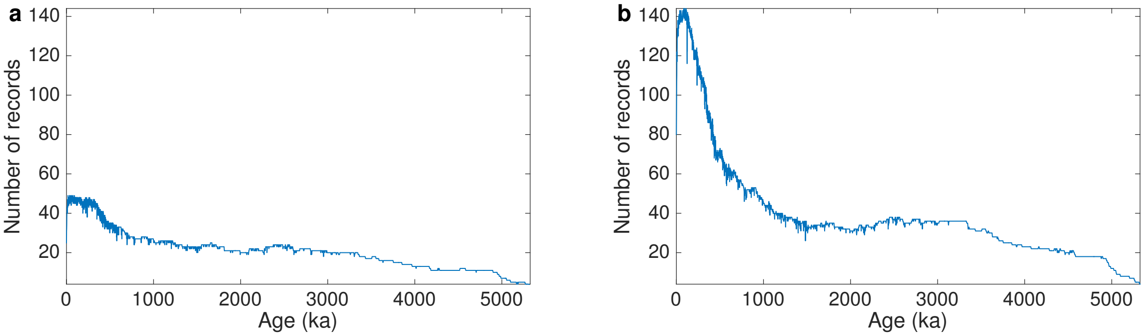

Figure 2.7: The number of records used to construct each stack point of (a) the Prob-LR04-stack and (b) the Prob-stack.

2.3.3 Sensitivity of results to initial values

The profile HMM algorithm does not require age information, except in the target selection. Also, the stack construction algorithm does not include any further age tuning process. However, the two Prob-stacks constructed in this study indirectly employ age information by taking the LR04 stack as initial values. This implies that the constructed stacks follow the same age model as the LR04 stack. Further analysis on the age model of the Prob-stack is beyond the scope of the current study.

There is a chance of the EM method converging to a local maximum instead of a global maximum depending on initial conditions [46]. To find the global maximum estimator, we may run the EM algorithm multiple times with various initial conditions. However, it requires too much time to run the EM algorithm multiple times, so we conduct the sensitivity analysis with different initial conditions for the recent 500-kyr interval.

Sensitivity analysis is done with two alternate initial values: a piecewise linear approximation of the LR04 stack and a constant value set to the overall mean of the LR04 stack (Figure 2.8(a), (b)). We call the two stacks constructed from these two initial values Prob-LR04-ICL and Prob-LR04-ICC, respectively. Prob-LR04 and

Table 2.3: Phase differences between Prob-LR04 and Prob-LR04-ICC. Positive values imply that Prob-LR04-ICC changes earlier than Prob-LR04.

Time [ka]	Phase difference between Prob-LR04 and Prob-LR04-ICC [ka]
0 - 50	4
50 - 100	11
100 - 150	10
150 - 200	6
200 - 250	6
250 - 300	2
300 - 350	0
350 - 400	-2
400 - 450	1
450 - 500	1

Prob-LR04-ICL almost overlap each other. However, we observe phase differences between Prob-LR04 and Prob-LR04-ICC. There phase differences are up to 11-kyr between 0 – 250 ka, but the differences are less than 2-kyr for the periods older than 250 ka. The size of the phase differences is estimated using a normalized cross-correlation which measures the similarity of the two stacks. The normalized cross-correlation is an inner product of one stack and the lagged version of another stack. The phase difference is determined as the lag size which maximizes normalized cross-correlation. Table 2.3 and Figures 2.9 - 2.18 show the estimated phase difference between two stacks. In these figures, the left panel shows Prob-LR04 and Prob-LR04-ICC, the center panel shows both Prob-LR04 and the lagged version of Prob-LR04-ICC for comparisons, and the right panel shows the normalized cross-correlation versus the size of lag.

Prob-LR04-ICC shows that the detailed stratigraphic features of Prob-LR04 are obtained well, even starting from a constant value. Figures 2.19 - 2.22 show updates of the stacks over iterations. These results mean that the algorithm does not require detailed stratigraphic features from initial values, but approximate periodic patterns are helpful for constraining the Prob-stack age model. We confirmed that the overall averages of relative accumulation rate are higher in the case of Prob-LR04-ICL where we observe phase differences (Figure 2.8(c), Figure 2.8(d)). The relative accumulation rate corresponds to the reciprocal of the rate in equation (2.8). Having a relative accumulation rate at a greater value than one indicates that records are expanded relative to the stack. This outcome implies that the recent records need to be contracted in their alignments to converge to the similar periodic patterns of the LR04 stack.

Figure 2.23 represents changes of the total likelihood of records over iterations, and indicates that the likelihoods are converged in both stacks. Even though the likelihoods are converged, the total likelihood of Prob-LR04-ICC is smaller than that of Prob-LR04-ICL. Thus, we can consider Prob-LR04-ICC as an example of a local maximum.

The sensitivity results confirm that the construction algorithm can obtain detailed stratigraphic features without any prior information regarding the benthic $\delta^{18}O$ signals. However, the likelihood comparison indicates that the algorithm may converge to local maximums instead of the global maximum. The stack starting from the linear approximation of the LR04 stack (Prob-LR04-ICL) returns similar periodic patterns to the LR04 stack and gains greater values in its total likelihood than Prob-LR04-ICC. Therefore, setting the initial values to be the LR04 stack can be considered as a better way to converge to similar periodic patterns to the LR04 stack while having a larger likelihood of records.

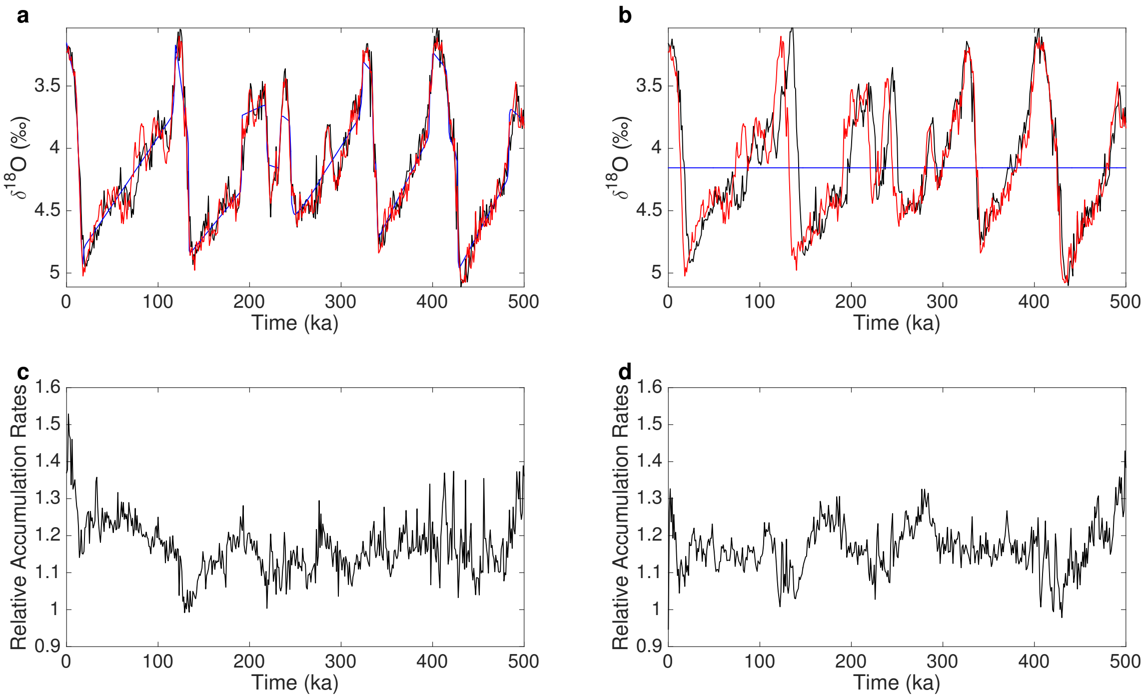

Figure 2.8: Sensitivity of results to initial values. Top panels: The red lines represent the Prob-LR04-stack when initial values are set to be the LR04 stack. The black lines represent the reconstructed stacks starting from the blue lines where the blue lines represent (a) the linear estimation of the LR04 core and (b) the mean value of the LR04 core. Bottom panels: The overall average of relative accumulation rates over the LR04 cores when initial values are set to be (c) the linear estimation and (d) the mean value of the LR04 core.

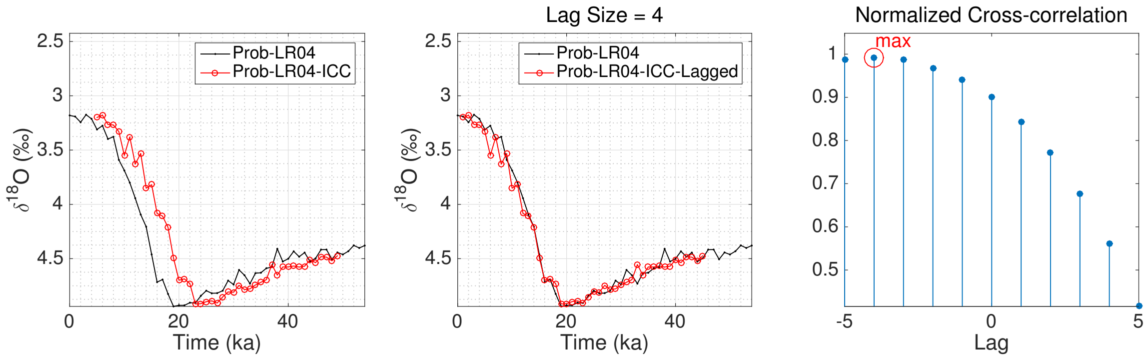

Figure 2.9: Lag Size of Prob-LR04-ICC compared against Prob-LR04 for $t \in [0, 50]$.

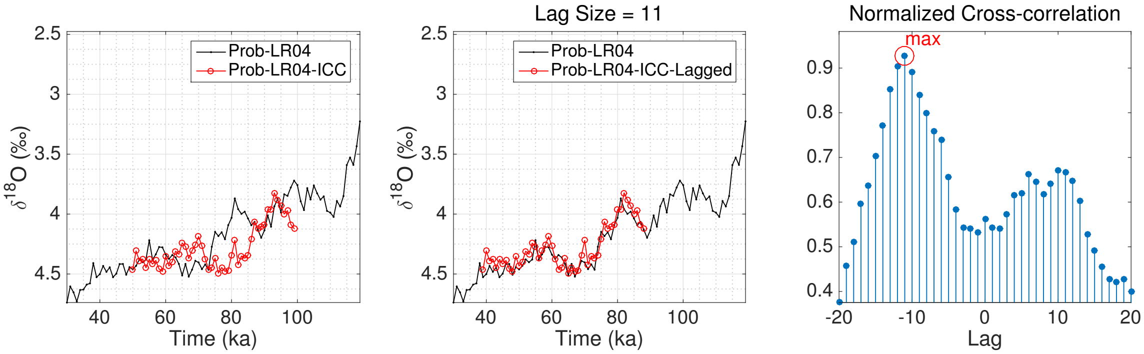

Figure 2.10: Lag Size of Prob-LR04-ICC compared against Prob-LR04 for $t \in [51, 100]$.

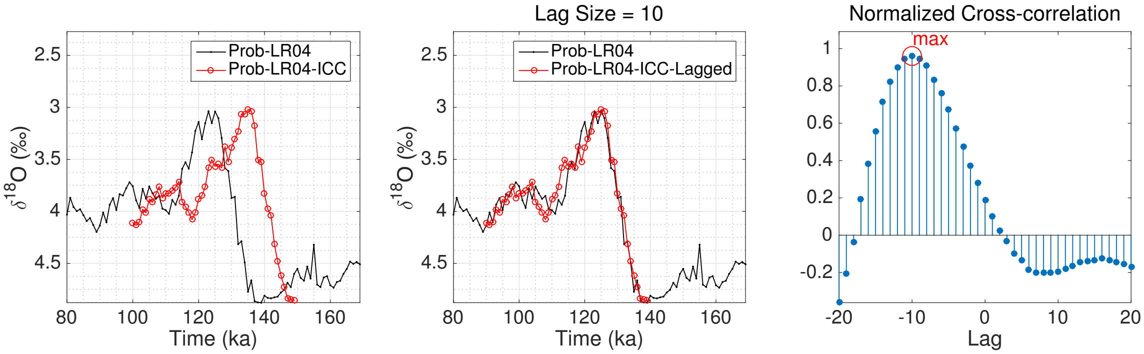

Figure 2.11: Lag Size of Prob-LR04-ICC compared against Prob-LR04 for $t \in [101, 150]$.

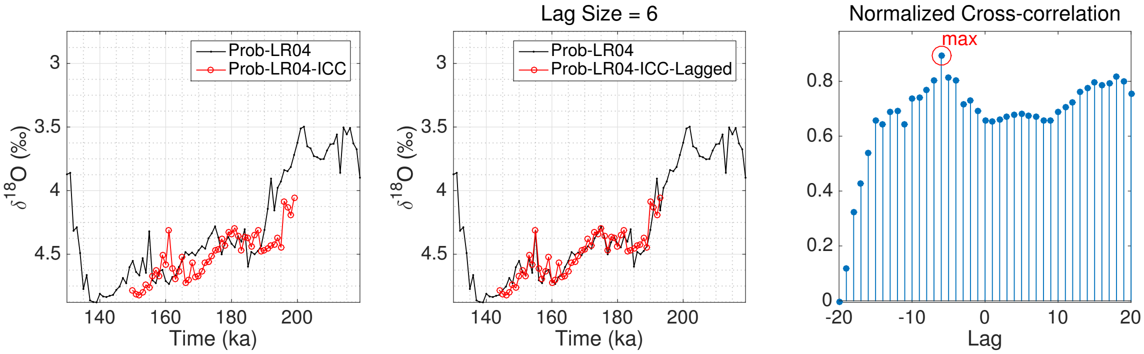

Figure 2.12: Lag Size of Prob-LR04-ICC compared against Prob-LR04 for $t \in [151, 200]$.

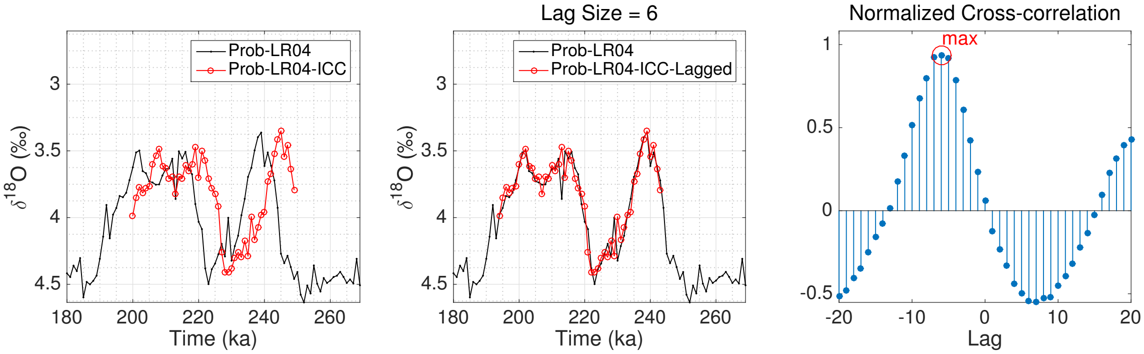

Figure 2.13: Lag Size of Prob-LR04-ICC compared against Prob-LR04 for $t \in [201, 250]$.

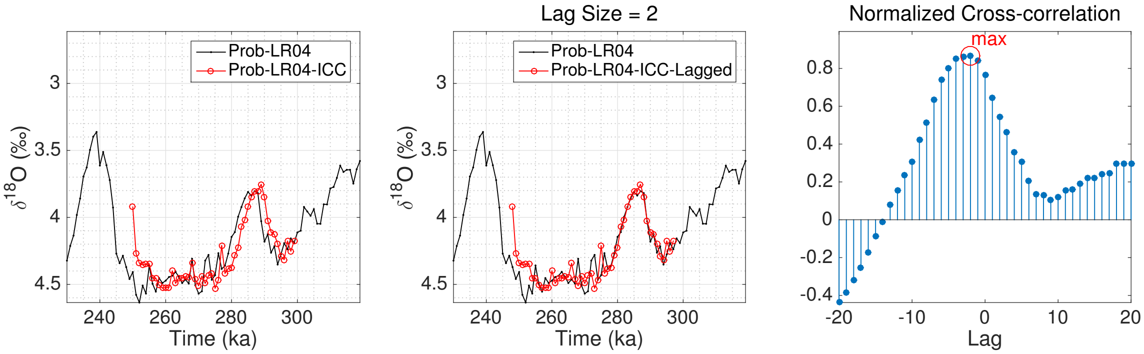

Figure 2.14: Lag Size of Prob-LR04-ICC compared against Prob-LR04 for $t \in [251, 300]$.

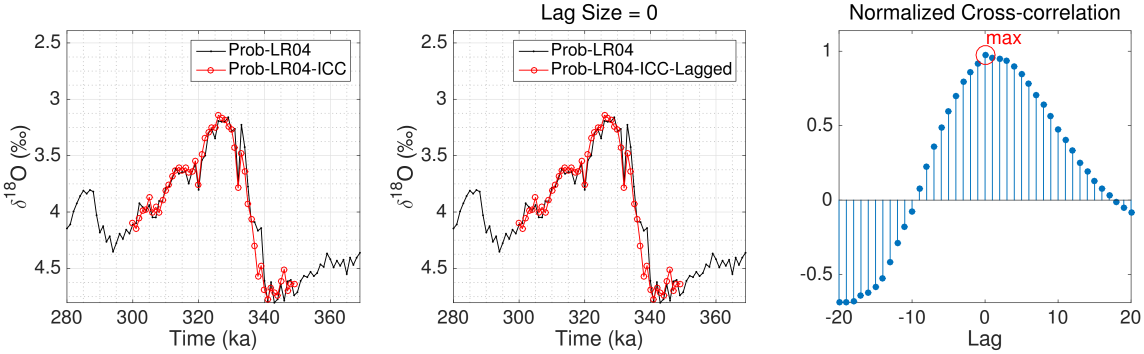

Figure 2.15: Lag Size of Prob-LR04-ICC compared against Prob-LR04 for $t \in [301, 350]$.

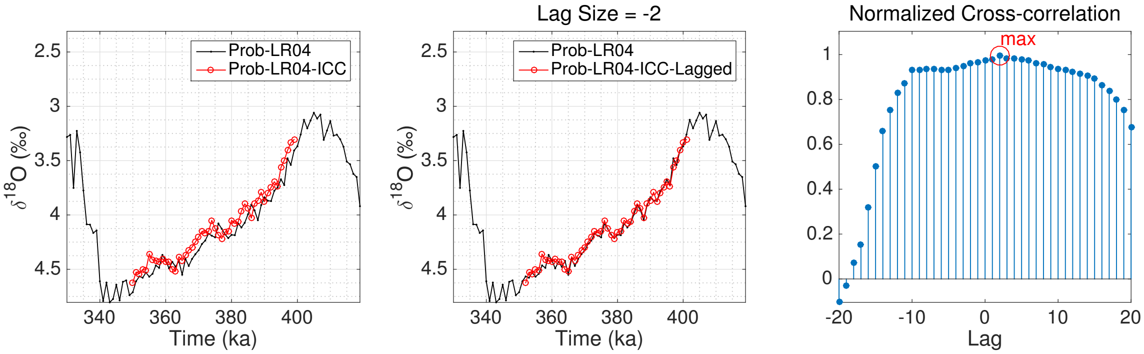

Figure 2.16: Lag Size of Prob-LR04-ICC compared against Prob-LR04 for $t \in [351, 400]$.

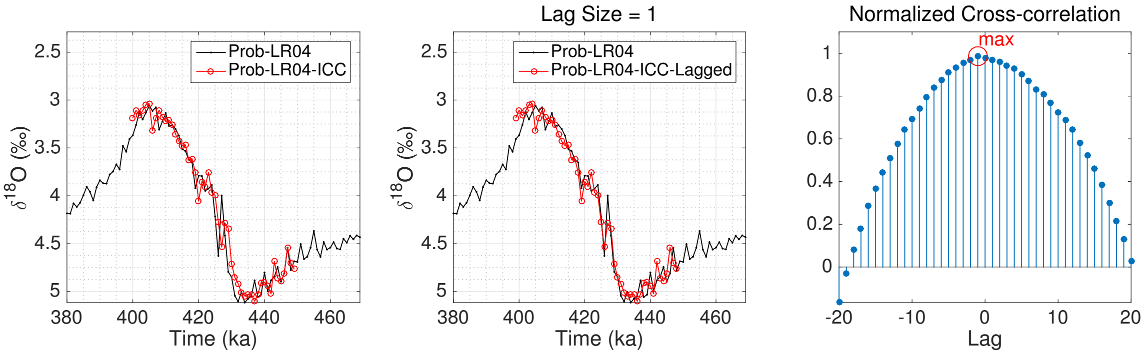

Figure 2.17: Lag Size of Prob-LR04-ICC compared against Prob-LR04 for $t \in [401, 450]$.

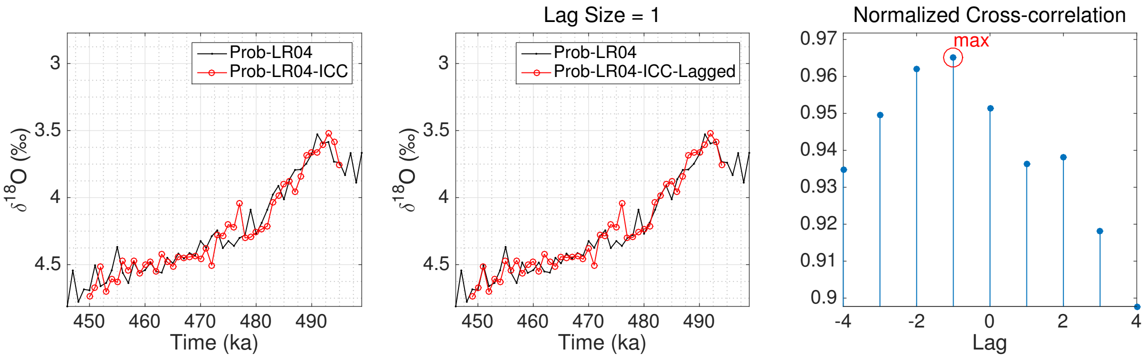

Figure 2.18: Lag Size of Prob-LR04-ICC compared against Prob-LR04 for $t \in [451, 500]$.

2.3.4 Probability model of the Prob-stack

The Prob-stack is assumed to follow the normal distribution with mean μ_t and variance σ_t^2. Here we examine the normality assumption of the Prob-stack using a Q-Q plot [205] comparing the distribution of the aligned samples and the assumed normal distributions of the $\delta^{18}O$ proxies at several points in the stack. As shown in Figure 2.24, most of the points on the Q-Q plot lie on the line $y = x$, which implies that the aligned samples follow the assumed normal distribution of the stack value.

In addition to the normality assumption of the Prob-stack, we assumed that each benthic $\delta^{18}O$ record is emitted from the stack, and thus we estimate the distribution of the stack from the cores. This also indicates that we assumed $\delta^{18}O$ values to be synchronous throughout the ocean. Strictly speaking, generalization to all locations in the oceans without bias would require records to be sampled randomly over the oceans. Although the records comprising the stack seem to follow this assumption, they are not random samples from all locations in the ocean. Thus, we cannot be confident that the estimates for all ocean sediments are unbiased, but rather that the estimates reflect any biases stemming from the decision made in selecting these locations. Also, we assumed that any autocorrelation in the $\delta^{18}O$ values is accounted for by the gradual changes in the mean μ_t. However, the Prob-stack represents a climate

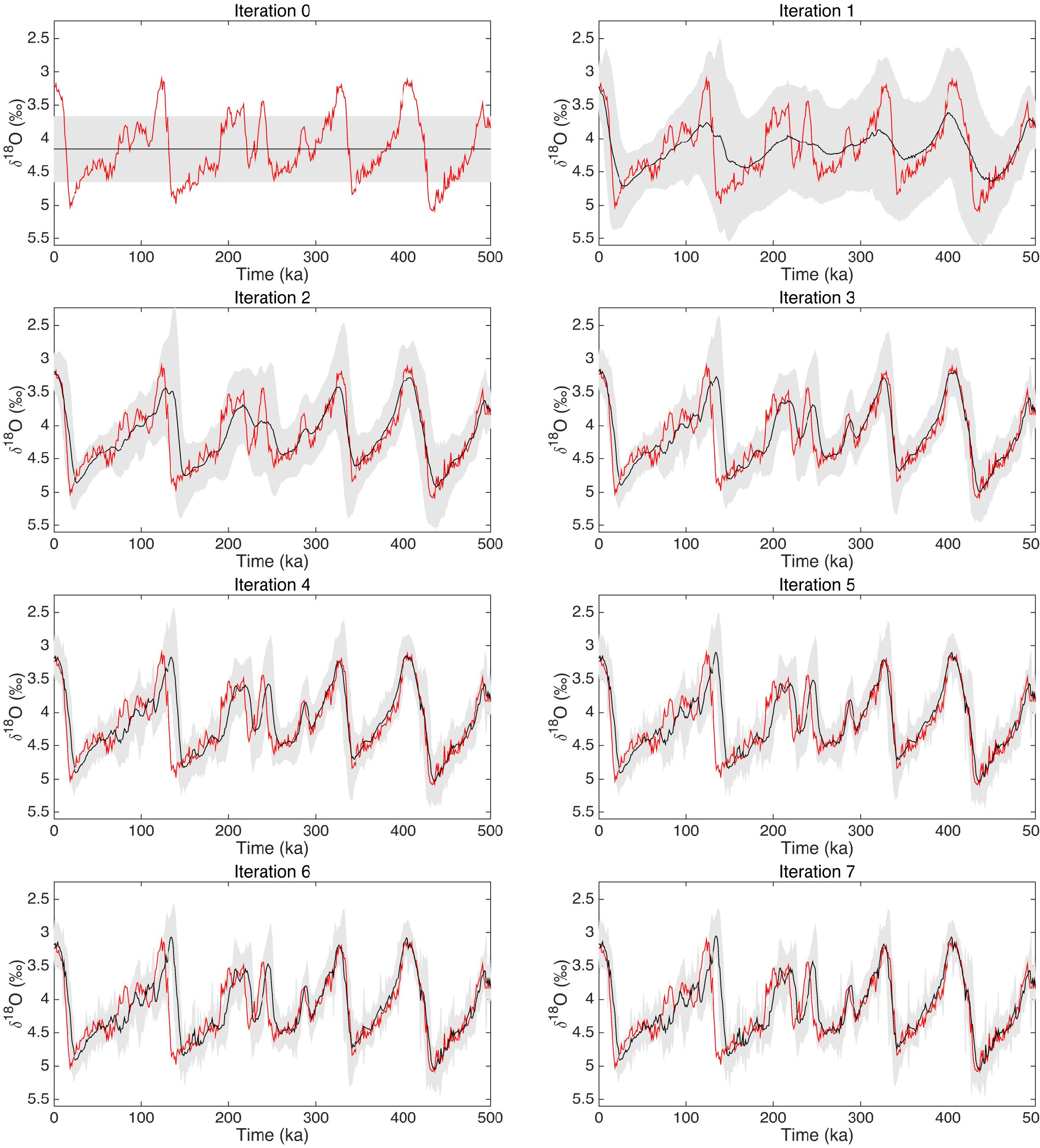

Figure 2.19: [Prob-LR04-ICC] Stack updates over iterations (iteration 0 to 7). Iteration 0 indicates the initial condition. The black lines represent the reconstructed stacks starting from the constant line (the overall mean of the LR04 stack) and the grey areas represent the 95% confidence interval of the reconstructed stack. The red lines represent the Prob-LR04 stack when initial values are set to be the LR04 stack.

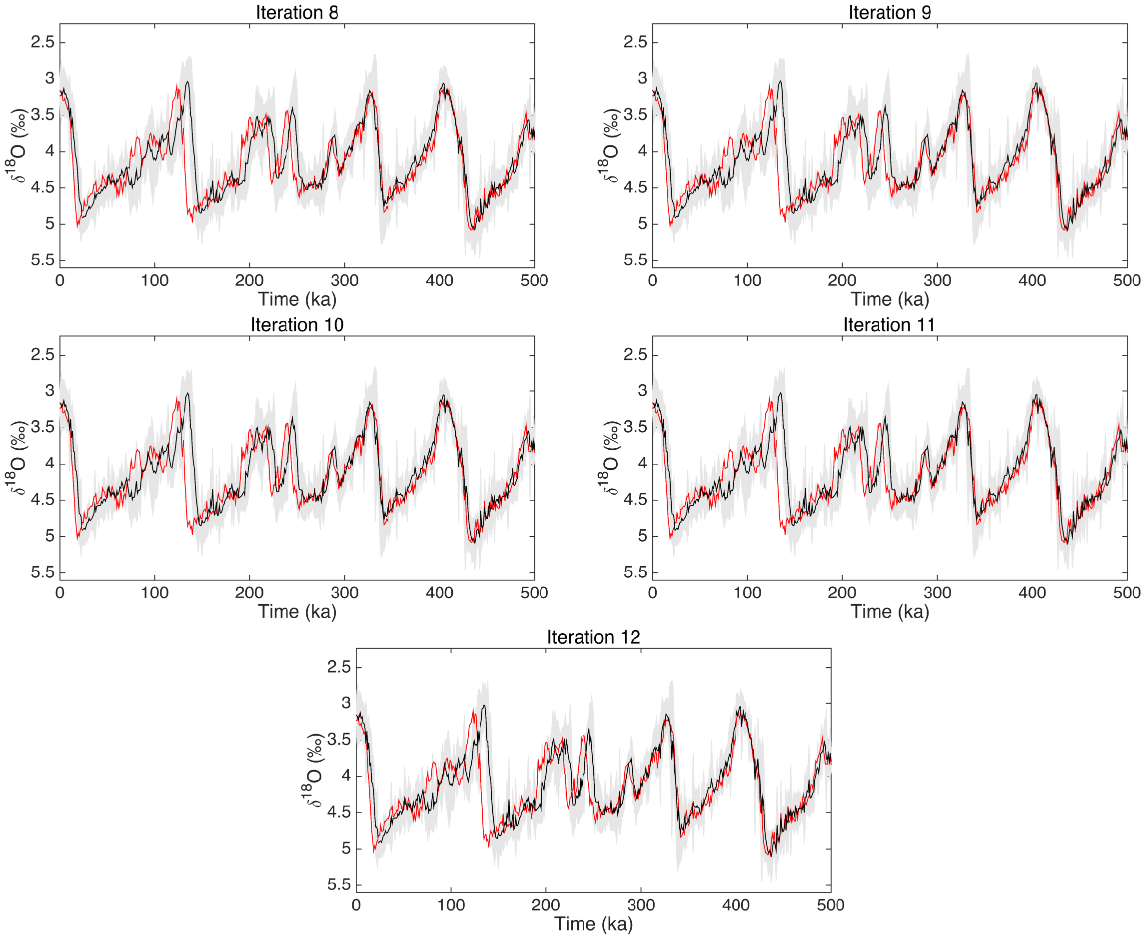
Iteration 8

Iteration 9

Iteration 10

Iteration 11

Iteration 12

Figure 2.20: [Prob-LR04-ICC] Stack updates over iterations (iteration 8 to 12). The black lines represent the reconstructed stacks starting from the constant line (the overall mean of the LR04 stack) and the grey areas represent the 95% confidence interval of the reconstructed stack. The red lines represent the Prob-LR04 stack when initial values are set to be the LR04 stack.

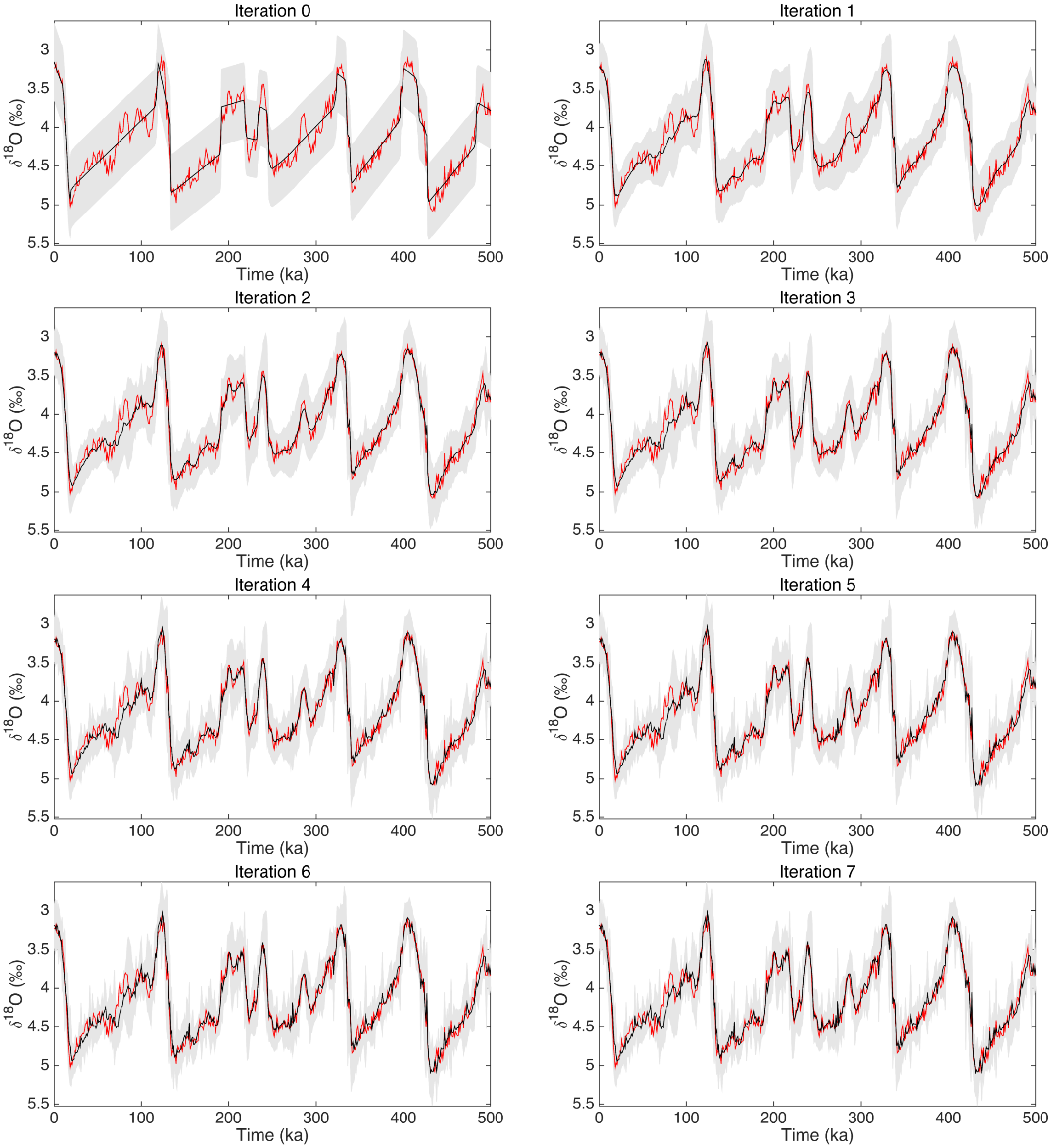

Figure 2.21: [Prob-LR04-ICL] Stack updates over iterations (iteration 0 to 7). Iteration 0 indicates the initial condition. The black lines represent the reconstructed stacks starting from the piecewise linear approximation of the LR04 stack and the grey areas represent the 95% confidence interval of the reconstructed stack. The red lines represent the Prob-LR04 stack when initial values are set to be the LR04 stack.

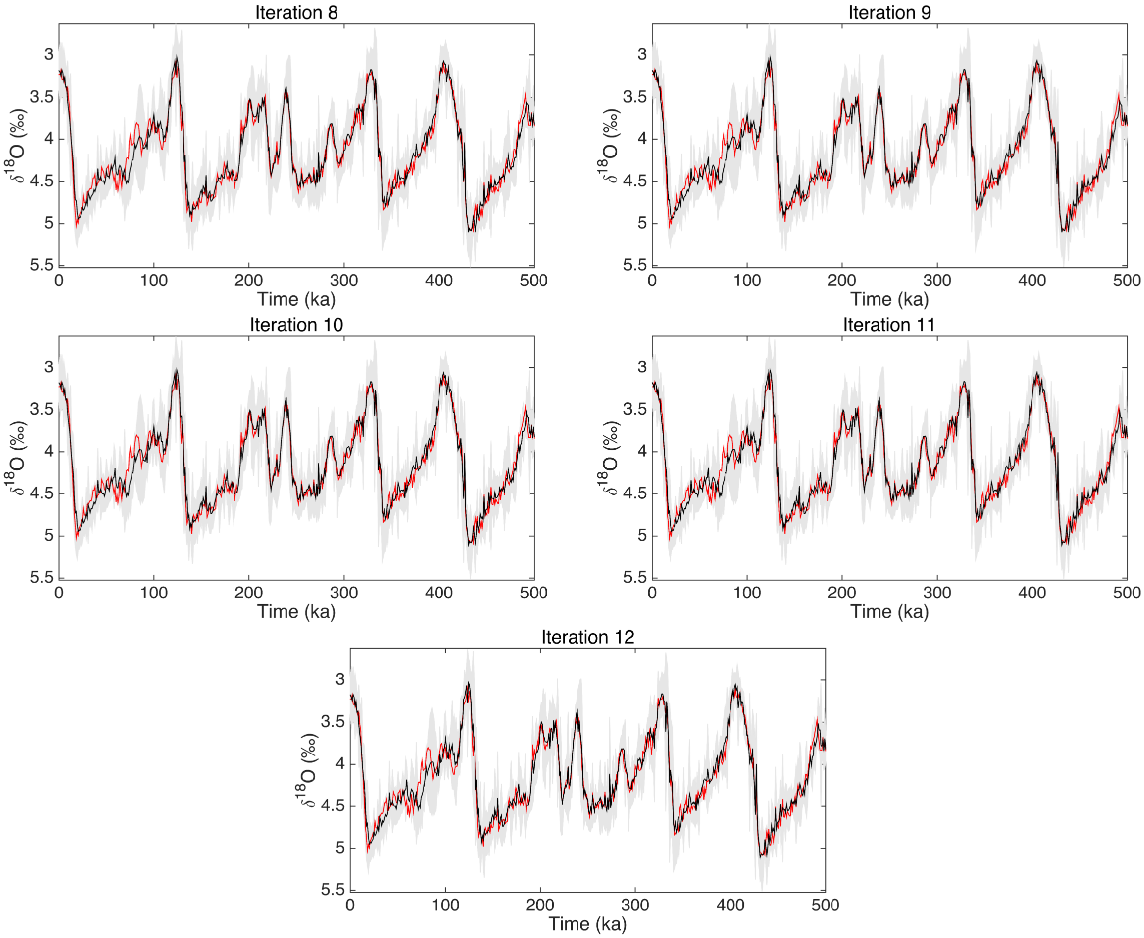

Figure 2.22: [Prob-LR04-ICL] Stack updates over iterations (iteration 8 to 12). The black lines represent the reconstructed stacks starting from the piecewise linear approximation of the LR04 stack and the grey areas represent the 95% confidence interval of the reconstructed stack. The red lines represent the Prob-LR04 stack when initial values are set to be the LR04 stack.

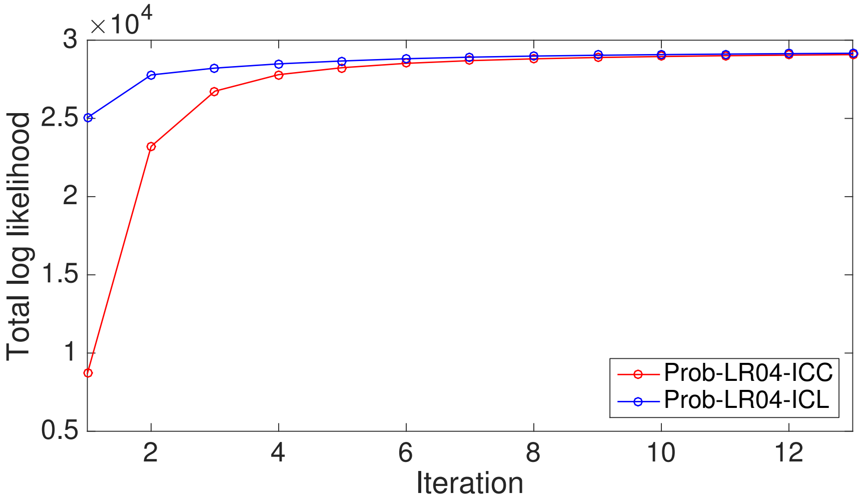

Figure 2.23: The likelihood of the Prob-LR04-ICL stack is larger than that of the Prob-LR04-ICC stack. Both stacks converged after 13 iterations. Red and blue circles represent the total log likelihood of the Prob-LR04-ICC stack, the Prob-LR04-ICL stack, respectively, and are shown over iterations.

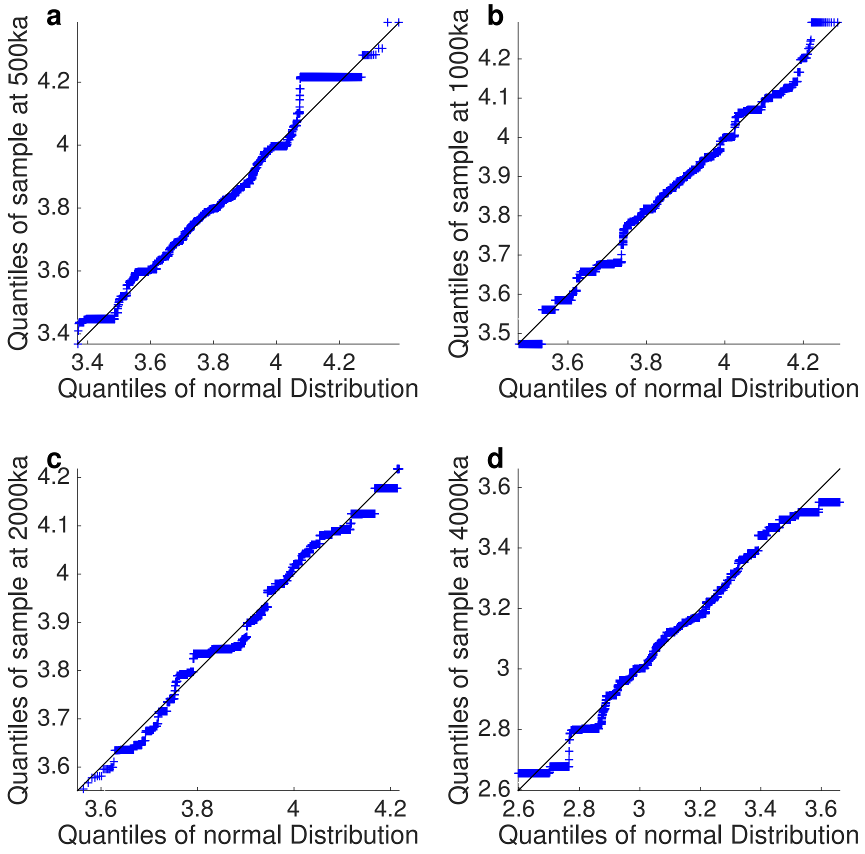

Figure 2.24: Q-Q plots: The empirical Q-Q plot of the samples aligned at (a) 500ka, (b) 1000ka, (c) 1500ka, and (d) 2000ka versus the distribution of the Prob-stack.

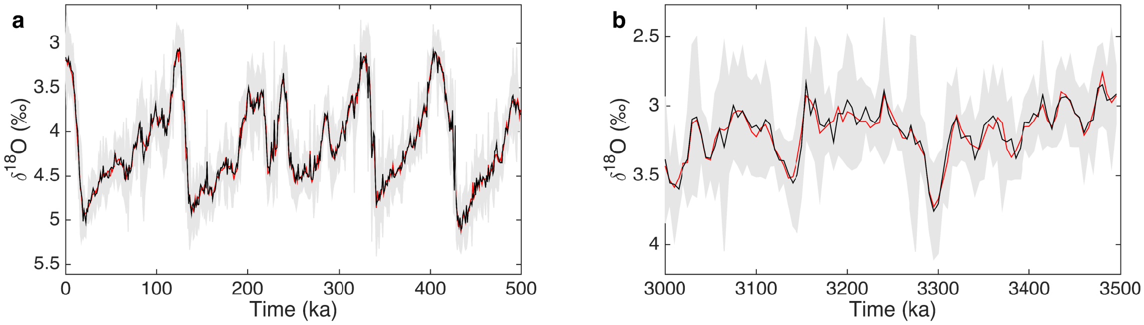

Figure 2.25: Reconstructed stack from the simulated records reflecting the period of (a) 0 - 500ka and (b) 3000 - 3500ka: The red lines represent the Prob-LR04 stack while black lines and the grey areas represent the mean and 95% confidence interval of the reconstructed stack from simulated records, respectively.

time series, where the intervals between the points in the stack are short compared to glacial cycle wave length. Thus, we can consider including further autocorrelation terms in models in future studies.

The algorithm constructing the new stacks can be validated through pseudo-proxy experiments. After setting parameter values using Prob-LR04-stack as known values, pseudo-proxies are generated based on the resulting probabilistic model. Two sets of pseudo-proxies are simulated: The first set contains 40 sample records reflecting the resolution of 0 to 500ka, and the second set includes 20 sample records reflecting the resolution of 3000 to 3500ka. Because we have known values of the parameters, we can evaluate the algorithm by comparing the reconstructed stacks and the exact values. As shown in the two plots in Figure 2.25, the algorithm can accurately reconstruct the distribution of the stacks. The root mean squared errors of the mean values of two stacks are 0.057 and 0.056.

2.4 Usage notes

The Prob-stack is probabilistic, i.e., it represents the distribution of the stack for each time step using a normal distribution with mean and variance. Both the mean and the variance information should be used simultaneously for the applications of the Prob-stack. Here we introduce two applications; age estimation of a benthic $\delta^{18}O$ core and lead/lag analysis between two events observed from different cores, which can reasonably be completed on a modern laptop or desktop. Open sources software for the Prob-stack, called HMM-Stack, (https://github.com/seonminahn/HMM-Stack) includes the codes for these two applications.

The algorithm of constructing the Prob-stack includes a procedure to find alignments of benthic $\delta^{18}O$ records to the Prob-stack. Because the Prob-stack is based on many additional records beyond LR04 and includes uncertainty estimates, it would be a mistake to use the LR04 stack for age estimations from this point forward. This procedure finds age estimates of a benthic $\delta^{18}O$ record using both the means and the variances of the Prob-stack. As an example, Figure 2.26(a) shows alignments of the benthic $\delta^{18}O$ record from the site GeoB 1041 [13]. Among possible alignment samples, the median alignment is chosen as it represents the central tendency of the posterior probability distribution of alignment [110]. The length of the confidence band varies from 2.5-kyr to 12.5-kyr. Note that it sometimes increases up to 1/4 of the obliquity cycle. When the signal varies a lot, the confidence band tends to decrease. For example, around 130 ka, the $\delta^{18}O$ signal increases significantly, causing the confidence band to decrease. We also display uncertainty information of age estimates (Figure 2.26(b)) and relative accumulation rates with respect to the Prob-stack (Figure 2.26(c)).

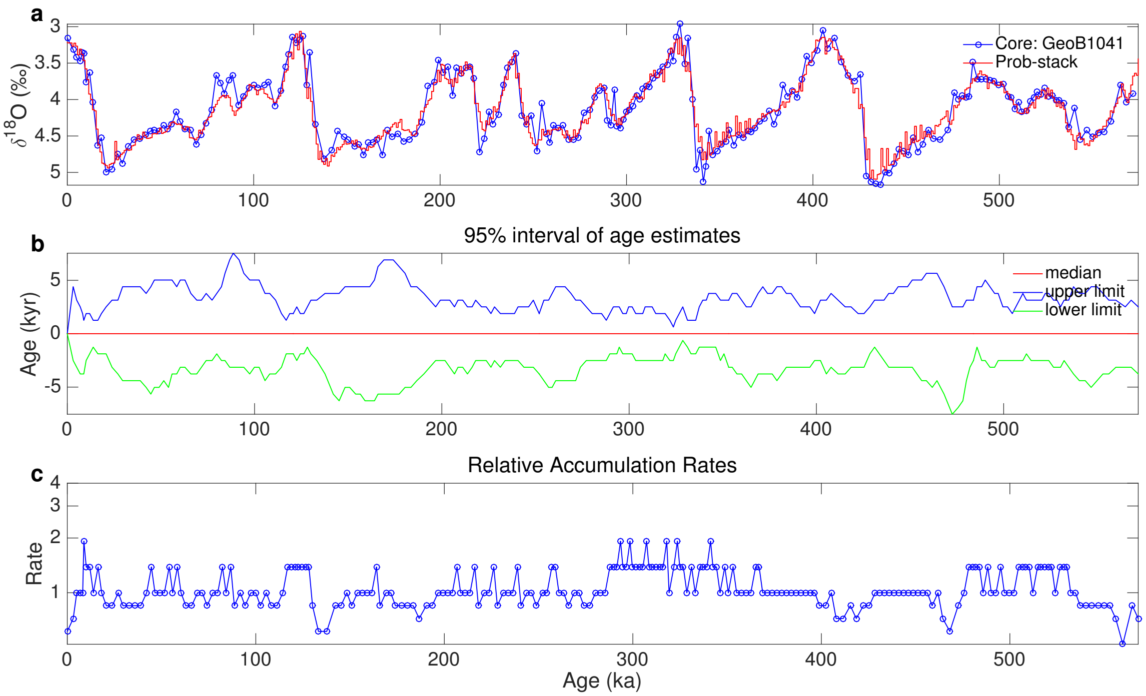

Figure 2.26: Example of benthic $\delta^{18}O$ record age estimation. (a) represents the median alignment of the GeoB1041 core (blue line) to the Prob-stack (red line), (b) describes time-varying uncertainty of the age estimates using the 95% interval of the age estimate for each time step, and (c) represents the relative accumulation rates of the GeoB1041 core with respect to the Prob-stack based on the median age estimate.

Lead/lag analysis between two events observed from different cores can be done using age estimates of the two events. For example, let a_1 and a_2 be the age estimates of ODP1143 [190] at 8.1m and ODP1123 [58, 63] at 7.3m below the sediment surface, respectively. The probability that a_1 occurs earlier than a_2 can be estimated by the joint distribution of a_1 and a_2 as follows:

$$\begin{aligned} P(a_1 > a_2 \mid \text{record}_{1143}, \text{record}_{1123}) &= \sum_{a_1 > a_2} P(a_1, a_2 \mid \text{record}_{1143}, \text{record}_{1123}) \\ &= \sum_{a_1 > a_2} P(a_1 \mid \text{record}_{1143}) P(a_2 \mid \text{record}_{1123}) \end{aligned} \tag{2.14}$$

The second equality holds as we assume benthic $\delta^{18}O$ records are independent samples emitted from the Prob-stack. After finding the age estimates a_1 and a_2 independently, the distribution of the age difference can obtained from equation (2.14) as shown in Figure 2.27. While the median age difference ($a_1 - a_2$) is -1.4-kyr, the 95% confidence interval is -4.1-kyr to 2.7-kyr. This outcome indicates that any apparent differences in age fall within the realm of chance. Both HMM-Match AND HMM-Stack can be used to infer lead/lag. However, since HMM-Stack takes into account the substantial differences in variances with age while HMM-Match does not, HMM-Stack should be used when using the HMM-Stack. HMM-Match remains useful for comparisons with other targets that do not incorporate uncertainty.

2.5 Discussion

In this study, we presented the Probabilistic stack (Prob-stack), which is a representative time series of 180 benthic $\delta^{18}O$ records constructed using a profile hidden Markov model. The construction algorithm finds alignments of multiple records and then obtains the Prob-stack which maximizes the likelihood of the records. We did

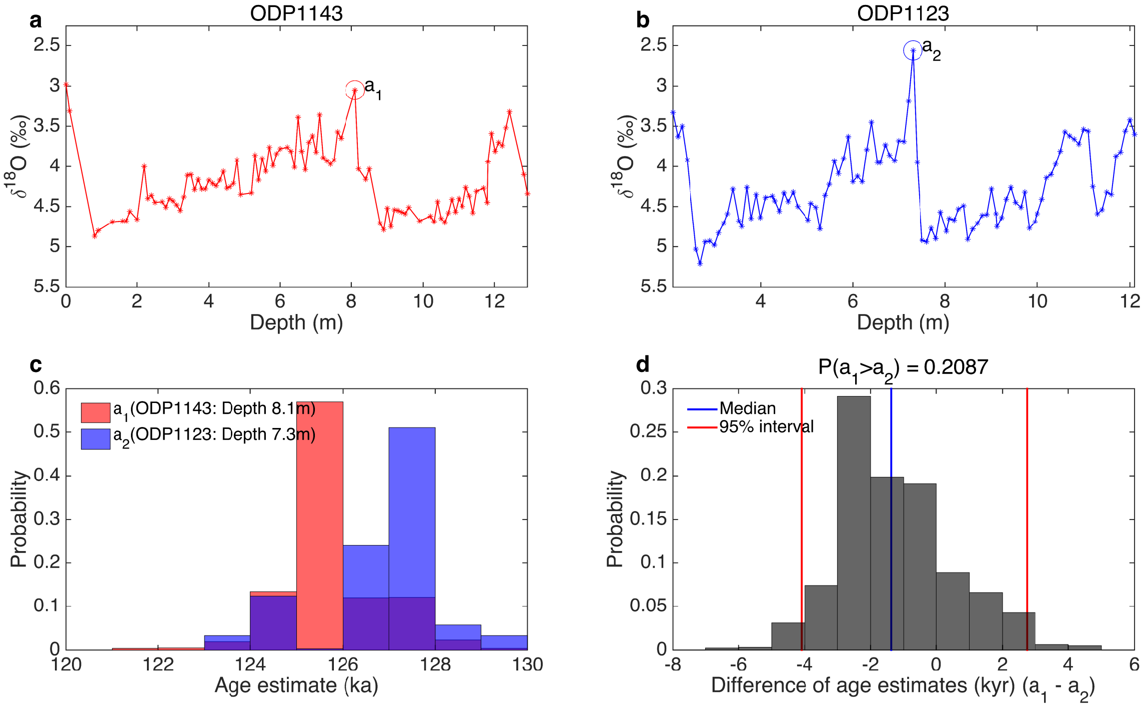

Figure 2.27: Lead/lag relationships between the two data points marked with circles in (a) ODP1143 (located 8.1m below the sediment surface) and (b) ODP1123 (located 7.3m below the sediment surface). The distributions of age estimates are shown in (c), and the distribution of the age difference is plotted in (d).

not include further age adjustments after aligning with the automated process. Thus, we could not guarantee that the assigned ages are consistent with absolute ages. We instead called it a synchronous age estimate because the alignment procedure synchronizes ages from multiple records. The phase differences between the Prob-mean and the LR04 stack may stem from the synchronous age estimates as well as lower compression near the tops of the cores. Further adjustments in age estimates can be considered in future studies; aligning the Prob-stack to 21 June insolation at 65°N or to the obliquity of Earth's movements could provide relative age estimates of the Prob-stack, and magnetic reversal indexes would act as milestones to determine absolute ages estimates.

When more data have become available, we can update the Prob-stack by including the new data and supposing the initial value of the stack set to be the current Prob-stack. The current algorithm requires iterations of the EM algorithm using all benthic $\delta^{18}O$ records to construct the new probabilistic stack. It took about one month to complete the construction of the stack with parallel running of the algorithm, as a high-resolution and long-coverage record require a heavy computing load. Further developing the stack algorithm to update the Prob-stack using only the newly-added record would greatly reduce the computing time of stack construction and speed up the development of new stacks.

The preceding study [112] that introduced the LR04 stack has been cited over 2900 times over the last twelve years since it was first introduced, thereby proving the usefulness of the benthic stack. As we added 123 additional records to the 57 LR04 cores to provide a probabilistic distribution of $\delta^{18}O$ values for each time step, the Prob-stack delivers a more complete description of the global nature of $\delta^{18}O$ values and allows assessment of the uncertainty in relative ages, such as lead-lag relationships.

Chapter Three

The role of uncertainty in estimating lead/lag relationships in sea surface temperatures in the tropical Pacific

3.1 Background & Summary

In order to understand glacial terminations, it is important to identify the timing of these events from the geological records. However, achieving this goal is challenging because of the limitations of the records and the complexity of the mechanisms for determining glacial terminations. Despite a long interval of cooling climate, termination occurred within a relatively short interval. The most widely accepted theory to explain this phenomenon is that the Northern Hemisphere ice sheets collapsed in response to summer insolation [40]. However, some paleoclimate records support a conflicting hypothesis which claims that tropical sea surface temperatures (SST) caused continental ice volume changes [105, 202]. Examining this hypothesis requires an analysis of the timing of SST changes during the glacial terminations between the North Atlantic and the tropical Pacific, as well as within the tropical Pacific [14].

In this study, we explore the relative timing of the glacial terminations I, II, and III across the tropical Pacific using 15 published SST records to evaluate the hypothesis and to better understand climate change mechanisms. Because the goal of this study is to examine the relative timing of the glacial termination, we can obtain the results using the SST records even though the time of warming does not coincide with the change in ice volume. The method to infer absolute termination ages from SST changes includes the following three steps: First, we use either Mg/Ca of the planktonic foraminifer *Globigerinoides ruber* or the $U_{37}^{k'}$ proxy to get a SST record using Bayesian calibration [99, 98]. Next, we use a benthic $\delta^{18}O$ proxy from the same core to obtain age estimates using the HMM-Match algorithm [110]. Combining them, we get the SST time series, and finally, we infer absolute termination ages in SST, which is determined using the change point algorithm [167, 166]. The relative timing of the glacial terminations for the 15 records is estimated with one reference record MD05-2920 [188]. Inference of unknowns always includes uncertainty by nature. Thus, deterministic approaches to assessing the potential differences might lead to conclusions that may well be the results of chance, i.e. differences that are often called not statistically significant. Through the timing analysis, when reflecting the uncertainty of the three steps, we could not conclude that there are differences in terminations between the eastern and western tropical Pacific due to high uncertainties.

Here we explain the three inference steps, the tool to analyze the uncertainties, and the relative timing results using the 15 SST records. Detailed discussions on the results will be described in the preliminary paper.[1]

3.2 Method

3.2.1 Data collection

In this study, we collected 15 published SST records (Figure 3.1, Table 3.1). SSTs were derived from either Mg/Ca of the planktonic foraminifer *Globigerinoides ruber* or the $U_{37}^{k'}$ proxy, and ages of records were estimated from benthic $\delta^{18}O$ records. Each of the collected records covers at least 100-kyr and has a resolution better than 2.5-kyr. The MD05-2920 record [188] includes two benthic curves based on *Uvigerina peregrina* and *Cibicidoides wuellerstorfi*. The MD05-2920 record based on *Uvigerina peregrina* is used as a reference record to find relative timings in this study.

---

[1] The work in this chapter is in collaboration with my advisor Dr. Charles E. Lawrence of Brown University, Dr. Lorraine Lisiecki of the University of California, Santa Barbara, and Dr. Deborah Khider of the University of California, Santa Barbara. This chapter includes materials from the draft of the preliminary paper associated with this work.

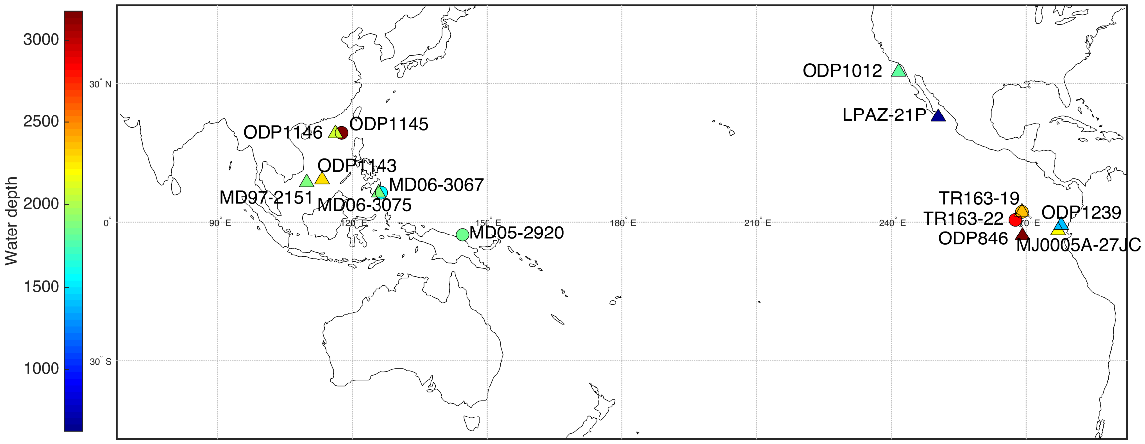

Figure 3.1: Location of the records used in this study. The colors represent water depths of the cites. Circle: Mg/Ca, Triangle: $U_{37}^{k'}$.

3.2.2 Relative timing of glacial terminations

The timings of the glacial terminations are obtained from the SST time series, which is composed of SSTs from based on Mg/Ca or $U_{37}^{k'}$ proxies and age estimates from benthic $\delta^{18}O$ records. Bayesian calibration [98] generates 1000 samples of SSTs and the HMM-Match algorithm [110] finds 1000 samples of age estimates. Pairing these two sets of samples, we get 1000 samples of SST time series. For each SST time series, we run the Bayesian change point algorithm [167, 166] to generate 500 samples of change point locations, which refer to the timing of glacial terminations. The probability distribution of the timing of the glacial terminations is estimated by combining the samples of change point locations across all 1000 SST time series. After finding the distribution of the absolute termination age for each record, we combine two distributions of the absolute termination age, one of which is the reference record, to construct the joint distribution. Next, we use this joint distribution to find the probability distribution of the relative termination timing for each record. The flowchart in Figure 3.2 summarizes these steps, and we briefly review these steps in this section.

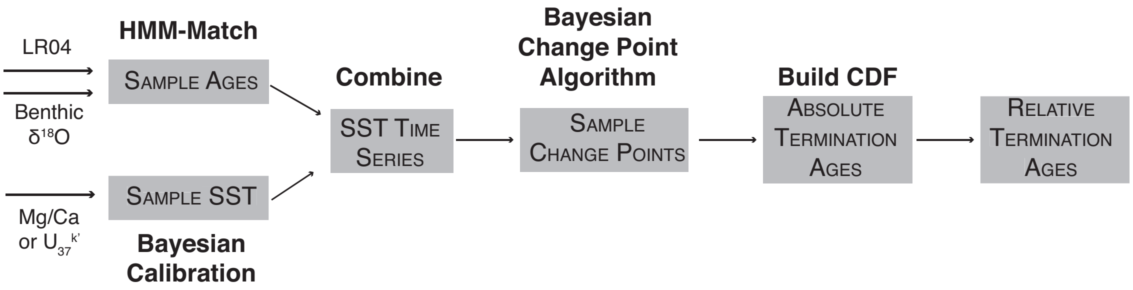

Figure 3.2: Flowchart of the relative timing of the glacial termination.

SST records are derived from either Mg/Ca or $U_{37}^{k'}$ based on Bayesian Calibration [98]. We use the following regression models to describe the relationship between SSTs and the proxies.

$$
\begin{aligned}
Mg/Ca &= \alpha_0 \exp(\alpha_1 T) + v, \quad && \text{where } v \sim \mathcal{N}(0, \sigma_v^2), \\
U_{37}^{k'} &= \beta_0 + \beta_1 T + w, && \text{where } w \sim \mathcal{N}(0, \sigma_w^2).
\end{aligned}
$$

The regression model of Mg/Ca uses the measured Mg/Ca and temperature from the culturing study [100]. The regression model of $U_{37}^{k'}$ uses the measured $U_{37}^{k'}$ and temperature from the global core-top database [32]. The calibration model based on the above-mentioned regression models is given by:

$$
\begin{aligned}
f(\Phi_\alpha \mid Mg/Ca, T) &\propto f(Mg/Ca \mid T, \Phi_\alpha) \cdot f(\Phi_\alpha), \\
f(\Phi_\beta \mid U_{37}^{k'}, T) &\propto f(U_{37}^{k'} \mid T, \Phi_\beta) \cdot f(\Phi_\beta),
\end{aligned}
$$

which implies that the posterior probability is proportional to the product of the likelihood and the prior probability. The first term refers to the posterior probability of the regression coefficients ($\Phi_{alpha} = (\alpha_0, \alpha_1, \sigma_v^2)$ and $\Phi_{beta} = (\beta_0, \beta_1, \sigma_w^2)$). The second term represents the likelihood of the proxy, and the third term represents the prior of the regression coefficients. The priors on α_0 and α_1 are assumed to follow normal distributions:

$$\alpha_0 \sim \mathcal{N}(0.075, 0.0006)$$

$$\alpha_1 \sim \mathcal{N}(0.5, 4)$$

The priors on β_0 and β_1 are uninformed, but β_1 is constrained to be positive. Inverting the calibration models, we get the following prediction model:

$$f(T \mid \Phi_\alpha, Mg/Ca) \propto f(Mg/Ca \mid T, \Phi_\alpha) \cdot f(T)$$

$$f(T \mid \Phi_\beta, U_{37}^{k'}) \propto f(U_{37}^{k'} \mid T, \Phi_\beta) \cdot f(T)$$

The SST samples are generated from the measured proxies using the above prediction model. The JAGS software package for Bayesian inference using Gibbs sampler (http://mcmc-jags.sourceforge.net) is used to generate 1000 samples of SSTs for each record.

Age estimates are obtained by aligning the benthic $\delta^{18}O$ record to the LR04 stack using the HMM-Match algorithm [110]. The HMM-Match finds the age estimates that reflect alignment uncertainties, as described in Section 2.2.3. This method aligns a record to the stack iteratively using the EM algorithm. The profile HMM, explained in Section 2.2.3, was developed based on the HMM-Match method. The two methods have similar structures except that the HMM-Match uses the predetermined LR04 stack and does not update the stack. Also, the two algorithms have different emission models. The emission model of the HMM-Match is given by

$$d_{i,j} | A_{i,j} = t \sim \mathcal{N}(\tau_i + l_t, \sigma_i^2) \tag{3.1}$$

where $d_{i,j}$ and $A_{i,j}$ represent the benthic $\delta^{18}O$ value and its age estimate for the j^{th} point of the record i, respectively. Also, τ_i and σ_i^2 refer to the mean shift and the variance of the record i, respectively. Lastly, l_t refers to the LR04 stack value at time

t. We are using the same notations with Section 2.2.3. The equation (3.1) implies that $d_{i,j}$ follows the normal distribution with mean $\tau_i + l_t$ and variance σ_i^2 when the age estimate of $d_{i,j}$ is equivalent to t, i.e., $A_{i,j} = t$. The variance term reflects the spatial variability between records and interlaboratory offsets [144]. The backward sampling step in the EM algorithm generates 1000 samples of alignments, which follow the posterior distribution (2.10), and we use these samples as age estimates of the records.

The 1000 samples of SSTs from the Bayesian calibration and the 1000 samples of age estimates from the HMM-Match make up the 1000 pairs of SST time series. Five pairs among these 1000 pairs of the reference record are illustrated in different colors in the left panel of Figure 3.3. The black curve in the right panel is the SST time series based on the median age estimate, and the grey area represents the 95% confidence interval of the SST time series.

The Bayesian change point algorithm [167, 166] finds the timing of the glacial terminations using the 1000 pairs of SST time series. Finding the termination using this algorithm is equivalent to fitting SST time series into a piecewise linear curve. The joints of linear segments become the location of change points, i.e. the timings of the glacial termination. The change point algorithm considers every possible subinterval for the piecewise approximation by dynamic programming, and generates 500 samples of change point locations for each record. These samples reflect uncertainties in the number and locations of the change points. The probability distribution of change point locations is estimated by using these samples. The lower curves in Figure 3.3 represent this probability distribution. A tall and thick peak indicates low uncertainty while a short and wide peak implies high uncertainty.

As a result of the three steps, we get 500 change point samples for the 1000 SST

time series. Now, we are ready to find the probability distribution of the timing of the glacial terminations. Let C be a random variable for the timing of change point representing the termination of a record. Let $\vec{A}$ be the vector of the age estimates of a record, and $\vec{T}$ be the SST vectors from the calibration for a record. Also, let $\vec{\delta}$ and $\vec{p}$ be the vectors of the benthic $\delta^{18}O$ values and the SST proxies for a record, respectively. The joint probability of the timing of change points, age estimates, and SSTs given the measured data is

$$P(C, \vec{A}, \vec{T} \mid \vec{\delta}, \vec{p}).$$

Recall that the age and SST estimates were obtained independently at each location. Thus, we have

$$P(C, \vec{A}, \vec{T} \mid \vec{\delta}, \vec{p}) = P(C \mid \vec{A}, \vec{T}, \vec{\delta}, \vec{p}) \cdot P(\vec{A} \mid \vec{\delta}) \cdot P(\vec{T} \mid \vec{p}).$$

Our interest is in the timing of the terminations given only the measured proxies $\vec{\delta}$ and $\vec{p}$, so we use our samples to compute the sums over all possible ages and SSTs to find the probability of the timing:

$$P(C \mid \vec{\delta}, \vec{p}) = \sum_{\text{all } \vec{A}} \sum_{\text{all } \vec{T}} P(C \mid \vec{A}, \vec{T}, \vec{\delta}, \vec{p}) \cdot P(\vec{A} \mid \vec{\delta}) \cdot P(\vec{T} \mid \vec{p}) \qquad (3.2)$$

In addition, we include the prior information about termination ranges for the inference of termination timings. The red shaded areas in Figure 3.3 represent these ranges of terminations. The change point algorithm finds the change points outside of these ranges, but our interests are constrained to the change points within these ranges. Thus, we normalize the probability of change point locations by the ranges. We assume that a termination time range is constrained by a_l and a_u. That is, C

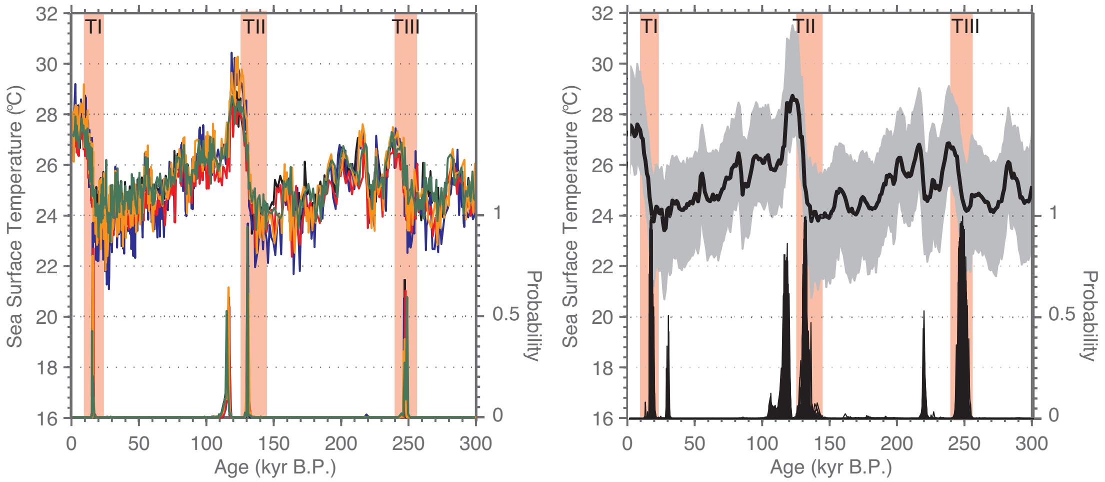

Figure 3.3: Results from the change point algorithm for the reference record MD05-2920 based on *U. peregrina*. The left panel shows the results of the first five SST time series, indicated using five different colors. The right panel shows the median age estimates and the 95% confidence interval of the 1000 pairs of SST time series, indicated using a black line and a grey area, respectively. The lower curves represent the probability distribution of change points.

must fall in the interval $[a_l, a_u]$. The conditional probability of C given the interval becomes

$$P(C = c \mid a_l \leq C \leq a_u) = \frac{P(C = c)}{\sum_{c'=a_l}^{c'=a_u} P(C = c')}. \tag{3.3}$$

The expression $P(C = c)$ will be used instead of the above conditional probability form in the following derivations for simplicity.

As the main focus of this study is to find the probability of the relative timing of glacial terminations that implies the lead/lag relationships between two locations, we seek the probability distribution of the length of the lead/lag based on the reference record (MD05-2920 with *U. peregrina*). We use the subscripts $_{\text{int}}$ and $_{\text{ref}}$ to indicate random variables for the record of interest and the reference record, respectively. The joint distribution of C_{int} and C_{ref} given proxies is

$$P\left(C_{\text{int}}, C_{\text{ref}} \mid \vec{\delta}_{\text{int}}, \vec{p}_{\text{int}}, \vec{\delta}_{\text{ref}}, \vec{p}_{\text{ref}}\right).$$

Note that we exclude the uncertainty originated from Bayesian calibration as the variation due to calibration is negligible. Recall that the change points given proxies are obtained independently at the two locations. Thus, we have

$$P\left(C_{\text{int}}, C_{\text{ref}}|\vec{\delta}_{\text{int}}, \vec{p}_{\text{int}}, \vec{\delta}_{\text{ref}}, \vec{p}_{\text{ref}}\right) = P\left(C_{\text{int}} \mid \vec{\delta}_{\text{int}}, \vec{p}_{\text{int}}\right) \cdot P\left(C_{\text{ref}} \mid \vec{\delta}_{\text{ref}}, \vec{p}_{\text{ref}}\right) \tag{3.4}$$

Now we can find the probability that the record of interest leads the reference record as follows:

$$P\left(C_{\text{int}} > C_{\text{ref}}|\vec{\delta}_{\text{int}}, \vec{p}_{\text{int}}, \vec{\delta}_{\text{ref}}, \vec{p}_{\text{ref}}\right) = \sum_{C_{\text{int}} > C_{\text{ref}}} P\left(C_{\text{int}}|\vec{\delta}_{\text{int}}, \vec{p}_{\text{int}}\right) P\left(C_{\text{ref}}|\vec{\delta}_{\text{ref}}, \vec{p}_{\text{ref}}\right)$$

Also, the probability distribution of the lead/lag of the record of interest compared to the reference record is

$$P\left(C_{\text{int}} - C_{\text{ref}} \leq \Delta|\vec{\delta}_{\text{int}}, \vec{p}_{\text{int}}, \vec{\delta}_{\text{ref}}, \vec{p}_{\text{ref}}\right) = \sum_{C_{\text{int}} - C_{\text{ref}} \leq \Delta} P\left(C_{\text{int}}|\vec{\delta}_{\text{int}}, \vec{p}_{\text{int}}\right) P\left(C_{\text{ref}}|\vec{\delta}_{\text{ref}}, \vec{p}_{\text{ref}}\right)$$

We employ this distribution to obtain the confidence limits.

The left panel of Figure 3.4 shows the histogram of the timing of Termination I using the MD05-2920 record. This record has two $\delta^{18}O$ proxies: *C. wuellerstorfi* and *U. peregrina*. The red and blue histograms correspond to the results from *C. wuellerstorfi* and *U. peregrina*, respectively. We chose the MD05-2920 record based on *U. peregrina* as a reference record and computed the histogram of the relative timing of the MD05-2920 record based on *C. wuellerstorfi*. The right panel of Figure 3.4 shows the histogram of the relative timing. Because these two records are measured from the same site, the histograms of the two timings overlap in most intervals and the histogram of the relative timing is centered on nearly 0.

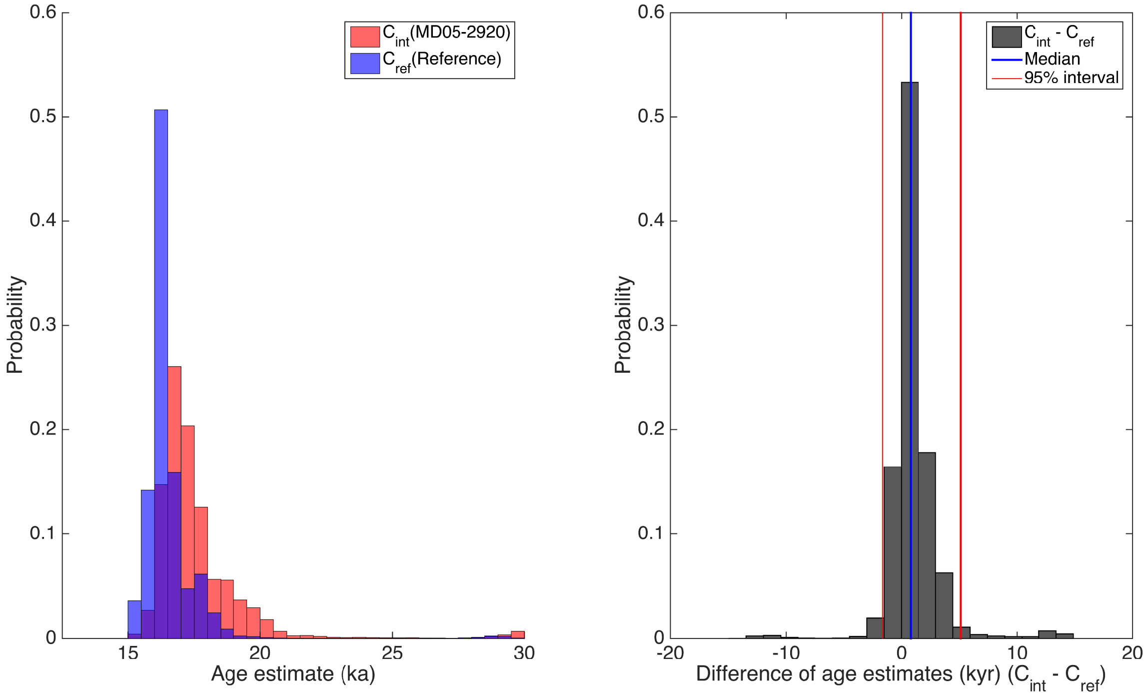

Figure 3.4: Left panel: Histograms of C_{int} and C_{ref}, which are the timings of Termination I for the record of interest (MD05-2920 based on *C. wuellerstorfi*) and the reference record (MD05-2920 based on *U. peregrina*), respectively. Right panel: Histogram of $C_{\text{int}} - C_{\text{ref}}$ that is the relative timing of Termination I for the record of interest (MD05-2920 based on *C. wuellerstorfi*) based on the reference record (MD05-2920 based on U. peregrina).

3.3 Results

3.3.1 Relative timing of glacial terminations

For each record, we found the relative timing of the glacial terminations using equation (3.4) as shown in Figure 3.5. Figure 3.5 shows the median difference of the Termination I and II between WP and EP. The results of Termination III are omitted as we do not have a sufficient number of records for Termination III. In Figure 3.5, the error bars and the confidence intervals overlap each other because of high uncertainty of the relative timings, and the filled symbols and the empty symbols seem to be mixed as well. In the Mann-Whitney U tests, we could not reject the null hypothesis that two samples come from the same population at the 5% sig-

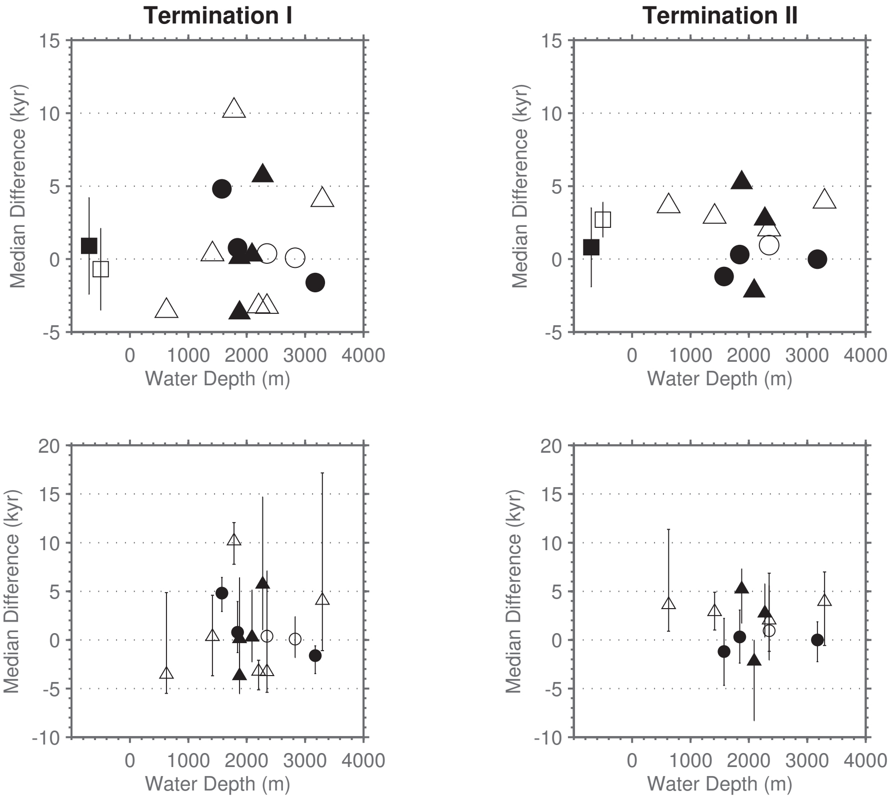

Figure 3.5: Relative timings of Terminations I and II. The upper panels display the median estimates of the relative timings and the lower panels display the 95% confidence intervals of the distributions of the relative timings. The filled symbols indicate records from the western Pacific (WP), and the empty symbols represent records from the eastern Pacific (EP). Circles and triangles indicate records whose SSTs were inferred from Mg/Ca and $U_{37}^{k'}$, respectively. The squares with lines in the upper panel represent the average of median estimates and their standard error.

nificance level. Even when considering only high-resolution records ($<$ 1-kyr), we cannot conclude that there are differences between WP and EP for Termination I and Termination II.

The SST records are based on either Mg/Ca or $U_{37}^{k'}$. As shown in Figure 3.5, the median results from Mg/Ca (circles) and $U_{37}^{k'}$ (triangles) are mixed. Statistical tests also confirm that there is no statistically significant difference due to the use of different proxies.

3.3.2 Decomposing contribution to termination uncertainty

The two main sources of uncertainty on the timing of glacial terminations arise from the uncertainties of change points and age estimates from $\delta^{18}O$ records. To compare the relative contribution of these two sources on the overall timing for each record, we employed Shannon entropy which is a measure of uncertainty in information theory. This measure enjoys three advantages: it can be estimated directly for the joint probability distribution of two or more variables or samples drawn from these distributions, it directly accounts for the dependence and thus the correlation between variables, and it is a very well established measure of uncertainty [183, 34].

For a discrete random variable A, the entropy $H(A)$ is defined by

$$H(A) = -\sum_{a} p_A(a) \log p_A(a),$$

where $p_A(a)$ is a probability mass function of a random variable A. The joint entropy $H(A, C)$ of two random variables A and C is defined with a joint probability mass function $p(a, c)$ as follows:

$$H(A, C) = -\sum_{a,c} p(a, c) \log p(a, c).$$

Let A and C be the random variable for the age and the location of a change point, respectively. Then, $H(A, C)$ represents the total uncertainty induced by A and C. For the timing analysis, the change point locations are determined based on the age estimates. In the same manner, the total entropy can be decomposed into two parts

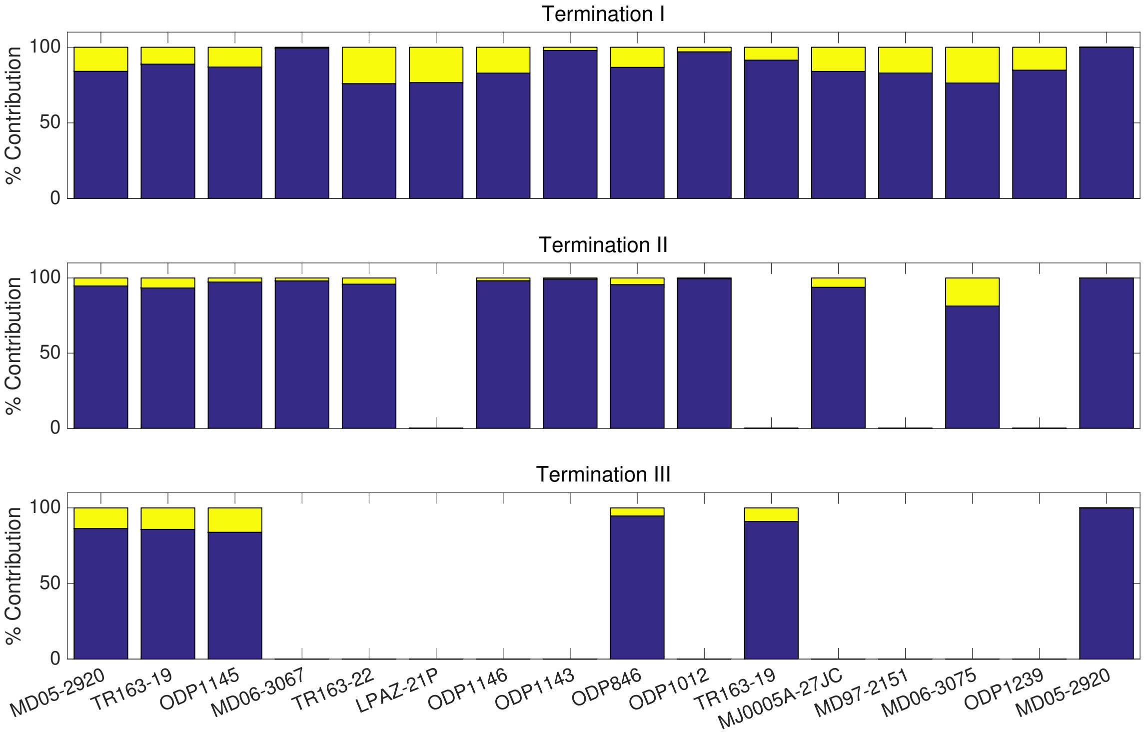

Figure 3.6: Relative contribution of age (blue) and change point (yellow) uncertainties.

as follows.

$$\begin{aligned} H(A,C) &= -\sum_{a,c} p(a,c)\log p(a,c) \\ &= -\sum_{a,c} p(a,c)\log(p(a)p(c|a)) \\ &= -\sum_{a,c} p(a,c)\log p(a) - \sum_{a,c} p(a,c)\log p(c|a) \\ &= -\sum_{a} p(a)\log p(a) - \sum_{a,c} p(a,c)\log p(c|a). \end{aligned}$$

The last equation states that the total entropy is the sum of the entropy of age and the conditional entropy of location given the age estimates. For each record, the two sources of uncertainty are evaluated using samples of these variables.

The relative contribution to the total uncertainty is shown in Figure 3.6. The contribution of age estimates ranges from 76% to nearly 100%. The average uncertainty across all records originated from ages depending on the terminations. The average age uncertainties of Termination I, II, and III are 2.8-kyr, 4.5-kyr, and 5.5-kyr, respectively. We have lower uncertainty for Termination I because the resolutions of Termination I are relatively higher than Terminations II and III. Inversely, we have higher uncertainty originated from the change point for Termination I due to the relative shortness of the Holocene. This shortness makes it difficult to find the terminations based on the change point algorithm.

3.3.3 Discussion

Because there are high uncertainties originating from proxies and methods, we could not conclude differences in the glacial termination timings between WP and EP. The results could be affected by temperature proxy bias or water mass bias as well. In this section, we focus on discussing further improvements of the inference methods to reduce the uncertainties originating from the methods.

After finding the change point locations without constraints, we conditioned the probability distribution by the ranges of terminations, as described in equation (3.3). Because we have the prior information about the ranges of terminations, we can restrict the locations of change points before running the change point algorithm. This additional information can reduce the uncertainty originating from the change points. Also, we can consider more sophisticated piecewise linear models with constraints on slope changes, which reflect a long interval of cooling climate and a relatively short interval of terminations.

The relative timings were evaluated with the reference record MD05-2920 based on *U. peregrina*. To deduce the lead/lag relationships, the reference record was used

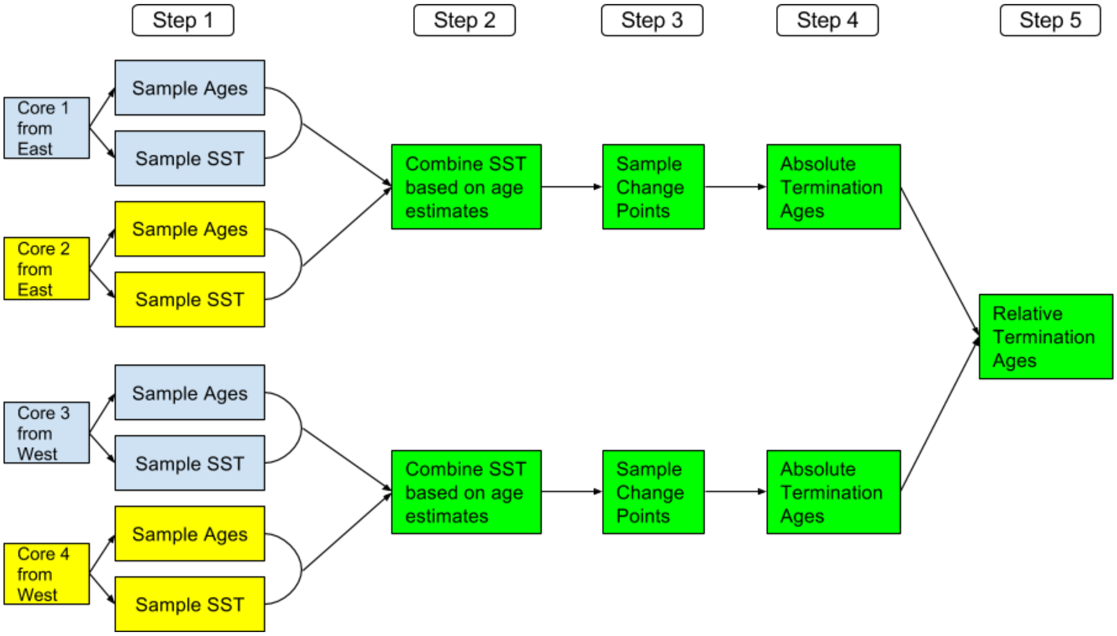

Figure 3.7: New scheme for the inference of the relative termination timings between EP and WP.

in comparison to all other records. Therefore, the uncertainty originating from the reference record is contained in all lead/lag analyses. To remove this uncertainty, we can consider the following idea, which directly compares the termination timings between EP and WP. Let N_{EP} be the number of records from the EP. For each core, we draw one sample of age and one sample of SST to get the N_{EP} data sets: one for each of the N_{EP} cores. Next, we can combine the SST samples into one combined data set. We then run the change point algorithm on this combined data set based on age estimates of each core. These steps are illustrated as steps one through three in Figure 3.7. By repeating these steps, we get the distribution of absolute termination ages. We apply the same approach to the WP. By comparing the absolute termination ages of EP and WP, we can find the probability of lead/lag (relative termination ages). This scheme enables us to remove the uncertainty originating from the use of a reference record, and to infer change points based on two very high resolution records obtained by all the records in the EP and all the records in the WP.

We investigated the relative timing of glacial terminations between EP and WP using 15 SST records. Instead of finding the best estimate for each record and comparing them across records, we estimated the probability distributions of the timings, which reflect the uncertainties that originated from age estimates and change point locations. At this point, we found that difference in EP and WP timings are all within the range of chance variations. According to the results, the relative timing uncertainty becomes less than 3-yrs when the average age uncertainty is less than 2-kyr. Thus, if we have more records with high resolutions and improve the inference method as suggested, then the ability to find better evidence for lead/lag relationships in future research will be improved.

Table 3.1: *SST* records used for this study.

Name	Longitude	Latitude	Water Depth (m)	Period (ka)	Resolution (kyr)	Age Confidence Interval (kyr)	Proxy	Analyzed Terminations
MD05-2920 [188]	144.5	-2.9	1843	0 - 388	0.7	5.0	Mg/Ca	I, II, III
TR163-19 [104, 105]	-91.0	2.3	2348	0 - 361	1.7	5.9	Mg/Ca	I, II, III
ODP1145 [143]	117.6	19.6	3175	2 - 143	0.5	4.1	Mg/Ca	I, II, III
MD06-3067 [16]	126.5	6.5	1575	4 - 158	0.4	1.6	Mg/Ca	I, II
TR163-22 [105]	-92.4	0.5	4830	1 - 135	0.3	2.1	Mg/Ca	I, II
LPAZ-21P [68]	-109.5	23.0	624	1 - 236	1.3	8.7	$U^{k'}_{37}$	I
ODP1146 [69]	116.2	19.5	2091	5 - 400	2.0	4.5	$U^{k'}_{37}$	I, II
ODP1143 [25, 108]	113.3	9.4	2272	0 - 403	1.7	9.2	$U^{k'}_{37}$	I, II
ODP846 [103]	-90.8	-3.1	3296	4 - 400	2.5	6.3	$U^{k'}_{37}$	I, II, III
ODP1012 [19]	-118.4	32.3	1783	2 - 400	1.2	5.1	$U^{k'}_{37}$	I, II
TR163-19 [43]	-91.0	2.3	2348	0 - 35	1.7	5.9	$U^{k'}_{37}$	I, III
MJ0005A-27JC [43]	-82.8	-1.9	2203	3 - 163	0.8	3.4	$U^{k'}_{37}$	I, II
MD97-2151 [213]	109.9	8.7	1598	1 - 145	0.1	2.1	$U^{k'}_{37}$	I
MD06-3075 [54]	125.9	6.5	1878	0 - 115	0.4	2.5	$U^{k'}_{37}$	I, II
ODP1239 [163]	-82.1	-0.7	1414	0 - 500	1.6	6.1	$U^{k'}_{37}$	I

CHAPTER FOUR

The flickering switch of Holocene oceanography along the Peru margin

4.1 Background & Summary

High-resolution multidimensional paleoclimate time series, including SST, C_{37}, $\delta^{15}N$ and $\%N$, over the Holocene epoch are collectively analyzed for a sediment core MW8708-PC2, retrieved from the central Peru margin. The four proxies explains sea surface temperature (SST) through the alkenon proxy, biological productivity (C_{37}) through analyses of the abundance of alkenones (representing haptophyte algal productivity), subsurface properties through $\delta^{15}N$ analyses (subsurface oxygenation/denitrification) and the percentage of organic nitrogen ($\%N$), which is a composite of all biological inputs to the sediment. We examine how the coupling of SST with other proxies has evolved and changed in the Holocene and evaluate whether we can employ these resulting relations in the prediction of the changes of the four proxies. In doing so, we also expect to explain climate phenomenon related to the four proxies.

The four proxies are measured in high-resolution, but their spacings are unevenly spaced. In order to compose an evenly spaced data set, we apply the Kalman filter to substitute the missing data. A visual analysis of the proxies suggested that the variability of four proxies follows two regimes: one state has high variability and another state has low variability. Thus, we hypothesize that the four proxies have two possible states and that their relations change over time between these two state, which we call biphasic. Because of this biphasic property, we employ the hidden Markov model (HMM) and autoregressive hidden Markov model (AR-HMM) to model their behavior. The HMM assumes conditional independence among observations, while the AR-HMM assumes that direct dependence with adjacent observations exists. This implies that the AR-HMM includes the immediate previous values of the four proxies in the model to explain the current values of the four proxies. The two models use different structures to explain the four proxies, and each structure explains their correlation and causality relations in different ways. Therefore, analyzing the four proxies using both models enables us to better evaluate their correlations and causality relations.

Our results show that there exist two regimes of variability in proxy space at site MW8708-PC2. Both regimes show high autocorrelation and low cross-correlation, thereby indicating that none of the proxies are good predictors of other proxies. Thus, we examine the correlation of SST with a possible remote driver, the Pacific Decadal Oscillation (PDO) in the discussion section.

In the following sections we describe the two probabilistic models, HMM and AR-HMM, and compare the two models using the simulated data. We also introduce the Kalman filter and its application for data augmentation. Results and discussion on estimated model parameters using the four paleoclimate proxies follow afterward.[1]

4.2 Method

4.2.1 Data collection

High-resolution records of four paleoclimate indicators are collectively analyzed for a sediment core retrieved from the central Peru margin (Site MW8708-PC2: 15.1°S, 75.7°, water depth of 250m). This site has an extremely high and uniform sedimentation rate (70cm/kyr) across most of the Holocene (∼10 - 1.4 ka), and frequently

---

[1] The work in this chapter is in collaboration with my advisor Dr. Charles E. Lawrence of Brown University, Dr. Timothy Herbert of Brown University, and Dr. Baylor Fox-Kemper of Brown University. This chapter includes materials from the draft of the preliminary paper associated with this work.

contains annual laminations. Records are obtained from 2cm (3 years) slices taken every 5cm (7 years). However, there are missing observations for all four proxies: 46% of data is missing for SST and C_{37}, and 65% of for $\delta^{15}N$ and $\%N$.

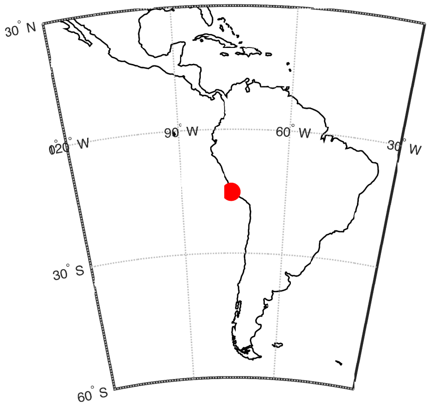

Figure 4.1: Location of the site MW8708-PC2 (15.1°S, 75.7°, water depth of 250m).

4.2.2 Probability models: HMM and AR-HMM

Statistical approaches are designed to capture phase transitions in climate records because visual analysis suggests that the correlations and variability of the four proxies varied over time in a potentially abrupt manner. We assume that there are two distinct states at this site, characterized by different levels of variability and predictability, and so employ two-state hidden Markov models (HMM). We consider two different emission models in the HMM: The first model assumes conditional independence among observations, and the second model considers direct dependence with adjacent observations. The first one is consistent with a general HMM, and the second one is called the autoregressive hidden Markov model, which is also known as a switching autoregressive model.

Both models consist of observed data $X(t)$ and two kinds of hidden states $S(t)$. Figure 4.2 illustrates dependencies among hidden states and observed data of the two

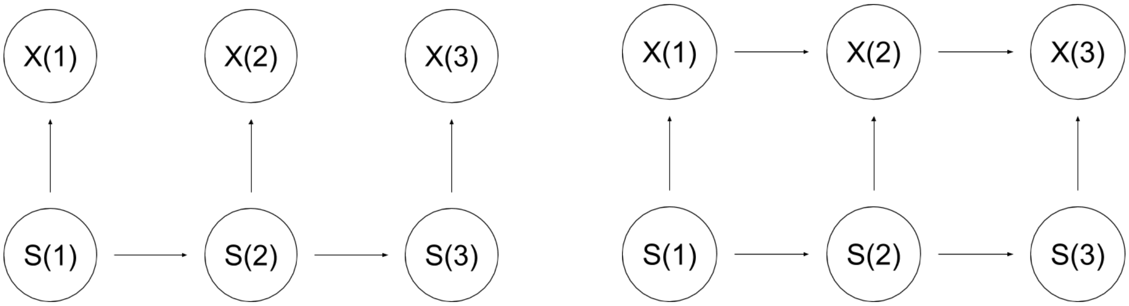

(a) HMM **(b)** AR-HMM

Figure 4.2: Dependencies among observations $X(t)$ and hidden states $S(t)$ for (a) HMM and (b) AR-HMM. Nodes are connected with an arrow if one node at the head of an arrow depends on another node at the origin of an arrow.

models. State dependencies are the same in both models. Both models have hidden states which demonstrate the Markov property while the difference between the two models is the relationship of the observations. In the HMM, a current observation is solely dependent on a current state. The HMM assumes that a current observation follows the normal distribution with means and variances determined by its state. Thus, a current observation is independent of the other observations given its state. In the AR-HMM, a current observation depends not only on a current state, but also on the previous observation. This model takes the summation of a constant and the contribution of the previous observations as a mean of the normal distribution.

These two models can be expressed with two layers of structure: observations $X(t)$ and hidden states $S(t)$. Let $X(t)$ be a four-dimensional vector, $X(t) = (x_1(t), x_2(t), x_3(t), x_4(t))$, which includes SST, C_{37}, $\delta^{15}N$, and $\%N$ for $0 \leq t \leq 563$, with $t = 563$ being the most recent point. For the following analysis, the time interval Δt is set to be 0.5, which corresponds to approximately 7 years. The proxy data at each data point, $X(t)$, is an average over approximates 3 years. Let $S(t)$ be a state at t. We assume that $S(t)$ can be either 1 (high variability) or 2 (low variability).

Consider a two-state hidden Markov model (HMM). The HMM assumes that

$X(t)$ follows the normal distribution with mean vector $\mu_{S(t)}$ and variance $\Sigma_{S(t)}$ determined by its state and that $X(t)$ is independent of $X(t^*)$ for all other t^* given its state.

$$X(t) \sim \mathcal{N}(\mu_{S(t)}, \Sigma_{S(t)}) \text{ for } S(t) = 1 \text{ or } 2. \tag{4.1}$$

The changes of state depend on a transition probability,

$$a = \begin{bmatrix} a_{11} & a_{12} \\ a_{21} & a_{22} \end{bmatrix}$$

where $a_{ij} = P(s(t+1) = j \mid S(t) = i)$. The unknown parameters, $\mu_1, \mu_2, \Sigma_1, \Sigma_2$ and a, can be estimated from the data using the Baum-Welch expectation maximization algorithm.

Consider a two-state autoregressive hidden Markov model (AR-HMM) [59, 60]. As in the two-state HMM, this model also assumes that $X(t)$ belongs either to state 1 or to state 2, and the state shifts from one to another depending on a transition probability, a. While the distribution of $X(t)$ is solely determined by its state at t in the HMM, the AR-HMM allows $X(t)$ to linearly depend on its immediately preceding value:

$$X(t) = c_{S(t)} + \theta_{S(t)} X(t - \Delta t) + \Sigma_{S(t)}^{1/2} \epsilon(t) \tag{4.2}$$

where $c_{S(t)}$ is a constant vector, $\theta_{S(t)}$ is a matrix of autocorrelation parameters, and $\Sigma_{S(t)}$ is a matrix of amplitudes of an error terms, $\epsilon(t)$. $\{\epsilon(t)\}$ is a series of random variables with $E[\epsilon(t)] = 0$, $Var(\epsilon(t)) = 1$, and $cov(\epsilon(p), \epsilon(q)) = 0$ for every $p \neq q$.

We can rewrite the above equation as:

$$\begin{bmatrix} x_1(t) \\ x_2(t) \\ x_3(t) \\ x_4(t) \end{bmatrix} = \begin{bmatrix} c_1 \\ c_2 \\ c_3 \\ c_4 \end{bmatrix} + \begin{bmatrix} \theta_{11} & \theta_{12} & \theta_{13} & \theta_{14} \\ \theta_{21} & \theta_{22} & \theta_{23} & \theta_{24} \\ \theta_{31} & \theta_{32} & \theta_{33} & \theta_{34} \\ \theta_{41} & \theta_{42} & \theta_{43} & \theta_{44} \end{bmatrix} \begin{bmatrix} x_1(t-\Delta t) \\ x_2(t-\Delta t) \\ x_3(t-\Delta t) \\ x_4(t-\Delta t) \end{bmatrix}$$
$$+ \begin{bmatrix} \sigma_{11} & \sigma_{12} & \sigma_{13} & \sigma_{14} \\ \sigma_{21} & \sigma_{22} & \sigma_{23} & \sigma_{24} \\ \sigma_{31} & \sigma_{32} & \sigma_{33} & \sigma_{34} \\ \sigma_{41} & \sigma_{42} & \sigma_{43} & \sigma_{44} \end{bmatrix} \begin{bmatrix} \epsilon_1(t) \\ \epsilon_2(t) \\ \epsilon_3(t) \\ \epsilon_4(t) \end{bmatrix}.$$

Taking a close look at the autocorrelation parameter θ, the diagonal entry θ_{ii} indicates how much $x_i(t)$ depends on its own past $x_i(t-\Delta t)$. If θ_{ii} is close to 1, then it implies that the current value is heavily dependent on its immediate past. The off-diagonal entry θ_{ij} for $i \neq j$ explains the relation between the current $x_i(t)$ and the preceding $x_j(t-\Delta t)$. Since an AR model finds the relations among entries of $X(t)$ through the parameter θ, the normalized data is recommended for an analysis, as shown in Figure 4.4. As in a two-state HMM, the unknown parameters of a two-state AR-HMM, $c_1, c_2, \theta_1, \theta_2, \Sigma_1, \Sigma_2$ and a are determined by the Baum-Welch expectation maximization algorithm.

The observations in the HMM are conditionally independent given their states (equation (4.1)) while the AR-HMM has direct dependence between adjacent observations (equation (4.2)). This difference adds the immediate previous term $X(t-\Delta t)$ in the emission model as shown in equation (4.2). In other words, the HMM is a special case of the AR-HMM with the autocorrelation term θ to be zero.

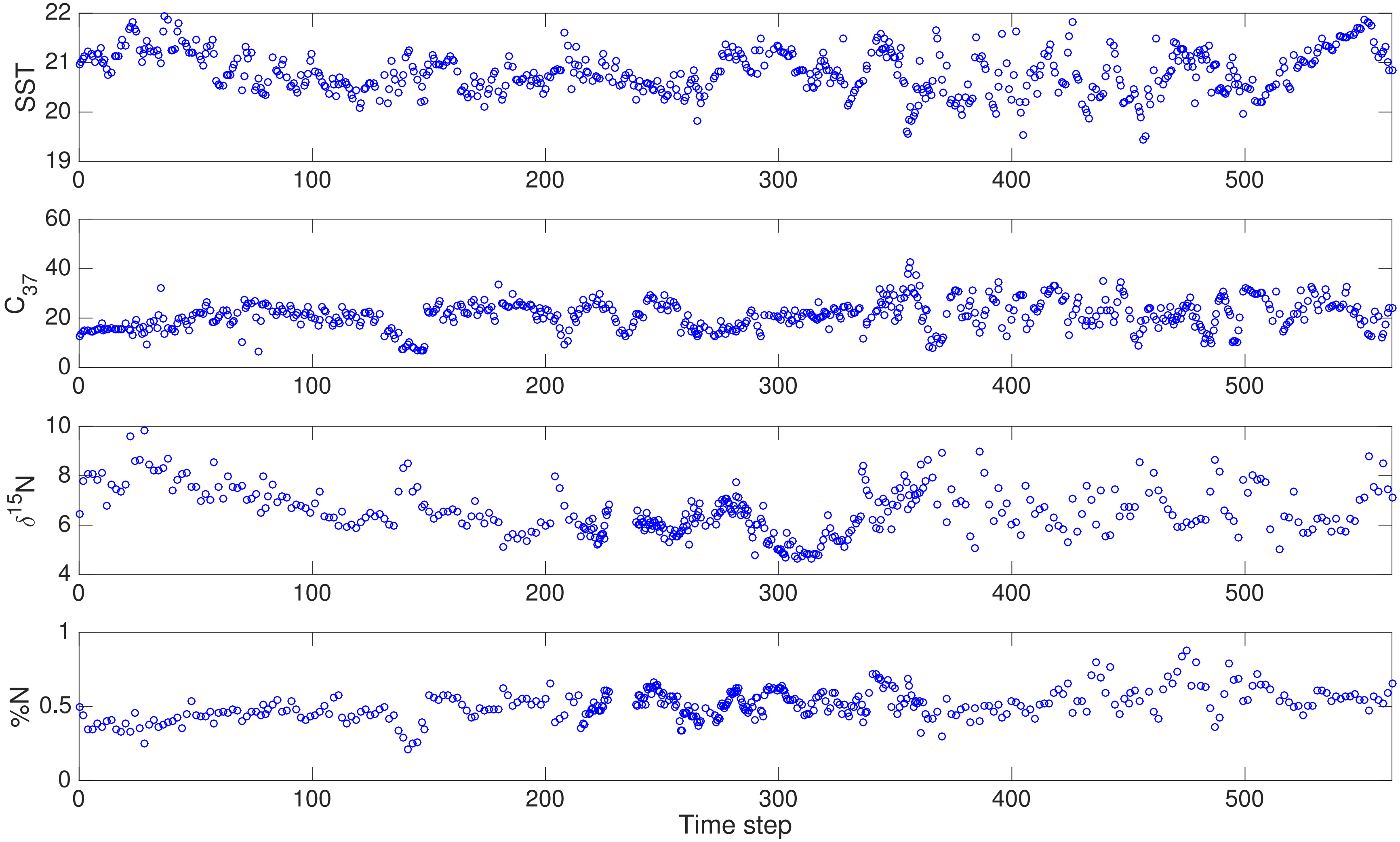

Figure 4.3: Observed data for $0 \leq t \leq 563$, with $t = 563$ being the most recent point.

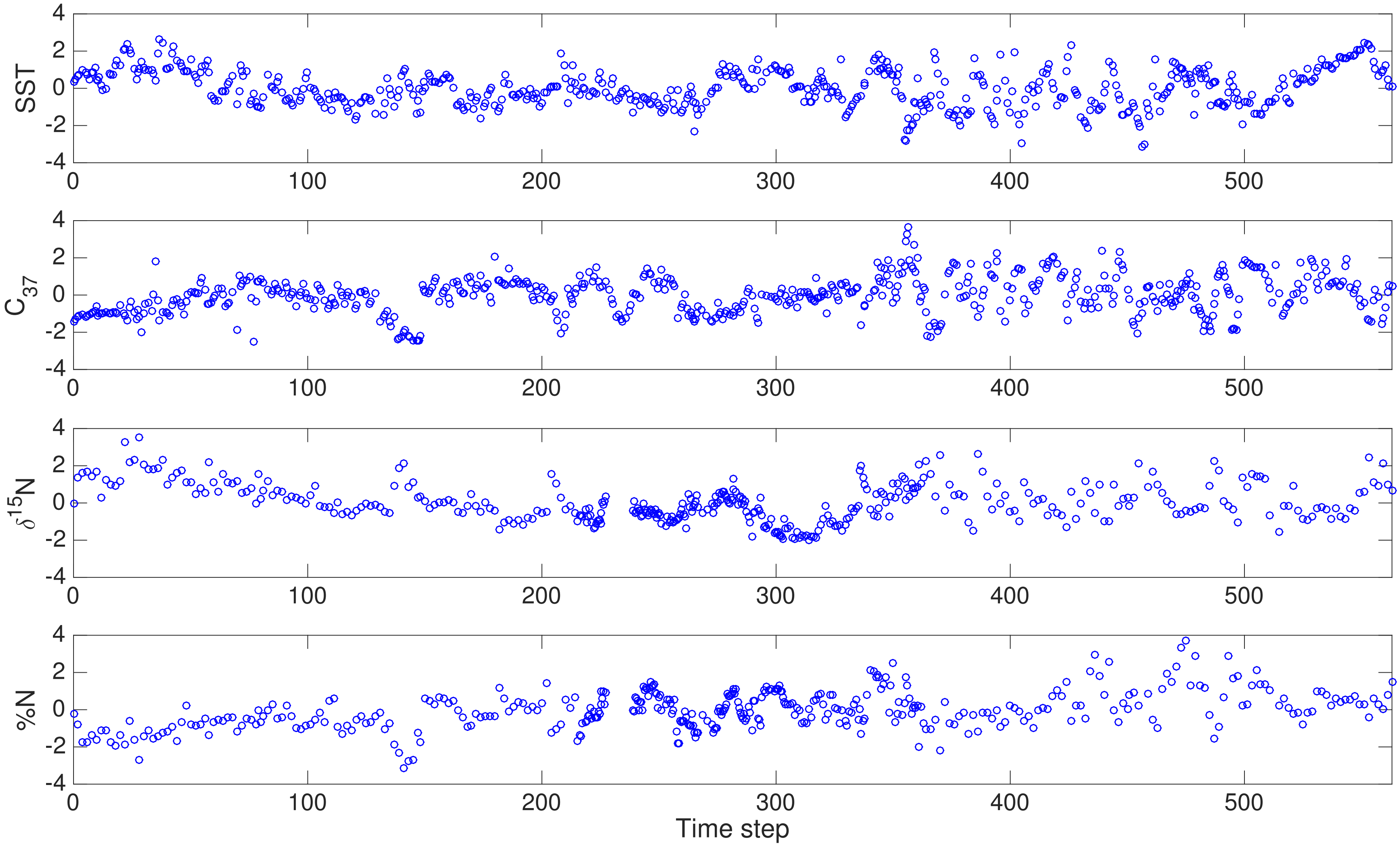

Figure 4.4: Normalized observed data for $0 \leq t \leq 563$, with $t = 563$ being the most recent point.

4.2.3 Comparisons between HMM and AR-HMM with simulated data sets

Model comparisons were done with two simulated data sets to decide which model is more suitable for this study. Two data sets were simulated based on HMM and AR-HMM with parameters described in Tables 4.1 and 4.2. Theses parameters were obtained from the analysis of preliminary data sets. We assumed that the sequence of state begins at state 1 and the first observation is $X(0) = [0.3380, -1.4559, -0.3002, -0.2954]$, and generated a 600 long sequence for each model. Figures 4.5 and 4.6 show the simulated data sets based on HMM and AR-HMM, respectively. For each data set, we used both HMM and AR-HMM to estimate parameters and hidden states, and then evaluated their accuracies.

In the first experiment, we explain the four proxies generated based the HMM (Tables 4.1) by using either the HMM or the AR-HMM. The results of the parameter estimations by the HMM and AR-HMM, based on the simulated data set with HMM, are shown in Tables 4.3 and 4.4. The parameter estimates by the HMM are accurate for both mean and covariance terms. While the data was generated using the HMM, the parameters of AR-HMM also properly describe the data by a nearly zero autocorrelation parameter θ. Both models find the hidden states accurately (Figure 4.7). For each model, we repeated state estimations with 10 different initial conditions. The average accuracies of the HMM and AR-HMM are 98.86% and 98.92%, respectively. Notice that the AR-HMM accurately finds parameters and hidden states when the data set was simulated with the HMM, while this is not surprising since the HMM is a special case of the AR-HMM. It does illustrate that there is sufficient data to accurately model HMM data with the AR-HMM in spite of the added degrees of freedom.

In the second experiment, we explain the four proxies generated based the AR-HMM (Tables 4.2) by using either the HMM or the AR-HMM. Tables 4.5 and 4.6 show the results of the parameter estimations by the HMM and AR-HMM based on the simulated data set with AR-HMM. The estimation of hidden states are shown in Figure 4.8. The AR-HMM finds the parameters accurately, but the HMM does not represent the data well with its mean and covariance. The average accuracies of the HMM and AR-HMM to find hidden states are 74.76%, 99.48%, respectively. This shows that the HMM does not model these data very well.

Through the analysis of model comparison, the AR-HMM has been proven to be superior to the HMM. When it is uncertain which model to use when deciding between the HMM and AR-HMM for the data set, we should first employ the AR-HMM and double-check the auto-correlation term to make a final determination which model is best to use. If the autocorrelation parameter θ is close to 0, then we can effectively employ the HMM. However, in this study, the characteristics of the data itself supports the AR-HMM. The records of the four-dimensional climate proxies are multidimensional time series. The sampling rate employed in this study is fast compared to the rate of changes in the underlying system, thus we observe auto-correlation in this circumstance. The correlation analysis of multidimensional records without considering auto-correlations can produce incorrect conclusions, so we should use the AR-HMM. However, in order to make comparisons, we continue to employ both models in this study.

Table 4.1: Parameters for the data simulation of HMM.

		Mean	Covariance			
State 1	SST	0.0006	1.3866	−0.5702	0.2717	−0.4291
	C_{37}	−0.1856	−0.5702	1.3575	−0.2683	0.6509
	$\delta^{15}N$	0.9220	0.2717	−0.2683	0.5450	−0.2348
	$\%N$	−0.5832	−0.4291	0.6509	−0.2348	0.7913
State 2	SST	−0.0004	0.7391	0.0040	−0.0052	0.2440
	C_{37}	0.1239	0.0040	0.7202	0.0158	−0.0813
	$\delta^{15}N$	−0.6157	−0.0052	0.0158	0.3544	0.0937
	$\%N$	0.3894	0.2440	−0.0813	0.0937	0.7578
Transition matrix			0.9494	0.0506		
			0.0332	0.9668		

Table 4.2: Parameters for the data simulation of AR-HMM.

		Constant	Autocorrelation				Covariance			
State 1	SST	−0.0219	0.8214	0.0034	0.0086	−0.0050	0.2416	0	0	0
	C_{37}	−0.0321	−0.0980	0.7649	0.0255	0.0580	0	0.2719	0	0
	$\delta^{15}N$	0.0411	0.0231	−0.0302	0.9421	−0.0008	0	0	0.0875	0
	$\%N$	−0.0241	−0.0200	0.0529	−0.0022	0.9049	0	0	0	0.0788
State 2	SST	0.0124	0.9212	−0.0104	0.0006	0.0105	0.0574	0	0	0
	C_{37}	0.0047	0.0329	0.9026	−0.0256	0.0183	0	0.0590	0	0
	$\delta^{15}N$	−0.0330	0.0057	0.0144	0.9593	−0.0147	0	0	0.0117	0
	$\%N$	0.0231	0.0013	0.0022	0.0049	0.9999	0	0	0	0.0130
Transition matrix					0.9892	0.0108				
					0.0083	0.9917				

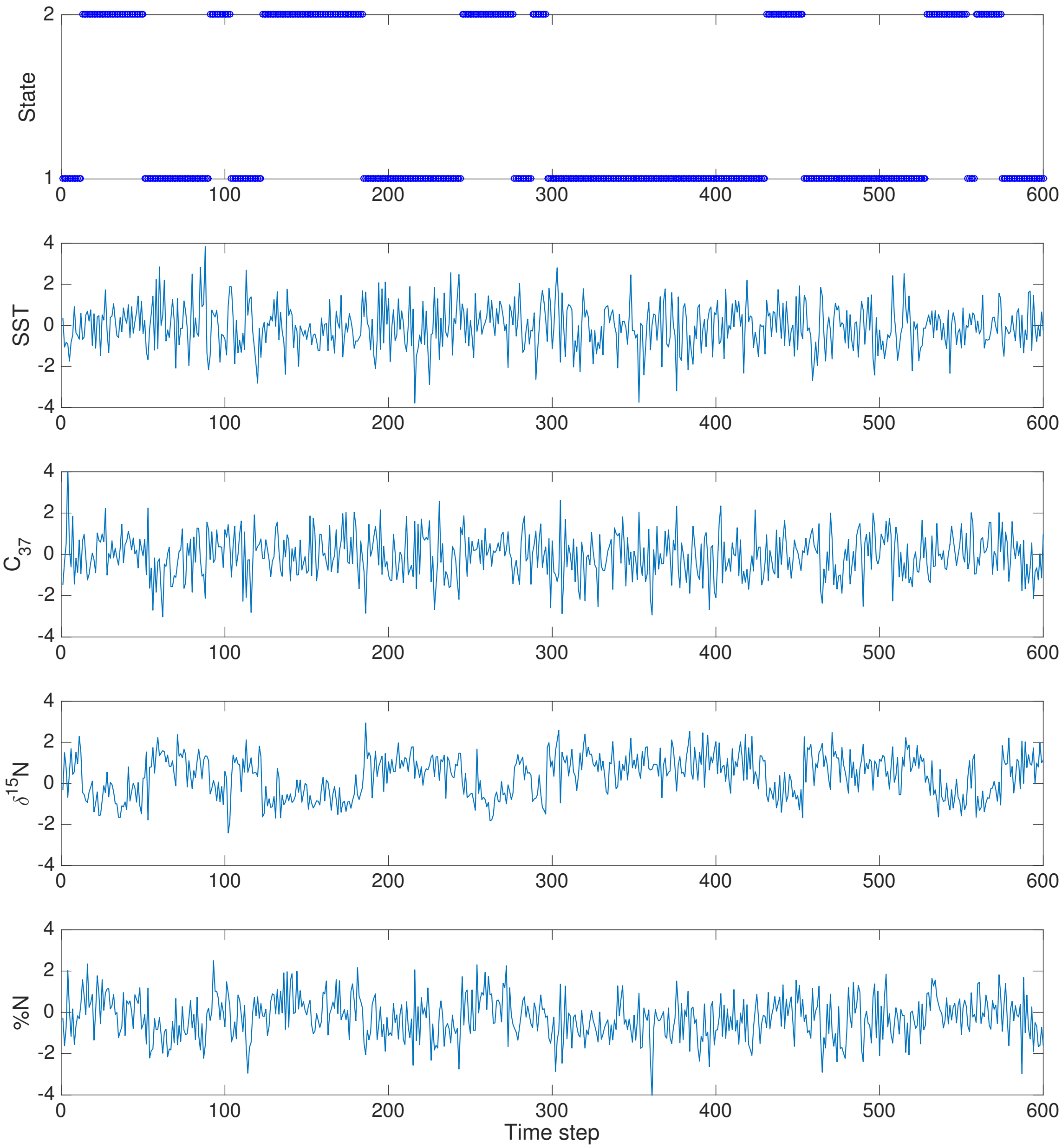

Figure 4.5: Simulated data from HMM with parameters as described in Table 4.1.

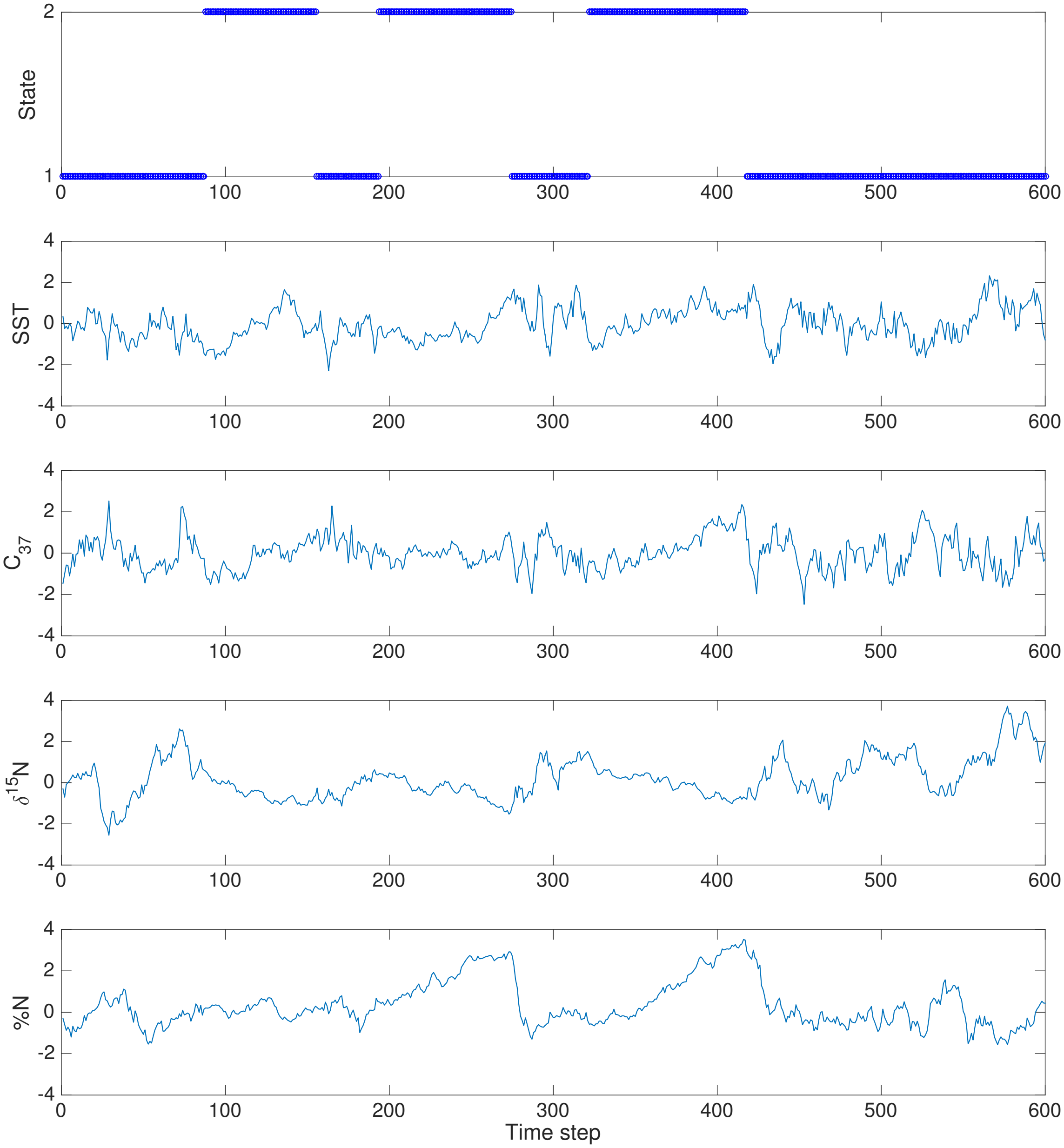

Figure 4.6: Simulated data from AR-HMM with parameters as described in Table 4.2.

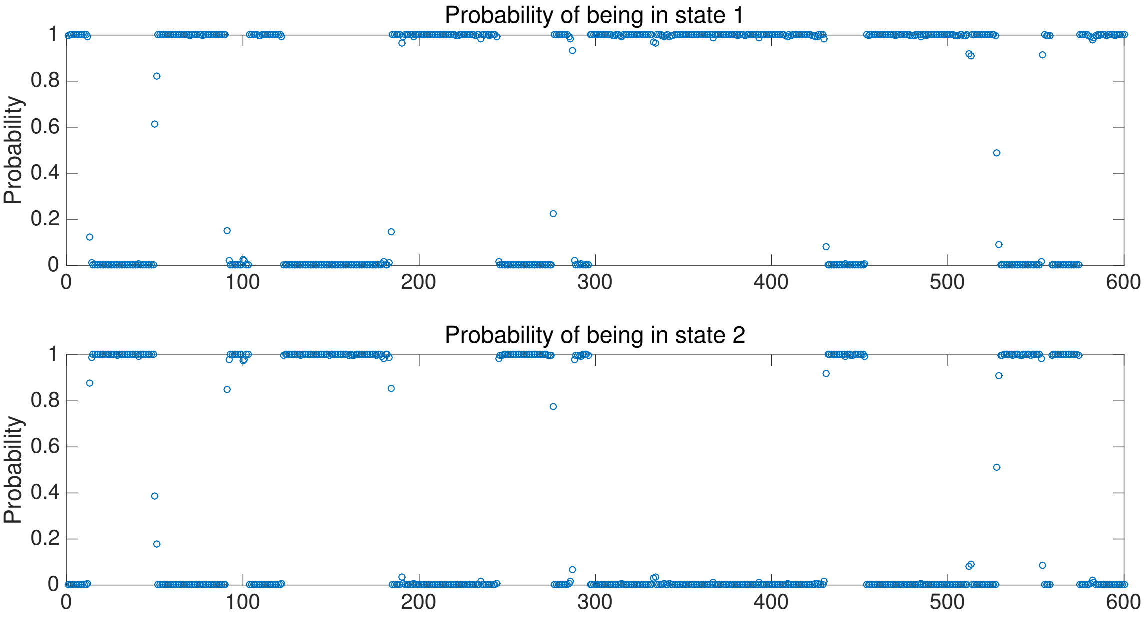

(a) HMM

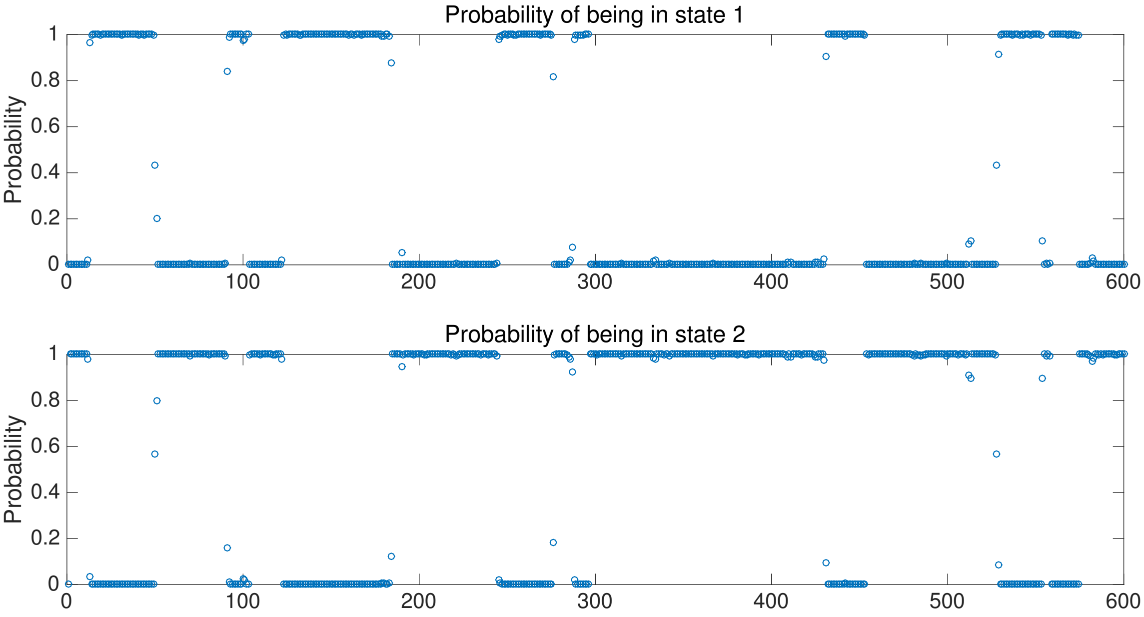

(b) AR-HMM

Figure 4.7: HMM based simulated data. The estimated states are displayed when estimation is done using (a) the HMM and (b) the AR-HMM. 598/600 points and 599/600 of the most probable state are matched with the original state for the HMM and AR-HMM, respectively.

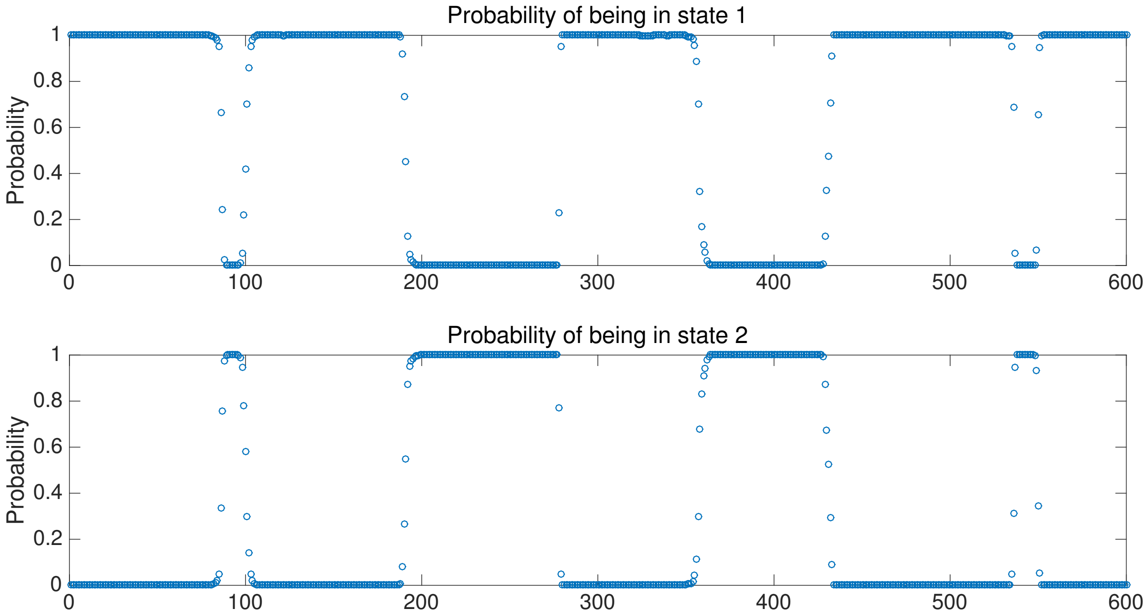

(a) HMM

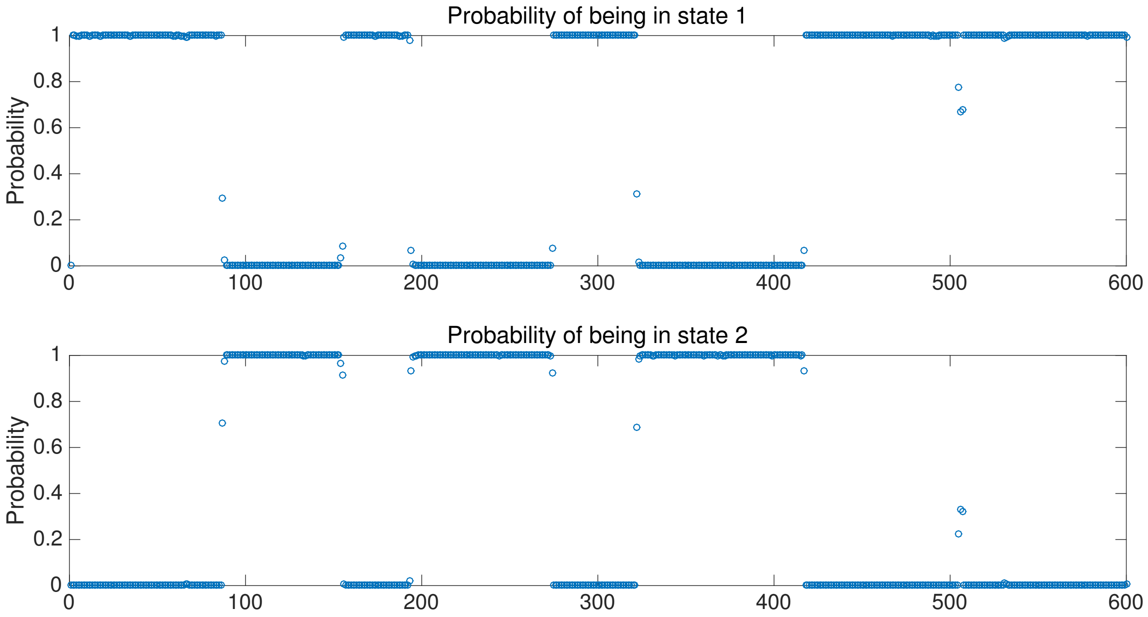

(b) AR-HMM

Figure 4.8: AR-HMM based simulated data. The estimated states are displayed when estimation is done using (a) the HMM and (b) the AR-HMM. 474/600 points and 598/600 of the most probable state are matched with the original state for the HMM and AR-HMM, respectively.

Table 4.3: [HMM]Parameter estimation by the HMM using the HMM based simulated data.

		Mean	Covariance			
State 1	SST	−0.1071	1.4001	−0.6020	0.2190	−0.5297
	C_{37}	−0.1891	−0.6020	1.3637	−0.2565	0.7033
	$\delta^{15}N$	0.9355	0.2190	−0.2565	0.4922	−0.2675
	$\%N$	−0.5881	−0.5297	0.7033	−0.2675	0.9280
State 2	SST	0.0006	0.7565	0.0338	−0.0239	0.2045
	C_{37}	0.1678	0.0338	0.6518	0.0173	−0.0384
	$\delta^{15}N$	−0.6375	−0.0239	0.0173	0.3719	0.0993
	$\%N$	0.3214	0.2045	−0.0384	0.0993	0.7166
Transition matrix			0.9779	0.0221		
			0.0388	0.9612		

Table 4.4: [AR-HMM] Parameter estimation by the AR-HMM using the HMM based simulated data.

		Constant	Autocorrelation				Covariance			
State 1	SST	−0.0364	−0.0498	0.0856	−0.0780	−0.0742	0.7406	0.0257	−0.0241	0.2078
	C_{37}	0.1233	−0.0755	−0.0121	−0.0875	−0.0203	0.0257	0.6435	0.0189	−0.0312
	$\delta^{15}N$	−0.5538	0.0472	−0.0293	0.0826	−0.0947	−0.0241	0.0189	0.3650	0.0883
	$\%N$	0.4411	0.0812	−0.0339	0.1391	−0.1046	0.2078	−0.0312	0.0883	0.7009
State 2	SST	−0.0521	0.0480	−0.0108	−0.0587	0.0028	1.3994	−0.6006	0.2193	−0.5268
	C_{37}	−0.1877	−0.0135	−0.0280	0.0354	0.0616	−0.6006	1.3610	−0.2623	0.7040
	$\delta^{15}N$	0.9903	0.0001	−0.0387	−0.0443	0.0326	0.2193	−0.2623	0.4870	−0.2650
	$\%N$	−0.6495	−0.0529	0.0013	0.0659	0.0056	−0.5268	0.7040	−0.2650	0.9240
Transition matrix			0.9613	0.0387						
			0.0222	0.9778						

Table 4.5: [HMM] Parameter estimation by the HMM using the AR-HMM based simulated data.

		Mean	Covariance			
State 1	SST	−0.0401	0.6312	−0.0923	0.1395	−0.0663
	C_{37}	−0.0633	−0.0923	0.6347	−0.0404	0.0999
	$\delta^{15}N$	0.4153	0.1395	−0.0404	1.2523	−0.2640
	$\%N$	−0.2258	−0.0663	0.0999	−0.2640	0.2660
State 2	SST	−0.0279	0.7063	0.2663	−0.1960	0.4772
	C_{37}	0.1537	0.2663	0.5820	−0.1503	0.3590
	$\delta^{15}N$	−0.2832	−0.1960	−0.1503	0.2330	−0.3651
	$\%N$	1.6508	0.4772	0.3590	−0.3651	0.9037
Transition matrix				0.9902	0.0098	
				0.0214	0.9786	

Table 4.6: [AR-HMM] Parameter estimation by the AR-HMM using the AR-HMM based simulated data.

		Constant	Autocorrelation				Covariance			
State 1	SST	−0.0298	0.8055	−0.0141	0.0348	0.0104	0.2354	0.0004	−0.0132	0.0046
	C_{37}	−0.0301	−0.1491	0.7171	0.0525	0.0055	0.0004	0.2714	−0.0133	0.0070
	$\delta^{15}N$	0.0466	0.0119	−0.0604	0.9488	−0.0132	−0.0132	−0.0133	0.0959	−0.0046
	$\%N$	−0.0224	0.0076	0.0627	−0.0137	0.8768	0.0046	0.0070	−0.0046	0.0678
State 2	SST	−0.0210	0.9423	−0.0301	−0.0541	0.0187	0.0537	0.0052	0.0001	−0.0005
	C_{37}	−0.0233	0.0862	0.8492	−0.0354	0.0382	0.0052	0.0591	0.0006	−0.0016
	$\delta^{15}N$	−0.0203	−0.0065	0.0132	0.9520	−0.0142	0.0001	0.0006	0.0108	0.0005
	$\%N$	0.0330	−0.0023	0.0252	0.0238	0.9999	−0.0005	−0.0016	0.0005	0.0148
Transition matrix						0.9903	0.0097			
						0.0139	0.9861			

4.2.4 Irregularly spaced measured proxies

While the observed data points from the central Peru margin are not evenly spaced (Figure 4.3), there are only four difference intervals: $\Delta t, 2\Delta t, 3\Delta t$, and $4\Delta t$. We can treat the observed data as a regularly spaced data set with missing observations, and fill in the missing values with their expected values. Another way to address this problem is to include the size of spacing Δt as a variable in modeling [49, 176, 129]. However, this method is not suitable in this study because the spacing patterns are different among the four climate proxies; for example, parts of $(x_1(t), x_2(t), x_3(t), x_4(t))$ are observed and parts are missing at time t. Thus, we decided to fill in the missing values with their expected values using the Kalman filter and Kalman smoother. Because the parameters of the Kalman filter and Kalman smoother are updated after running each iteration of the EM algorithm, we add the data augmentation step at the beginning of every iteration.

The simplest method to fill in the missing value is an interpolation. While the estimations using interpolations use only the adjacent data points near a missing point, the Kalman filter and Kalman smoother find the expected values using information of all measured data and the underlying model. Here, we briefly describe the Kalman filter following the descriptions and notations in [184]. See [184, 212] for further details of the Kalman filter.

4.2.4.1 Kalman filter for data augmentation

The Kalman filter is a useful tool to express the state-space model or the dynamic linear model. This method was first introduced in [91, 92] to model aerospace-related problems, and has since been applied to various fields including economics [64, 201], medicine [109, 27], and climate analysis [4, 62]. In this study, we employ the AR-HMM in modeling two hidden states and use the Kalman filter for data augmentation. This structure was first introduced in [201] for use in the field of economics as a mixed-frequency vector autoregression (VAR) with Markov regime switching in the parameters, which is the extension of the Markov switching VAR [60, 61]. The method in [201] was designed to simultaneously model multiple proxies with different frequencies in a vector form, and is thus called a mixed-frequency VAR. The difference between the method in [201] and the method used in this study is that we are using the EM algorithm instead of the Bayesian Markov chain Monte Carlo (MCMC) algorithm used in [201].

The state-space model can be described with the state equation and the observation equation. The state equation describes the target of modeling by a first order autoregression:

$$\text{State equation: } \mathbf{x}_t = \Phi \mathbf{x}_{t-1} + \mathbf{w}_t \tag{4.3}$$

where $\mathbf{x}_t$ is a $p \times 1$ vector representing a state at time t, Φ is a $p \times p$ matrix describing state changes, and $\mathbf{w}_t$ represents a $p \times 1$ vector describing a model error. We assumed that the linear model starts with an initial vector $\mathbf{x}_0$ which follows a normal distribution with mean μ_0 and a covariance matrix Σ_0. In most studies, it is almost impossible to directly observe $\mathbf{x}_t$ without noise. Instead, we observe a linear transformed version, $\mathbf{y}_t$, with noise added. This can be written of the form

$$\text{Observation equation: } \mathbf{y}_t = A\mathbf{x}_t + \mathbf{v}_t, \tag{4.4}$$

where A is a $q \times p$ observation matrix and $\mathbf{v}_t$ represents a $q \times 1$ vector describing a measurement error. We assume that $\{\mathbf{w}_t\}$ and $\{\mathbf{v}_t\}$ follow a zero mean multivariate normal distribution with a covariance matrix Q and R, respectively.

Here is a glossary of all symbols used for the state-space model:

$\mathbf{x}_t$: state vector

$\mathbf{y}_t$: observation vector

Φ : state matrix

A : observation matrix

$\mathbf{w}_t$ and Q : model error and the corresponding covariance matrix

$\mathbf{v}_t$ and R : observation error and the corresponding covariance matrix

$\mathbf{x}_0$: initial state vector $\sim \mathcal{N}(\mu_0, \Sigma_0)$

In this study, $\mathbf{x}_t$ refers to a full data set without missing parts and $\mathbf{y}_t$ indicates data with missing parts. The size of $\mathbf{x}_t$ and $\mathbf{y}_t$ (p and q) does not need to be the same in general, but in this study, p and q are set to be four as we have four proxies. The state equation (4.3) corresponds to the autoregressive emission model (4.2):

$$(4.2) \quad X(t) = c_{S(t)} + \theta_{S(t)} X(t - \Delta t) + \Sigma_{S(t)}^{1/2} \epsilon(t)$$

$$(4.3) \quad \mathbf{x}_t = \Phi \mathbf{x}_{t-1} + \mathbf{w}_t$$

The missing observations can be described using the observation equation (4.4) as described in [184, 201].

$$(4.4) \quad \mathbf{y}_t = A \mathbf{x}_t + \mathbf{v}_t$$

When we have a full observation at time t, we assume A to be an identity matrix and R (the covariance matrix of $\mathbf{v}_t$) to be 0. On the other hand, if we do not have any observations at time t, we set A to be 0 and R to be an identity matrix. These two terms change depending on the pattern of missing parts. For example, if the second term of $\mathbf{y}_t$ is missing, then we assume A and R as follows:

$$A = \begin{bmatrix} 1 & 0 & 0 & 0 \\ 0 & 0 & 0 & 0 \\ 0 & 0 & 1 & 0 \\ 0 & 0 & 0 & 1 \end{bmatrix}, \quad R = \begin{bmatrix} 0 & 0 & 0 & 0 \\ 0 & 1 & 0 & 0 \\ 0 & 0 & 0 & 0 \\ 0 & 0 & 0 & 0 \end{bmatrix}$$

In this way, $\mathbf{y}_t$ takes the exact measured values when we have observed data and it takes values describing noise when we do not have observed data.

Based on the state-space model structure, the Kalman filter and Kalman smoother find the expected values of $\mathbf{x}_t$ given all observations. Let Y_s represent the set of observations up to time s, $\mathbf{x}_t^s$ refer to the expected values of $\mathbf{x}_t$ given the observations up to time s, and P_t^s represent the conditional error covariance. That is,

$$\begin{aligned} &Y_s := \{\mathbf{y}_1, \ldots, \mathbf{y}_s\}, \\ &\mathbf{x}_t^s := E(\mathbf{x}_t | Y_s), \\ &P_t^s := E[(\mathbf{x}_t - \mathbf{x}_t^s)(\mathbf{x}_t - \mathbf{x}_t^s)|Y_s]. \end{aligned}$$

The Kalman filter finds the expected values of $\mathbf{x}_t$ given the observations up to time t, $\mathbf{x}_t^t$, which minimizes the conditional error covariance P_t^t. The Kalman smoother finds the expected values of $\mathbf{x}_t$ given all observations, $\mathbf{x}_t^n$.

The Kalman filter and Kalman smoother find the expected value of $\mathbf{x}_t$ recursively. The Kalman filter starts with initial conditions, $x_0^0 = \mu_0$ and $P_0^0 = \Sigma_0$, and recursively finds $\mathbf{x}_t^t$ as follows:

For $t = 1 : n$

$$\begin{aligned} \mathbf{x}_t^{t-1} &= \Phi \mathbf{x}_{t-1}^{t-1}, \\ P_t^{t-1} &= \Phi P_{t-1}^{t-1} \Phi' + Q, \end{aligned} \tag{4.5}$$

with

$$K_t = P_t^{t-1} A_t' [A_t P_t^{t-1} A_t' + R]^{-1},$$

$$\mathbf{x}_t^t = \mathbf{x}_t^{t-1} + K_t(\mathbf{y}_t - A_t \mathbf{x}_t^{t-1}),$$

$$P_t^t = [I - K_t A_t] P_t^{t-1},$$

After finding $\mathbf{x}_t^t$ up to the end of the data, we employ the Kalman smoother to find $\mathbf{x}_t^n$ starting from $t = n$ to $t = 1$.

For $t = n : -1 : 1$

$$\begin{aligned} \mathbf{x}_{t-1}^n &= \mathbf{x}_{t-1}^{t-1} + J_{t-1}(\mathbf{x}_t^n - \mathbf{x}_t^{t-1}), \\ P_{t-1}^n &= P_{t-1}^{t-1} + J_{t-1}(P_t^n - P_t^{t-1}) J_{t-1}', \end{aligned} \tag{4.6}$$

with

$$J_{t-1} = P_{t-1}^{t-1} \Phi' [P_t^{t-1}]^{-1}.$$

Through the Kalman filter (4.5) and the Kalman smoother (4.6), we find the expected values of the missing observations given measured data and the assumed autoregressive model (4.2). These data augmentation processes are added before each iteration of the EM algorithm. Therefore, we iteratively estimate the unknown parameters and the most probable states based on data filled in by the Kalman filter and the Kalman smoother.

4.3 Results

4.3.1 Parameter estimation

The parameter estimations are done using the EM algorithm for both HMM and AR-HMM. As described in Section 2.2.3, the EM algorithm updates parameters iteratively using the forward and backward sampling algorithm. The data augmentation step is added at the beginning of each iteration because of the updated parameters. Depending on initial conditions of the EM algorithm, it is possible that the EM algorithm converges to local maximum estimators instead of global maximum estimators. To avoid local maximums, we repeat parameter estimations with 100 different initial conditions and determine the parameters with the one that achieves maximum likelihood.

4.3.1.1 Results based on HMM

For a two-state HMM, there are five unknown parameters which have 44 degrees of freedom in total: $\mu_1, \mu_2, \Sigma_1, \Sigma_2$ and a. Table 4.7 shows the results of the parameter estimations. The distinctive difference between two states is the size of covariance. The absolute values of Σ_1 are larger than that of Σ_2. $X(t)$ fluctuates more when $X(t)$ is in state 1 than in state 2. In terms of transition probability, a_{11} and a_{22} are close to 1, which implies that there is a high probability of staying in a state.

According to the parameter estimations, the most probable state is determined for every t using the backward samplings. Figure 4.9 shows the most probable states with data $X(t)$: Four plots show the results of SST, C_{37}, $\delta^{15}N$ and $\%N$ from top to bottom with the black dots indicating the most probable states. For the black dots between state 1 and 2, the closer to state 1, the higher the probability of them being in state 1, and the same applies for state 2. The blue circles represent observed data $X(t)$ while the red lines represent the augmented data $X(t)$, whose missing parts are filled by their expected values. For the comparison with the AR-HMM, the correlations of the four proxies in HMM are estimated as in Tables 4.8 and 4.12. We obtain correlation matrices using the data set in which the missing parts have been augmented by their expected value. The signs of correlations are usually the same between the two states, but the strength of the correlations varies.

4.3.1.2 Results based on AR-HMM

There are seven unknown parameters, which have 76 degrees of freedom in total, in a two-state AR-HMM: $c_1, c_2, \theta_1, \theta_2, \Sigma_1, \Sigma_2$ and a. The estimated parameters are shown in Table 4.9. The diagonal entries of θ_2 are close to 1: each variable of $X(t)$ in state 2 strongly depends on its own immediate past. The diagonal entries of θ_1 are smaller than that of θ_2 while the off-diagonal entries of θ_1 are larger than that of θ_2: more interactions exist among the four variables in state 1 than state 2. Table 4.13 depicts the relation among the four variables for each state according to the autocorrelation parameter θ. For example, the current SST in state 1 is modeled to be the sum of an error with the previous values $(0.9083 \cdot SST, -0.0094 \cdot C_{37}, 0.0004 \cdot \delta^{15}N$, and $-0.0082 \cdot \%N)$. The correlations of the four proxies are shown in Table 4.11.

The amplitude of an error term Σ of state 1 is larger than that of state 2: state 1 is a high-variability state and state 2 is a low-variability state. Also, the variance of observed data $X(t)$ being in state 1 is larger than that of state 2 and the means in the two states are somewhat different, as shown in Table 4.10. $X(t)$ fluctuates more when being in state 1 than in state 2. This indicates that extremes of the three year average of these proxies occur more commonly in state 1.

In terms of transition probability, a_{11} and a_{22} are around 0.8, which are smaller than that of the HMM. Thus, there are more frequent state changes than shown by the HMM as in Figure 4.10. While the filled portion for missing data highly fluctuates in the HMM, the missing data is filled in by similar values to its adjacent points in the AR-HMM.

Table 4.7: [HMM] Parameter estimation by the HMM.

	State 1	State 2
Mean	$\begin{array}{cccccc} & SST & C_{37} & \delta^{15}N & \%N & \\ [& 0.5044 & -0.1731 & 0.7302 & 0.0602 &] \end{array}$	$\begin{array}{cccccc} & SST & C_{37} & \delta^{15}N & \%N & \\ [& -0.4007 & 0.1769 & -0.5051 & -0.0728 &] \end{array}$
Covariance	$\begin{bmatrix} 0.9962 & -0.2371 & -0.0818 & -0.1988 \\ -0.2371 & 1.4041 & -0.3311 & 0.7157 \\ -0.0818 & -0.3311 & 0.4766 & -0.4672 \\ -0.1988 & 0.7157 & -0.4672 & 1.0716 \end{bmatrix}$	$\begin{bmatrix} 0.5076 & -0.0479 & -0.2130 & 0.1769 \\ -0.0479 & 0.5212 & -0.0875 & 0.2075 \\ -0.2130 & -0.0875 & 0.3323 & -0.1307 \\ 0.1769 & 0.2075 & -0.1307 & 0.3702 \end{bmatrix}$
Transition Probability	$\begin{bmatrix} 0.9555 & 0.0445 \\ 0.0341 & 0.9659 \end{bmatrix}$	

Table 4.8: [HMM] Correlation matrix of SST, C_{37}, $\delta^{15}N$, and $\%N$ for each state. The correlation matrices are obtained from the data set augmented by their expected values.

State 1	State 2
$\begin{bmatrix} 1.0000 & -0.2151 & -0.0793 & -0.1957 \\ -0.2151 & 1.0000 & -0.4136 & 0.5516 \\ -0.0793 & -0.4136 & 1.0000 & -0.6738 \\ -0.1957 & 0.5516 & -0.6738 & 1.0000 \end{bmatrix}$	$\begin{bmatrix} 1.0000 & -0.1491 & -0.4888 & 0.4157 \\ -0.1491 & 1.0000 & -0.1757 & 0.4393 \\ -0.4888 & -0.1757 & 1.0000 & -0.3795 \\ 0.4157 & 0.4393 & -0.3795 & 1.0000 \end{bmatrix}$

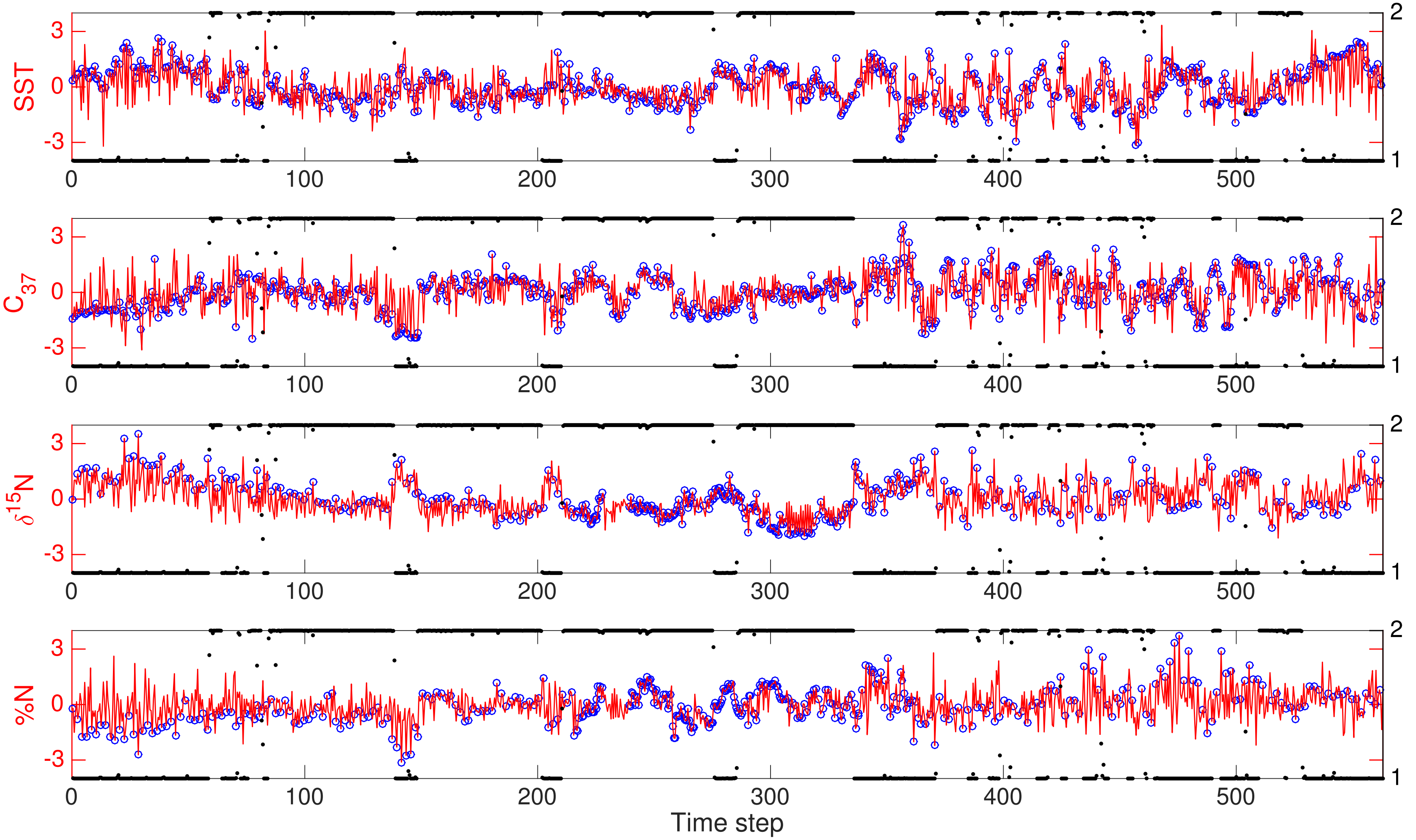

Figure 4.9: [HMM] State assignments by the HMM and data $X(t)$ whose missing parts are filled by an expected value: SST, C_{37}, $\delta^{15}N$ and $\%N$ from top to bottom. Blue circles represent observed values and red lines represent expected values of missing observations. Black dots describe the most probable states.

Table 4.9: [AR-HMM] Parameter estimation by the AR-HMM.

	State 1	State 2
c	$\begin{array}{cccc} SST & C_{37} & \delta^{15}N & \%N \\ [\ 0.0211 & -0.0001 & 0.0557 & -0.0067\ ] \end{array}$	$\begin{array}{cccc} SST & C_{37} & \delta^{15}N & \%N \\ [\ -0.0185 & -0.0012 & -0.0358 & 0.0124\ ] \end{array}$
θ	$\begin{bmatrix} 0.9083 & -0.0094 & 0.0004 & -0.0082 \\ -0.0617 & 0.8596 & -0.0031 & 0.0211 \\ 0.0446 & -0.0242 & 0.9424 & -0.0291 \\ -0.0619 & 0.0232 & -0.0405 & 0.9166 \end{bmatrix}$	$\begin{bmatrix} 0.9621 & 0.0016 & -0.0074 & 0.0110 \\ 0.0329 & 0.9838 & 0.0333 & 0.0029 \\ -0.0163 & 0.0117 & 0.9400 & 0.0086 \\ 0.0226 & -0.0154 & 0.0401 & 0.9785 \end{bmatrix}$
$\|\Sigma\|^{1/2}$	$\begin{bmatrix} 0.4645 & 0.1583 & 0.0892 & 0.1901 \\ 0.1583 & 0.4930 & 0.2631 & 0.2482 \\ 0.0892 & 0.2631 & 0.4055 & 0.1993 \\ 0.1901 & 0.2482 & 0.1993 & 0.4545 \end{bmatrix}$	$\begin{bmatrix} 0.1824 & 0.0609 & 0.1026 & 0.0351 \\ 0.0609 & 0.1827 & 0.0472 & 0.0731 \\ 0.1026 & 0.0472 & 0.0795 & 0.0356 \\ 0.0351 & 0.0731 & 0.0356 & 0.0791 \end{bmatrix}$
Σ	$\begin{bmatrix} 0.2157 & -0.0250 & -0.0080 & 0.0361 \\ -0.0250 & 0.2430 & -0.0692 & 0.0616 \\ -0.0080 & -0.0692 & 0.1644 & -0.0397 \\ 0.0361 & 0.0616 & -0.0397 & 0.2066 \end{bmatrix}$	$\begin{bmatrix} 0.0333 & -0.0037 & 0.0105 & -0.0012 \\ -0.0037 & 0.0334 & 0.0022 & 0.0053 \\ 0.0105 & 0.0022 & 0.0063 & -0.0013 \\ -0.0012 & 0.0053 & -0.0013 & 0.0063 \end{bmatrix}$
Transition Probability	$\begin{bmatrix} 0.8077 & 0.1923 \\ 0.1720 & 0.8280 \end{bmatrix}$	

Table 4.10: [AR-HMM] Mean and Variance for each state. The means and variances are obtained from the data set augmented by the Kalman filter.

		SST	C_{37}	$\delta^{15}N$	$\%N$
Mean	State 1	0.0095	-0.0692	0.2097	-0.0274
	State 2	0.0113	0.0499	0.1014	-0.0719
Variance	State 1	1.0422	1.0609	1.0663	1.3010
	State 2	0.8716	0.7708	0.8401	0.7703

Table 4.11: [AR-HMM] Correlation matrix of SST, C_{37}, $\delta^{15}N$, and $\%N$ for each state. The correlation matrices are obtained from the data set augmented by the Kalman filter.

State 1	State 2
$\begin{bmatrix} 1.0000 & -0.2139 & 0.1081 & -0.0145 \\ -0.2139 & 1.0000 & -0.3406 & 0.4048 \\ 0.1081 & -0.3406 & 1.0000 & -0.4365 \\ -0.0145 & 0.4048 & -0.4365 & 1.0000 \end{bmatrix}$	$\begin{bmatrix} 1.0000 & -0.2555 & 0.2065 & -0.0175 \\ -0.2555 & 1.0000 & -0.2853 & 0.3684 \\ 0.2065 & -0.2853 & 1.0000 & -0.3714 \\ -0.0175 & 0.3684 & -0.3714 & 1.0000 \end{bmatrix}$

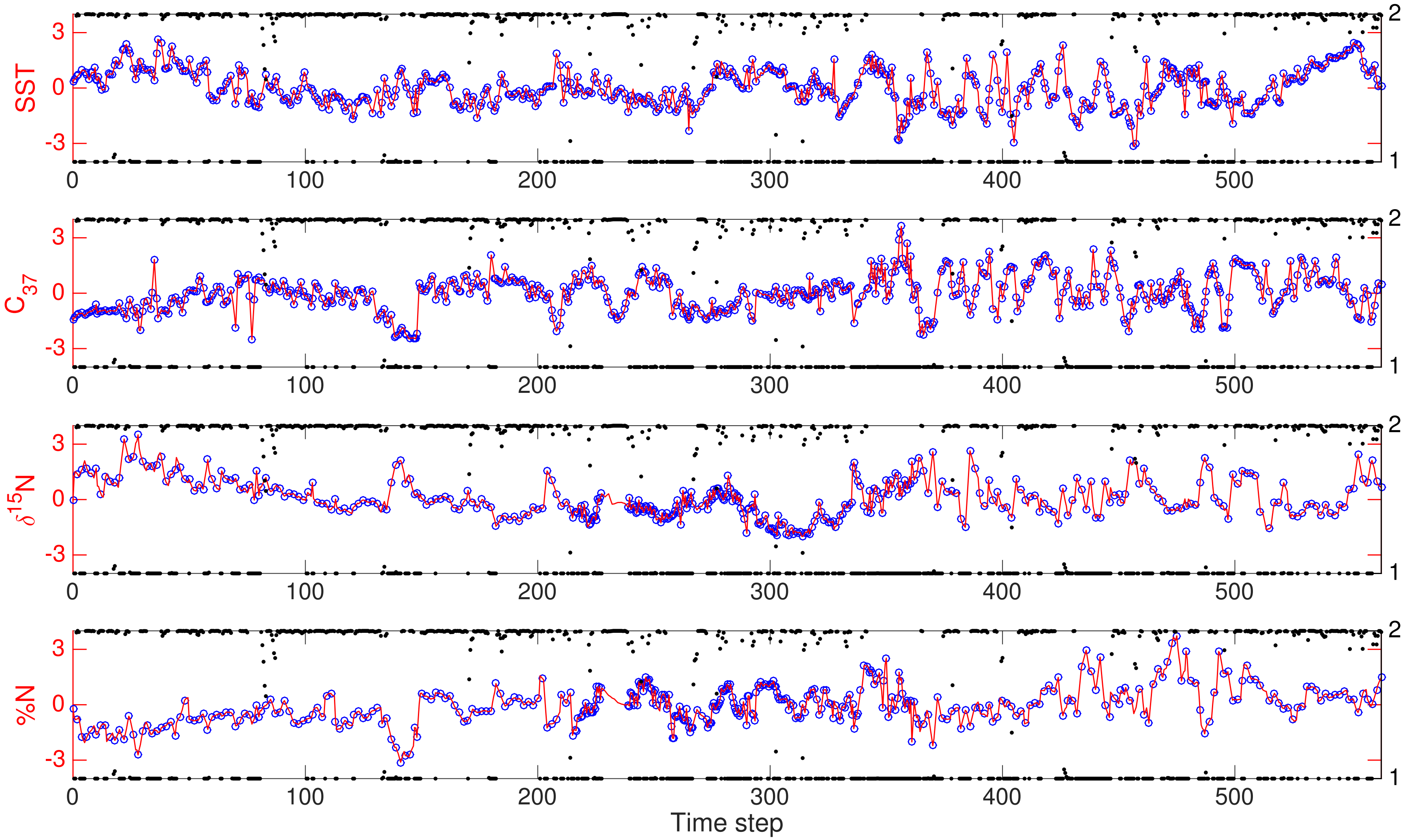

Figure 4.10: [AR-HMM] State assignments by the AR-HMM and data $X(t)$ whose missing parts are filled by the Kalman filter: SST, C_{37}, $\delta^{15}N$ and $\%N$ from top to bottom. Blue circles represent observed values and red lines represent expected values of missing observations. Black dots describe the most probable states.

4.3.2 Predictability of future events

We are interested in evaluating the predictability of the four proxies (SST, C_{37}, $\delta^{15}N$ and $\%N$) based on the AR-HMM. While we can assess predictability using the parameters estimated in the previous section, this assessment is not ideal because it uses all of the data to estimate the parameters including a predicted point and those that came later. A better alternative is to use only the data that precedes points we seek to predict. We did this in two ways: Predict new parameters using the data sequence preceding the points we predict, and sample values using these parameters.

Predictability of the AR-HMM is evaluated over two time windows: 236-266 and 535-563. When evaluating predictability, all of the four variables at the starting point and at the end point are required as initial conditions and exact values, respectively. The interval 236-266 is chosen because the resolution of the interval 236-266 is relatively higher than other intervals. Taking 266 as an end point, the predictability of one-step to thirty-step is assessed. The interval 535-563 includes the most recent data. Nitrogen data ($\delta^{15}N$ and $\%N$) is available every 4 steps (an average of 28 years apart) for this recent data range, so the predictability of four-step to twenty eight-step is evaluated. Each prediction is repeated 1000 times.

Depending on the most probable state of an initial point, the entries of the next step are computed with the emission model (4.2) with parameters estimated in the previous section. The state of the next step is determined by the transition probability, and then the entries of the following step are computed with the equation (4.2) in the same way. State determination and entry computations are repeated until reaching the end point.

The accuracy of predictability based on the AR-HMM is examined using mean squared errors (MSE). Figures 4.11-4.19 and Figures 4.20-4.26 show the prediction plots for the interval 236-266 and 535-563, respectively. The first row represents the states: the red dots

Table 4.12: [HMM] Visual description of the correlation matrix (Table 4.8) for each state obtained based on HMM.

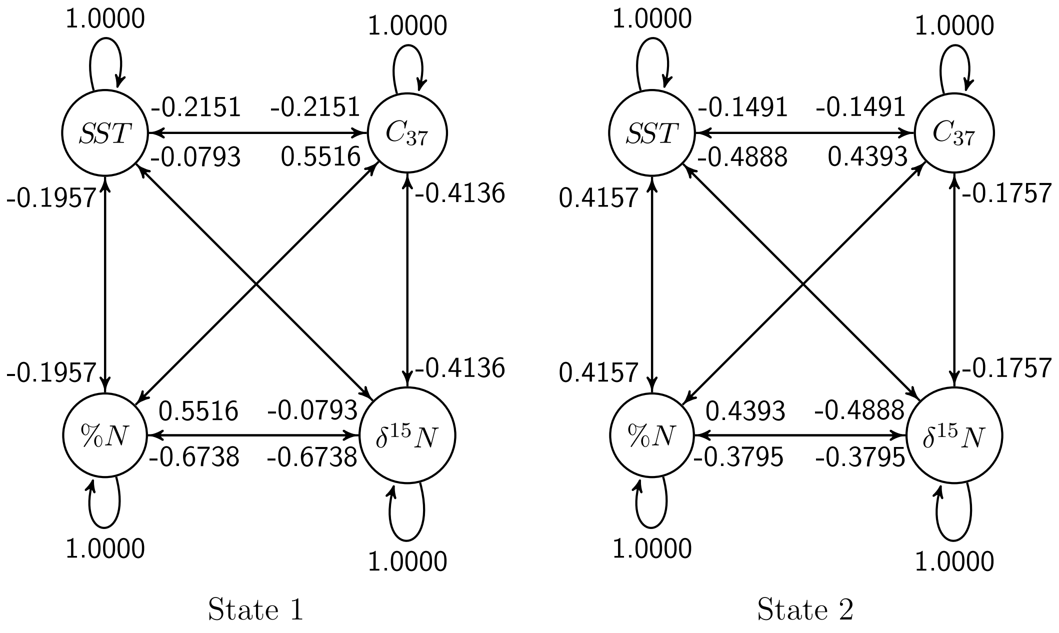

Table 4.13: [AR-HMM] Visual description of the autocorrelation parameter θ of the AR-HMM (Table 4.9).

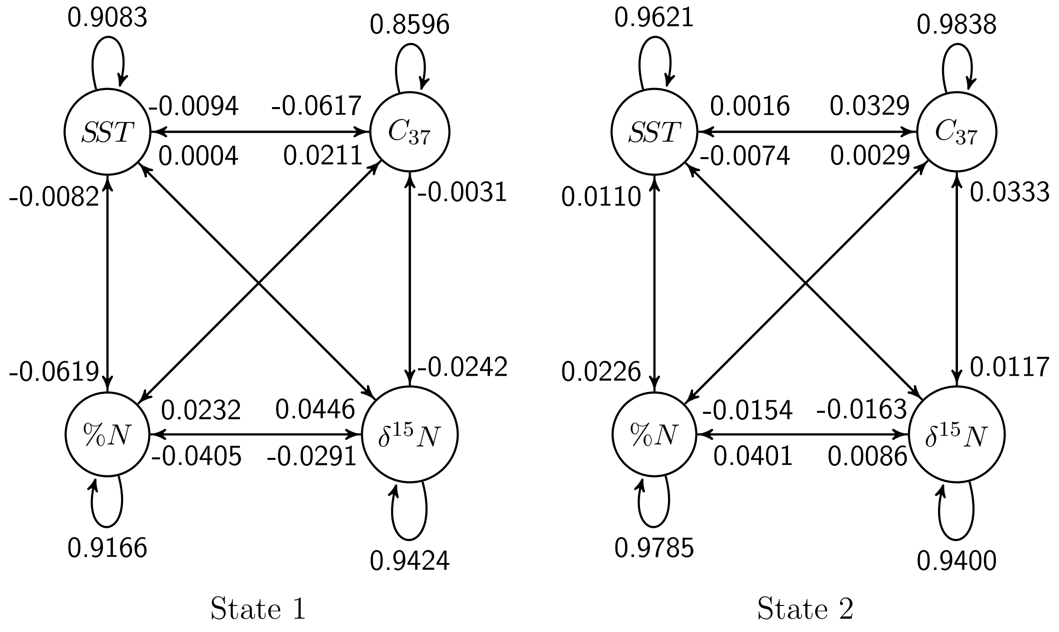

are the most probable states and the gray dots indicate the average state over 1000 runs. The second to the fifth rows represent the observations and predictions of SST, C_{37}, $\delta^{15}N$ and $\%N$: the red dots are observation data. The red dotted lines indicate the range of the observation data and the red solid lines show the 0.05 quantile to 0.95 quantile of the observed data. The gray lines indicate the 1000-run predictions. The black error bar at each prediction shows the 0.05 quantile to 0.95 quantile of 1000-runs. Predictions up to four-step, which corresponds to approximately three decades, achieve reduction of the MSE by 40-80%, depending on the proxy. The results do not show a tight range of prediction when the length of prediction is longer than four-step. However, it remains significant that the probability of being in a given state for the future steps can be predicted from the transition probability.

The predictability depending on the state of a starting point is examined by comparing the predictions up to 266 and 563. Tables 4.14-4.17 show mean squared errors (MSE) of the prediction up to 266 and 563. The numbers in parenthesis indicate the percentage of MSE by taking the MSE of the longest prediction as 100. The amount of MSE heavily depends on the most probable state of a starting point. Consider the four-step predictions of 262 to 266 and 559 to 563. The overall MSEs of the prediction 262 to 266 are higher than that of the prediction 559 to 563. This is because the most probable state at 262 is state 1, which is a high-variability state, while that of 559 is state 2, which is a low-variability state.

In order to compare the HMM with the AR-HMM, we assessed the predictability of the HMM is assessed in the same manner as the that of AR-HMM. Tables 4.18-4.21 show the results of HMM. While the MSEs increase as the length of prediction increases in AR-HMM, the MSEs of HMM keep the same size regardless of the length of prediction. The 4-step prediction plots based on HMM (Figures 4.27 and 4.28) show that the size of error bars does not change depending on the length of prediction. This outcome is from the fact that prediction is solely determined by its predicted states when using the HMM and indicates that the HMM is not proper for the predictions.

Table 4.14: [AR-HMM] MSE of the prediction up to 266. (The numbers in parenthesis represent the percentage over the longest prediction.)

Length of Prediction	1	2	3	4	5	10	16	20	30
SST	0.0541	0.1545	0.1013	0.1323	0.2949	0.1328	0.2848	0.2267	0.2390
	(22.66)	(64.64)	(42.38)	(55.34)	(123.42)	(55.55)	(119.17)	(94.84)	(100)
C_{37}	6.9571	12.3363	14.4638	18.5064	20.9084	58.0843	28.7893	95.2723	94.6705
	(7.35)	(13.03)	(15.28)	(19.55)	(22.09)	(61.35)	(30.41)	(100.64)	(100)
$\delta^{15}N$	0.1540	0.3695	0.4412	0.6155	0.2937	1.0272	0.6053	1.2117	1.0513
	(14.65)	(35.15)	(41.97)	(58.55)	(27.94)	(97.70)	(57.57)	(115.25)	(100)
$\%N$	0.0012	0.0021	0.0044	0.0110	0.0050	0.0154	0.0048	0.0206	0.0207
	(5.97)	(10.20)	(21.11)	(53.41)	(24.36)	(74.31)	(23.34)	(99.50)	(100)

Table 4.15: [AR-HMM] Squared bias, variance and MSE of the prediction up to 266.

Length of Prediction		1	2	3	4	5	10	16	20	30
SST	Bias^2	0.0305	0.1005	0.0459	0.0919	0.2360	0.0441	0.1698	0.0958	0.1004
	Variance	0.0237	0.0540	0.0554	0.0404	0.0589	0.0887	0.1150	0.1308	0.1386
	MSE	0.0541	0.1545	0.1013	0.1323	0.2949	0.1328	0.2848	0.2267	0.2390
C_{37}	Bias^2	2.0373	2.6533	0.0302	3.2239	4.9811	38.4687	0.9536	71.5074	68.0915
	Variance	4.9198	9.6830	14.4336	15.2824	15.9273	19.6156	27.8357	23.7648	26.5790
	MSE	6.9571	12.3363	14.4638	18.5064	20.9084	58.0843	28.7893	95.2723	94.6705
$\delta^{15}N$	Bias^2	0.0691	0.1700	0.1266	0.3130	0.0014	0.6392	0.1249	0.6550	0.4763
	Variance	0.0849	0.1996	0.3146	0.3026	0.2924	0.3880	0.4804	0.5566	0.5750
	MSE	0.1540	0.3695	0.4412	0.6155	0.2937	1.0272	0.6053	1.2117	1.0513
$\%N$	Bias^2	0.0002	0.0003	0.0014	0.0083	0.0019	0.0114	0.0003	0.0154	0.0154
	Variance	0.0011	0.0018	0.0030	0.0027	0.0032	0.0040	0.0045	0.0051	0.0053
	MSE	0.0012	0.0021	0.0044	0.0110	0.0050	0.0154	0.0048	0.0206	0.0207

Table 4.16: [AR-HMM] MSE of the prediction up to 563. (The numbers in parenthesis represent the percentage over the longest prediction.)

Length of Prediction	4	8	12	16	20	24	28
SST	0.0860	0.1989	0.1556	0.1967	0.2585	0.2370	0.1710
	(50.32)	(116.33)	(91.04)	(115.06)	(151.20)	(138.66)	(100)
C_{37}	14.4714	71.4603	35.7690	39.7473	57.5197	50.9346	40.6577
	(35.59)	(175.76)	(87.98)	(97.76)	(141.47)	(125.28)	(100)
$\delta^{15}N$	0.2108	1.5380	0.6201	0.6848	1.4787	0.7823	0.8482
	(24.86)	(181.33)	(73.11)	(80.74)	(174.33)	(92.23)	(100)
$\%N$	0.0090	0.0353	0.0268	0.0252	0.0546	0.0391	0.03856
	(23.29)	(91.78)	(69.78)	(65.64)	(142.04)	(101.58)	(100)

Table 4.17: [AR-HMM] Squared bias, variance and MSE of the prediction up to 563.

Length of Prediction		4	8	12	16	20	24	28
SST	Bias^2	0.0269	0.0645	0.0051	0.0408	0.0767	0.0520	0.0090
	Variance	0.0592	0.1344	0.1505	0.1559	0.1817	0.1851	0.1620
	MSE	0.0860	0.1989	0.1556	0.1967	0.2585	0.2370	0.1710
C_{37}	Bias^2	3.6656	46.9522	7.1700	9.2051	22.3467	15.2570	10.0923
	Variance	10.8058	24.5082	28.5990	30.5421	35.1729	35.6776	30.5654
	MSE	14.4714	71.4603	35.7690	39.7473	57.5197	50.9346	40.6577
$\delta^{15}N$	Bias^2	0.0249	1.0078	0.0039	0.0015	0.4950	0.0192	0.0678
	Variance	0.1859	0.5302	0.6162	0.6834	0.9837	0.7631	0.7804
	MSE	0.2108	1.5380	0.6201	0.6848	1.4787	0.7823	0.8482
$\%N$	Bias^2	0.0066	0.0283	0.0196	0.0158	0.0427	0.0284	0.0281
	Variance	0.0024	0.0070	0.0073	0.0095	0.0119	0.0106	0.0104
	MSE	0.0090	0.0353	0.0268	0.0252	0.0546	0.0391	0.0385

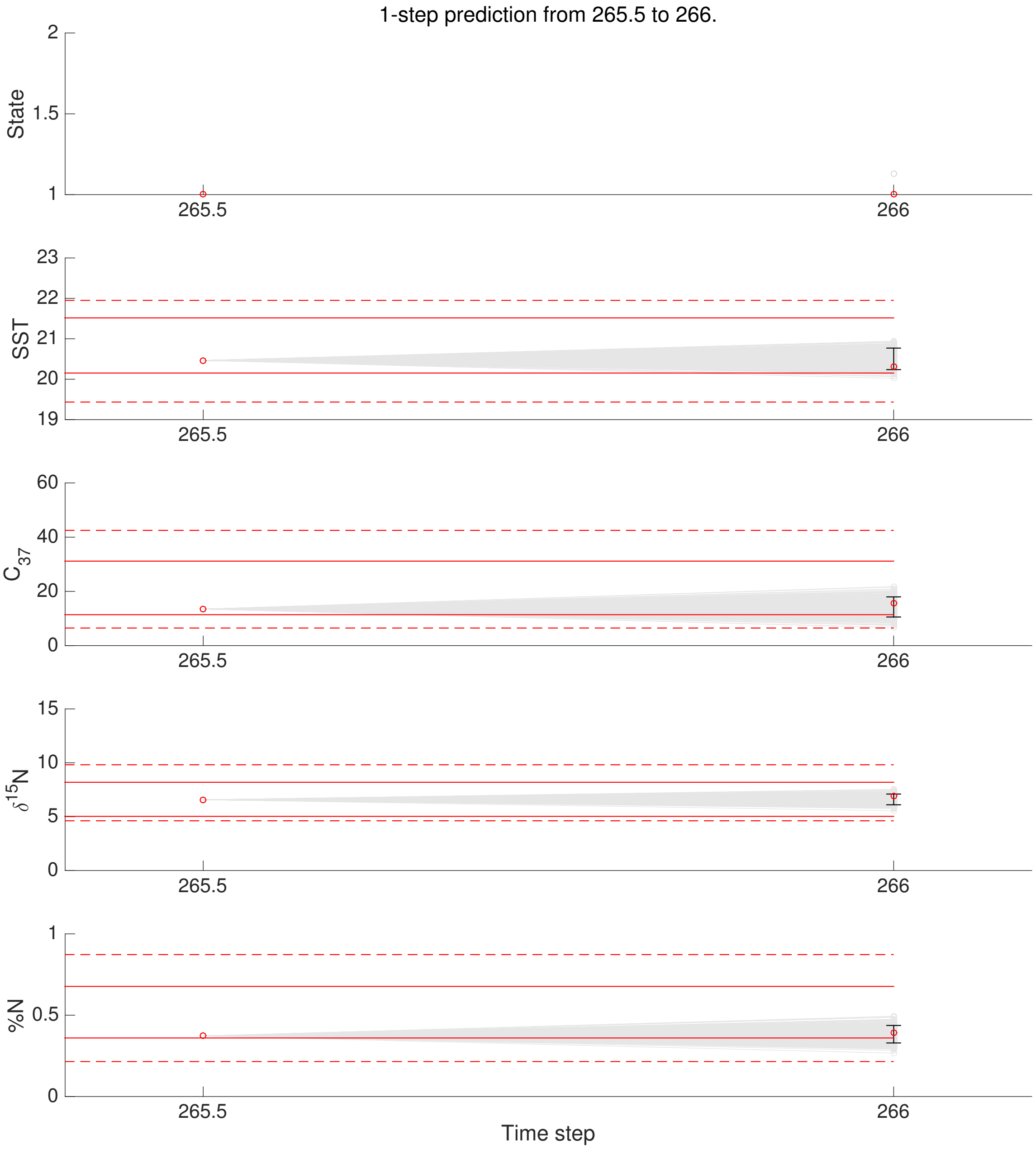

Figure 4.11: [AR-HMM] 1-step prediction from 265.5 to 266.

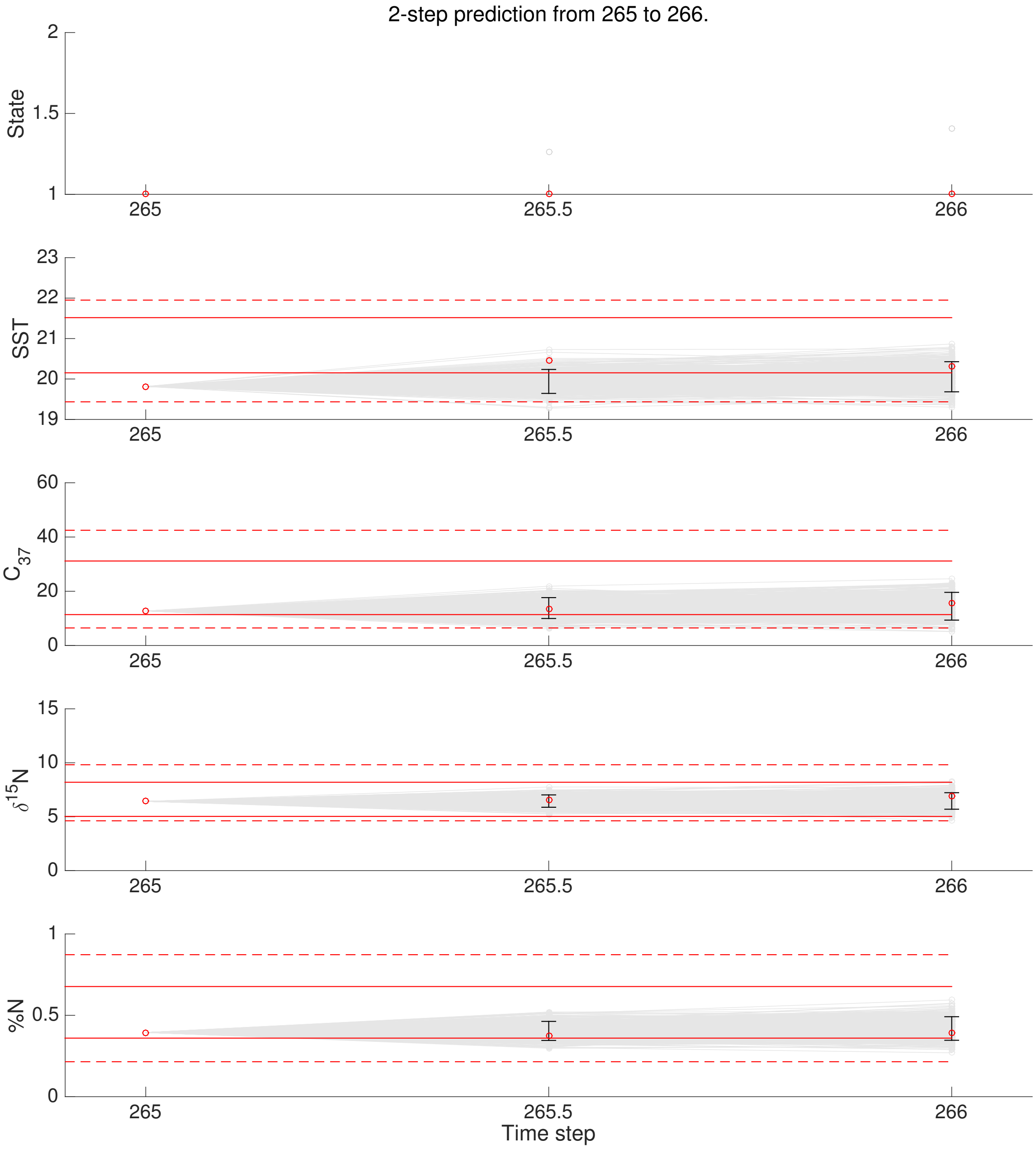

Figure 4.12: [AR-HMM] 2-step prediction from 265 to 266.

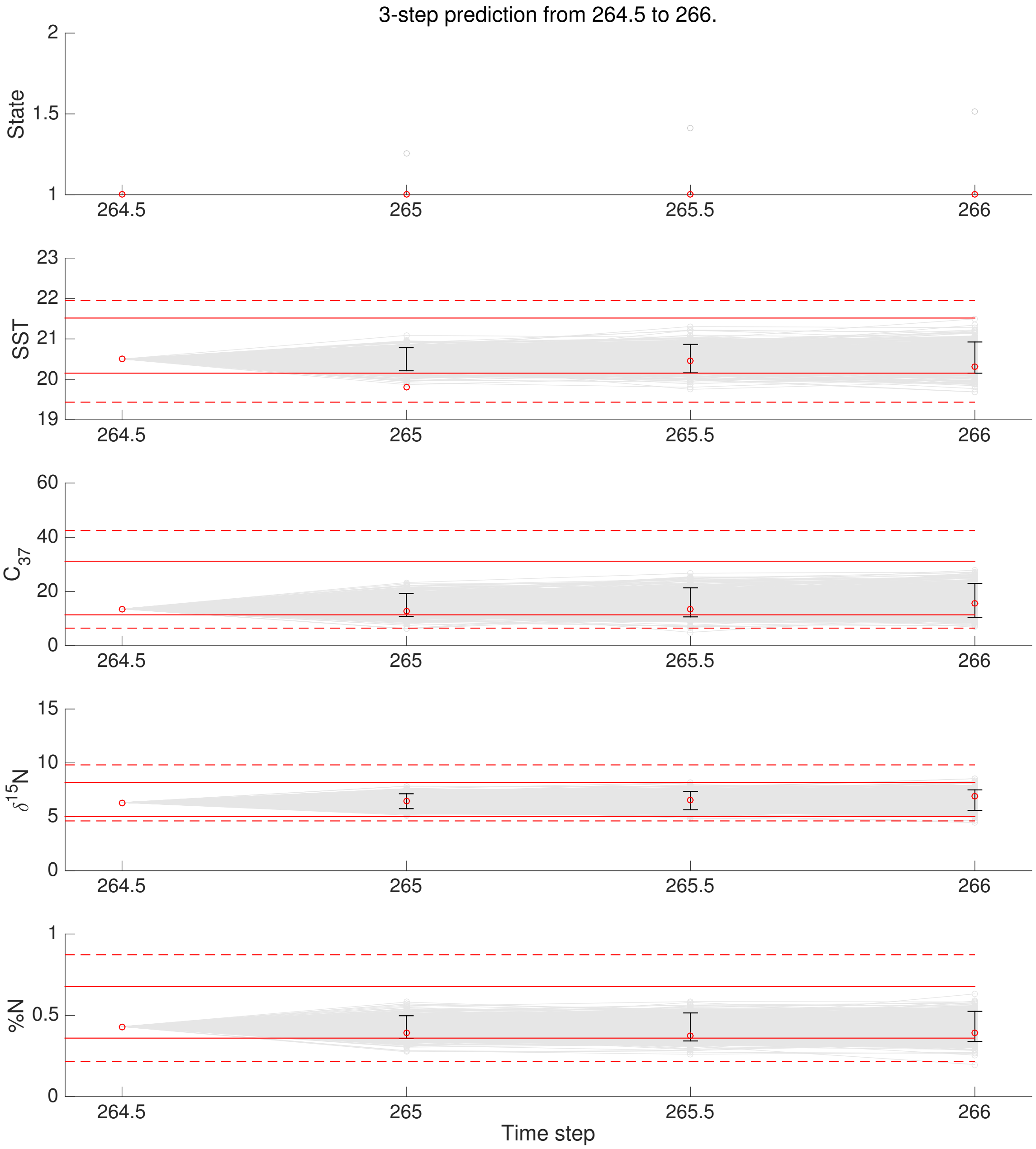

Figure 4.13: [AR-HMM] 3-step prediction from 264.5 to 266.

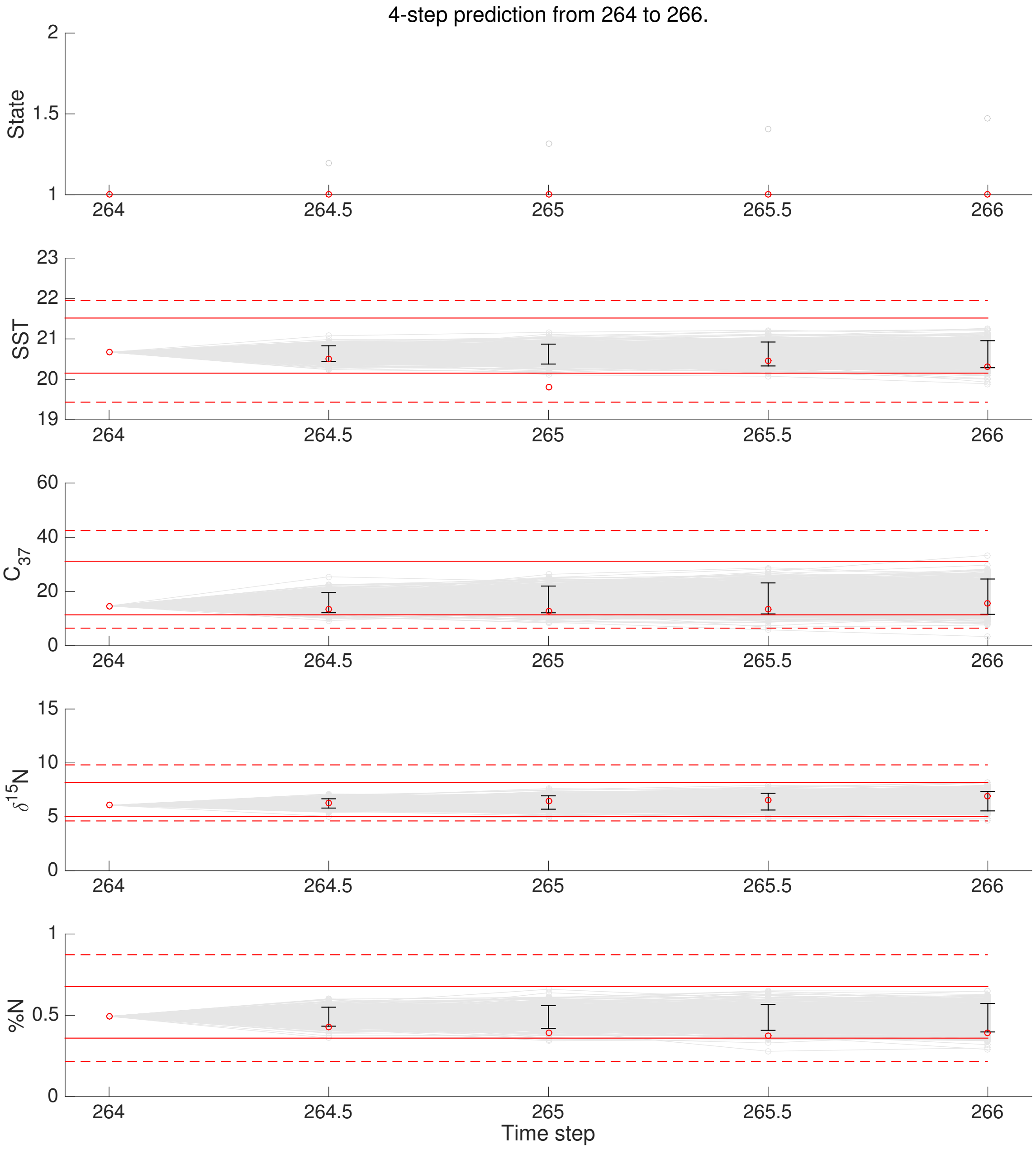

Figure 4.14: [AR-HMM] 4-step prediction from 264 to 266.

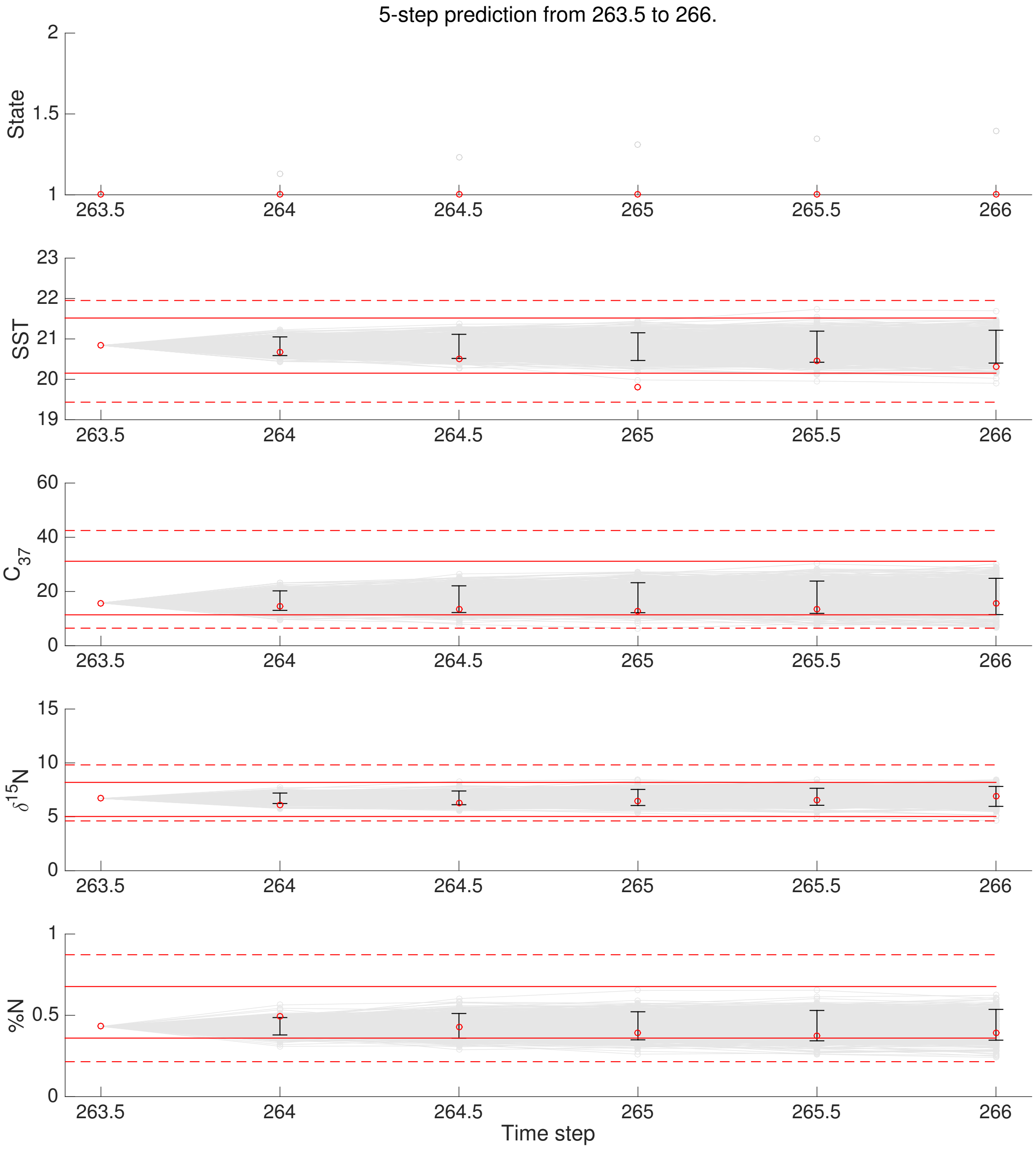

Figure 4.15: [AR-HMM] 5-step prediction from 263.5 to 266.

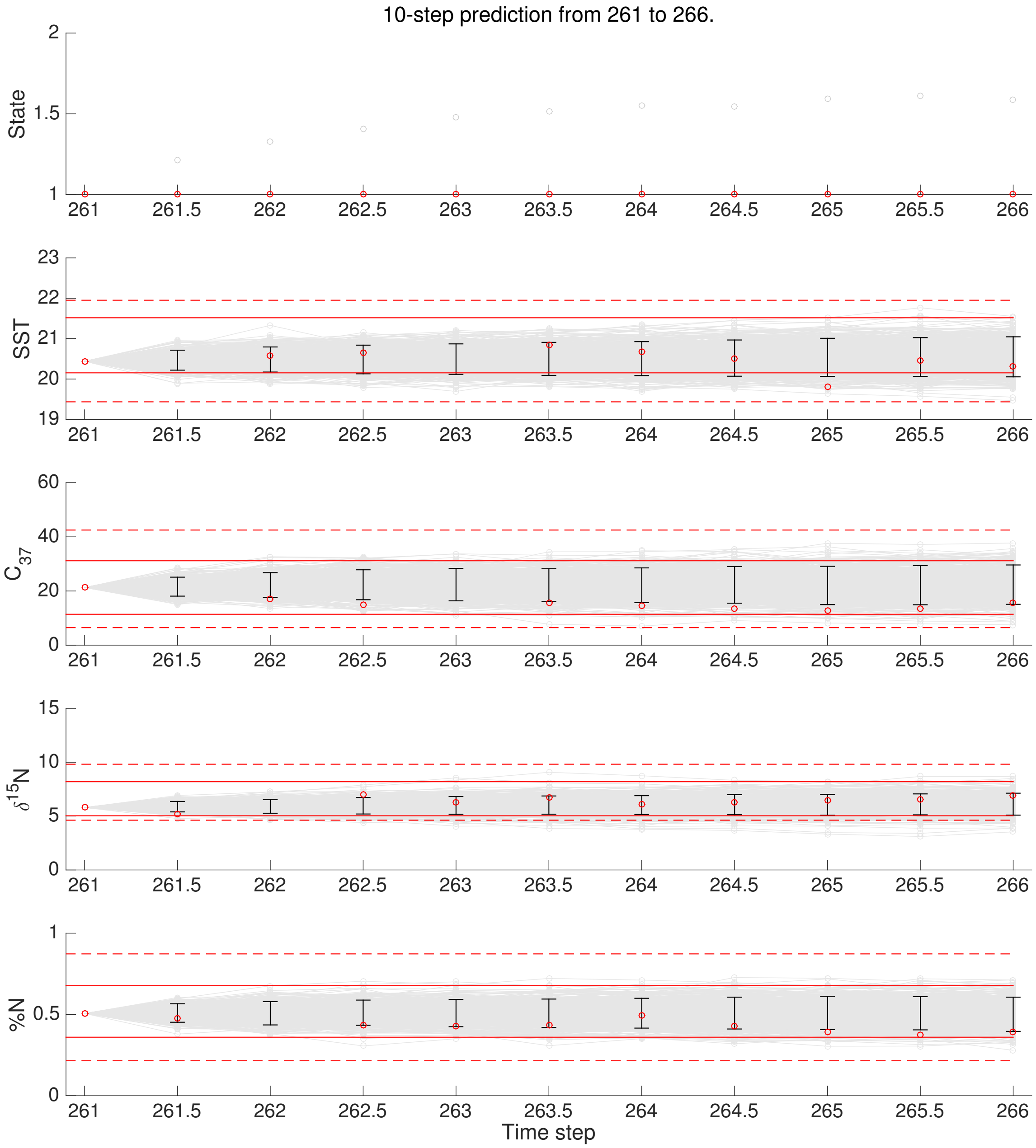

Figure 4.16: [AR-HMM] 10-step prediction from 261 to 266.

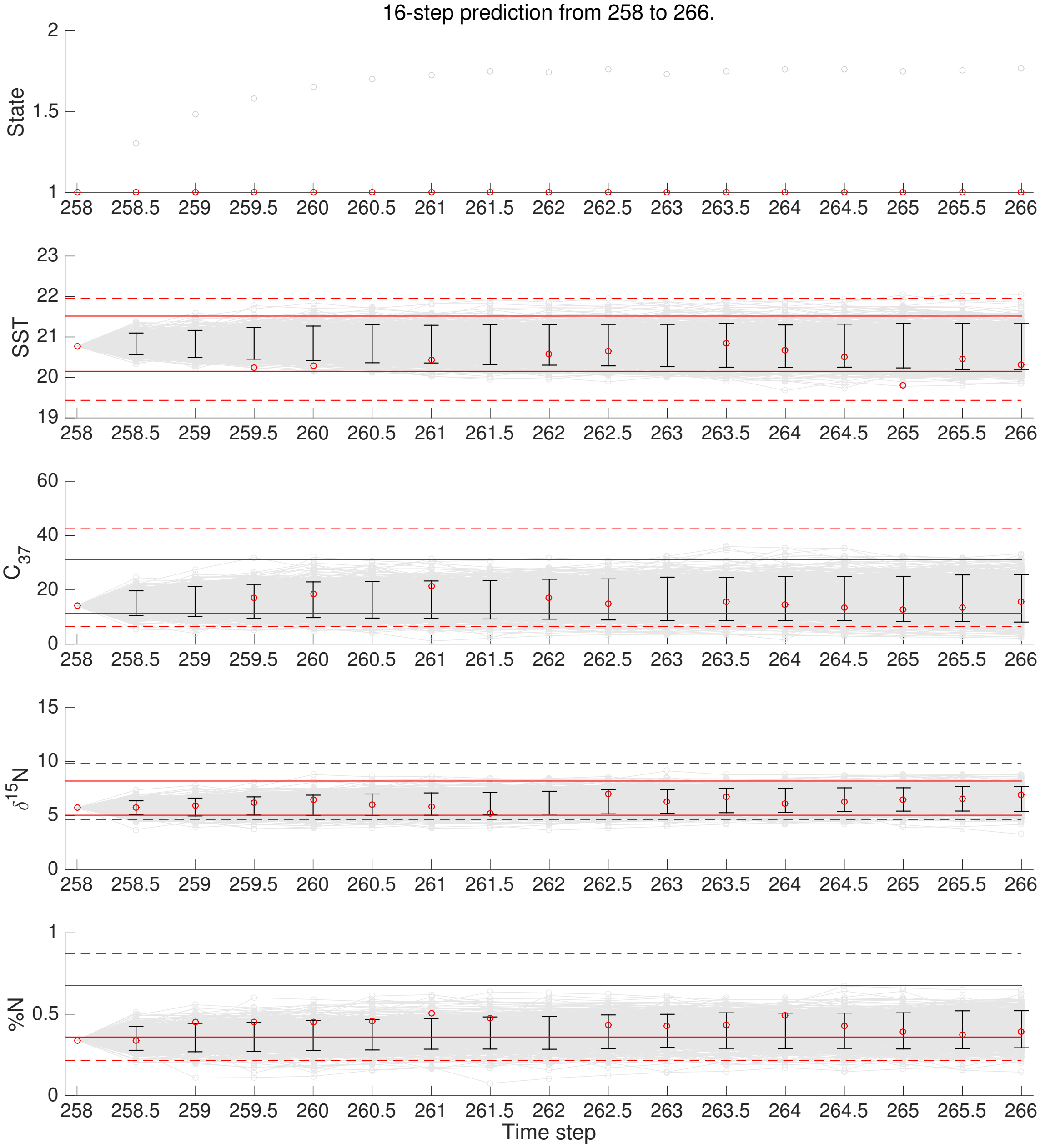

Figure 4.17: [AR-HMM] 16-step prediction from 258 to 266.

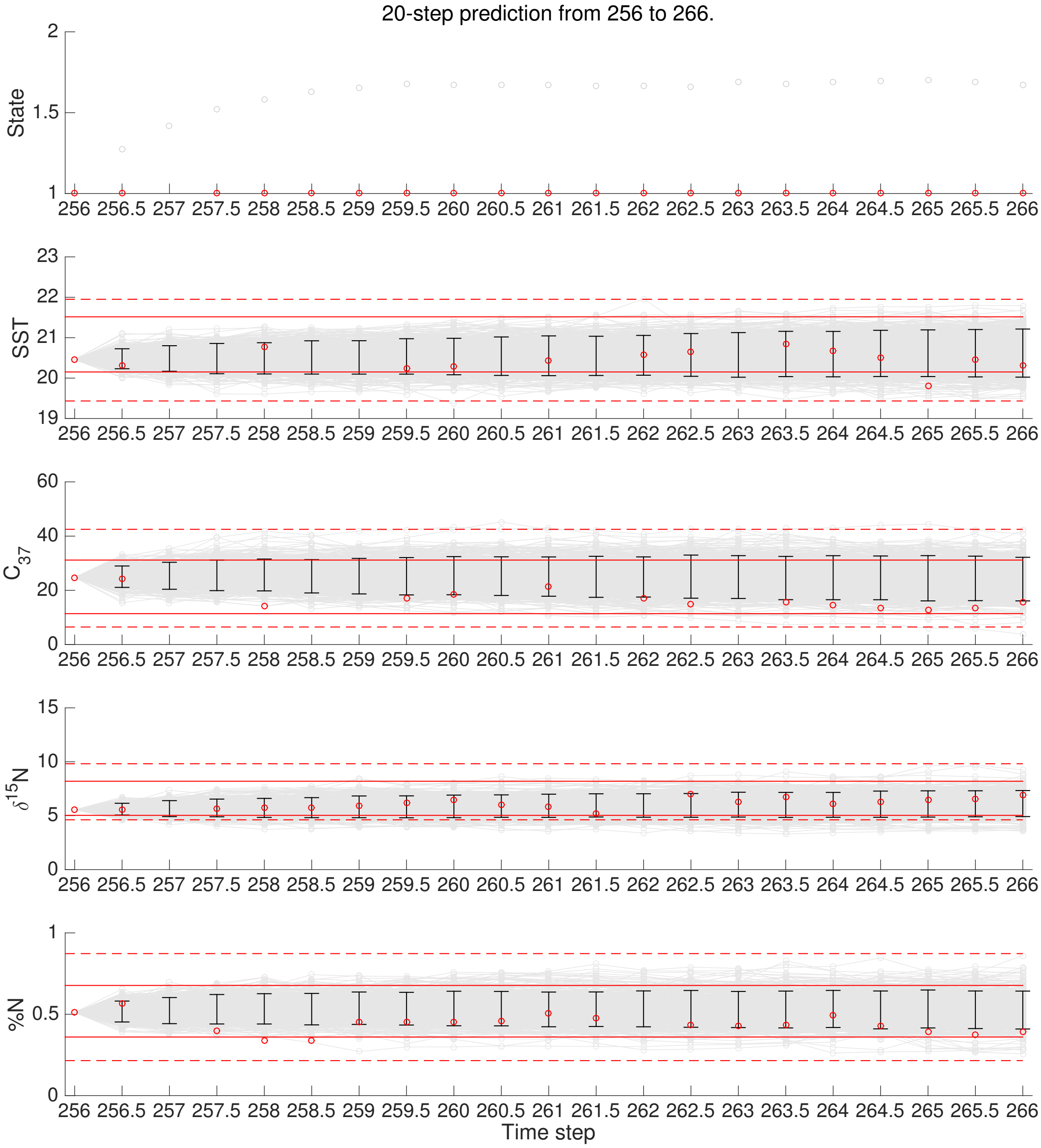

Figure 4.18: [AR-HMM] 20-step prediction from 256 to 266.

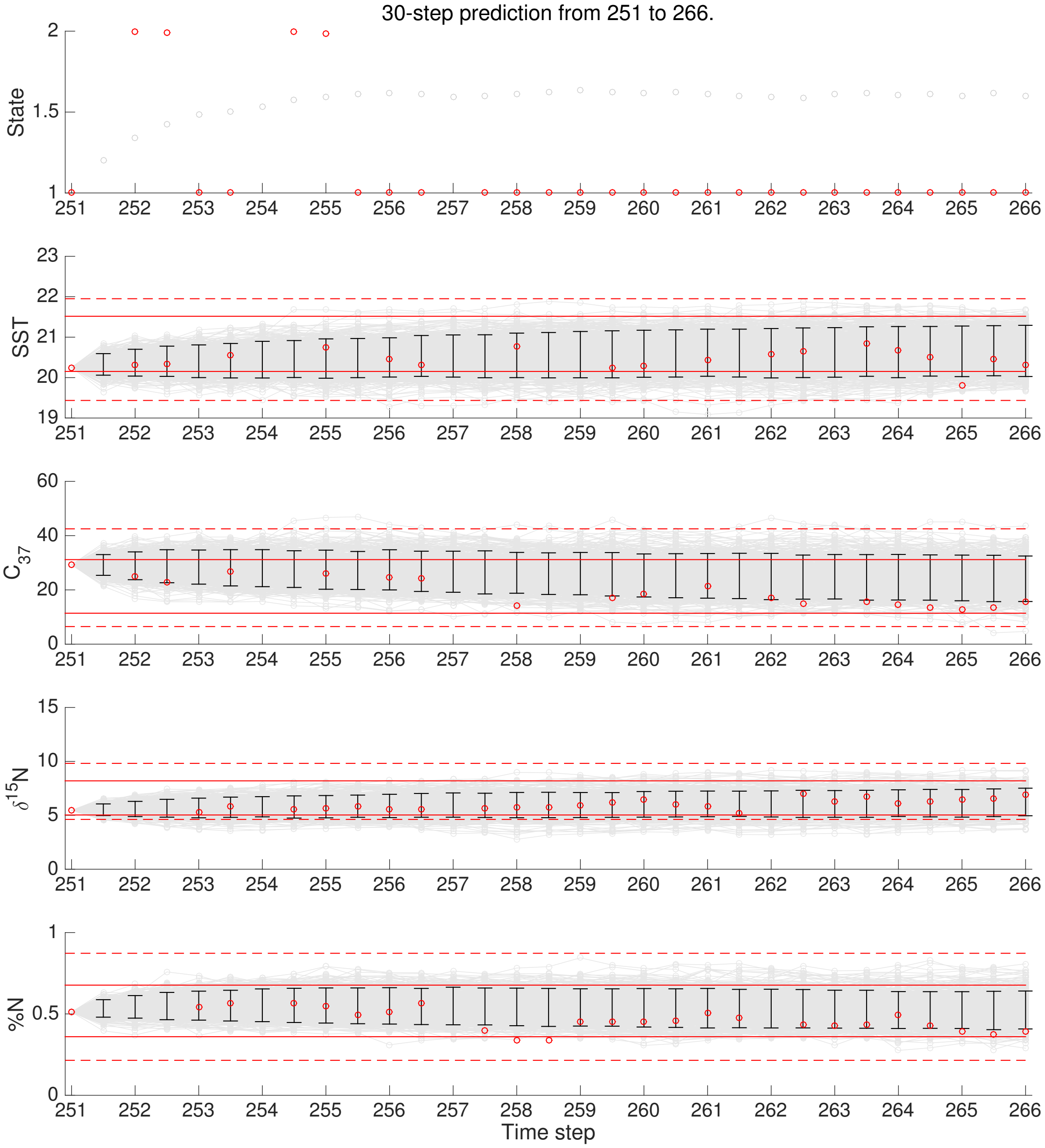

Figure 4.19: [AR-HMM] 30-step prediction from 251 to 266.

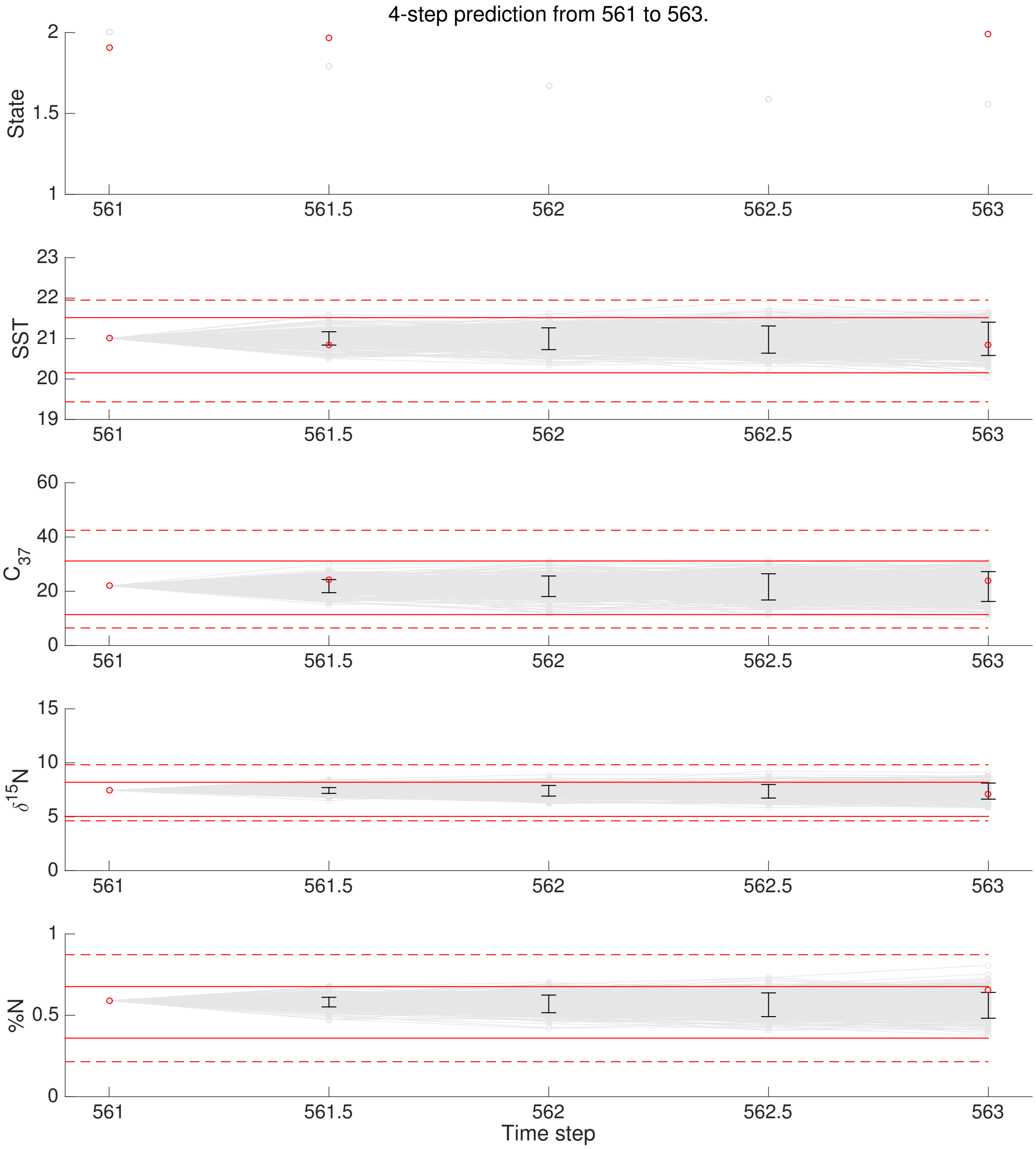

Figure 4.20: [AR-HMM] 4-step prediction from 561 to 563.

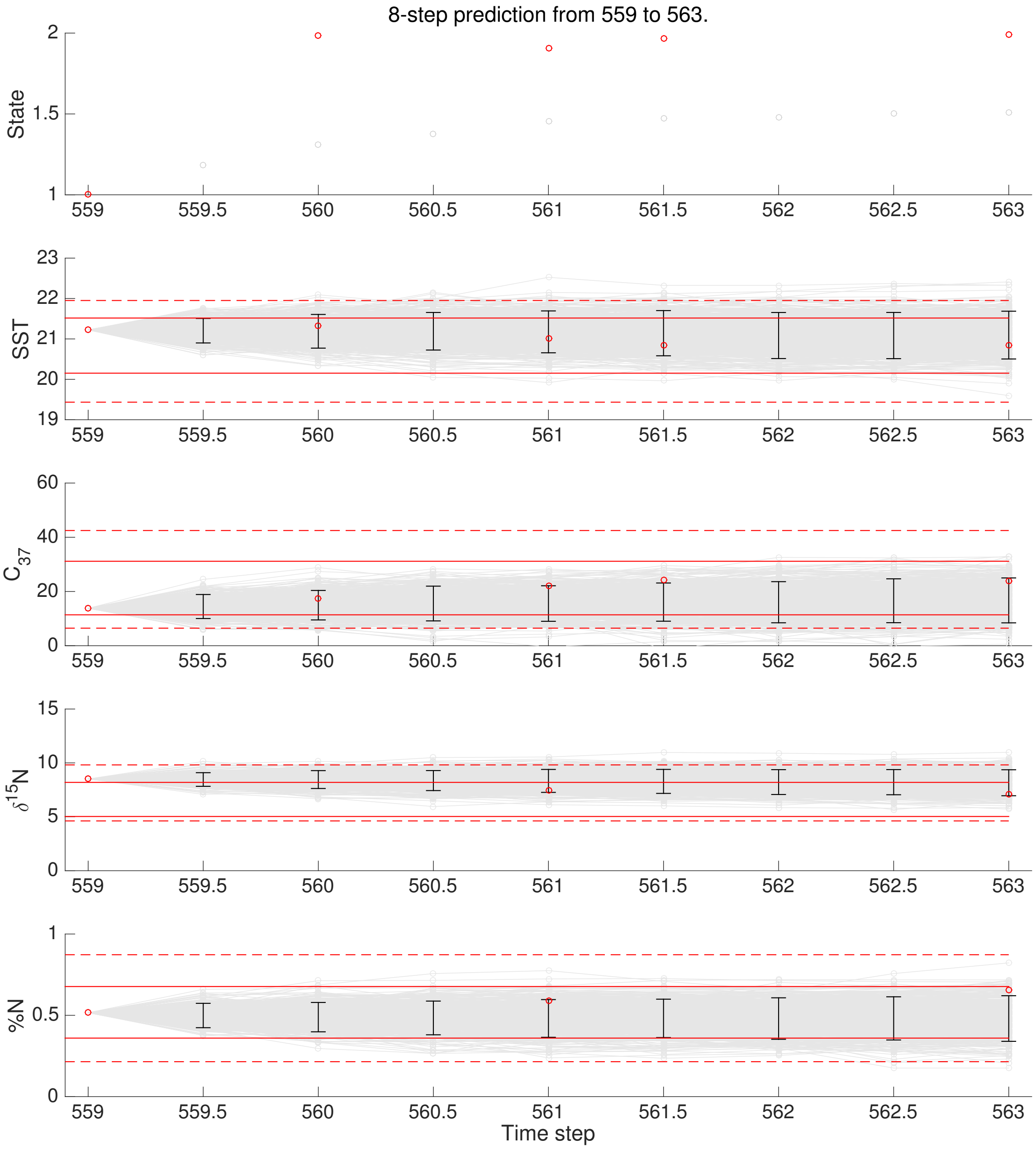

Figure 4.21: [AR-HMM] 8-step prediction from 559 to 563.

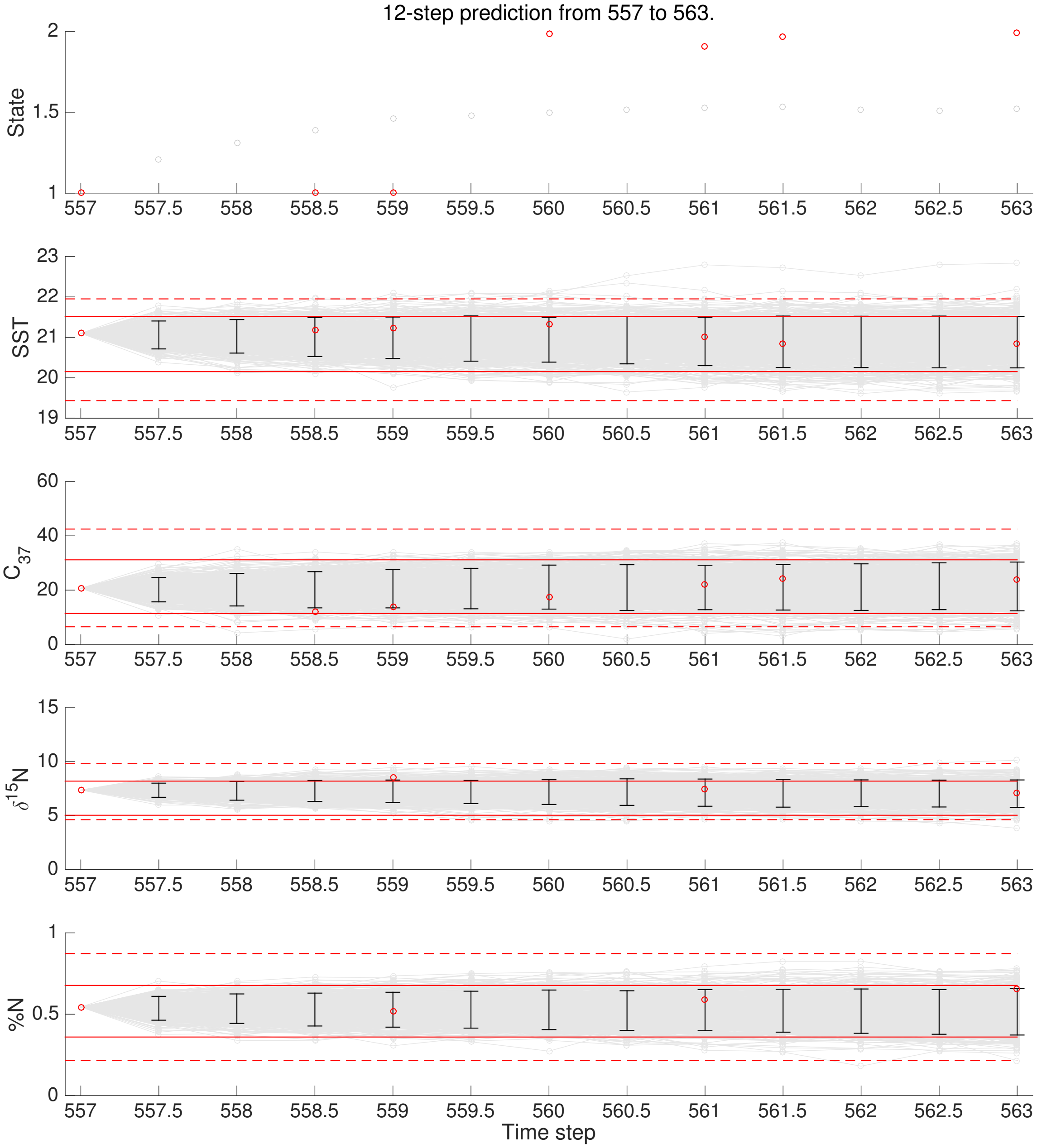

Figure 4.22: [AR-HMM] 12-step prediction from 557 to 563.

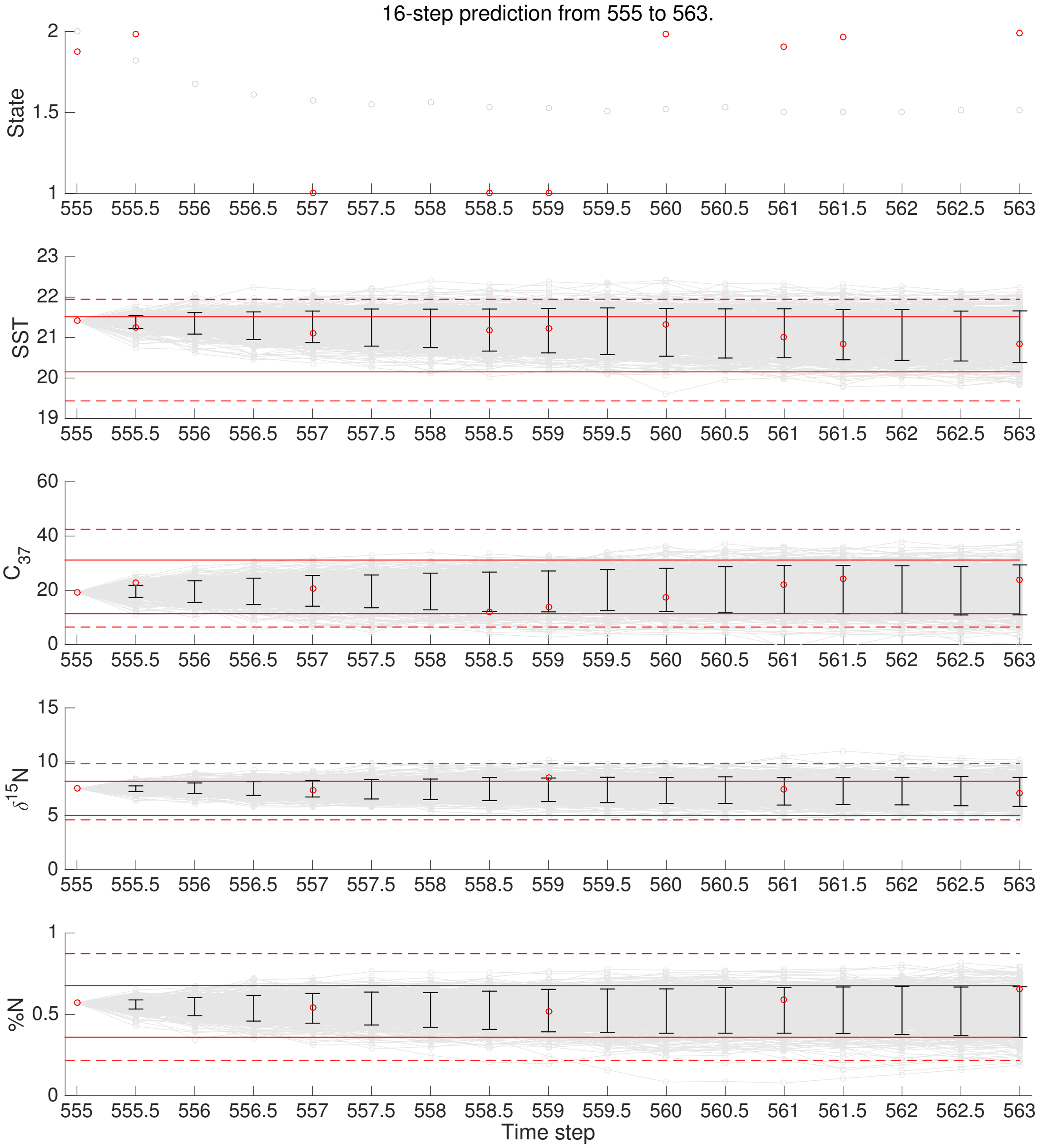

Figure 4.23: [AR-HMM] 16-step prediction from 555 to 563.

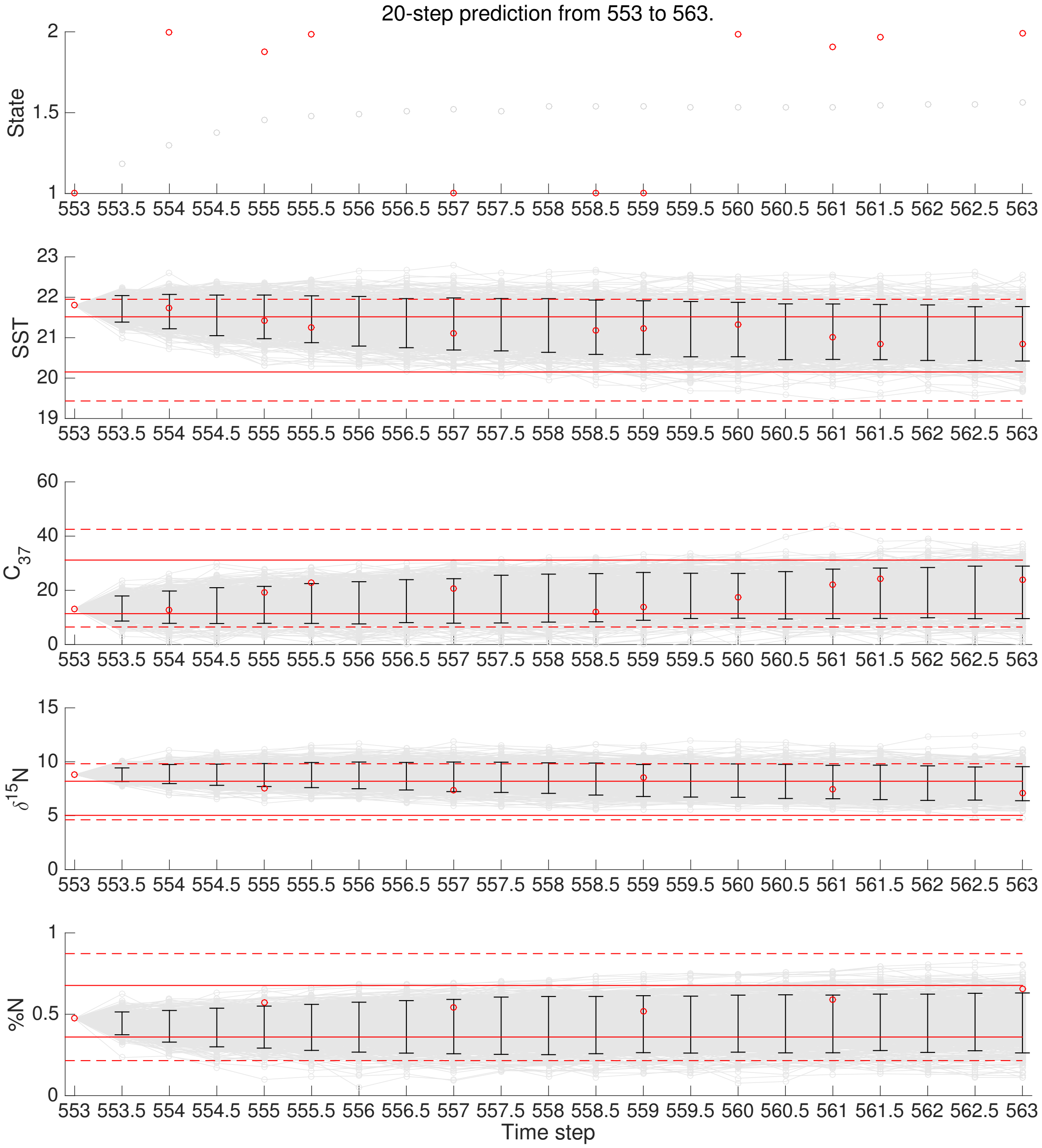

Figure 4.24: [AR-HMM] 20-step prediction from 553 to 563.

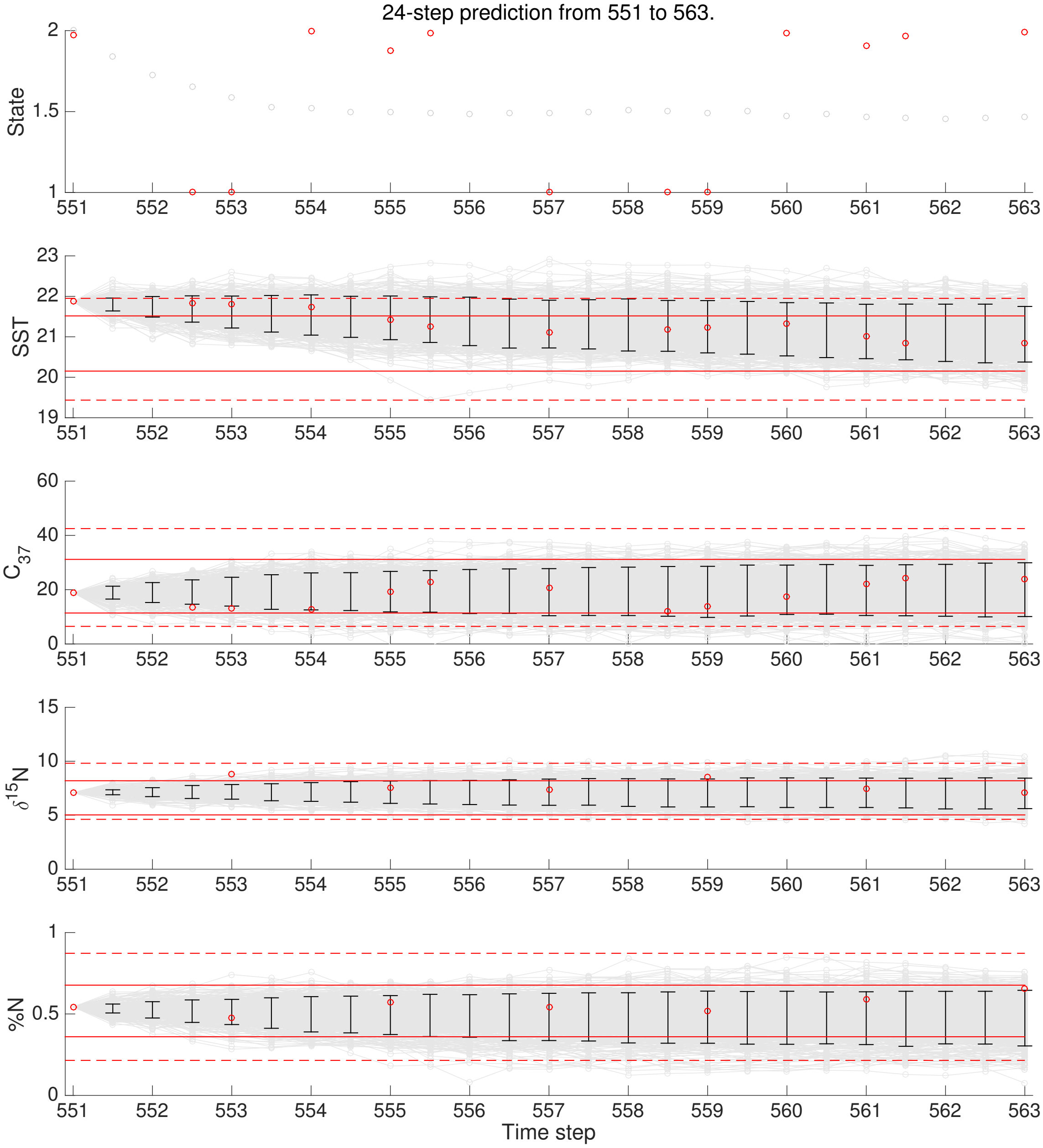

Figure 4.25: [AR-HMM] 24-step prediction from 551 to 563.

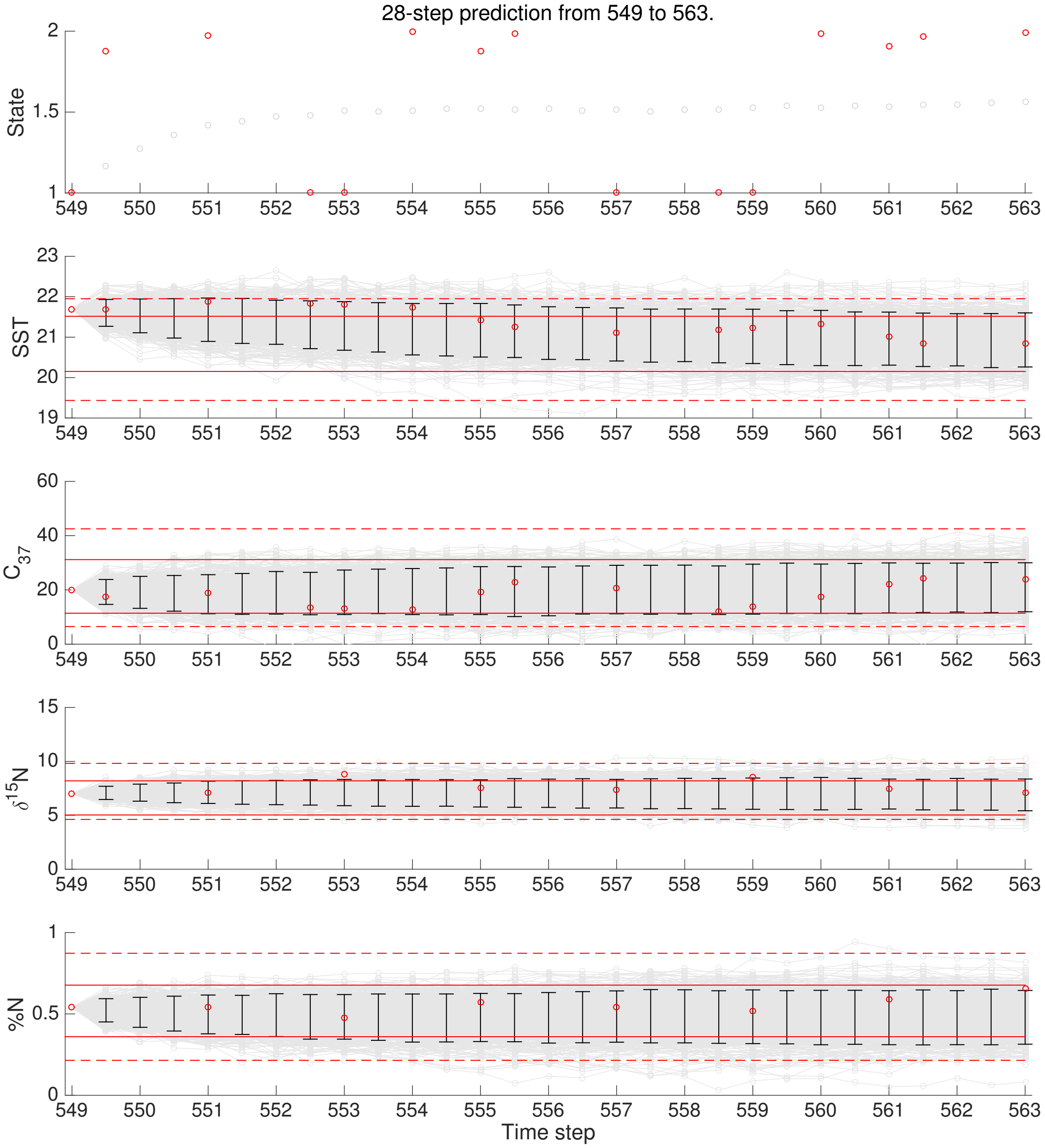

Figure 4.26: [AR-HMM] 28-step prediction from 549 to 563.

Table 4.18: [HMM] MSE of the prediction up to 266. (The numbers in parenthesis represent the percentage over the longest prediction.)

Length of Prediction	1	2	3	4	5	10	16	20	30
SST	0.1665 (50.50)	0.1958 (59.37)	0.2287 (69.37)	0.1594 (48.34)	0.2063 (62.57)	0.1929 (58.51)	0.2913 (88.36)	0.2737 (83.02)	0.3297 (100)
C47	67.7282 (134.04)	61.1064 (120.93)	60.0484 (118.84)	57.1512 (113.11)	57.7126 (114.22)	59.7901 (118.33)	59.0757 (116.91)	55.7505 (110.33)	50.5289 (100)
$\delta^{15}N$	0.6393 (99.75)	0.6543 (102.10)	0.5893 (91.95)	0.7088 (110.60)	0.6540 (102.04)	0.6176 (96.36)	0.6871 (107.21)	0.6596 (102.92)	0.6409 (100)
%N	0.0173 (141.66)	0.0153 (124.93)	0.0149 (121.73)	0.0168 (137.66)	0.0138 (113.21)	0.0152 (124.59)	0.0153 (124.77)	0.0151 (123.78)	0.0122 (100)

Table 4.19: [HMM] Squared bias, variance and MSE of the prediction up to 266.

Length of Prediction		1	2	3	4	5	10	16	20	30
SST	Bias^2	0.1098	0.1186	0.1436	0.1027	0.1235	0.1169	0.1929	0.1776	0.2203
	Variance	0.0568	0.0772	0.0851	0.0567	0.0828	0.0760	0.0985	0.0961	0.1094
	MSE	0.1665	0.1958	0.2287	0.1594	0.2063	0.1929	0.2913	0.2737	0.3297
C47	Bias^2	56.9347	48.8775	46.9825	42.4506	42.1690	45.1391	38.0106	33.2796	28.3141
	Variance	10.7936	12.2289	13.0659	14.7006	15.5436	14.6511	21.0651	22.4709	22.2148
	MSE	67.7282	61.1064	60.0484	57.1512	57.7126	59.7901	59.0757	55.7505	50.5289
$\delta^{15}N$	Bias^2	0.4084	0.3585	0.2397	0.5274	0.2469	0.2728	0.1112	0.0996	0.0314
	Variance	0.2309	0.2958	0.3496	0.1814	0.4071	0.3448	0.5759	0.5600	0.6095
	MSE	0.6393	0.6543	0.5893	0.7088	0.6540	0.6176	0.6871	0.6596	0.6409
%N	Bias^2	0.0140	0.0115	0.0110	0.0123	0.0093	0.0116	0.0094	0.0095	0.0064
	Variance	0.0033	0.0038	0.0039	0.0045	0.0046	0.0037	0.0059	0.0057	0.0058
	MSE	0.0173	0.0153	0.0149	0.0168	0.0138	0.0152	0.0153	0.0151	0.0122

Table 4.20: [HMM] MSE of the prediction up to 563. (The numbers in parenthesis represent the percentage over the longest prediction.)

Length of Prediction	4	8	12	16	20	24	28
SST	0.1890	0.2055	0.1868	0.2028	0.1963	0.1675	0.1540
	(122.73)	(133.43)	(121.25)	(131.65)	(127.46)	(108.76)	(100)
C47	56.5878	49.5813	52.2155	49.4299	44.3488	38.7476	39.9981
	(141.48)	(123.96)	(130.54)	(123.58)	(110.88)	(96.87)	(100)
$\delta^{15}N$	0.7102	0.7476	0.8938	0.8695	0.8148	1.0295	1.1240
	(63.18)	(66.52)	(79.53)	(77.36)	(72.49)	(91.59)	(100)
%N	0.0332	0.0291	0.0344	0.0280	0.0286	0.0281	0.0269
	(123.41)	(108.08)	(128.06)	(104.16)	(106.40)	(104.34)	(100)

Table 4.21: [HMM] Squared bias, variance and MSE of the prediction up to 563.

Length of Prediction		4	8	12	16	20	24	28
SST	Bias^2	0.0248	0.0020	0.0116	0.0002	0.0004	0.0003	0.0006
	Variance	0.1642	0.2035	0.1752	0.2026	0.1960	0.1672	0.1534
	MSE	0.1890	0.2055	0.1868	0.2028	0.1963	0.1675	0.1540
C47	Bias^2	23.4969	11.7083	16.6004	13.3992	7.4904	9.1860	7.4263
	Variance	33.0910	37.8730	35.6151	36.0307	36.8584	29.5616	32.5718
	MSE	56.5878	49.5813	52.2155	49.4299	44.3488	38.7476	39.9981
$\delta^{15}N$	Bias^2	0.0079	0.0443	0.0440	0.1453	0.0873	0.3207	0.4090
	Variance	0.7023	0.7033	0.8499	0.7242	0.7275	0.7087	0.7150
	MSE	0.7102	0.7476	0.8938	0.8695	0.8148	1.0295	1.1240
%N	Bias^2	0.0224	0.0210	0.0240	0.0201	0.0206	0.0195	0.0191
	Variance	0.0108	0.0080	0.0104	0.0079	0.0081	0.0085	0.0078
	MSE	0.0332	0.0291	0.0344	0.0280	0.0286	0.0281	0.0269

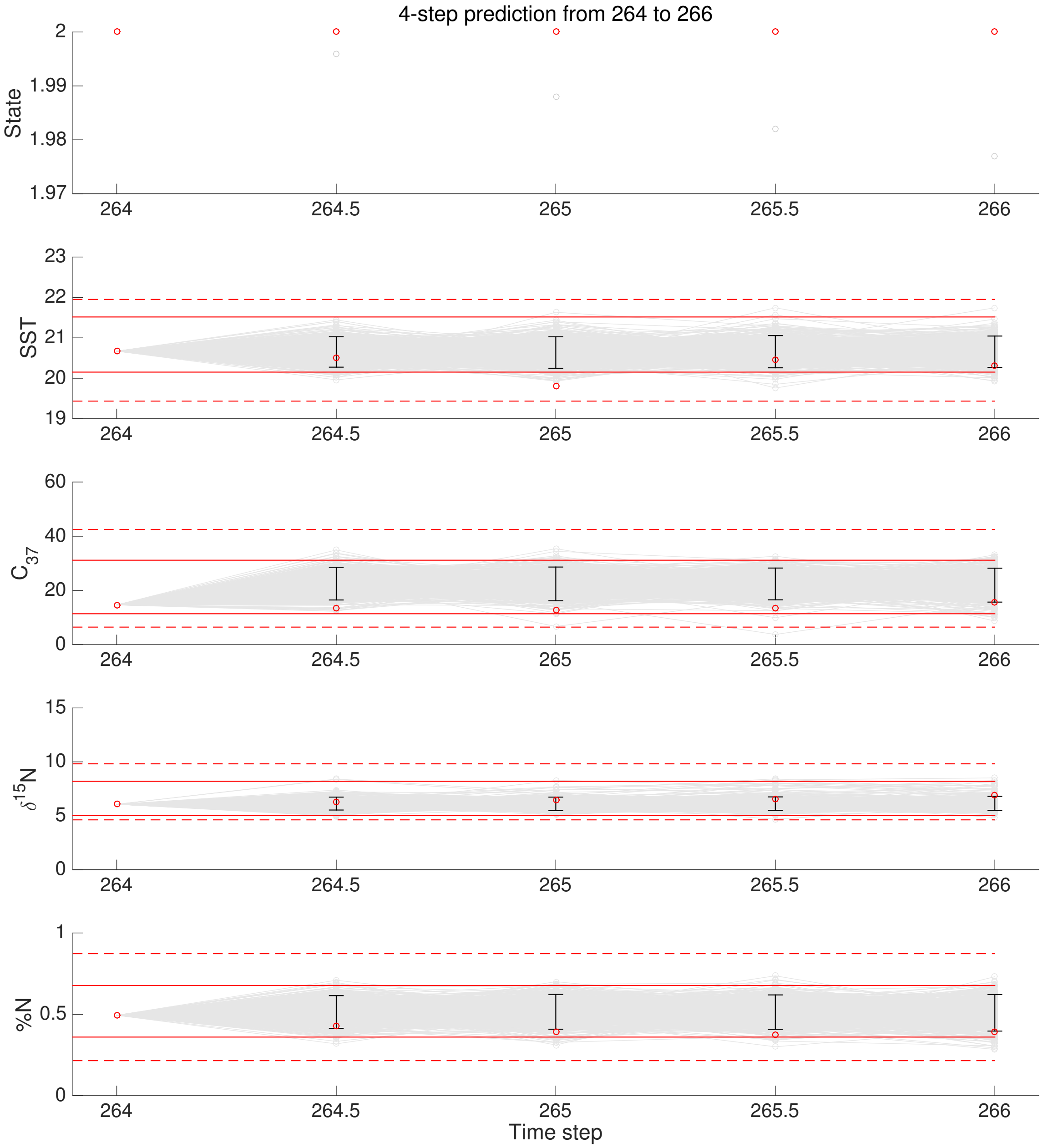

Figure 4.27: [HMM] 4-step prediction from 264 to 266.

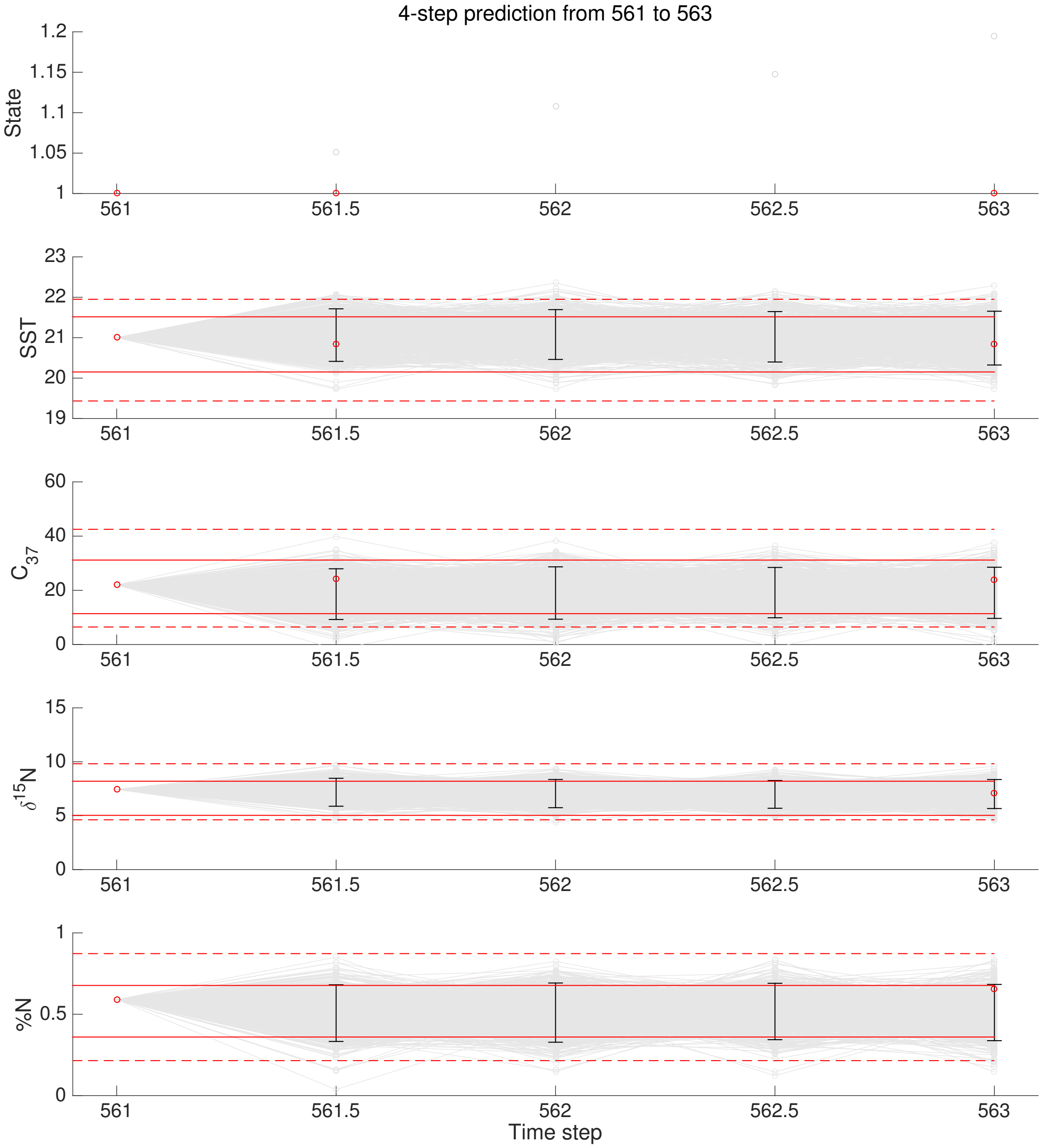

Figure 4.28: [HMM] 4-step prediction from 561 to 563.

4.3.3 Discussion

Four simultaneous and collocated paleoclimate indicators (SST, C_{37}, $\delta^{15}N$, and $\%N$) from the central Peru margin (site MW8708-PC2) were analyzed based on the AR-HMM to understand the interaction among the four proxies and their predictability. We obtained these four proxies from high-resolution records, but the spacings of the records were not regular. Thus, we considered the records as the data set with missing observations, and filled in the missing parts with their expected values using the Kalman filter. The parameter estimation and the data augmentation were iteratively repeated until the EM algorithm converges.

Results based on the AR-HMM confirmed that there are two distinct states at this site, characterized by different levels of variability and predictability. The record switches back and forth between the two states, where one state has high variability with low correlation and another state has low variability with relatively high correlation. Even in the state with relatively high correlations, cross-correlations between the different proxies are much lower than the autocorrelation of each proxy with its previous value. The large autocorrelations may increase the accuracy of predictability, while small cross-correlation indicates that the different proxies are not causally related to one another. Thus, we concluded that the four proxies are not directly related to each other in this location.

Paleoclimate analyses with multiple simultaneous, co-located proxy data often assume that cross-correlations indicate shared causality. The basic cross-correlation analysis based on the HMM indicates the existence of two states, which differ in magnitude of cross-correlation. However, the strength of cross-correlation decreases by allowing for the persistence of variables, i.e. using the AR-HMM. This tells us that simple analyses of cross-correlation cannot be interpreted as true relationships between the different proxies in paleoclimate analyses.

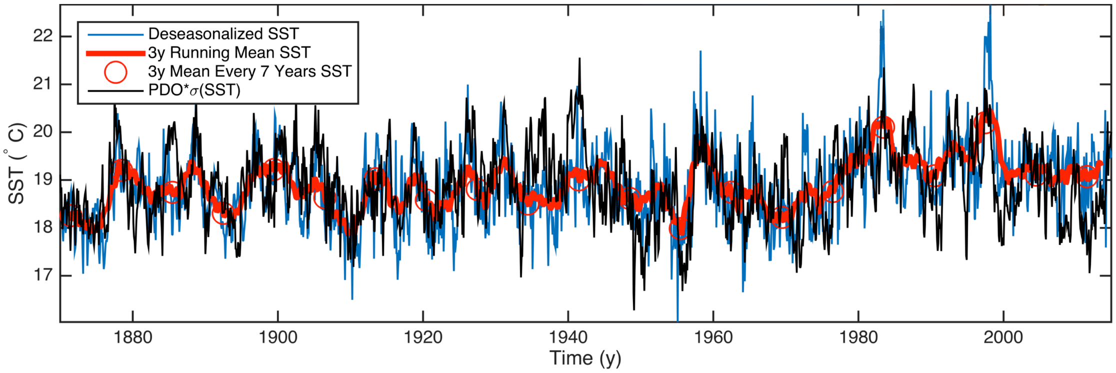

Figure 4.29: Time series of sea surface temperature and rescaled PDO index. The blue line represents the El Niño-dominated temporal variability of the nearest monthly HadISST data after removal of a seasonal cycle (using 1900-2014 climatology). The red line indicates the 3-year running mean of the same data, and the red circles are exemplars of 3-year averages plotted every seventh year. Also, the black line represents the PDO index.

Further analysis on SST was done to examine which ocean variability would be correlated with the paleoclimate proxies at this site. Warming in this region correlates well with warming along the central and eastern equatorial Pacific, and cooling over most of the extratropical Pacific, and weakly correlates with temperatures in other basins. The warming pattern resembles both the El Niño pattern and the Pacific Decadal Oscillation (PDO) pattern [41].

Accordingly, three SST datasets (The HadISST - version 1.1 [162], ERSST version - 4 [79], and HadSST - version 3.1.1[96]) were examined to reveal the relationships with the PDO pattern. Here we only display the results of the HadISST data in Figure 4.29 as the results are similar among the datasets. While some of the biggest El Niño events (1982-3, 1997-8) are still visible in the filtered data, it is evident that the time filtering has removed most of the high-frequency El Niño variability. Deser et al. [41] follow Mantua et al. [118] in tracking the PDO using the first empirical orthogonal function and principal component of North Pacific sea surface temperature after the removal of seasonal and global mean variability. The first principal component of North Pacific (20°N to 70°N, 100°E to 100°W) variability after removing the global mean and seasonal variability is taken as a PDO index. The index captures much of the low-frequency variability near the sediment location, even though the core location is remote from all data in the PDO index and the monthly index, and core location SST have a correlation coefficient of only 0.16. However, the running means over 2 to 22-years have coefficients above 0.53 and a peak just above 0.6 for 7-year averages. Thus, we interpret the dominant variability in the core measurements to be associated the PDO.

CHAPTER FIVE

Conclusion

In this thesis, we focused on analyzing paleoclimate records based on Bayesian statistical tools. We introduced the probability stack, combining multiple benthic $\delta^{18}O$ records in Chapter 2, and investigated the uncertainties in glacial termination timings in Chapter 3. In Chapter 4, we analyzed the multidimensional proxies to find their correlation and underlying state changes. In this final chapter, we summarize these three studies.

In the first study, we presented a newly constructed probabilistic benthic $\delta^{18}O$ stack (Prob-stack) from globally distributed 180 benthic $\delta^{18}O$ records using a profile hidden Markov model. We assumed that each stack value follows a normal distribution and estimated its mean and variance. The mean of the Prob-stack represents the global nature of ice volume signal and deep water temperature, and the variance term describes the variability across the 180 records and the uncertainty of their alignments to the stack. The alignment process assigned age estimates for each record, and we constructed the Prob-stack based on these age estimates. To validate the stack algorithm, we simulated the benthic $\delta^{18}O$ records and the stack and then reconstructed the stack using the simulated records. This validation confirmed that the algorithm accurately returns the stack based on the probabilistic models. The comparisons between the LR04 stack and the means of the Prob-stack showed that the means of the Prob-stack are smoother than the LR04 stack and that there are phase differences at some intervals. The LR04 stack was constructed based on deterministic alignments of the 57 LR04 cores. Each point of the records only contributes to a single time interval of the stack. On the other hand, the Prob-stack was obtained based on age assignment samples of the full 180 cores. Thus, each point of the records can contribute to more than one time interval of the stack depending on the alignment uncertainties, thereby producing a smoother signal of $\delta^{18}O$ values than the LR04 stack. Regarding phase differences, the algorithm used to construct the LR04 stack includes age adjustments after alignments, while the new algorithm does not include any further adjustments after synchronizing the records. This difference, along with stretching or lower compression near the tops of most sediment cores, induces the phase differences. Further analysis on age estimates of the Prob-stack could provide a better understanding of the phase differences and age uncertainties. The novelty of the Prob-stack is to provide the probabilistic distribution of benthic $\delta^{18}O$ values at each point in the stack. In doing so, it captures the time-varying variability of the stack and allows assessment of the uncertainty in ages and lead/lag relationships.

Next, the relative timing of glacial termination between the eastern and western tropical Pacific (EP and WP) was investigated using sea surface temperature (SST) records. We designed the timing algorithm to track uncertainties that originated from each step. First, we obtained SST records from either Mg/Ca of $U_{37}^{k'}$ using the Bayesian calibration and found the age estimates of the records from benthic $\delta^{18}O$ values using the HMM-match algorithm. Next, the Bayesian change point algorithm was employed to find the distribution of a change point, which corresponds to the timing of glacial termination, using the SST time series composed of SST records and age estimates. After obtaining the distribution of a change point for each record, we then compared each finding to the distribution from the reference record in order to find the distribution of the relative timings. The distribution of relative timing determines whether the record of interest leads or lags the reference record. Based on the current SST time series and timing algorithm, we could not conclude whether the EP or WP were lead/lag in relation to each other due to large uncertainties. The novelty of this study lies in the design of combining statistical tools to find relative timing and quantitative assessments of the various sources of uncertainties. This approach can be widely applicable to rigorously analyze lead/lag relationships of other climate proxies as well.

Lastly, we analyzed collocated multidimensional proxies from the central Peru margin to find their correlations and changes of their variabilities. It was challenging to analyze these multidimensional records due to their irregular spacing patterns. We augmented the data sets using both the Kalman filter and the Kalman smoother to have evenly spaced data sets. The parameter estimations of the autoregressive HMM (AR-HMM) and data augmentations were done iteratively until the EM algorithm converged. To prevent the algorithm converging to local maximum estimators instead of the global maximum estimator, we ran the algorithm with 100 different initial values and chose one that achieved the maximum likelihood. The results based on the AR-HMM confirmed that the data sets underwent flickering switches between two states that differ in their variability and persistence. While we found high and low cross-correlation states based on the HMM, different proxy-to-proxy cross-correlations based on the AR-HMM were negligible compared to the autocorrelation with its own lagged term. This finding showed that apparent correlation between SST, C_{37}, $\delta^{15}N$, and $\%N$ is the result of a confounding effect of an external variable. Specifically, the AR-HMM showed that each of these four variables is highly autocorrelated, i.e. predictive of their own future course, but they are not cross-correlated, i.e. each has little impact on the future course of the other. Our subsequent analysis of the relationship of SST in this location is consistent with PDO and indicates that the PDO is a possible driver to SST. This outcome also implies that all four proxies are driven by some outside variables in a similar manner, thereby inducing an apparent correlation between the four proxies, when auto-correlation is ignored, as in the HMM. By its nature, the AR-HMM does not reveal the identity of the common factor, but rather implies that the dynamic system behind this underlying process has a dependence only of its own previous state.

Paleoclimatology analyzes climate changes imprinted on geological records. Uncertainty exists even in the first step of analysis, as it is found beginning in the very first of measurements of proxies and continues throughout all stages. Therefore, it is crucial to consider uncertainty and the variability of results for every step of investigating paleoclimate records. We expect the statistical tools we introduced in this thesis to play an essential role in rigorously analyzing paleoclimate data.

APPENDIX A

Metadata table

Table A.1: Information regarding 57 benthic $\delta^{18}O$ records used to construct the Prob-LR04-stack (site name, file name, latitude, longitude, water depth, period of record, and comments).

Site Name	File Name	Latitude	Longitude	Water Depth	Period of Record [kyr]	Comments
DSDP502	502_LR04age_1.txt	11.4910	-79.3797	3051 (1800 sill)	2.71-2205.28	Divided into multiple files due to age gap
DSDP502	502_LR04age_2.txt	11.4910	-79.3797	3051 (1800 sill)	2287.55-2609.37	
DSDP552	552_LR04age.txt	56.0427	-23.2313	2301	4.28-1326.34	
DSDP607	607_LR04age.txt	41.0012	-32.2313	3427	12-5317.9	
DSDP610	610_LR04age.txt	53.2215	-18.8868	2417	2091.7-3585.8	
ODP658	658_LR04age.txt	20.7492	-18.5808	2263	0.54-710	
ODP659	659_LR04age.txt	18.0772	-21.0262	3071	0-4987.94	
ODP662	662_LR04age_1.txt	-1.3902	-11.7392	3814	1550-1737.79	Divided into multiple files due to age gap
ODP662	662_LR04age_2.txt	-1.3902	-11.7392	3814	2271.39-3550	
ODP664	664_LR04age.txt	0.1073	-23.2275	3806	5.31-1250	
ODP665	ODP665.txt	2.9512	-19.6678	4741	2153-2565	
ODP677	677_LR04age_1.txt	1.2023	-83.7370	3472	12.83-2483.96	Divided into multiple files due to changes in sampling resolution
ODP677	677_LR04age_2.txt	1.2023	-83.7370	3472	2512.05-2597.93	
ODP704	704_LR04age_1.txt	-46.8790	7.4208	2532	1059.65-2148.59	Divided into multiple files due to age gap
ODP704	704_LR04age_2.txt	-46.8790	7.4208	2532	2374.91-3966.29	
ODP722	722_LR04age.txt	16.6218	59.7953	2022	1.99-3850.4	
ODP758	758_LR04age.txt	5.3842	90.3612	2923	4.13-3750	
ODP806	806_LR04age.txt	0.3190	159.3610	2520	0-649.97	

Table A.1 – continued from previous page

Site Name	File Name	Latitude	Longitude	Water Depth	Period of Record [kyr]	Comments
ODP846	846_LR04age.txt	-3.0949	-90.8180	3296	3.65-5334.91	
ODP849	849_LR04age_1.txt	0.1823	-110.5197	3839	3.41-3731.9	Divided into multiple files due to changes in sampling resolution
ODP849	849_LR04age_2.txt	0.1823	-110.5197	3839	3732.26-4966.71	
ODP925	925_LR04age_1.txt	4.2042	-43.4889	3041	0-527.05	Divided into multiple files due to changes in sampling resolution
ODP925	925_LR04age_2.txt	4.2042	-43.4889	3041	527.83-1186.84	
ODP925	925_LR04age_3.txt	4.2042	-43.4889	3041	1192.35-4375.52	
ODP925	925_LR04age_4.txt	4.2042	-43.4889	3041	4379.78-5096.59	
ODP927	927_LR04age_1.txt	5.4627	-44.4805	3315	6.45-3432.58	Divided into multiple files due to changes in sampling resolution
ODP927	927_LR04age_2.txt	5.4627	-44.4805	3315	3506.51-4166.55	
ODP927	927_LR04age_3.txt	5.4627	-44.4805	3315	4519.57-4947.28	
ODP928	928_LR04age.txt	5.4553	-43.7480	4011	4.47-3347.31	
ODP929	929_LR04age.txt	5.9762	-43.7399	4356	0-3360	
ODP980	980_LR04age.txt	55.4848	-14.7022	2172	0-998.46	
ODP981	981_LR04age.txt	55.4772	-14.6508	2173	859-4580	
ODP982	982_LR04age.txt	57.5167	-15.8667	1135	0-5333.83	
ODP983	983_LR04age_1.txt	60.4033	-23.6407	1983	0.99-312.58	Divided into multiple files due to changes in sampling resolution
ODP983	983_LR04age_2.txt	60.4033	-23.6407	1983	312.84-717.11	
ODP983	983_LR04age_3.txt	60.4033	-23.6407	1983	717.38-1387.41	
ODP983	983_LR04age_4.txt	60.4033	-23.6407	1983	1387.63-1992.26	

Table A.1 – continued from previous page

Site Name	File Name	Latitude	Longitude	Water Depth	Period of Record [kyr]	Comments
ODP984	984_LR04age_1.txt	61.4251	-24.0825	1649	0.02-176.37	Divided into multiple files due to changes in sampling resolution
ODP984	984_LR04age_2.txt	61.4251	-24.0825	1649	196.82-1721.44	
ODP984	984_LR04age_3.txt	61.4251	-24.0825	1649	1754.95-1810	
ODP999	999_LR04age.txt	12.7433	-78.7400	2828	1652.78-5266.99	
ODP1012	1012_LR04age.txt	32.2828	-118.3830	1772	0-1810	
ODP1020	1020_LR04age.txt	41.0090	-126.4340	3040	2.78-1670	
ODP1085	1085_LR04age.txt	-29.3743	13.9902	1713	2100-4898.23	
ODP1087	1087_LR04age.txt	-31.4650	15.3108	1372	0.14-340	
ODP1088	1088_LR04age.txt	-41.1361	13.5628	2082	12.21-1220	
ODP1089	1089_LR04age_1.txt	-40.9364	9.8941	4620	0-193.95	Divided into multiple files due to changes in sampling resolution
ODP1089	1089_LR04age_2.txt	-40.9364	9.8941	4620	216.19-283.14	
ODP1089	1089_LR04age_3.txt	-40.9364	9.8941	4620	311.6-649.8	
ODP1090	1090_LR04age.txt	-42.9137	8.8997	3700	0-2800	
ODP1092	ODP1092.txt	-46.4118	7.0799	1973	2680-4280	
ODP1123	1123_LR04age.txt	-41.7860	-171.4990	3290	0-2990	
ODP1143	1143_LR04age.txt	9.3620	113.2851	2772	5.66-5050	
ODP1146	1146_LR04age_1.txt	19.4567	116.2728	2092	0-313.99	Divided into multiple files due to changes in sampling resolution
ODP1146	1146_LR04age_2.txt	19.4567	116.2728	2092	319.28-477.85	
ODP1148	1148_LR04age.txt	18.8362	116.5655	3295	0-5316.65	

Table A.1 – continued from previous page

Site Name	File Name	Latitude	Longitude	Water Depth	Period of Record [kyr]	Comments
GeoB1032	GeoB1032_LR04age.txt	-22.9100	6.0317	2500	1.42-380	
GeoB1034	GeoB1034_LR04age.txt	-21.7280	5.4258	3772	3.1-930	
GeoB1035	GeoB1035_LR04age.txt	-21.5942	5.0300	4453	1.31-426	
GeoB1041	GeoB1041_LR04age.txt	-3.4750	-7.5941	4034	0.35-575	
GeoB1101	GeoB1101_LR04age.txt	1.6633	-10.9767	4567	0.77-542	
GeoB1105	GeoB1105_LR04age.txt	-1.6650	-12.4280	3230	0-363.71	
GeoB1113	GeoB1113_LR04age.txt	-5.7540	-11.0362	2374	0-350	
GeoB1117	GeoB1117_LR04age.txt	-3.8080	-14.7200	3984	0-362	
GeoB1211	GeoB1211_LR04age.txt	-24.4730	7.5360	4089	0.32-667	
GeoB1214	GeoB1214_LR04age.txt	-24.6900	7.2400	3210	2.09-450	
GeoB1312	GeoB1312_LR04age.txt	-31.6617	-29.6567	3436	9.1-448.74	
GeoB1505	GeoB1505_LR04age.txt	2.2700	-33.0100	3705	1.3-419.97	
MD95-2042	MD952042_LR04age.txt	37.7990	-10.1665	3146	0-160	
PC-72	PC72_LR04age.txt	0.1130	-139.4000	4298	0.1-1010	
RC13-110	RC13110_LR04age.txt	-0.0970	-95.6500	3231	0.1-781	
RC13-229	RC13229_LR04age.txt	-25.4900	11.3070	4191	0-708.35	
V19-28	V1928_LR04age.txt	-2.3667	-84.6500	2720	0-435	
V19-30	V1930_LR04age.txt	-3.3833	-83.3500	3091	2.88-344.44	
V21-146	V21146_LR04age.txt	37.6800	163.0300	3968	10.19-530	

Table A.2: Information regarding 57 benthic $\delta^{18}O$ records used to construct the Prob-LR04-stack (site name, reference name, and reference link).

Site Name	Reference Name	Reference Link
DSDP502	deMenocal et al. (1992)	doi:10.1029/92PA00420
DSDP552	Shackleton and Hall (1984)	doi:10.2973/dsdp.proc.81.116.1984
DSDP607	Ruddiman et al. (1989); Raymo et al. (1989); Raymo et al. (1992); Lisiecki and Raymo (2005)	doi:10.1029/PA004i004p00353; doi:10.1029/PA004i004p00413; doi:10.1029/92PA01609; doi:10.1029/2004PA001071
DSDP610	Raymo et al. (1992)	doi:10.1029/92PA01609
ODP658	Tiedemann (1991)	http://epic.awi.de/17863/
ODP659	Tiedemann et al. (1994)	doi:10.1029/94PA00208
ODP662	Lisiecki and Raymo (2005)	doi:10.1029/2004PA001071
ODP664	Raymo et al. (1997)	doi:10.1029/97PA01019
ODP665	Curry and Miller (1989)	doi:10.2973/odp.proc.sr.108.134.1989
ODP677	Shackleton et al. (1990)	doi:10.1017/S0263593300020782
ODP704	Hodell and Venz (1992)	doi:10.1029/AR056p0265
ODP722	Clemens et al. (1996)	doi:10.1126/science.274.5289.943
ODP758	Chen et al. (1995)	doi:10.1029/94PA02290
ODP806	Berger et al. (1993)	doi:10.2973/odp.proc.sr.130.023.1993
ODP846	Mix et al. (1995a); Shackleton et al.(1995)	doi:10.2973/odp.proc.sr.138.160.1995; doi:10.2973/odp.proc.sr.138.117.1995
ODP849	Mix et al. (1995b)	doi:10.2973/odp.proc.sr.138.120.1995

Table A.2 – continued from previous page

Site Name	Reference Name	Reference Link
ODP925	Bickert et al. (1997); Billups et al. (1998); Franz (1999)	doi:10.2973/odp.proc.sr.154.110.1997; doi:10.1029/97PA02995; doi:10.3289/GEOMAR_Report_084_1999
ODP927	Bickert et al. (1997); Franz (1999)	doi:10.2973/odp.proc.sr.154.110.1997; doi:10.3289/GEOMAR_Report_084_1999
ODP928	Franz (1999)	doi:10.3289/GEOMAR_Report_084_1999
ODP929	Bickert et al. (1997); Billups et al. (1998); Franz (1999)	doi:10.2973/odp.proc.sr.154.110.1997; doi:10.1029/97PA02995; doi:10.3289/GEOMAR_Report_084_1999
ODP980	Oppo et al. (1998); McManus et al. (1999); Flower et al. (2000)	doi:10.1126/science.279.5355.1335; doi:10.1126/science.283.5404.971; doi:10.1029/1999PA000430
ODP981	Mc Intyre et al. (1999); Raymo et al. (2004)	doi:10.1029/1998PA900005; doi:10.1029/2003PA000921
ODP982	Venz et al. (1999); Venz and Hodell (2002); Lisiecki and Raymo (2005)	doi:10.1029/1998PA900013; doi:10.1016/S0031-0182(01)00496-5; doi:10.1029/2004PA001071
ODP983	Mc Intyre et al. (1999); Raymo et al. (2004)	doi:10.1029/1998PA900005; doi:10.1029/2003PA000921
ODP984	Raymo et al. (2004)	doi:10.1029/2003PA000921
ODP999	Haug and Tiedemann (1998)	doi:10.1038/31447
ODP1012	Herbet et al. (2001); Z. Liu, Personal Communication (2002)	doi:10.1126/science.1059209
ODP1020	Herbet et al. (2001); Z. Liu, Personal Communication (2002)	doi:10.1126/science.1059209
ODP1085	D. Andreasen, Personal Communication 2001	
ODP1087	Pierre et al. (2001)	doi:10.2973/odp.proc.sr.175.230.2001

Table A.2 – continued from previous page

Site Name	Reference Name	Reference Link
ODP1088	Hodell et al. (2003)	doi:10.2973/odp.proc.sr.177.120.2003
ODP1089	Hodell et al. (2001)	doi:10.1016/S0012-821X(01)00430-7
ODP1090	Venz and Hodell (2002)	doi:10.1016/S0031-0182(01)00496-5
ODP1092	Andersson et al. (2002)	doi:10.1016/S0031-0182(01)00494-1
ODP1123	Hall et al. (2001); Harris (2002)	doi:10.1038/35090552; doi:10.2973/odp.proc.sr.181.203.2002
ODP1143	Tian et al. (2002)	doi:10.1016/S0012-821X(02)00923-8
ODP1146	S. Clemens, Personal Communication (2002)	
ODP1148	Jian et al. (2003)	doi:10.1016/S0031-0182(03)00259-1
GeoB1032	Bickert and Wefer (1996)	doi:10.1007/978-3-642-80353-6_30
GeoB1034	Bickert and Wefer (1996)	doi:10.1007/978-3-642-80353-6_30
GeoB1035	Bickert and Wefer (1996)	doi:10.1007/978-3-642-80353-6_30
GeoB1041	Bickert and Wefer (1996)	doi:10.1007/978-3-642-80353-6_30
GeoB1101	Bickert and Wefer (1996)	doi:10.1007/978-3-642-80353-6_30
GeoB1105	Bickert and Wefer (1996)	doi:10.1007/978-3-642-80353-6_30
GeoB1113	Sarnthein et al. (1994)	doi:10.1029/93PA03301
GeoB1117	Bickert and Wefer (1996)	doi:10.1007/978-3-642-80353-6_30
GeoB1211	Bickert and Wefer (1996)	doi:10.1007/978-3-642-80353-6_30
GeoB1214	Bickert and Wefer (1996)	doi:10.1007/978-3-642-80353-6_30
GeoB1312	Hale and Pflaumann (1999)	doi:10.1007/978-3-642-58646-0_2

Table A.2 – continued from previous page

Site Name	Reference Name	Reference Link
GeoB1505	Zabel et al. (1999)	doi:10.1029/1999PA900027
MD95-2042	Shackleton et al. (2000)	doi:10.1029/2000PA000513
PC-72	Murray et al. (2000)	doi:10.1029/1999PA000457
RC13-110	Mix et al. (1991); Imbrie et al. (1992)	doi:10.1029/90PA02303; doi:10.1029/92PA02253
RC13-229	Oppo et al. (1990)	doi:10.1029/PA005i001p00043
V19-28	Ninkovitch and Shackleton (1975)	doi:10.1016/0012-821X(75)90156-9
V19-30	Shackleton and Pisias (1985)	doi:10.1029/GM032p0303
V21-146	Hovan et al. (1991)	doi:10.1029/91PA00559

Table A.3: Information regarding an additional 123 benthic $\delta^{18}O$ records used to construct the Prob-stack (site name, file name, latitude, longitude, water depth, depth reference and period of record).

Site Name	File Name	Latitude	Longitude	Water Depth	Depth reference	Period of Record [kyr]
82-24-23PC	82-24-23PC.txt	43.0000	-31.0000	3406		9.33-278
AII107-131	AII107-131.txt	-30.8800	-38.0483	2925		4-302
C9001C	C9001C.txt	41.1773	142.2014	1180	mbsf	0-750
DSDP214	DSDP214.txt	-11.3400	88.7200	1665	mbsf	2175-4410
DSDP548	DSDP548.txt	48.9158	-12.1640	1251	Not Specified	3018-3690
DSDP590	DSDP590.txt	-31.1670	163.3585	1299	mbsf	2710-4460
DSDP593	DSDP593.txt	-40.5087	167.6747	1080	N/A	4-5200
DSDP594	DSDP594.txt	-45.5235	174.9480	1204	N/A	4-1000
DSDP607	DSDP607.txt	41.0000	-32.0000	3427	mcd	255-1910
ELT49.019-PC	ELT49.019-PC.txt	-43.8870	90.1000	3057		3-298
EW9209-1JPC	EW9209-1JPC.txt	5.9067	-44.1950	4056		0-530
EW9209-2JPC	EW9209-2JPC.txt	5.6000	-44.5000	3528		0-415
EW9209-3JPC	EW9209-3JPC.txt	5.3000	-44.3000	3288		0-448
EW9504-02	EW9504-02.txt	31.2500	-117.5833	2042		0-200
EW9504-03	EW9504-03.txt	32.0667	-117.3667	1299		0-170
EW9504-04	EW9504-04.txt	32.2833	-118.4000	1759		1-200
EW9504-05	EW9504-05.txt	32.4833	-118.1333	1818		2-110
EW9504-08	EW9504-08.txt	32.8000	-118.8000	1442		0-130

Table A.3 – continued from previous page

Site Name	File Name	Latitude	Longitude	Water Depth	Depth reference	Period of Record [kyr]
EW9504-09	EW9504-09.txt	32.8667	-119.9667	1194		0-135
GeoB1112	GeoB1112.txt	-5.7783	-10.7500	3125		1-271
GeoB1118	GeoB1118.txt	-3.5600	-16.4317	4675		0-387
GeoB1710	GeoB1710.txt	-23.4317	11.6983	2987		2-247
GeoB3004	GeoB3004.txt	14.6050	52.9200	1803		0-190
GeoB3327-5	GeoB3327.txt	-43.2400	-79.9917	3531		7-513
GeoB3388-1	GeoB3388.txt	-25.2200	-75.5250	3558		10-1100
GeoB3935	GeoB3935.txt	12.6133	-59.3867	1558		0-176
GeoB3938	GeoB3938.txt	12.2583	-58.3300	1972		0-244
GeoB4216	GeoB4216.txt	30.6300	-12.3967	2324		0-256
GIK12392-1	GIK12392.txt	25.1717	-16.8450	2575		0-150
GIK13519-1	GIK13519_1.txt	5.6700	-19.8517	2862		0-750
GIK13519-1	GIK13519_2.txt	5.6700	-19.8517	2862		0-140
GIK15612	GIK15612.txt	44.3600	-26.5433	3050		4-144
GIK15627	GIK15627.txt	29.1667	-12.0867	1024		7-268
GIK15637	GIK15637.txt	27.0050	-18.9867	3849		7-420
GIK16772	GIK16772.txt	-1.3500	-11.9617	3912		17-334
GIK17049	GIK17049.txt	55.2600	-26.7250	3331		0-334
GIK23414	GIK23414.txt	53.5367	-20.2883	2196		0-250

Table A.3 – continued from previous page

Site Name	File Name	Latitude	Longitude	Water Depth	Depth reference	Period of Record [kyr]
GIK23415	GIK23415.txt	53.1783	-19.1450	2472		0-250
INMD114	INMD114.txt	-8.8000	-138.9900	3135		4-312
LV28-42-4	LV28-42-4.txt	51.7148	150.9855	1041		1-346
M16772	M16772.txt	-1.3500	-11.9667	3912		0-331
M35027	M35027.txt	17.6483	-67.1667	1814		10-350
MD01-2378	MD01-2378_1.txt	-13.0825	121.7880	1783		1-461
MD01-2378	MD01-2378_2.txt	-13.0825	121.7880	1783		23.9-63.9
MD01-2415	MD01-2415.txt	53.9515	149.9586	822		1-1090
MD01-2416	MD01-2416.txt	51.2680	167.7250	2317		0-450
MD01-2443	MD01-2443_1.txt	37.8800	-10.1800	2925		193-423
MD01-2443	MD01-2443_2.txt	37.8815	-10.1762	2952		0-433
MD01-2446	MD01-2446.txt	39.0558	-12.6240	3570		305-545
MD01-2448	MD01-2448.txt	44.7798	-11.2745	3460		0-1183
MD02-2575	MD02-2575_1.txt	29.0017	-87.1188	847		1.2-300
MD02-2575	MD02-2575_2.txt	29.0017	-87.1189	847		0-400
MD02-2588	MD02-2588.txt	-41.3317	25.8283	2907		0-353
MD03-2692	MD03-2692.txt	46.8333	-9.5167	4064		7-350
MD03-2699	MD03-2699.txt	39.0367	-10.6605	1865		300-580
MD03-2705	MD03-2705.txt	18.0968	-21.1532	3085		0-1108

Table A.3 – continued from previous page

Site Name	File Name	Latitude	Longitude	Water Depth	Depth reference	Period of Record [kyr]
MD04-2881	MD04-2881.txt	22.2000	63.0800	2387		8-762
MD05-2920	MD05-2920.txt	-2.8633	144.5344	1843		1-388
MD06-3018	MD06-3018.txt	-23.0000	166.1500	2470		0-1557
MD12-3409	MD12-3409.txt	-1.1012	89.2687	2429		0-1757
MD95-2042	MD95-2042.txt	37.7998	-10.1665	3146		0-417
MD96-2048	MD96-2048.txt	-26.1660	34.0200	660		0-790
MD96-2080	MD96-2080.txt	-36.3200	19.4700	2488		0-450
MD96-2086	MD96-2086.txt	-25.8100	12.1300	3606		10-243
MD96-2098	MD96-2098.txt	-25.5900	12.6300	2909		6-193
MD97-2120	MD97-2120.txt	-45.5343	174.9308	1210		2-341
MD97-2125	MD97-2125.txt	-22.5667	161.7333	1684		5-362
MV0502-4JC	MV0502_1.txt	-50.3333	-148.1333	4286		23-210
MV0502-4JC	MV0502_2.txt	-50.3333	-148.1333	4286		441-679
MV0502-4JC	MV0502_3.txt	-50.3333	-148.1333	4286		1575-2975
ODP1011	ODP1011.txt	31.2833	-117.6333	2033 (1600)	mcd	0-340
ODP1014	ODP1014_1.txt	32.8339	-119.9810	1165.8	mcd	386-916
ODP1014	ODP1014_2.txt	32.8341	-119.9813	1177	mcd	0-187
ODP1018	ODP1018.txt	36.9833	-123.2833	2476	N/A	0-188
ODP1019	ODP1019.txt	41.6828	-124.9330	988	mcd	0-255

Table A.3 – continued from previous page

Site Name	File Name	Latitude	Longitude	Water Depth	Depth reference	Period of Record [kyr]
ODP1058	ODP1058.txt	31.6898	-75.4300	2984	N/A	69-144
ODP1082	ODP1082.txt	-21.0939	11.8206	1279.3	mcd	1711-3625
ODP1083	ODP1083.txt	-20.8947	11.2179	2178.1	mcd	2038-2676
ODP1143	ODP1143.txt	9.3600	113.2800	2772	mcd	0-5021
ODP1146	ODP1146.txt	19.4500	116.2700	2092	mcd	4.1-5049
ODP1147	ODP1147.txt	18.8352	116.5546	3245.5	mcd	6-5324
ODP1168	ODP1168.txt	-42.6097	-144.4128	2463	N/A	8-930
ODP1170	ODP1170.txt	-47.1506	-146.0497	2705	N/A	0-450
ODP1172	ODP1172.txt	-43.9597	-49.9283	2622	N/A	0-411
ODP1208	ODP1208.txt	36.1000	158.5000	3346	mbsf	1760-3700
ODP1209	ODP1209.txt	32.6518	158.5059	2387	mbsf	0-350
ODP1236	ODP1236.txt	-21.3590	-81.4361	1323	mcd	2322-5258
ODP1237	ODP1237.txt	-16.0070	-76.3781	3212	N/A	4160-5338
ODP1239	ODP1239.txt	-0.6720	-82.0808	1415	N/A	2700-4964
ODP1241	ODP1241_1.txt	5.8428	-86.4445	2027	cmcd	0-2129
ODP1241	ODP1241_2.txt	5.8428	-86.4445	2027	N/A	2443-5691
ODP723	ODP723.txt	18.0518	57.6087	816.3	mbsf	0-1500
ODP724	ODP724.txt	18.4625	57.7865	603	N/A	6-352
ODP806	ODP806.txt	0.3190	159.3610	2520	ambsf	6.5-1389

Table A.3 – continued from previous page

Site Name	File Name	Latitude	Longitude	Water Depth	Depth reference	Period of Record [kyr]
ODP871	ODP871.txt	5.5500	172.3400	1255	mbsf	0-537
ODP926	ODP926.txt	3.7180	-42.9080	3598	mcd	0-4939
ODP928	ODP928.txt	5.5000	-44.8000	4010		0-3347
ODP959	ODP959.txt	3.6278	-2.7353	2090	N/A	0-981
ODP978	ODP978.txt	36.2311	-2.0570	438	Not Specified	3000-3627
ODP980	ODP980.txt	55.4848	-14.7022	2172	mcd	0-191
PC-S2	PC-S2.txt	33.3625	159.1283	3107		6-526
PS2561-2	PS2561-2.txt	-41.8583	28.5417	4465		0-198
SU92-03	SU92-03.txt	43.1958	-10.1130	3005		0-152
TR163-31P	TR163-31P.txt	-3.5833	-83.9500	3205		0-234
TT013-PC18	TT013-PC18.txt	-1.8339	-139.7011	4354		2-780
TTN057-6-PC4	TTN057-6-PC4.txt	-42.9213	8.6000	3751	mcd	1-1104
U1308	U1308.txt	49.8800	-24.2400	3883	mcd	0-1513
U1313	U1313_1.txt	41.0000	-32.9573	3426	mcd	2414-3331
U1313	U1313_2.txt	41.0000	-32.9570	3411	mcd	788-913
U1313	U1313_3.txt	41.0000	-32.9570	3411	amcd	600-700
U1313	U1313_4.txt	41.0000	-32.9573	3426	rmcd	356-549
U1314	U1314_1.txt	56.3640	-27.8880	2800	mcd	403-775
U1314	U1314_2.txt	56.3600	-27.8800	2820	mcd	779-1070

Table A.3 – continued from previous page

Site Name	File Name	Latitude	Longitude	Water Depth	Depth reference	Period of Record [kyr]
U1343	U1343_1.txt	54.5567	176.8167	1950	CCSF-A	7-1190
U1343	U1343_2.txt	54.5567	176.8167	1950		1190-2350
V19-27	V19-27.txt	-0.4670	-82.0700	1373		0-377
V22-108	V22-108.txt	-43.1800	-3.2500	4171		0-237
V29-135	V29-135.txt	-19.7000	8.8830	2675		0-300
V29-202	V29-202.txt	-61.0000	-21.0000	2658		0-200
V30-97	V30-97.txt	41.0000	-32.9300	3371		0-250
Y74-2-22PC	Y74-2-22PC.txt	23.7300	-112.4380	3054		0-661
MD06-2990	MD06-2990.txt	-42.3080	169.8800	943		67.94-350.19
SO136-003	SO136-003.txt	-42.2957	169.8780	944		2.87-67.09
MD06-2986	MD06-2986.txt	-43.4485	167.9000	1477		0.48-350

Table A.4: Information regarding an additional 123 benthic $\delta^{18}O$ records used to construct the Prob-stack (site name, file name, species, offset, and comments). Note that (1) indicates that the offset is applied by author of the reference and (2) indicates that the offset is applied in this study.

Site Name	File Name	Species	Offset	Comments
82-24-23PC	82-24-23PC.txt	C.wuellerstorfi/ Uvigerina spp	0.64 (1)	
AII107-131	AII107-131.txt	C.wuellerstorfi	0.64 (2)	
C9001C	C9001C.txt	U.akitaensis/ U.peregrina	(1)	
DSDP214	DSDP214.txt	C.wuellerstorfi	0.64 (2)	
DSDP548	DSDP548.txt	C.mundulus	Corrected to LR04 stack values (1)	
DSDP590	DSDP590.txt	U.peregrina	–	
DSDP593	DSDP593.txt	Uvigerina spp	–	
DSDP594	DSDP594.txt	Uvigerina spp	–	
DSDP607	DSDP607.txt	C.wuellerstorfi/ Uvigerina spp	0.64 (1)	
ELT49.019-PC	ELT49.019-PC.txt	Cibicidoides spp	0.64 (2)	
EW9209-1JPC	EW9209-1JPC.txt	C.wuellerstorfi	0.64 (2)	
EW9209-2JPC	EW9209-2JPC.txt	C.wuellerstorfi	0.64 (2)	
EW9209-3JPC	EW9209-3JPC.txt	C.wuellerstorfi	0.64 (2)	
EW9504-02	EW9504-02.txt	C.mckannai	0.64 (2)	
EW9504-03	EW9504-03.txt	C.mckannai	0.64 (2)	
EW9504-04	EW9504-04.txt	C.mckannai	0.64 (2)	

Table A.4 – continued from previous page

Site Name	File Name	Species	Offset	Comments
EW9504-05	EW9504-05.txt	C.mckannai	0.64 (2)	Age reversal caused by piecewise interpolation. Redid the interpolation over this interval. Consequently, age at 2.1m and 2.12m changed from 30.75kyr to 30.54 and 31.02kyr to 30.61kyr respectively
EW9504-08	EW9504-08.txt	C.mckannai	0.64 (2)	
EW9504-09	EW9504-09.txt	C.mckannai	0.64 (2)	
GeoB1112	GeoB1112.txt	Cibicidoides spp	0.64 (2)	
GeoB1118	GeoB1118.txt	Cibicidoides spp	0.64 (2)	
GeoB1710	GeoB1710.txt	C.wuellerstorfi	0.64 (2)	
GeoB3004	GeoB3004.txt	Multiple	0.64 (2), 0.49 (2), -0.3 (2)	
GeoB3327-5	GeoB3327.txt	C.wuellerstorfi	(1) but not explicit	
GeoB3388-1	GeoB3388.txt	C.wuellerstorfi	0.64 (2)	
GeoB3935	GeoB3935.txt	C.wuellerstorfi	0.64 (2)	
GeoB3938	GeoB3938.txt	C.wuellerstorfi	0.64 (2)	
GeoB4216	GeoB4216.txt	C.wuellerstorfi	0.64 (2)	
GIK12392-1	GIK12392.txt	C.wuellerstorfi/ U.hollicki	0.64 (2)	

Table A.4 – continued from previous page

Site Name	File Name	Species	Offset	Comments
GIK13519-1	GIK13519_1.txt	C.wuellerstorfi	0.64 (2)	
GIK13519-1	GIK13519_2.txt	C.wuellerstorfi	0.64 (2)	Type at 0.995 m. Redid a linear interpolation. Data change from 78.24kyr to 73.37kyr
GIK15612	GIK15612.txt	C.wuellerstorfi/ U.peregrina	0.64 (2)	
GIK15627	GIK15627.txt	C.wuellerstorfi	0.64 (2)	
GIK15637	GIK15637.txt	C.wuellerstorfi/ U.hollicki	0.64 (2)	
GIK16772	GIK16772.txt	C.wuellerstorfi	0.64 (2)	
GIK17049	GIK17049.txt	C.wuellerstorfi	0.64 (2)	
GIK23414	GIK23414.txt	C.wuellerstorfi	0.64 (2)	
GIK23415	GIK23415.txt	C.wuellerstorfi	0.64 (2)	
INMD114	INMD114.txt	Uvigerina spp	–	Age estimate at 3.19m is 0 in original author file. Corrected to 171.9kyr
LV28-42-4	LV28-42-4.txt	Uvigerina spp	–	
M16772	M16772.txt	C.wuellerstorfi	0.64 (2)	
M35027	M35027.txt	C.wuellerstorfi	0.64 (2)	
MD01-2378	MD01-2378_1.txt	C.wuellerstorfi	0.64 (2)	

Table A.4 – continued from previous page

Site Name	File Name	Species	Offset	Comments
MD01-2378	MD01-2378_2.txt	C.wuellerstorfi	0.64 (2)	Repeated ages due to resolution of the core and rounding errors. Taken directly from the contributor
MD01-2415	MD01-2415.txt	Uvigerina spp	–	
MD01-2416	MD01-2416.txt	Uvigerina spp	–	
MD01-2443	MD01-2443_1.txt	Not Specified	–	
MD01-2443	MD01-2443_2.txt	Not Specified	0.64 (2) after comparison with Tzedakis et al. (2009)	
MD01-2446	MD01-2446.txt	C.wuellerstorfi	0.64 (1)	
MD01-2448	MD01-2448.txt	C.wuellerstorfi/ Uvigerina spp	0.64 (1)	
MD02-2575	MD02-2575_1.txt	U.peregrina	–	
MD02-2575	MD02-2575_2.txt	U.peregrina	–	
MD02-2588	MD02-2588.txt	C.wuellerstorfi	0.64 (1)	
MD03-2692	MD03-2692.txt	Multiple	(1)	
MD03-2699	MD03-2699.txt	Cibicidoides spp/ Uvigerina spp	0.64(1)	
MD03-2705	MD03-2705.txt	C.wuellerstorfi	0.64(2)	
MD04-2881	MD04-2881.txt	U.peregrina	–	
MD05-2920	MD05-2920.txt	C.wuellerstorfi/ U.peregrina	0.64 (2)	

Table A.4 – continued from previous page

Site Name	File Name	Species	Offset	Comments
MD06-3018	MD06-3018.txt	C.wuellerstorfi	0.64 (1)	
MD12-3409	MD12-3409.txt	C.wuellerstorfi	0.64 (2)	
MD95-2042	MD95-2042.txt	Multiple	– (1)	
MD96-2048	MD96-2048.txt	C.wuellerstorfi	0.64 (2)	
MD96-2080	MD96-2080.txt	C.wuellerstorfi	0.64 (2)	
MD96-2086	MD96-2086.txt	C.wuellerstorfi	0.64 (2)	
MD96-2098	MD96-2098.txt	C.wuellerstorfi	0.64 (2)	
MD97-2120	MD97-2120.txt	C.wuellerstorfi	0.64 (1)	
MD97-2125	MD97-2125.txt	C.wuellerstorfi	0.64 (2)	
MV0502-4JC	MV0502_1.txt	Cibicidoides spp	0.64 (1)	
MV0502-4JC	MV0502_2.txt	Cibicidoides spp	0.64 (1)	
MV0502-4JC	MV0502_3.txt	Cibicidoides spp	0.64 (1)	
ODP1011	ODP1011.txt	C.wuellerstorfi	0.64 (2)	
ODP1014	ODP1014_1.txt	Multiple	–	
ODP1014	ODP1014_2.txt	Uvigerina spp	–	Age reversal in original author file. Not corrected. My guess is that they aligned the different pieces separately causing the age reversal

Table A.4 – continued from previous page

Site Name	File Name	Species	Offset	Comments
ODP1018	ODP1018.txt	Uvigerina spp/ C.wuellerstorfi/ C.pachyderma	0.64 (2)	
ODP1019	ODP1019.txt	C.wuellerstorfi/ Uvigerina spp	(1)	
ODP1058	ODP1058.txt	C.wuellerstorfi/ U.peregrina	0.64 (2)	
ODP1082	ODP1082.txt	C.wuellerstorfi	0.64 (2)	
ODP1083	ODP1083.txt	C.wuellerstorfi	0.64 (2)	
ODP1143	ODP1143.txt	C.wuellerstorfi/ U.peregrina	0.64 (1)	
ODP1146	ODP1146.txt	C.wuellerstorfi/ U.peregrina	–	
ODP1147	ODP1147.txt	Multiple	(1) Shackleton (1995)	
ODP1168	ODP1168.txt	C.wuellerstorfi	0.64 (2)	
ODP1170	ODP1170.txt	C.wuellerstorfi	0.64 (2)	
ODP1172	ODP1172.txt	C.wuellerstorfi	0.64 (2)	
ODP1208	ODP1208.txt	C.wuellerstorfi	0.64 (2)	
ODP1209	ODP1209.txt	C.wuellerstorfi/ U.peregrina	–	
ODP1236	ODP1236.txt	C.wuellerstorfi	0.64 (2)	
ODP1237	ODP1237.txt	C.wuellerstorfi	0.64 (2)	Ash layers
ODP1239	ODP1239.txt	C.wuellerstorfi	0.64 (2)	
ODP1241	ODP1241_1.txt	C.wuellerstorfi	0.64 (2)	
ODP1241	ODP1241_2.txt	C.wuellerstorfi	0.64 (2)	

Table A.4 – continued from previous page

Site Name	File Name	Species	Offset	Comments
ODP723	ODP723.txt	Uvigerina excellens	–	
ODP724	ODP724.txt	C.wuellerstorfi/ U.peregrina	0.64 (2)	
ODP806	ODP806.txt	C.wuellerstorfi	–	
ODP871	ODP871.txt	Uvigerina spp	–	Typo at 5.2. Corrected to 501.95kyr
ODP926	ODP926.txt	C.wuellerstorfi/ C.kullenbergi/ Uvigerina spp	0.64/–	Age reversals between 82.85 and 104.08. Do a linear interpolation. Deviation from original age models by up to 17kyr
ODP928	ODP928.txt	C.wuellerstorfi	0.64 (1)	
ODP959	ODP959.txt	C.wuellerstorfi	0.64 (2)	
ODP978	ODP978.txt	C.mundulus/ C.wuellerstorfi	0.64 (2)	
ODP980	ODP980.txt	C.wuellerstorfi	0.64 (2)	
PC-S2	PC-S2.txt	C.wuellerstorfi	0.64(2)	Age at 0.456m identified as -0.2 in the contributor file. Corrected to 30.19 by doing a linear interpolation in-between the two other points
PS2561-2	PS2561-2.txt	F. wuellerstorfi	0.64 (2)	

Table A.4 – continued from previous page

Site Name	File Name	Species	Offset	Comments
SU92-03	SU92-03.txt	C.wuellerstorfi/ U.peregrina	–	
TR163-31P	TR163-31P.txt	C.wuellerstorfi	0.64 (2)	
TT013-PC18	TT013-PC18.txt	C.wuellerstorfi	0.64 (2)	
TTN057-6-PC4	TTN057-6-PC4.txt	C.wuellerstorfi/ C.kullenbergi	0.64 (2)	
U1308	U1308.txt	C.wuellerstorfi	0.64 (2)	
U1313	U1313_1.txt	C.wuellerstorfi	0.64 (1)	
U1313	U1313_2.txt	C.wuellerstorfi	0.64 (1)	
U1313	U1313_3.txt	C.wuellerstorfi	0.64 (1)	
U1313	U1313_4.txt	C.mundulus/ C.wuellerstorfi/ Cibicidoides spp/ Uvigerina spp	0.64 (1)	
U1314	U1314_1.txt	C.wuellerstorfi	(1)	
U1314	U1314_2.txt	Cibicidoides spp	(1)	
U1343	U1343_1.txt	Multiple	(1)	Divided into multiple files due to change in sampling resolution
U1343	U1343_2.txt	C.wuellerstorfi	0.64 (1)	Divided into multiple files due to change in sampling resolution
V19-27	V19-27.txt	Cibicidoides spp	0.64 (2)	
V22-108	V22-108.txt	C.wuellerstorfi/ U.peregrina	0.64 (2)	
V29-135	V29-135.txt	C.wuellerstorfi	0.64 (2)	

Table A.4 – continued from previous page

Site Name	File Name	Species	Offset	Comments
V29-202	V29-202.txt	Multiple	(1)	
V30-97	V30-97.txt	C.wuellerstorfi/ Uvigerina spp	(1)	
Y74-2-22PC	Y74-2-22PC.txt	C.wuellerstorfi	0.64 (2)	
MD06-2990	MD06-2990.txt	C.wuellerstorfi	0.64(2)	
SO136-003	SO136-003.txt	C.wuellerstorfi	0.64(2)	
MD06-2986	MD06-2986.txt	C.wuellerstorfi	0.64(2)	

Table A.5: Information regarding an additional 123 benthic $\delta^{18}O$ records used to construct the Prob-stack (site name, file name, reference name, and reference link).

Site Name	File Name	Reference Name	Reference Link
82-24-23PC	82-24-23PC.txt	Sosdian and Rosenthal (2009)	doi:10.1126/science.1169938
AII107-131	AII107-131.txt	Jones et al. (1984)	doi:10.1016/0025-3227(84)90116-6
C9001C	C9001C.txt	Domituse et al. (2011)	doi:10.1127/0078-0421/2011/0007
DSDP214	DSDP214.txt	Karas et al. (2009)	doi:10.1038/ngeo520
DSDP548	DSDP548.txt	Khelifi et al. (2009)	doi:10.1130/G30058A.1
DSDP590	DSDP590.txt	Karas et al. (2011)	doi:10.1016/j.epsl.2010.10.028
DSDP593	DSDP593.txt	Cooke et al. (2008)	doi:10.1080/00288300809509846
DSDP594	DSDP594.txt	Dudley et al. (1994), Nelson et al. (1993)	doi:10.1016/0377-8398(94)90008-6; doi:10.1029/93PA01162
DSDP607	DSDP607.txt	Sosdian and Rosenthal (2009)	doi:10.1126/science.1169938
ELT49.019-PC	ELT49.019-PC.txt	Charles et al. (1991)	doi:10.1029/91PA02477
EW9209-1JPC	EW9209-1JPC.txt	Curry et al. (1999)	doi:10.1029/GM112p0059
EW9209-2JPC	EW9209-2JPC.txt	Curry et al. (1999)	doi:10.1029/GM112p0059
EW9209-3JPC	EW9209-3JPC.txt	Curry et al. (1999)	doi:10.1029/GM112p0059
EW9504-02	EW9504-02.txt	Stott et al. (2000)	doi:10.1029/1999PA000375
EW9504-03	EW9504-03.txt	Stott et al. (2000)	doi:10.1029/1999PA000375
EW9504-04	EW9504-04.txt	Stott et al. (2000)	doi:10.1029/1999PA000375
EW9504-05	EW9504-05.txt	Stott et al. (2000)	doi:10.1029/1999PA000375

Table A.5 – continued from previous page

Site Name	File Name	Reference Name	Reference Link
EW9504-08	EW9504-08.txt	Stott et al. (2000)	doi:10.1029/1999PA000375
EW9504-09	EW9504-09.txt	Stott et al. (2000)	doi:10.1029/1999PA000375
GeoB1112	GeoB1112.txt	Bickert and Wefer (1996), Mackensen and Bickert (1999)	doi:10.1007/978-3-642-80353-6_30; doi:10.1007/978-3-642-58646-0_9
GeoB1118	GeoB1118.txt	Bickert and Wefer (1996), Mackensen and Bickert (1999)	doi:10.1007/978-3-642-80353-6_30; doi:10.1007/978-3-642-58646-0_9
GeoB1710	GeoB1710.txt	Schmiedl and Mackensen (1997)	doi:10.1016/S0031-0182(96)00137-X
GeoB3004	GeoB3004.txt	Schmiedl and Mackensen (2006)	doi:10.1029/2006PA001284
GeoB3327-5	GeoB3327.txt	Ho et al. (2012)	doi:10.1029/2012PA002317
GeoB3388-1	GeoB3388.txt	Mohtadi et al. (2006)	doi:10.1029/2005PA001190
GeoB3935	GeoB3935.txt	Schlunz et al. (2000)	doi:10.1016/S0967-0637(99)00076-X
GeoB3938	GeoB3938.txt	Schlunz et al. (2000)	doi:10.1016/S0967-0637(99)00076-X
GeoB4216	GeoB4216.txt	Freudenthal et al. (2002)	doi:10.1016/S0967-0645(02)00101-7
GIK12392-1	GIK12392.txt	Zahn et al. (1986)	doi:10.1029/PA001i001p00027
GIK13519-1	GIK13519_1.txt	Sarnthein et al. (1984)	doi:10.1594/PANGAEA.548488
GIK13519-1	GIK13519_2.txt	Zahn et al. (1986)	doi:10.1029/PA001i001p00027
GIK15612	GIK15612.txt	Sarnthein et al. (1994)	doi:10.1029/93PA03301
GIK15627	GIK15627.txt	Sarnthein et al. (1994)	doi:10.1029/93PA03301
GIK15637	GIK15637.txt	Sarnthein et al. (1994)	doi:10.1029/93PA03301

Table A.5 – continued from previous page

Site Name	File Name	Reference Name	Reference Link
GIK16772	GIK16772.txt	Sarnthein et al. (1994)	doi:10.1029/93PA03301
GIK17049	GIK17049.txt	Jung (1996), Trauth (1995), Sarnthein et al. (1994)	doi:10.2312/reports-sfb313.1996.61; doi:10.2312/reports-gpi.1995.74; doi:10.1029/93PA03301
GIK23414	GIK23414.txt	Jung (1996)	doi:10.2312/reports-sfb313.1996.61
GIK23415	GIK23415.txt	Jung (1996)	doi:10.2312/reports-sfb313.1996.61
INMD114	INMD114.txt	Lyle et al. (2002)	doi:10.1029/2000PA000538
LV28-42-4	LV28-42-4.txt	Nurnberg and Tiedemann (2004)	doi:10.1029/2004PA001023
M16772	M16772.txt	Martin et al. (2002)	doi:10.1016/S0012-821X(02)00472-7
M35027	M35027.txt	Hüls (2000)	http://hdl.handle.net/10068/254146
MD01-2378	MD01-2378_1.txt	Holbourn et al. (2005)	doi:10.1029/2004PA001094
MD01-2378	MD01-2378_2.txt	Dürkop et al. (2008)	doi:10.1016/j.marmicro.2007.10.002
MD01-2415	MD01-2415.txt	Nurnberg and Tiedemann (2004)	doi:10.1029/2004PA001023
MD01-2416	MD01-2416.txt	Gebhardt et al. (2008)	doi:10.1029/2007PA001513
MD01-2443	MD01-2443_1.txt	Tzedakis et al. (2009)	doi:10.1016/j.epsl.2008.10.027
MD01-2443	MD01-2443_2.txt	Hodell et al. (2013), de Abreu et al. (2005), Martrat et al. (2007)	doi:10.1002/palo.20017; doi:10.1029/2004PA001091; doi:10.1126/science.1139994
MD01-2446	MD01-2446.txt	Voekler et al. (2010)	doi:10.5194/cp-6-531-2010

Table A.5 – continued from previous page

Site Name	File Name	Reference Name	Reference Link
MD01-2448	MD01-2448.txt	Toucanne et al. (2009)	doi:10.1016/j.quascirev.2009.01.006
MD02-2575	MD02-2575_1.txt	Ziegler et al. (2008)	doi:10.1038/ngeo277
MD02-2575	MD02-2575_2.txt	Nurnberg et al. (2008)	doi:10.1016/j.epsl.2008.04.051
MD02-2588	MD02-2588.txt	Ziegler et al. (2013)	doi:10.1038/ngeo1782
MD03-2692	MD03-2692.txt	Toucanne et al.(2008, 2010), Toucanne et al. (2009b), Penaud et al. (2008, 2009), Eynaud et al. (2007), Zaragosi et al. (2006), Mojtahid et al. (2005)	doi:10.1016/j.margeo.2007.08.006; doi:10.1016/j.epsl.2009.12.050; doi:10.1016/j.quascirev.2009.08.003; doi:10.1016/j.marmicro.2008.01.007; doi:10.1016/j.palaeo.2009.07.012; doi:10.1029/2006GC001496; doi:10.1007/s00367-006-0048-9; doi:10.1016/j.margeo.2005.07.007
MD03-2699	MD03-2699.txt	Voekler et al. (2010)	doi:10.5194/cp-6-531-2010
MD03-2705	MD03-2705.txt	Malaize et al. (2012)	doi:10.1016/j.yqres.2011.09.010
MD04-2881	MD04-2881.txt	Ziegler et al. (2010)	doi:10.5194/cp-6-63-2010
MD05-2920	MD05-2920.txt	Tachikawa et al. (2011)	doi:10.1016/j.quascirev.2011.09.016
MD06-3018	MD06-3018.txt	Russon et al. (2009)	doi:10.1029/2009PA001755
MD12-3409	MD12-3409.txt	Casse et al. (2015)	http://adsabs.harvard.edu/abs/2015EGUGA..17.5920C
MD95-2042	MD95-2042.txt	Martrat et al. (2007), Shackleton et al. (2000)	doi:10.1126/science.1139994; doi:10.1029/2000PA000513

Table A.5 – continued from previous page

Site Name	File Name	Reference Name	Reference Link
MD96-2048	MD96-2048.txt	Caley et al. (2011)	doi:10.5194/cp-7-1285-2011
MD96-2080	MD96-2080.txt	Rau et al. (2002)	doi:10.1016/S0025-3227(01)00213-4
MD96-2086	MD96-2086.txt	Pichevin et al. (2005)	doi:10.1016/j.margeo.2005.04.003
MD96-2098	MD96-2098.txt	Pichevin et al. (2005)	doi:10.1016/j.margeo.2005.04.003
MD97-2120	MD97-2120.txt	Pahnke and Zahn (2005)	doi:10.1126/science.1102163
MD97-2125	MD97-2125.txt	Tachikawa et al. (2009)	doi:10.1016/j.quascirev.2008.12.013
MV0502-4JC	MV0502_1.txt	Waddell et al. (2009)	doi:10.1029/2008PA001661
MV0502-4JC	MV0502_2.txt	Waddell et al. (2009)	doi:10.1029/2008PA001661
MV0502-4JC	MV0502_3.txt	Waddell et al. (2009)	doi:10.1029/2008PA001661
ODP1011	ODP1011.txt	Andreasen et al. (2000)	doi:10.2973/odp.proc.sr.167.225.2000
ODP1014	ODP1014_1.txt	deMenocal and Baker (2000)	doi:10.2973/odp.proc.sr.167.202.2000
ODP1014	ODP1014_2.txt	Hendy and Kennett (2000)	doi:10.2973/odp.proc.sr.167.205.2000
ODP1018	ODP1018.txt	Andreasen et al. (2000)	doi:10.2973/odp.proc.sr.167.225.2000
ODP1019	ODP1019.txt	Lyle et al. (2000)	doi:10.2973/odp.proc.sr.167.214.2000
ODP1058	ODP1058.txt	Bahr et al. (2013)	doi:10.1016/j.gloplacha.2013.08.013
ODP1082	ODP1082.txt	Dupont et al. (2005)	doi:10.1130/G21401.1
ODP1083	ODP1083.txt	Dupont et al. (2005)	doi:10.1130/G21401.1
ODP1143	ODP1143.txt	Cheng et al. (2004)	doi:10.2973/odp.proc.sr.184.221.2004
ODP1146	ODP1146.txt	Clemens et al. (2008)	doi:10.1029/2008PA001638

Table A.5 – continued from previous page

Site Name	File Name	Reference Name	Reference Link
ODP1147	ODP1147.txt	Cheng et al. (2004)	doi:10.2973/odp.proc.sr.184.221.2004
ODP1168	ODP1168.txt	Nuernberg et al. (2004)	doi:10.1029/151GM17
ODP1170	ODP1170.txt	Nuernberg et al. (2004)	doi:10.1029/151GM17
ODP1172	ODP1172.txt	Nuernberg et al. (2004)	doi:10.1029/151GM17
ODP1208	ODP1208.txt	Venti and Billups (2012)	doi:10.1016/j.palaeo.2012.02.001
ODP1209	ODP1209.txt	Bordiga et al. (2013)	doi:10.1016/j.palaeo.2012.12.021
ODP1236	ODP1236.txt	Tiedemann et al. (2007)	doi:10.2973/odp.proc.sr.202.210.2007
ODP1237	ODP1237.txt	Tiedemann et al. (2007)	doi:10.2973/odp.proc.sr.202.210.2007
ODP1239	ODP1239.txt	Tiedemann et al. (2007)	doi:10.2973/odp.proc.sr.202.210.2007
ODP1241	ODP1241_1.txt	Lalicata and Lea (2011)	doi:10.1016/j.marmicro.2011.01.002
ODP1241	ODP1241_2.txt	Tiedemann et al. (2007)	doi:10.2973/odp.proc.sr.202.210.2007
ODP723	ODP723.txt	Niitsuma et al. (1991)	doi:10.2973/odp.proc.sr.117.168.1991
ODP724	ODP724.txt	Zahn and Pedersen (1991)	doi:10.2973/odp.proc.sr.117.162.1991
ODP806	ODP806.txt	Lea et al. (2000)	doi:10.1126/science.289.5485.1719
ODP871	ODP871.txt	Dyez and Ravelo (2013)	doi:10.1130/G33425.1
ODP926	ODP926.txt	Franz (1999), Lisiecki et al. (2008)	doi:10.3289/GEOMAR_Report_084_1999; doi:10.1038/nature07425
ODP928	ODP928.txt	Lisiecki et al. (2008)	doi:10.1038/nature07425
ODP959	ODP959.txt	Giresse et al. (1998)	doi:10.2973/odp.proc.sr.159.041.1998

Table A.5 – continued from previous page

Site Name	File Name	Reference Name	Reference Link
ODP978	ODP978.txt	Khelifi et al. (2009)	doi:10.1130/G30058A.1
ODP980	ODP980.txt	Oppo et al. (2006)	doi:10.1016/j.quascirev.2006.07.006
PC-S2	PC-S2.txt	Yamane (2003)	doi:10.1016/S0377-8398(03)00017-3
PS2561-2	PS2561-2.txt	Krueger et al. (2012)	doi:10.1016/j.gloplacha.2011.10.001
SU92-03	SU92-03.txt	Salgueiro et al. (2010)	doi:10.1016/j.quascirev.2009.11.013
TR163-31P	TR163-31P.txt	Martin et al. (2002)	doi:10.1016/S0012-821X(02)00472-7
TT013-PC18	TT013-PC18.txt	Murray et al. (2000)	doi:10.1029/1999PA000457
TTN057-6-PC4	TTN057-6-PC4.txt	Hodell et al. (2003)	doi:10.2973/odp.proc.sr.177.120.2003
U1308	U1308.txt	Hodell ey al. (2008)	doi:10.1029/2008PA001591
U1313	U1313_1.txt	Bolton et al. (2010)	doi:10.1029/2010PA001951
U1313	U1313_2.txt	Ferretti et al. (2010)	doi:10.1016/j.epsl.2010.02.016
U1313	U1313_3.txt	Naafs et al. (2011)	doi:10.1029/2011PA002135
U1313	U1313_4.txt	Voelker et al. (2010)	doi:10.5194/cp-6-531-2010
U1314	U1314_1.txt	Alonso-Garcia et al. (2011)	doi:10.1016/j.palaeo.2011.09.004
U1314	U1314_2.txt	Hernandez-Almeida et al. (2012)	doi:10.1029/2011PA002209
U1343	U1343_1.txt	Asahi et al. (2014)	doi:10.1016/j.dsr2.2014.01.004
U1343	U1343_2.txt	Asahi et al. (2014)	doi:10.1016/j.dsr2.2014.01.004
V19-27	V19-27.txt	Mix et al. (1991)	doi:10.1029/90PA02303
V22-108	V22-108.txt	Charles et al. (1991)	doi:10.1029/91PA02477

Table A.5 – continued from previous page

Site Name	File Name	Reference Name	Reference Link
V29-135	V29-135.txt	Sarnthein et al. (1994)	doi:10.1029/93PA03301
V29-202	V29-202.txt	Oppo and Lehman (1995)	doi:10.1029/95PA02089
V30-97	V30-97.txt	McIntyre et al. (1989), Imbrie et al. (1989), Imbrie et al. (1992)	doi:10.1029/PA004i001p00019; doi:10.1007/978-94-009-2446-8_7; doi:10.1029/92PA02253
Y74-2-22PC	Y74-2-22PC.txt	Lyle et al. (2000)	doi:10.2973/odp.proc.sr.167.214.2000
MD06-2990	MD06-2990.txt	Ronge et al. (2015)	doi:10.1002/2014PA002727
SO136-003	SO136-003.txt	Ronge et al. (2015)	doi:10.1002/2014PA002727
MD06-2986	MD06-2986.txt	Ronge et al. (2015)	doi:10.1002/2014PA002727

Bibliography

[1] Montserrat Alonso-Garcia, Francisco J Sierro, and José A Flores. Arctic front shifts in the subpolar North Atlantic during the Mid-Pleistocene (800–400 ka) and their implications for ocean circulation. *Palaeogeography, Palaeoclimatology, Palaeoecology*, 311(3–4):268–280, 2011.

[2] C Andersson, D A Warnke, J E T Channell, J Stoner, and E Jansen. The mid-Pliocene (4.3–2.6 Ma) benthic stable isotope record of the Southern Ocean: ODP Sites 1092 and 704, Meteor Rise. *Palaeogeography, Palaeoclimatology, Palaeoecology*, 182(3–4):165–181, 2002.

[3] Dyke Andreasen, M Flower, M Harvey, S Chang, and A C Ravelo. Data Report: Late Pleistocene oxygen and carbon isotopic records from Sites 1011, 1012, and 1018. *Proceedings of the Ocean Drilling Program, Scientific Results*, 167:141–144, July 2000.

[4] J D Annan, D J Lunt, J C Hargreaves, and P J Valdes. Parameter estimation in an atmospheric GCM using the Ensemble Kalman Filter. *Nonlinear Processes in Geophysics*, 12(3):363–371, February 2005.

[5] H Asahi, S Kender, M Ikehara, T Sakamoto, K Takahashi, A C Ravelo, C A Alvarez Zarikian, B K Khim, and M J Leng. Orbital-scale benthic foraminiferal oxygen isotope stratigraphy at the northern Bering Sea Slope Site U1343 (IODP Expedition 323) and its Pleistocene paleoceanographic significance. *Deep Sea Research Part II: Topical Studies in Oceanography*, 2014.

[6] Kiyoshi Asai, Satoru Hayamizu, and Ken'ichi Handa. Prediction of protein secondary structure by the hidden Markov model. *Computer applications in the biosciences : CABIOS*, 9(2):141–146, 1993.

[7] André Bahr, Dirk Nurnberg, Cyrus Karas, and Jens Grützner. Millennial-scale versus long-term dynamics in the surface and subsurface of the western North Atlantic Subtropical Gyre during Marine Isotope Stage 5. *Global and Planetary Change*, 111:77–87, 2013.

[8] Frank C Bassinot, Laurent D Labeyrie, Edith Vincent, Xavier Quidelleur, Nicholas J Shackleton, and Yves Lancelot. The astronomical theory of cli-

mate and the age of the Brunhes-Matuyama magnetic reversal. *Earth and Planetary Science Letters*, 126(1):91–108, 1994.

[9] L E Baum. An equality and associated maximization technique in statistical estimation for probabilistic functions of markov processes. *Inequalities*, 3:1–8, 1972.

[10] Leonard E Baum, Ted Petrie, George Soules, and Norman Weiss. A Maximization Technique Occurring in the Statistical Analysis of Probabilistic Functions of Markov Chains. *The Annals of Mathematical Statistics*, 41(1):164–171, 1970.

[11] Wolfgang H Berger, Torsten Bickert, H Schmidt, and G Wefer. Quaternary Oxygen Isotope Record of Pelagic Foraminifers: Site 806, Ontong Java Plateau. *Proceedings of the Ocean Drilling Program, Scientific Results*, 130:381–395, April 1993.

[12] Torsten Bickert, William B Curry, and G Wefer. Late Pliocene to Holocene (2.6–0 Ma) western equatorial Atlantic deep-water circulation: inferences from benthic stable isotopes. *Proceedings of the Ocean Drilling Program, Scientific Results*, 154:239–254, September 1997.

[13] Torsten Bickert and G Wefer. Late Quaternary Deep Water Circulation in the South Atlantic: Reconstruction from Carbonate Dissolution and Benthic Stable Isotopes. In Gerold Wefer, Wolfgang H Berger, Gerold Siedler, and David J Webb, editors, *The South Atlantic*, pages 599–620. Springer Berlin Heidelberg, Berlin, Heidelberg, 1996.

[14] Katharina Billups. Climate science: Timing is everything during deglaciations. *Nature*, 522(7555):163–164, June 2015.

[15] Katharina Billups, A C Ravelo, and J C Zachos. Early Pliocene deep water circulation in the western equatorial Atlantic: Implications for high-latitude climate change. *Paleoceanography*, 13(1):84–95, February 1998.

[16] Timothé Bolliet, Ann Holbourn, Wolfgang Kuhnt, Carlo Laj, Catherine Kissel, Luc Beaufort, Markus Kienast, Nils Andersen, and Dieter Garbe-Schönberg. Mindanao Dome variability over the last 160 kyr: Episodic glacial cooling of the West Pacific Warm Pool. *Paleoceanography*, 26(1):PA1208, 2011.

[17] Clara T Bolton, Paul A Wilson, Ian Bailey, Oliver Friedrich, Christopher J Beer, Julia Becker, Soma Baranwal, and Ralf Schiebel. Millennial-scale climate variability in the subpolar North Atlantic Ocean during the late Pliocene. *Paleoceanography*, 25(4):PA4218, 2010.

[18] Manuela Bordiga, Luc Beaufort, Miriam Cobianchi, Claudia Lupi, Nicoletta Mancin, Valeria Luciani, Nicola Pelosi, and Mario Sprovieri. Calcareous plankton and geochemistry from the ODP site 1209B in the NW Pacific Ocean (Shatsky Rise): New data to interpret calcite dissolution and paleoproductivity changes of the last 450 ka. *Palaeogeography, Palaeoclimatology, Palaeoecology*, 371:93–108, 2013.

[19] Chris M Brierley, Alexey V Fedorov, Zhonghui Liu, Timothy D Herbert, Kira T Lawrence, and Jonathan P LaRiviere. Greatly Expanded Tropical Warm Pool and Weakened Hadley Circulation in the Early Pliocene. *Science*, 323(5922):1714–1718, 2009.

[20] Thibaut Caley, J H Kim, B Malaiz 'e, J Giraudeau, T Laepple, N Caillon, K Charlier, H Rebaubier, L Rossignol, I S Casta neda, S Schouten, and J S Sinninghe Damst 'e. High-latitude obliquity as a dominant forcing in the Agulhas current system. *Climate of the Past*, 7(4):1285–1296, 2011.

[21] M Casse, Bruno Malaizé, F Bassinot, N Caillon, T Degaridel-Thoron, H Rebaubier, K Charlier, Thibaut Caley, V Marieu, L Beaufort, V Rojas, L Meynadier, J P Valet, and Y Reaud. Gradual and small decrease of glacial sea surface temperatures in the eastern equatorial Indian ocean across the Mid-Pleistocene Transition. *EGU General Assembly Conference Abstracts*, 17:5920, April 2015.

[22] Christopher D Charles, Philip N Froelich, Michael A Zibello, Richard A Mortlock, and Joseph J Morley. Biogenic opal in Southern Ocean sediments over the last 450,000 years: Implications for surface water chemistry and circulation. *Paleoceanography*, 6(6):697–728, 1991.

[23] Jiajie Chen, John W Farrell, David W Murray, and Warren L Prell. Timescale and paleoceanographic implications of a 3.6 m.y. oxygen isotope record from the northeast Indian Ocean (Ocean Drilling Program Site 758). *Paleoceanography*, 10(1):21–47, February 1995.

[24] X Cheng, Jun Tian, and P Wang. Data Report: Stable Isotopes from Site 1143. *Proceedings of the Ocean Drilling Program, Scientific Results*, 184:1–8, 2004.

[25] X Cheng, Q Zhao, J Wang, Z Jain, P Xia, B Huang, D Fang, J Xu, Z Zhou, and P Wang. Data Report: Stable Isotopes from Sites 1147 and 1148. *Proceedings of the Ocean Drilling Program, Scientific Results*, 184:1–12, 2004.

[26] Gary A Churchill. Stochastic models for heterogeneous DNA sequences. *Bulletin of Mathematical Biology*, 51(1):79–94, 1989.

[27] O Chutatape, Liu Zheng, and S M Krishnan. Retinal blood vessel detection and tracking by matched Gaussian and Kalman filters. In *Engineering in Medicine and Biology Society, 1998. Proceedings of the 20th Annual International Conference of the IEEE*, pages 3144–3149 vol.6. IEEE, October 1998.

[28] Peter U Clark, David Archer, David Pollard, Joel D Blum, Jose A Rial, Victor Brovkin, Alan C Mix, Nicklas G Pisias, and Martin Roy. The middle Pleistocene transition: characteristics, mechanisms, and implications for long-term changes in atmospheric pCO2. *Quaternary Science Reviews*, 25(23–24):3150–3184, 2006.

[29] Peter U Clark, Arthur S Dyke, Jeremy D Shakun, Anders E Carlson, Jorie Clark, Barbara Wohlfarth, Jerry X Mitrovica, Steven W Hostetler, and A Marshall McCabe. The Last Glacial Maximum. *Science*, 325(5941):710–714, August 2009.

[30] Steven Clemens, David W Murray, and W L Prell. Nonstationary Phase of the Plio-Pleistocene Asian Monsoon. *Science*, 274(5289):943–948, November 1996.

[31] Steven C Clemens, Warren L Prell, Youbin Sun, Zhengyu Liu, and Guangshan Chen. Southern Hemisphere forcing of Pliocene δ^{18}O and the evolution of Indo-Asian monsoons. *Paleoceanography*, 23(4):PA4210, 2008.

[32] Maureen H Conte, Marie-Alexandrine Sicre, Carsten Rühlemann, John C Weber, Sonja Schulte, Detlef Schulz-Bull, and Thomas Blanz. Global temperature calibration of the alkenone unsaturation index ($U_{37}^{K'}$) in surface waters and comparison with surface sediments. *Geochem Geophys Geosyst*, 7(2):1–22, February 2006.

[33] Penelope J Cooke, Campbell S Nelson, and Martin P Crundwell. Miocene isotope zones, paleotemperatures, and carbon maxima events at intermediate water-depth, Site 593, Southwest Pacific. *New Zealand Journal of Geology and Geophysics*, 51(1):1–22, 2008.

[34] Thomas M Cover and Joy A Thomas. *Elements of Information Theory.* Wiley Series in Telecommunications. John Wiley & Sons, Inc., New York, USA, 1991.

[35] William B Curry, T M Marchitto, J F McManus, Delia W Oppo, and K L Laarkamp. Millennial-scale changes in ventilation of the thermocline, intermediate, and deep waters of the glacial North Atlantic. In *The Carbon Cycle and Atmospheric CO2: Natural Variations Archean to Present*, pages 59–76. American Geophysical Union, Washington, D. C., 1999.

[36] William B Curry and K G Miller. Oxygen and carbon isotopic variation in Pliocene benthic foraminifers of the Equatorial Atlantic. *Proceedings of the Ocean Drilling Program, Scientific Results*, 108:157–166, 1989.

[37] Lúcia de Abreu, Fátima F Abrantes, Nicholas J Shackleton, Polychronis C Tzedakis, Jerry F McManus, Delia W Oppo, and Michael A Hall. Ocean climate variability in the eastern North Atlantic during interglacial marine isotope stage 11: A partial analogue to the Holocene? *Paleoceanography*, 20(3):PA3009, 2005.

[38] P deMenocal and L Baker. Data Report: Benthic stable isotope data from Sites 1014 and 1020 (0.6–1.2 Ma). *Proceedings of the Ocean Drilling Program, Scientific Results*, 167:145–150, July 2000.

[39] Peter B deMenocal, Delia W Oppo, Richard G Fairbanks, and Warren L Prell. Pleistocene δ13C Variability of North Atlantic Intermediate Water. *Paleoceanography*, 7(2):229–250, April 1992.

[40] G H Denton, R F Anderson, J R Toggweiler, R L Edwards, J M Schaefer, and A E Putnam. The last glacial termination. *Science*, 328(5986):1652–1656, June 2010.

[41] Clara Deser, Adam S Phillips, and Michael A Alexander. Twentieth century tropical sea surface temperature trends revisited. *Geophysical Research Letters*, 37(10):L10701, 2010.

[42] Hanako Domitsu, Jun-Ichi Uchida, Kaoru Ogane, Nana Dobuchi, Tokiyuki Sato, Minoru Ikehara, Hiroshi Nishi, Shiro Hasegawa, and Motoyoshi Oda. Stratigraphic relationships between the last occurrence of Neogloboquadrina inglei and marine isotope stages in the northwest Pacific, D/V Chikyu Expedition 902, Hole C9001C. *Newsletters on Stratigraphy*, 44(2):113–122, June 2011.

[43] Nathalie Dubois, Markus Kienast, Claire Normandeau, and Timothy D Herbert. Eastern equatorial Pacific cold tongue during the Last Glacial Maximum as seen from alkenone paleothermometry. *Paleoceanography*, 24(4):PA4207, 2009.

[44] Walter C Dudley and Campbell S Nelson. The influence of non-equilibrium isotope fractionation on the Quaternary calcareous nannofossil stable isotope signal in the southwest Pacific Ocean, DSDP Site 594. *Marine Micropaleontology*, 24(1):3–27, 1994.

[45] Lydie M Dupont, Barbara Donner, Laurence Vidal, Elena M Pérez, and Gerold Wefer. Linking desert evolution and coastal upwelling: Pliocene climate change in Namibia. *Geology*, 33(6):461–464, 2005.

[46] Richard Durbin, Sean R Eddy, Anders Krogh, and Graeme Mitchison. Biological sequence analysis. *Cambridge university press*, 1998.

[47] Anke Dürkop, Ann Holbourn, Wolfgang Kuhnt, Rina Zuraida, Nils Andersen, and Pieter M Grootes. Centennial-scale climate variability in the Timor Sea during Marine Isotope Stage 3. *Marine Micropaleontology*, 66(3–4):208–221, 2008.

[48] Kelsey A Dyez and A Christina Ravelo. Late Pleistocene tropical Pacific temperature sensitivity to radiative greenhouse gas forcing. *Geology*, 41(1):23–26, 2013.

[49] Bjørn Eraker, C W Chiu, Andrew Foerster, Tae Bong Kim, and Hernan Seoane. Bayesian Mixed Frequency VAR's. *Manuscript, University of Wisconsin*, 2008.

[50] F Eynaud, Sébastien Zaragosi, J D Scourse, M Mojtahid, J F Bourillet, I R Hall, A Penaud, M Locascio, and A Reijonen. Deglacial laminated facies on the NW European continental margin: The hydrographic significance of British-Irish Ice Sheet deglaciation and Fleuve Manche paleoriver discharges. *Geochemistry, Geophysics, Geosystems*, 8(6):Q06019, 2007.

[51] Patrizia Ferretti, Simon J Crowhurst, Michael A Hall, and Isabel Cacho. North Atlantic millennial-scale climate variability 910 to 790 ka and the role of the equatorial insolation forcing. *Earth and Planetary Science Letters*, 293(1–2):28–41, 2010.

[52] B P Flower, Delia W Oppo, J F McManus, K A Venz, David A Hodell, and J L Cullen. North Atlantic Intermediate to Deep Water circulation and chemical stratification during the past 1 Myr. *Paleoceanography*, 15(4):388–403, 2000.

[53] Sven-Oliver Franz. *Pliozäne Zeitreihen zur Rekonstruktion der Tiefenwasserzirkulation und der siliziklastischen Amazonasfracht im äquatorialen Westatlantik (Ceara-Schwelle, ODP Leg 154).* PhD thesis, Christian-Albrechts-Universität, 1999.

[54] Nicholas Fraser, Wolfgang Kuhnt, Ann Holbourn, Timothé Bolliet, Nils Andersen, Thomas Blanz, and Luc Beaufort. Precipitation variability within the West Pacific Warm Pool over the past 120ka: Evidence from the Davao Gulf, southern Philippines. *Paleoceanography*, 29(11):1094–1110, 2014.

[55] Tim Freudenthal, Helge Meggers, Jorijntje Henderiks, Holger Kuhlmann, Ana Moreno, and Gerold Wefer. Upwelling intensity and filament activity off Morocco during the last 250,000 years. *Deep Sea Research Part II: Topical Studies in Oceanography*, 49(17):3655–3674, 2002.

[56] Holger Gebhardt, Michael Sarnthein, Pieter M Grootes, Thorsten Kiefer, Hartmut Kuehn, Frank Schmieder, and Ursula Röhl. Paleonutrient and productivity records from the subarctic North Pacific for Pleistocene glacial terminations I to V. *Paleoceanography*, 23(4):PA4212, 2008.

[57] W Hale and U Pflaumann. Sea-Surface Temperature Estimations Using a Modern Analog Technique with Foraminiferal Assemblages from Western Atlantic Quaternary Sediments. In *Use of Proxies in Paleoceanography*, pages 69–90. Springer Berlin Heidelberg, Berlin, Heidelberg, 1999.

[58] Ian R Hall, I Nicholas McCave, Nicholas J Shackleton, Graham P Weedon, and Sara E Harris. Intensified deep Pacific inflow and ventilation in Pleistocene glacial times. *Nature*, 412(6849):809–812, August 2001.

[59] James D Hamilton. Rational-expectations econometric analysis of changes in regime. *Journal of Economic Dynamics and Control*, 12(2):385–423, 1988.

[60] James D Hamilton. A New Approach to the Economic Analysis of Nonstationary Time Series and the Business Cycle. *Econometrica*, 57(2):357–384, March 1989.

[61] James D Hamilton. *The Time Series Analysis.* Princeton University Press, 1994.

[62] J C Hargreaves, J D Annan, N R Edwards, and R Marsh. An efficient climate forecasting method using an intermediate complexity Earth System Model and the ensemble Kalman filter. *Climate Dynamics*, 23(7):745–760, 2004.

[63] S E Harris. Data Report: Late Pliocene-Pleistocene Carbon and Oxygen Stable Isotopes from Benthic Foraminifers at Ocean Drilling Program Site 1123 in the Southwest Pacific. *Proceedings of the Ocean Drilling Program, Scientific Results*, 181:1–20, May 2002.

[64] A C Harvey and R G Pierse. Estimating Missing Observations in Economic Time Series. *Journal of the American Statistical Association*, 79(385):125–131, 1984.

[65] M R Hassan and B Nath. Stock market forecasting using hidden Markov model: a new approach. In *Intelligent Systems Design and Applications, 2005. ISDA '05. Proceedings. 5th International Conference on*, pages 192–196. IEEE, September 2005.

[66] Gerald H Haug and Ralf Tiedemann. Effect of the formation of the Isthmus of Panama on Atlantic Ocean thermohaline circulation. *Nature*, 393(6686):673–676, June 1998.

[67] I L Hendy and J P Kennett. Stable isotope stratigraphy and paleoceanography of the last 170 k.y.: Site 1014, Tanner Basin, California. *Proceedings of the Ocean Drilling Program, Scientific Results*, 167:129–140, July 2000.

[68] T D Herbert, J D Schuffert, Dyke Andreasen, L Heusser, Mitchell W Lyle, A C Mix, A C Ravelo, Lowell D Stott, and J C Herguera. Collapse of the California Current During Glacial Maxima Linked to Climate Change on Land. *Science*, 293(5527):71–76, 2001.

[69] Timothy D Herbert, Laura Cleaveland Peterson, Kira T Lawrence, and Zhonghui Liu. Tropical Ocean Temperatures Over the Past 3.5 Million Years. *Science*, 328(5985):1530–1534, 2010.

[70] I Hernández-Almeida, F J Sierro, I Cacho, and J A Flores. Impact of suborbital climate changes in the North Atlantic on ice sheet dynamics at the Mid-Pleistocene Transition. *Paleoceanography*, 27(3):PA3214, 2012.

[71] Sze Ling Ho, Gesine Mollenhauer, Frank Lamy, Alfredo Martínez-Garcia, Mahyar Mohtadi, Rainer Gersonde, Dierk Hebbeln, Samuel Nunez-Ricardo, Antoni Rosell-Melé, and Ralf Tiedemann. Sea surface temperature variability in the Pacific sector of the Southern Ocean over the past 700 kyr. *Paleoceanography*, 27(4):PA4202, 2012.

[72] David A Hodell, James E T Channell, Jason H Curtis, Oscar E Romero, and Ursula Röhl. Onset of "Hudson Strait" Heinrich events in the eastern North Atlantic at the end of the middle Pleistocene transition (∼640 ka)? *Paleoceanography*, 23(4):PA4218, 2008.

[73] David A Hodell, Christopher D Charles, J H Curtis, P G Mortyn, U S Ninnemann, and K A Venz. Data report: Oxygen isotope stratigraphy of ODP Leg 177 Sites 1088, 1089, 1090, 1093, and 1094. *Proceedings of the Ocean Drilling Program, Scientific Results*, 177:1–26, January 2003.

[74] David A Hodell, Christopher D Charles, and F J Sierro. Late Pleistocene evolution of the ocean's carbonate system. *Earth and Planetary Science Letters*, 192(2):109–124, 2001.

[75] David A Hodell, Simon Crowhurst, Luke Skinner, Polychronis C Tzedakis, Vasiliki Margari, James E T Channell, George Kamenov, Suzanne Maclachlan, and Guy Rothwell. Response of Iberian Margin sediments to orbital and suborbital forcing over the past 420ka. *Paleoceanography*, 28(1):185–199, 2013.

[76] David A Hodell and Kathryn Venz. Toward a high-resolution stable isotopic record of the Southern Ocean during the Pliocene-Pleistocene (4.8 TO 0.8 MA). In J P Kennett and D A Warkne, editors, *The Antarctic Paleoenvironment: A Perspective on Global Change: Part One*, pages 265–310. American Geophysical Union, Washington, D. C., 1992.

[77] Ann Holbourn, Wolfgang Kuhnt, Hiroshi Kawamura, Zhimin Jian, Piet Grootes, Helmut Erlenkeuser, and Jian Xu. Orbitally paced paleoproductivity variations in the Timor Sea and Indonesian Throughflow variability during the last 460 kyr. *Paleoceanography*, 20(3):PA3002, 2005.

[78] S A Hovan, D K Rea, and N G Pisias. Late Pleistocene Continental Climate and Oceanic Variability Recorded in Northwest Pacific Sediments. *Paleoceanography*, 6(3):349–370, 1991.

[79] Boyin Huang, Viva F Banzon, Eric Freeman, Jay Lawrimore, Wei Liu, Thomas C Peterson, Thomas M Smith, Peter W Thorne, Scott D Woodruff, and Huai-Min Zhang. Extended Reconstructed Sea Surface Temperature Version 4 (ERSST.v4). Part I: Upgrades and Intercomparisons. *Journal of Climate*, 28(3):911–930, 2015.

[80] J P Hughes, P Guttorp, and S P Charles. A non-homogeneous hidden Markov model for precipitation occurrence. *Journal of the Royal Statistical Society: Series C (Applied Statistics)*, 48(1):15–30, 1999.

[81] C M Hüls. Millennial-scale SST variability as inferred from planktonic foraminifera sensus counts in the western subtropical Atlantic. *GEOMAR Report, GEOMAR Research Center for Marine Geosciences, Christian Albrechts University in Kiel*, 95:1–118, 2000.

[82] Peter Huybers and Carl Wunsch. A depth-derived Pleistocene age model: Uncertainty estimates, sedimentation variability, and nonlinear climate change. *Paleoceanography*, 19(1):PA1028, 2004.

[83] John Z Imbrie, E A Boyle, Steven Clemens, A Duffy, W R Howard, G Kukla, J Kutzbach, D G Martinson, A McIntyre, A C Mix, B Molfino, J J Morley, L C Peterson, N G Pisias, W L Prell, Maureen E Raymo, Nicholas J Shackleton, and J R Toggweiler. On the Structure and Origin of Major Glaciation Cycles 1. Linear Responses to Milankovitch Forcing. *Paleoceanography*, 7(6):701–738, 1992.

[84] John Z Imbrie, J D Hays, D G Martinson, A McIntyre, A C Mix, J J Morley, N G Pisias, W L Prell, and Nicholas J Shackleton. The orbital theory of Pleistocene climate: support from a revised chronology of the marine δ^{18} O record. In Andre Berger, John Z Imbrie, J Hays, G Kukla, and B Saltzman, editors, *Milankovitch and Climate: Understanding the Response to Astronomical Forcing*, page 269, 1984.

[85] John Z Imbrie, Andrew McIntyre, and Alan Mix. Oceanic Response to Orbital Forcing in the Late Quaternary: Observational and Experimental Strategies. In Andre Berger, S Schneider, and J Cl Duplessy, editors, *Climate and Geo-Sciences*, pages 121–164. Springer Netherlands, Dordrecht, 1989.

[86] Zhimin Jian, Quanhong Zhao, Xinrong Cheng, Jiliang Wang, Pinxian Wang, and Xin Su. Pliocene–Pleistocene stable isotope and paleoceanographic changes in the northern South China Sea. *Palaeogeography, Palaeoclimatology, Palaeoecology*, 193(3–4):425–442, 2003.

[87] Glenn A Jones, David A Johnson, and William B Curry. High-resolution stratigraphy in late Pleistocene/Holocene sediments of the Vema Channel. *Marine Geology*, 58(1–2):59–87, 1984.

[88] J Jouzel, V Masson-Delmotte, O Cattani, G Dreyfus, S Falourd, G Hoffmann, B Minster, J Nouet, J M Barnola, J Chappellaz, H Fischer, J C Gallet, S Johnsen, M Leuenberger, L Loulergue, D Luethi, H Oerter, F Parrenin, G Raisbeck, D Raynaud, A Schilt, J Schwander, E Selmo, R Souchez, R Spahni, B Stauffer, J P Steffensen, B Stenni, T F Stocker, J L Tison, M Werner, and E W Wolff. Orbital and millennial Antarctic climate variability over the past 800,000 years. *Science*, 317(5839):793–796, August 2007.

[89] B H JUANG and L R RABINER. Mixture Autoregressive Hidden Markov-Models for Speech Signals. *Acoustics, Speech and Signal Processing, IEEE Transactions on*, 33(6):1404–1413, 1985.

[90] S J.A. Jung. Wassermassenaustausch zwischen NE-Atlantik und Nordmeer während der letzten 300.000/80.000 Jahre im Abbild stabiler 0- und C-lsotope. *Berichte aus dem Sonderforschungsbereich 313, Christian-Albrechts-Universität zu Kiel*, 61:1–154, 1996.

[91] R E Kalman. A New Approach to Linear Filtering and Prediction Problems. *Journal of Basic Engineering*, 82(1):35–45, 1960.

[92] R E Kalman and R S Bucy. New Results in Linear Filtering and Prediction Theory. *Journal of Basic Engineering*, 83(1):95–108, 1961.

[93] Cyrus Karas, Dirk Nurnberg, Anil K Gupta, Ralf Tiedemann, Kuppusamy Mohan, and Torsten Bickert. Mid-Pliocene climate change amplified by a switch in Indonesian subsurface throughflow. *Nature Geoscience*, 2(6):434–438, May 2009.

[94] Cyrus Karas, Dirk Nurnberg, Ralf Tiedemann, and Dieter Garbe-Schönberg. Pliocene climate change of the Southwest Pacific and the impact of ocean gateways. *Earth and Planetary Science Letters*, 301(1–2):117–124, 2011.

[95] D B Karner, J Levine, B P Medeiros, and R A Muller. Constructing a stacked benthic δ^{18}O record. *Paleoceanography*, 17(3):2–1–2–16, July 2002.

[96] J J Kennedy, N A Rayner, R O Smith, D E Parker, and M Saunby. Reassessing biases and other uncertainties in sea surface temperature observations measured in situ since 1850: 1. Measurement and sampling uncertainties. *Journal of Geophysical Research: Atmospheres*, 116(D14):D14103, 2011.

[97] Nabil Khélifi, Michael Sarnthein, N Andersen, Thomas Blanz, M Frank, D Garbe-Schonberg, B A Haley, R Stumpf, and M Weinelt. A major and long-term Pliocene intensification of the Mediterranean outflow, 3.5-3.3 Ma ago. *Geology*, 37(9):811–814, September 2009.

[98] D Khider, G Huerta, C Jackson, Lowell D Stott, and J Emile-Geay. A Bayesian, multivariate calibration for Globigerinoides ruber Mg/Ca. *Geochemistry, Geophysics, Geosystems*, 16(9):2916–2932, 2015.

[99] D Khider, C S Jackson, and Lowell D Stott. Assessing millennial-scale variability during the Holocene: A perspective from the western tropical Pacific. *Paleoceanography*, 29(3):143–159, 2014.

[100] B Kısakürek, A Eisenhauer, F Böhm, D Garbe-Schonberg, and J Erez. Controls on shell Mg/Ca and Sr/Ca in cultured planktonic foraminiferan, Globigerinoides ruber (white). *Earth and Planetary Science Letters*, 273(3-4):260–269, September 2008.

[101] S Krueger, D C Leuschner, W Ehrmann, Gerhard Schmiedl, and Andreas Mackensen. North Atlantic Deep Water and Antarctic Bottom Water variability during the last 200 ka recorded in an abyssal sediment core off South Africa. *Global and Planetary Change*, 80–81:180–189, 2012.

[102] Joseph J Lalicata and David W Lea. Pleistocene carbonate dissolution fluctuations in the eastern equatorial Pacific on glacial timescales: Evidence from ODP Hole 1241. *Marine Micropaleontology*, 79(1–2):41–51, 2011.

[103] Kira T Lawrence, Zhonghui Liu, and Timothy D Herbert. Evolution of the eastern tropical Pacific through Plio-Pleistocene glaciation. *Science*, 312(5770):79–83, April 2006.

[104] David W Lea, Pamela A Martin, Dorothy K Pak, and Howard J Spero. Reconstructing a 350 ky history of sea level using planktonic Mg/Ca and oxygen isotope records from a Cocos Ridge core. *Quaternary Science Reviews*, 21(1–3):283–293, 2002.

[105] David W Lea, Dorothy K Pak, Christina L Belanger, Howard J Spero, Mike A Hall, and Nicholas J Shackleton. Paleoclimate history of Galápagos surface waters over the last 135,000 yr. *Quaternary Science Reviews*, 25(11–12):1152–1167, 2006.

[106] David W Lea, Dorothy K Pak, and Howard J Spero. Climate Impact of Late Quaternary Equatorial Pacific Sea Surface Temperature Variations. *Science*, 289(5485):1719–1724, 2000.

[107] Ted Petrie Leonard E Baum. Statistical Inference for Probabilistic Functions of Finite State Markov Chains. *The Annals of Mathematical Statistics*, 37(6):1554–1563, 1966.

[108] Li Li, Qianyu Li, Jun Tian, Pinxian Wang, Hui Wang, and Zhonghui Liu. A 4-Ma record of thermal evolution in the tropical western Pacific and its implications on climate change. *Earth and Planetary Science Letters*, 309(1–2):10–20, 2011.

[109] Q Li, R G Mark, and G D Clifford. Robust heart rate estimation from multiple asynchronous noisy sources using signal quality indices and a Kalman filter. *Physiological Measurement*, 29(1):15, 2008.

[110] Luan Lin, Deborah Khider, Lorraine E Lisiecki, and Charles E Lawrence. Probabilistic sequence alignment of stratigraphic records. *Paleoceanography*, 29(10):976–989, 2014.

[111] Lorraine E Lisiecki and Philip A Lisiecki. Application of dynamic programming to the correlation of paleoclimate records. *Paleoceanography*, 17(4):1049, October 2002.

[112] Lorraine E Lisiecki and Maureen E Raymo. A Pliocene-Pleistocene stack of 57 globally distributed benthic δ^{18}O records. *Paleoceanography*, 20(1):PA1003, March 2005.

[113] Lorraine E Lisiecki, Maureen E Raymo, and William B Curry. Atlantic overturning responses to Late Pleistocene climate forcings. *Nature*, 456(7218):85–88, November 2008.

[114] Mitchell W Lyle, A C Mix, A C Ravelo, Dyke Andreasen, L Heusser, and A Olivarez. Millennial-scale CaCO3 and Corg events along the northern and central California margins: stratigraphy and origins. *Proceedings of the Ocean Drilling Program, Scientific Results*, 167:163–182, July 2000.

[115] Mitchell W Lyle, Alan Mix, and Nicklas Pisias. Patterns of CaCO3 deposition in the eastern tropical Pacific Ocean for the last 150 kyr: Evidence for a southeast Pacific depositional spike during marine isotope stage (MIS) 2. *Paleoceanography*, 17(2):3–1–3–13, 2002.

[116] Andreas Mackensen and Torsten Bickert. Stable Carbon Isotopes in Benthic Foraminifera: Proxies for Deep and Bottom Water Circulation and New Production. In *Use of Proxies in Paleoceanography*, pages 229–254. Springer Berlin Heidelberg, Berlin, Heidelberg, 1999.

[117] Bruno Malaizé, Elsa Jullien, Amandine Tisserand, Charlotte Skonieczny, E Francis Grousset, Frédérique Eynaud, Catherine Kissel, Jérôme Bonnin, Svenja Karstens, Philippe Martinez, Aloys Bory, Vivianne Bout-Roumazeilles, Thibaut Caley, Xavier Crosta, Karine Charlier, Linda Rossignol, José-Abel Flores, and Ralph Schneider. The impact of African aridity on the isotopic signature of Atlantic deep waters across the Middle Pleistocene Transition. *Quaternary Research*, 77(1):182–191, 2012.

[118] Nathan J Mantua, Steven R Hare, Yuan Zhang, John M Wallace, and Robert C Francis. A Pacific Interdecadal Climate Oscillation with Impacts on Salmon Production. *Bull. Amer. Meteor. Soc.*, 78(6):1069–1079, June 1997.

[119] Pamela A Martin, David W Lea, Yair Rosenthal, Nicholas J Shackleton, Michael Sarnthein, and Thomas Papenfuss. Quaternary deep sea temperature histories derived from benthic foraminiferal Mg/Ca. *Earth and Planetary Science Letters*, 198(1–2):193–209, 2002.

[120] Belen Martrat, Joan O Grimalt, Nicholas J Shackleton, Lúcia de Abreu, Manuel A Hutterli, and Thomas F Stocker. Four Climate Cycles of Recurring Deep and Surface Water Destabilizations on the Iberian Margin. *Science*, 317(5837):502–507, 2007.

[121] K Mc Intyre, A C Ravelo, and M L Delaney. North Atlantic Intermediate Waters in the Late Pliocene to Early Pleistocene. *Paleoceanography*, 14(3):324–335, 1999.

[122] Andrew McIntyre, William F Ruddiman, Karen Karlin, and Alan C Mix. Surface water response of the equatorial Atlantic Ocean to orbital forcing. *Paleoceanography*, 4(1):19–55, 1989.

[123] Jerry F McManus, Delia W Oppo, and James L Cullen. A 0.5-Million-Year Record of Millennial-Scale Climate Variability in the North Atlantic. *Science*, 283(5404):971–975, 1999.

[124] A C Mix, J Le, and Nicholas J Shackleton. Benthic Foraminiferal Stable Isotope Stratigraphy of Site 846: 0-1.8 Ma. *Proceedings of the Ocean Drilling Program, Scientific Results*, 138:839–854, August 1995.

[125] A C Mix, N G Pisias, W Rugh, J Wilson, A Morey, and T K Hagelberg. Benthic Foraminifer Stable Isotope Record from Site 849 (0-5 Ma): Local and Global Climate Changes. *Proceedings of the Ocean Drilling Program, Scientific Results*, 138:371–412, August 1995.

[126] A C Mix, N G Pisias, R Zahn, W Rugh, C Lopez, and K Nelson. Carbon 13 in Pacific Deep and Intermediate Waters, 0-370 ka: Implications for Ocean Circulation and Pleistocene CO2. *Paleoceanography*, 6(2):205–226, 1991.

[127] Mahyar Mohtadi, Dierk Hebbeln, Samuel Nunez-Ricardo, and Carina B Lange. El Niño–like pattern in the Pacific during marine isotope stages (MIS) 13 and 11? *Paleoceanography*, 21(1):PA1015, 2006.

[128] M Mojtahid, F Eynaud, Sébastien Zaragosi, J Scourse, J F Bourillet, and T Garlan. Palaeoclimatology and palaeohydrography of the glacial stages on Celtic and Armorican margins over the last 360000 yrs. *Marine Geology*, 224(1-4):57–82, November 2005.

[129] M Mudelsee. TAUEST: a computer program for estimating persistence in unevenly spaced weather/climate time series. *Computers & Geosciences*, 28:69–72, February 2002.

[130] R W Murray, C Knowlton, M Leinen, A C Mix, and C H Polsky. Export production and carbonate dissolution in the central equatorial Pacific Ocean over the past 1 Myr. *Paleoceanography*, 15(6):570–592, 2000.

[131] B David A Naafs, Jens Hefter, Patrizia Ferretti, Ruediger Stein, and Gerald H Haug. Sea surface temperatures did not control the first occurrence of Hudson Strait Heinrich Events during MIS 16. *Paleoceanography*, 26(4):PA4201, 2011.

[132] A V Nefian and M H Hayes. An embedded HMM-based approach for face detection and recognition. In *Acoustics, Speech, and Signal Processing, 1999. Proceedings., 1999 IEEE International Conference on*, pages 3553–3556 vol.6. IEEE, March 1999.

[133] Campbell S Nelson, Penelope J Cooke, Chris H Hendy, and Alison M Cuthbertson. Oceanographic and climatic changes over the past 160,000 years at Deep Sea Drilling Project Site 594 off southeastern New Zealand, southwest Pacific Ocean. *Paleoceanography*, 8(4):435–458, 1993.

[134] Nobuaki Niitsuma, Tadamichi Oba, and Makoto Okada. Oxygen and carbon isotope stratigraphy at Site 723, Oman Margin. *Proceedings of the Ocean Drilling Program, Scientific Results*, 117:321–341, 1991.

[135] Dragoslav Ninkovich and Nicholas J Shackleton. Distribution, stratigraphic position and age of ash layer "L", in the Panama Basin region. *Earth and Planetary Science Letters*, 27(1):20–34, 1975.

[136] Dirk Nurnberg, Natasja Brughmans, Joachim Schönfeld, Ulysses Ninnemann, and Christian Dullo. Paleo-export production, terrigenous flux and sea surface temperatures around Tasmania: Implications for glacial/interglacial changes in the Subtropical Convergence zone. In N F Exon, J P Kennett, and M J Malone, editors, *The Carbon Cycle and Atmospheric CO2: Natural Variations Archean to Present*, pages 291–318. American Geophysical Union, Washington, D. C., 2004.

[137] Dirk Nurnberg and Ralf Tiedemann. Environmental change in the Sea of Okhotsk during the last 1.1 million years. *Paleoceanography*, 19(4):PA4011, 2004.

[138] Dirk Nurnberg, Martin Ziegler, Cyrus Karas, Ralf Tiedemann, and Matthew W Schmidt. Interacting Loop Current variability and Mississippi River discharge over the past 400 kyr. *Earth and Planetary Science Letters*, 272(1–2):278–289, 2008.

[139] Delia W Oppo, R G Fairbanks, A L Gordon, and Nicholas J Shackleton. Late Pleistocene Southern Ocean δ13C variability. *Paleoceanography*, 5(1):43–54, 1990.

[140] Delia W Oppo and Scott J Lehman. Suborbital timescale variability of North Atlantic Deep Water during the past 200,000 years. *Paleoceanography*, 10(5):901–910, 1995.

[141] Delia W Oppo, Jerry F McManus, and James L Cullen. Evolution and demise of the Last Interglacial warmth in the subpolar North Atlantic. *Quaternary Science Reviews*, 25(23–24):3268–3277, 2006.

[142] Delia W Oppo, JF McManus, and JL Cullen. Abrupt climate events 500,000 to 340,000 years ago: evidence from subpolar north atlantic sediments. *Science*, 279(5355):1335–1338, February 1998.

[143] Delia W Oppo and Youbin Sun. Amplitude and timing of sea-surface temperature change in the northern South China Sea: Dynamic link to the East Asian monsoon. *Geology*, 33(10):785–788, 2005.

[144] D R Ostermann and William B Curry. Calibration of stable isotopic data: An enriched δ18O standard used for source gas mixing detection and correction. *Paleoceanography*, 15(3):353–360, 2000.

[145] F Gadel L Serve P Giresse, J P Barusseau, L Serve, and J P Barusseau. Indicators of climate and sediment-source variations at Site 959: implications for the reconstruction of paleoenvironments in the Gulf of Guinea through Pleistocene times. *Proceedings of the Ocean Drilling Program, Scientific Results*, 159:585–603, 1998.

[146] Katharina Pahnke and Rainer Zahn. Southern Hemisphere Water Mass Conversion Linked with North Atlantic Climate Variability. *Science*, 307(5716):1741–1746, 2005.

[147] A Penaud, F Eynaud, J L Turon, Sébastien Zaragosi, Bruno Malaizé, Samuel Toucanne, and J F Bourillet. What forced the collapse of European ice sheets during the last two glacial periods (150 ka B.P. and 18 ka cal B.P.)? Palynological evidence. *Palaeogeography, Palaeoclimatology, Palaeoecology*, 281(1–2):66–78, 2009.

[148] A Penaud, F Eynaud, J L Turon, Sébastien Zaragosi, F Marret, and J F Bourillet. Interglacial variability (MIS 5 and MIS 7) and dinoflagellate cyst assemblages in the Bay of Biscay (North Atlantic). *Marine Micropaleontology*, 68(1–2):136–155, 2008.

[149] L Pichevin, M Cremer, J Giraudeau, and P Bertrand. A 190 ky record of lithogenic grain-size on the Namibian slope: Forging a tight link between past wind-strength and coastal upwelling dynamics. *Marine Geology*, 218(1–4):81–96, 2005.

[150] C Pierre, J F Saliege, M J Urrutiaguer, and J Giraudeau. Stable isotope record of the last 500 k.y. at Site 1087 (Southern Cape Basin). *Proceedings of the Ocean Drilling Program, Scientific Results*, 175:1–22, April 2001.

[151] N G Pisias, D G Martinson, T C Moore, Nicholas J Shackleton, W Prell, J Hays, and G Boden. High resolution stratigraphic correlation of benthic oxygen isotopic records spanning the last 300,000 years. *Marine Geology*, 56(1):119–136, 1984.

[152] David Pollard and Robert M DeConto. Modelling West Antarctic ice sheet growth and collapse through the past five million years. *Nature*, 458(7236):329–332, March 2009.

[153] Warren L Prell, John Z Imbrie, Douglas G Martinson, Joseph J Morley, Nicklas G Pisias, Nicholas J Shackleton, and Harold F Streeter. Graphic correlation of oxygen isotope stratigraphy application to the Late Quaternary. *Paleoceanography*, 1(2):137–162, 1986.

[154] Lawrence R Rabiner. A tutorial on hidden Markov models and selected applications in speech recognition. *Proceedings of the IEEE*, 77(2):257–286, February 1989.

[155] L Bruce Railsback, Philip L Gibbard, Martin J Head, Ny Riavo G Voarintsoa, and Samuel Toucanne. An optimized scheme of lettered marine isotope substages for the last 1.0 million years, and the climatostratigraphic nature of isotope stages and substages. *Quaternary Science Reviews*, 111:94–106, 2015.

[156] A J Rau, J Rogers, J R E Lutjeharms, J Giraudeau, J A Lee-Thorp, M T Chen, and C Waelbroeck. A 450-kyr record of hydrological conditions on the western Agulhas Bank Slope, south of Africa. *Marine Geology*, 180(1–4):183–201, 2002.

[157] Maureen E Raymo, David A Hodell, and E Jansen. Response of deep ocean circulation to initiation of northern hemisphere glaciation (3-2 MA). *Paleoceanography*, 7(5):645–672, 1992.

[158] Maureen E Raymo, Delia W Oppo, and William B Curry. The Mid-Pleistocene climate transition: A deep sea carbon isotopic perspective. *Paleoceanography*, 12(4):546–559, August 1997.

[159] Maureen E Raymo, Delia W Oppo, B P Flower, David A Hodell, J F McManus, K A Venz, K F Kleiven, and K McIntyre. Stability of North Atlantic water masses in face of pronounced climate variability during the Pleistocene. *Paleoceanography*, 19(2):PA2008, 2004.

[160] Maureen E Raymo, William F Ruddiman, J Backman, B M Clement, and D G Martinson. Late Pliocene variation in northern hemisphere ice sheets and North Atlantic deep water circulation. *Paleoceanography*, 4(4):413–446, August 1989.

[161] Maureen E Raymo, William F Ruddiman, Nicholas J Shackleton, and Delia W Oppo. Evolution of Atlantic-Pacific δ13C gradients over the last 2.5 m.y. *Earth and Planetary Science Letters*, 97(3–4):353–368, 1990.

[162] N A Rayner, D E Parker, E B Horton, C K Folland, L V Alexander, D P Rowell, E C Kent, and A Kaplan. Global analyses of sea surface temperature, sea ice, and night marine air temperature since the late nineteenth century. *Journal of Geophysical Research: Atmospheres*, 108(D14):4407, 2003.

[163] Daniel Rincón-Martínez, Frank Lamy, Sergio Contreras, Guillaume Leduc, Edouard Bard, Cornelia Saukel, Thomas Blanz, Andreas Mackensen, and Ralf Tiedemann. More humid interglacials in Ecuador during the past 500 kyr linked to latitudinal shifts of the equatorial front and the Intertropical Convergence Zone in the eastern tropical Pacific. *Paleoceanography*, 25(2):PA2210, 2010.

[164] Thomas A Ronge, Silke Steph, Ralf Tiedemann, Matthias Prange, Ute Merkel, Dirk Nurnberg, and Gerhard Kuhn. Pushing the boundaries: Glacial/interglacial variability of intermediate and deep waters in the southwest Pacific over the last 350,000 years. *Paleoceanography*, 30(2):23–38, 2015.

[165] William F Ruddiman, Maureen E Raymo, D G Martinson, B M Clement, and J Backman. Pleistocene evolution: Northern hemisphere ice sheets and North Atlantic Ocean. *Paleoceanography*, 4(4):353–412, August 1989.

[166] Eric Ruggieri. A Bayesian approach to detecting change points in climatic records. *International Journal of Climatology*, 33(2):520–528, March 2012.

[167] Eric Ruggieri and Charles E Lawrence. The Bayesian Change Point and Variable Selection Algorithm: Application to the δ^{18}O Proxy Record of the Plio-Pleistocene. *Journal of Computational and Graphical Statistics*, 23(1):87–110, February 2014.

[168] T Russon, M Elliot, C Kissel, G Cabioch, P De Deckker, and T Corrège. Middle-late Pleistocene deep water circulation in the southwest subtropical Pacific. *Paleoceanography*, 24(4):PA4205, 2009.

[169] E Salgueiro, A H L Voelker, Lúcia de Abreu, Fátima F Abrantes, H Meggers, and G Wefer. Temperature and productivity changes off the western Iberian margin during the last 150 ky. *Quaternary Science Reviews*, 29(5–6):680–695, 2010.

[170] F S Samaria and A C Harter. Parameterisation of a stochastic model for human face identification. In *Applications of Computer Vision, 1994., Proceedings of the Second IEEE Workshop on*, pages 138–142. IEEE, December 1994.

[171] Michael Sarnthein, H Erlenkeuser, R Von Grafenstein, and C Schröder. Stable-isotope stratigraphy for the last 750,000 years: “Meteor” core 13519 from the eastern equatorial Atlantic. *Meteor Forschungsergebnisse, Reihe C: Geologie und Geophysik*, 38:9–24, 1984.

[172] Michael Sarnthein, Kyaw Winn, Simon J A Jung, Jean-Claude Duplessy, Laurent Labeyrie, Helmut Erlenkeuser, and Gerald Ganssen. Changes in East Atlantic Deepwater Circulation over the last 30,000 years: Eight time slice reconstructions. *Paleoceanography*, 9(2):209–267, 1994.

[173] B Schlünz, R R Schneider, P J Müller, and G Wefer. Late Quaternary organic carbon accumulation south of Barbados: influence of the Orinoco and Amazon rivers? *Deep Sea Research Part I: Oceanographic Research Papers*, 47(6):1101–1124, 2000.

[174] Gerhard Schmiedl and Andreas Mackensen. Late Quaternary paleoproductivity and deep water circulation in the eastern South Atlantic Ocean: Evidence from benthic foraminifera. *Palaeogeography, Palaeoclimatology, Palaeoecology*, 130(1–4):43–80, 1997.

[175] Gerhard Schmiedl and Andreas Mackensen. Multispecies stable isotopes of benthic foraminifers reveal past changes of organic matter decomposition and deepwater oxygenation in the Arabian Sea. *Paleoceanography*, 21(4):PA4213, 2006.

[176] M Schulz and Manfred Mudelsee. REDFIT: estimating red-noise spectra directly from unevenly spaced paleoclimatic time series. *Computers & Geosciences*, 28:421–426, April 2002.

[177] Nicholas J Shackleton. New data on the evolution of Pliocene climatic variability. Vrba, ES, Denton, GH, Partridge, TC and Burckle, LH (eds.) : 242-248. In E S Vrba, Denton G H, T C Partridge, and L H Burckle, editors, *Paleoclimate and evolution with emphasis on human origins*, pages 242–248. Yale University Press, 1995.

[178] Nicholas J Shackleton, Andre Berger, and W R Peltier. An alternative astronomical calibration of the lower Pleistocene timescale based on ODP Site 677. *Transactions of the Royal Society of Edinburgh: Earth Sciences*, 81(04):251–261, January 1990.

[179] Nicholas J Shackleton and M A Hall. Oxygen and Carbon Isotope Stratigraphy of Deep Sea Drilling Project Hole 552A: Plio-Pleistocene Glacial History. *Initial Reports of the Deep Sea Drilling Project*, 81:599–609, December 1984.

[180] Nicholas J Shackleton, M A Hall, and D Pate. Pliocene Stable Isotope Stratigraphy of Site 846. *Proceedings of the Ocean Drilling Program, Scientific Results*, 138:337–355, August 1995.

[181] Nicholas J Shackleton, Michael A Hall, and Edith Vincent. Phase relationships between millennial-scale events 64,000–24,000 years ago. *Paleoceanography*, 15(6):565–569, 2000.

[182] Nicholas J Shackleton and N G Pisias. Atmospheric carbon dioxide, orbital forcing, and climate. In *The Carbon Cycle and Atmospheric CO2: Natural Variations Archean to Present*, pages 303–317. American Geophysical Union, Washington, D. C., 1985.

[183] C E Shannon. A Mathematical Theory of Communication. *Bell System Technical Journal*, 27(3):379–423, 1948.

[184] Robert H Shumway and David S Stoffer. *Time Series Analysis and Its Applications.* Springer Science, November 2010.

[185] Sindia Sosdian and Yair Rosenthal. Deep-Sea Temperature and Ice Volume Changes Across the Pliocene-Pleistocene Climate Transitions. *Science*, 325(5938):306–310, 2009.

[186] Lowell D Stott, M Neumann, and D Hammond. Intermediate water ventilation on the Northeastern Pacific Margin during the Late Pleistocene inferred from benthic foraminiferal δ13C. *Paleoceanography*, 15(2):161–169, 2000.

[187] Kazuyo Tachikawa, Olivier Cartapanis, Laurence Vidal, Luc Beaufort, Tatiana Barlyaeva, and Edouard Bard. The precession phase of hydrological variability in the Western Pacific Warm Pool during the past 400 ka. *Quaternary Science Reviews*, 30(25–26):3716–3727, 2011.

[188] Kazuyo Tachikawa, Axel Timmermann, Laurence Vidal, Corinne Sonzogni, and Oliver Elison Timm. CO_2 radiative forcing and Intertropical Convergence Zone influences on western Pacific warm pool climate over the past 400 ka. *Quaternary Science Reviews*, 86:24–34, 2014.

[189] Kazuyo Tachikawa, Laurence Vidal, Corinne Sonzogni, and Edouard Bard. Glacial/interglacial sea surface temperature changes in the Southwest Pacific ocean over the past 360 ka. *Quaternary Science Reviews*, 28(13–14):1160–1170, 2009.

[190] Jun Tian, Pinxian Wang, Xinrong Cheng, and Qianyu Li. Astronomically tuned Plio–Pleistocene benthic δ18O record from South China Sea and Atlantic–Pacific comparison. *Earth and Planetary Science Letters*, 203(3–4):1015–1029, 2002.

[191] Ralf Tiedemann. Acht Millionen Jahre Klimageschichte von Nordwest Afrika und Paläozeanographie des angrenzenden Atlantiks. *Geologisches Paläontologisches Institut Universität Kiel*, 46, 1991.

[192] Ralf Tiedemann, Michael Sarnthein, and Nicholas J Shackleton. Astronomic timescale for the Pliocene Atlantic δ18O and dust flux records of Ocean Drilling Program Site 659. *Paleoceanography*, 9(4):619–638, August 1994.

[193] Ralf Tiedemann, Arne Sturm, Silke Steph, Steven P Lund, and Joseph Stoner. Astronomically calibrated timescales from 6 to 2.5 Ma and benthic isotope stratigraphies, Sites 1236, 1237, 1239, and 1241. *Proceedings of the Ocean Drilling Program, Scientific Results*, 202:1–69, 2007.

[194] Samuel Toucanne, Sébastien Zaragosi, J F Bourillet, M Cremer, F Eynaud, B Van Vliet-Lanoë, A Penaud, C Fontanier, J L Turon, and E Cortijo. Timing of massive 'Fleuve Manche' discharges over the last 350kyr: insights into the European ice-sheet oscillations and the European drainage network from MIS 10 to 2. *Quaternary Science Reviews*, 28(13-14):1238–1256, June 2009.

[195] Samuel Toucanne, Sébastien Zaragosi, J F Bourillet, P L Gibbard, F Eynaud, J Giraudeau, J L Turon, M Cremer, E Cortijo, P Martinez, and L Rossignol. A 1.2 Ma record of glaciation and fluvial discharge from the West European Atlantic margin. *Quaternary Science Reviews*, 28(25–26):2974–2981, 2009.

[196] Samuel Toucanne, Sébastien Zaragosi, J F Bourillet, F Naughton, M Cremer, F Eynaud, and B Dennielou. Activity of the turbidite levees of the Celtic–Armorican margin (Bay of Biscay) during the last 30,000 years: Imprints of the last European deglaciation and Heinrich events. *Marine Geology*, 247(1–2):84–103, 2008.

[197] Samuel Toucanne, Sébastien Zaragosi, Jean-François Bourillet, Vincent Marieu, Michel Cremer, Masa Kageyama, Brigitte Van Vliet-Lanoë, Frédérique Eynaud, Jean-Louis Turon, and Philip L Gibbard. The first estimation of Fleuve Manche palaeoriver discharge during the last deglaciation: Evidence for Fennoscandian ice sheet meltwater flow in the English Channel ca 20–18 ka ago. *Earth and Planetary Science Letters*, 290(3–4):459–473, 2010.

[198] Martin H. Trauth. Bioturbate Signalverzerrung hochauflösender paläoozeanographischer Zeitreihen. *Reports, Geologisch-Paläontologisches Institut und Museum, Christian-Albrechts-Universität, Kiel*, 74:1–167, 1995.

[199] Polychronis C Tzedakis, H Pälike, K H Roucoux, and Lúcia de Abreu. Atmospheric methane, southern European vegetation and low-mid latitude links on orbital and millennial timescales. *Earth and Planetary Science Letters*, 277(3–4):307–317, 2009.

[200] Nicholas L Venti and Katharina Billups. Stable-isotope stratigraphy of the Pliocene–Pleistocene climate transition in the northwestern subtropical Pacific. *Palaeogeography, Palaeoclimatology, Palaeoecology*, 326–328:54–65, 2012.

[201] Paul Viefers. Bayesian Inference for the Mixed-Frequency VAR Model, 2011.

[202] Katherine Visser, Robert Thunell, and Lowell Stott. Magnitude and timing of temperature change in the Indo-Pacific warm pool during deglaciation. *Nature*, 421(6919):152–155, January 2003.

[203] A H L Voelker, T Rodrigues, K Billups, Delia W Oppo, J McManus, R Stein, J Hefter, and J O Grimalt. Variations in mid-latitude North Atlantic surface water properties during the mid-Brunhes (MIS 9-14) and their implications for the thermohaline circulation. *Climate of the Past*, 6(4):531–552, 2010.

[204] Lindsey M Waddell, Ingrid L Hendy, Theodore C Moore, and Mitchell W Lyle. Ventilation of the abyssal Southern Ocean during the late Neogene: A new perspective from the subantarctic Pacific. *Paleoceanography*, 24(3):PA3206, 2009.

[205] M B Wilk and R Gnanadesikan. Probability plotting methods for the analysis for the analysis of data. *Biometrika*, 55(1):1–17, 1968.

[206] Douglas F Williams, Robert C Thunell, Eric Tappa, Domenico Rio, and Isabella Raffi. Chronology of the pleistocene oxygen isotope record: 0–1.88 m.y. B.P. *Palaeogeography, Palaeoclimatology, Palaeoecology*, 64(3):221–240, 1988.

[207] Masayuki Yamane. Late Quaternary variations in water mass in the Shatsky Rise area, northwest Pacific Ocean. *Marine Micropaleontology*, 48(3–4):205–223, 2003.

[208] Matthias Zabel, Torsten Bickert, Lars Dittert, and Ralf R Haese. Significance of the sedimentary AlTi ratio as an indicator for variations in the circulation patterns of the equatorial North Atlantic. *Paleoceanography*, 14(6):789–799, 1999.

[209] R Zahn and T F Pedersen. Late Pleistocene evolution of surface and mid-depth hydrography at the Oman Margin: planktonic and benthic isotope records at Site 724. *Proceedings of the Ocean Drilling Program, Scientific Results*, 117:291–308, 1991.

[210] Rainer Zahn, Kyaw Winn, and Michael Sarnthein. Benthic foraminiferal δ13C and accumulation rates of organic carbon: Uvigerina Peregrina group and Cibicidoides Wuellerstorfi. *Paleoceanography*, 1(1):27–42, 1986.

[211] Sébastien Zaragosi, Jean-François Bourillet, Frédérique Eynaud, Samuel Toucanne, Benjamin Denhard, Aurélie Van Toer, and Valentine Lanfumey. The impact of the last European deglaciation on the deep-sea turbidite systems of the Celtic-Armorican margin (Bay of Biscay). *Geo-Marine Letters*, 26(6):317–329, November 2006.

[212] Paul Zarchan and Howard Musoff. *Fundamentals Of Kalman Filtering.* A Practical Approach. Aiaa, April 2005.

[213] Meixun Zhao, Chi-Yue Huang, Chia-Chun Wang, and Ganjian Wei. A millennial-scale $U_{37}^{K'}$ sea-surface temperature record from the South China Sea (8°N) over the last 150 kyr: Monsoon and sea-level influence. *Palaeogeography, Palaeoclimatology, Palaeoecology*, 236(1–2):39–55, 2006.

[214] M Ziegler, L J Lourens, E Tuenter, and G J Reichart. High Arabian Sea productivity conditions during MIS 13 - odd monsoon event or intensified overturning circulation at the end of the Mid-Pleistocene transition? *Climate of the Past*, 6(1):63–76, 2010.

[215] Martin Ziegler, Paula Diz, Ian R Hall, and Rainer Zahn. Millennial-scale changes in atmospheric CO_2 levels linked to the Southern Ocean carbon isotope gradient and dust flux. *Nature Geoscience*, 6(6):457–461, April 2013.

[216] Martin Ziegler, Dirk Nurnberg, Cyrus Karas, Ralf Tiedemann, and Lucas J Lourens. Persistent summer expansion of the Atlantic Warm Pool during glacial abrupt cold events. *Nature Geoscience*, 1(9):601–605, August 2008.

[217] Walter Zucchini and Peter Guttorp. A Hidden Markov Model for Space-Time Precipitation. *Water Resources Research*, 27(8):1917–1923, 1991.